O. G. Bagmut

TRANSMISSION ELECTRON MICROSCOPY OF STRUCTURAL AND PHASE TRANSFORMATIONS IN FILMS AT “IN SITU” IMPACTS

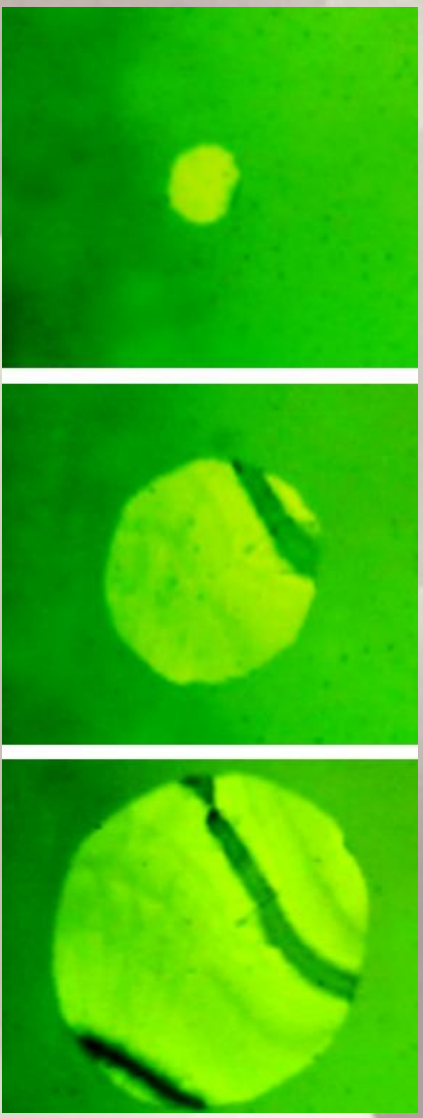

Monograph

MINISTRY OF EDUCATION AND SCIENCE OF UKRAINE
THE NATIONAL TECHNICAL UNIVERSITY
"KHARKIV POLYTECHNIC INSTITUTE"

O. G. Bagmut

TRANSMISSION ELECTRON MICROSCOPY OF STRUCTURAL AND PHASE TRANSFORMATIONS IN FILMS AT “IN SITU” IMPACTS

Monograph

Recommended by the Academic Council
National Technical University
«Kharkiv Polytechnic Institute»

Kharkiv - 2026

UDC 548.4/620.18
B14

Reviewers:
S. I. Shevchenko, Doctor of science in physics and mathematics, Laureate of the State Prize of Ukraine, leading researcher B. Verkin Institute for Low Temperature Physics and Engineering;
V. M. Beresnev, Honored Worker of Science and Technology of Ukraine, Doctor of Technical Sciences, Professor of V.N. Karazin Kharkiv National University

Published by decision of the Academic Council NTU «KhPI», circular number 12 dated November 28, 2025

Bagmut O. G.

B14 Transmission electron microscopy of structural and phase transformations in films at “in situ” impacts : Monograph / O. G. Bagmut. - Kharkiv : NTU «KhPI», 2026. - 225 p.

ISBN 978-617-05-0581-1

The monograph describes the results of electron microscopic studies of the kinetics of structural and phase transformations in amorphous films initiated by radiation and thermal exposure directly in the microscope column.

For graduate students and students of physical and technical specialties, scientists.

Ill. 118. Tab. 23. Bibliogr. 197 names.

UDC 548.4/620.18

ISBN 978-617-05-0581-1

INTRODUCTION

Currently, there is a significant intensification of research on the structure and properties of amorphous (non-crystalline) materials in the form of thin-layer coatings and films. Amorphous materials are used in almost all areas of electronic instrumentation. The reliable and trouble-free operation of electronic devices is directly dependent on the stability of the amorphous structure of the substances that make up the elements of an electronic device.

However, for most materials the amorphous state is metastable. Hence, amorphous films can crystallize spontaneously or due to physical actions, transforming into a more stable crystalline state. The transition between amorphous and crystalline states has no fixed transformation temperature (as opposed to melting or boiling temperature) and can occur at different rates in a wide temperature range. Crystallization of an amorphous substance is a first-order phase transition. One of its types is polymorphous crystallization, whereby a substance converts from the amorphous into the crystalline state without changes in composition. This is typical for both pure elements and stoichiometric chemical compounds.

Spontaneous polymorphous crystallization of an amorphous layer (natural aging) can take a long time (years and decades). This complicates the prediction of the reliability and durability of an electronic device. However, there is a possibility of a comprehensive study of the structural transition from the amorphous to the crystalline state of matter outside the device. It is possible to model and analyze the phase transition by means of a controlled physical impact on the substance.

Electron irradiation is effective in causing the crystallization of amorphous films. Crystallization modeling can be done inside a transmission electron microscope (TEM). In a certain mode of operation of the microscope, the electron beam that forms an image can initiate the crystallization of an object with an amorphous structure. In this case, film crystallization can be observed visually (“in situ” method). The combination of different TEM operating

modes and electron microscopy provides comprehensive information on the structural, morphological, and kinetic parameters of the crystallization process.

Each substance reveals its transition path from an amorphous state to a crystalline one. The classification of these pathways carried out according to the most appropriate parameters, provides both qualitative and quantitative systematization of the phase transformation. As applied to thin amorphous films that crystallize under the influence of electron irradiation, the appropriate parameters are structural and morphological characteristics. These are the size, shape, structure, orientation, and number density of crystalline nuclei growing in an amorphous medium. They make it possible to attribute the reaction qualitatively to one or another crystallization mode.

The relative length δ, considered in this work, can serve as a quantitative characteristic of the crystallization mode. This is a dimensionless number equal to the ratio of the characteristic unit of length to the value of the geometric parameter of the elementary cell of the crystal. Determination of δ is possible using the electron microscopic method “in situ” and video recording of the fast crystallization process.

This monograph is devoted to the results of experimental studies of thin films, associated with the use of transmission electron microscopy only. It consists of nine sections.

The first section "Structural and phase transformations at “in situ” impacts" is devoted to radiation and thermal initiation of structural and phase transformations, as well as the destruction of thin amorphous films. Particular attention is paid to the electron microscopic method for determining changes in the density of a substance during crystallization of an amorphous films.

The second section "Polymorphous transformation in Ni and Ni-Pd films". Phase, structural, magnetic and volume transformations in thin-film laser condensates of Ni and Ni-Pd alloys under thermal and electron beam exposure were investigated.

The third section "Crystallization of oxygen-containing amorphous films" is devoted to the preparation and study of amorphous oxygen-saturated gold and selenium films. Crystallization is accompanied by stratification of the

medium into crystalline and gas components. In Au-O films electrical resistance decreases abruptly.

The fourth section "On the classification of crystallization reactions in thin amorphous films". Crystallization of amorphous films is classified based on electron microscopic analysis of the process. Four crystallization modes are identified and their qualitative (structure and morphology) and quantitative (dimensionless length δ_0) characteristics are given. These are layer, island, dendritic polymorphous crystallization, as well as fluid-phase crystallization.

The fifth section "Layer polymorphous crystallization mode". The results of studies of the layer polymorphous crystallization of amorphous films of Cr_2O_3, V_2O_3, Nb_2O_5 and Ti-Zr-Ni alloy are presented. The kinetics of disk-shaped, sickle-shaped, needle-shaped growth and epitaxy of Cr_2O_3 crystals are described in detail.

The sixth section "One-stage and two-stage crystallization of amorphous films of antimony sulfide". The results of electron microscopic studies of the kinetics of one-stage and two-stage crystallization of amorphous films of Sb2S3 are presented.

The seventh section "Polymodal polymorphous crystallization of tantalum pentoxide". Three crystallization modes in amorphous Ta_2O_5 films were studied. Namely layer, interjacent and island polymorphous crystallization mode as a result of polyamorphism in amorphous film.

The eighth section "Island polymorphous crystallization mode". The results of electron microscopic studies “in situ” with video recording of the crystallization kinetics of amorphous films of ZrO_2, Sb_2Se_3 and Yb_2O_2S are presented.

The ninth section "Dendrite polymorphous crystallization mode of HfO_2" is devoted to a comprehensive study of the kinetics of dendritic crystallization of hafnium dioxide. The one-stage and two-stage process of dendrite formation and the implementation of geometric selection during the formation of dendritic branches are described. The relative change in the density of the film substance during its crystallization is measured.

The author express his sincere gratitude to the reviewers of the monograph: Doctor of Technical Sciences, Laureate of the State Prize of Ukraine, Professor V. M. Beresnev and Doctor of science in physics and mathematics, Laureate of the State Prize of Ukraine, Professor Shevchenko S. I. for valuable comments on the content of the manuscript, as well as engineer Reznik N. A. for help in conducting electron microscopy studies.

1. STRUCTURAL AND PHASE TRANSFORMATIONS AT "IN SITU" IMPACTS

1.1. About the electron-beam induced and heat-induced crystallization of amorphous films

The passage of electrons through the film causes its Joule-Lenz heating (excitation of phonons) and can creates radiation damage. For excitation of phonons, energy of ~ 0.01 eV is sufficient [1]. Therefore, heating of the film to one degree or another is always present. When using accelerating voltage of 100 - 125 kV and a current of 50 - 75 μA without a condenser diaphragm and with appropriate beam focusing at the object, it is possible to obtain a high temperature, sufficient not only for crystallization of amorphous Fe-C films [2], but also for the melting of refractory materials, such as carbon [3]).

An important damage to unstable and organic substances is ionization, which leads to the chemical decomposition of a substance under the influence of an electron beam. Elementary radiation action is the direct knocking out of atoms from their positions and the formation of primary point defects. Their coagulation (at the appropriate temperature) can initiate the crystallization of an amorphous substance, that is resistant to chemical decomposition.

To create radiation damage, an electron must transfer energy to atom E_T, that exceeds the threshold displacement energy E_D (24 - 40 eV for metals [4]).

$$E_T = 2E\cdot(E+2m_0c^2)\, M_X^{-1}c^{-2}, \qquad (1.1)$$

where m_0 is the electron rest mass, M_X is the mass of the atom and c is the speed of light. With an accelerating voltage of 100 kV, the electron energy E = 100 keV. The masses of the atoms M_X, that make up the film under study, and the corresponding energies E_T, calculated according to relation (1.1), are given in Table 1.1. According to this table, E_T are in the range of 1 - 8 eV, which is clearly less than the threshold displacement energy E_D.

At an accelerating voltage of 100 kV (as in our case), the electron energy is not enough to create significant radiation damage in the studied film.

Table 1.1. Transferred energy E_T to an atom by electron, accelerated with voltage of 100 kV (according to relation (1.1))

№	Atom X	Atomic weight	Mass of the atom M_X (kg)	Transfer energy to atom E_T, (eV)	Crystallizable amorphous film	References
1	S	32.065	$5.32 \cdot 10^{-26}$	7.51	Yb_2O_2S	[5]
2	Ti	47.867	$7.95 \cdot 10^{-26}$	5.03	$Ti_{41}Zr_{41}Ni_{18}$	[6]
3	V	50.941	$8.46 \cdot 10^{-26}$	4.72	V_2O_3	[7]
4	Cr	51.996	$8.63 \cdot 10^{-26}$	4.63	Cr_2O_3	[8]
5	Ni	58.693	$9.79 \cdot 10^{-26}$	4.08	$Ti_{41}Zr_{41}Ni_{18}$	[6]
6	Se	78.96	$1.31 \cdot 10^{-25}$	3.05	Sb_2Se_3	[9]
7	Zr	91.225	$1.51 \cdot 10^{-25}$	2.65	$Ti_{41}Zr_{41}Ni_{18}$ ZrO_2	[6, 10]
8	Nb	92.906	$1.54 \cdot 10^{-25}$	2.6	Nb_2O_5	[11]
9	Sb	121.76	$2.02 \cdot 10^{-25}$	2.59	Sb_2Se_3	[9]
10	Yb	173.04	$2.87 \cdot 10^{-25}$	1.39	Yb_2O_2S	[5]
11	Hf	178.49	$2.96 \cdot 10^{-25}$	1.35	HfO_2	[12, 13]
12	Ta	180.947	$3.0 \cdot 10^{-25}$	1.33	Ta_2O_5	[14]

Therefore, we are of the opinion, that the main reason for the crystallization of amorphous film in our case is Joule-Lenz heating of the film due to phonon excitation by electrons. This is confirmed by the fact, that in both cases of the electron-beam induced and heat-induced crystallization of $Ti_{41}Zr_{41}Ni_{18}$ film phase transformation has a one-stage character and leads to the formation of crystals with the same fcc lattice [6].

In addition, previous studies of amorphous films of Cr_2O_3, obtained by laser sputtering of chromium in an oxygen atmosphere, have shown that there are no significant differences between the electron-beam induced and heat-induced crystallization. The impact of an electron beam (E = 100 keV) on amorphous free-standing film was initiated growth of a rounded and crescent-shaped Cr_2O_3 crystals with a hexagonal lattice. A similar structure and morphology of Cr_2O_3 crystals was observed during thermal annealing of amorphous free-standing film in a muffle furnace for five minutes at a temperature of 400°C (Fig. 1.1) [6, 15, 16].

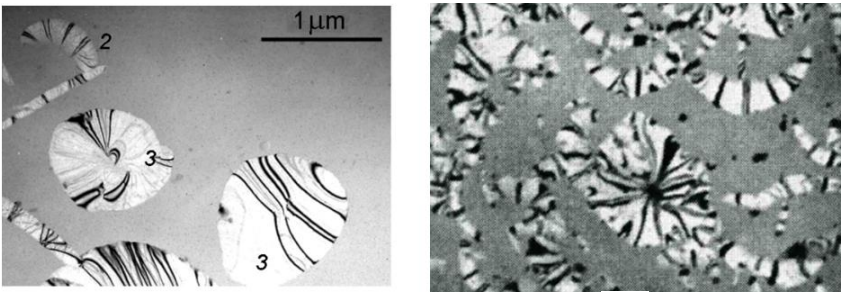

a b

Figure 1.1. a). Electron-beam induced crystallization of amorphous free-standing films of Cr_2O_3, obtained by laser sputtering of chromium in an oxygen atmosphere. E = 100 keV [15]. b). Heat-induced crystallization of amorphous films of Cr_2O_3, obtained by laser sputtering of chromium in an oxygen atmosphere. Thermal annealing of amorphous free-standing film in a muffle furnace for five minutes at a temperature of 400°C [16]

There was a strong diffraction contrast of extinction bend contours (depicting the regions where Bragg's law is satisfied), caused by a change in the density of the substance during crystallization. The only difference was in the distribution of crystals over the area of the film. During thermal initiation,

crystals grew over the entire area of the film, while during electron beam initiation, they grew only in the region of the electron beam impact. Dominant role of the heat-induced crystallization of amorphous *a*-GeAu films under the action of an electron beam also was noted in [17].

However, the situation may change with increasing of electrons energy, acting on the film. For example, when $E = 400$ keV, for an atom of Ti according to (1.1) $E_T \approx 25$ eV ~ $E_D \approx 29$ eV. In this case contribution of the electron-beam induced crystallization can increase significantly. The differences between the electron-beam induced and heat-induced crystallization of amorphous films of $Ge_2Sb_2Te_5$ with electrons with $E = 200$ and 400 keV were previously described in [18].

1.2. Volumetric changes during phase transformations

Phase transition (phase transformation) - an abrupt change in physical properties with a continuous change in external parameters. There are two kinds of phase transitions. During a phase transition of the first kind, such thermodynamic characteristics of a substance as density, concentration of components, etc. change abruptly. This is a widespread phenomenon in nature. Phase transitions of the first kind include: evaporation and condensation, melting and solidification, sublimation and condensation into a solid phase.

Some structural transitions in solids are also phase transformations of the first kind, for example, the formation of martensite in an Fe-C alloy. In pure superconductors, a sufficiently strong magnetic field causes a first-order phase transformation from the superconducting to the normal state. During phase transition of the first kind, a certain amount of heat is released or absorbed per unit mass of a substance, called the heat of the phase transition.

Phase transitions of the second kind are characterized by the absence of an abrupt change in the density of a substance, the concentration of components, and the heat of transition. Phase transitions of the second kind include: the transition of a paramagnet-ferromagnet, accompanied by the appearance of a macroscopic magnetic moment; paramagnet-antiferromagnet transition,

accompanied by the appearance of antiferromagnetic ordering; transition of ^{3}He and ^{4}He to the superfluid state, etc [19].

Phase transition of a substance from amorphous to a crystalline state, i.e. crystallization refers to the phase transitions of the first order. As a result of crystallization, the heat of the phase transition (heat of crystallization) is released and the density of the substance ρ changes abruptly by a value of $\Delta\rho=\rho_c-\rho_a$, where ρ_c and ρ_a are the density of the substance in the crystalline and amorphous states respectively.

The relative change of the substance density η during its crystallization is defined as:

$$\eta = \frac{\Delta\rho}{\rho_a} = \frac{\rho_c - \rho_a}{\rho_a}. \qquad (1.2)$$

Let's single out in amorphous sample a parallelepiped with sides X_a, Y_a и Z_a, inside of which is concentrated the mass of a matter, equal to m (Fig. 1.2).

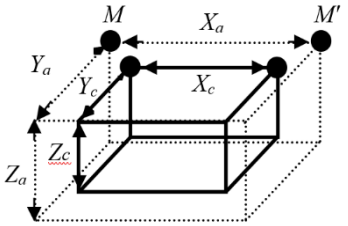

Figure 1.2. To the method of electron microscope determination of the relative change of the substance density during its crystallization

Then the density of the amorphous substance $\rho_a = \frac{m}{X_a Y_a Z_a}$. After crystallization of the sample, the same mass m will be located inside a parallelepiped with sides X_c, Y_c, and Z_c. Density of crystalline matter $\rho_c = \frac{m}{X_c Y_c Z_c}$. Substituting ρ_a and ρ_c into (1.2), we obtain:

$$\eta = \frac{X_a Y_a Z_a}{X_c Y_c Z_c} - 1 . \quad (1.3)$$

In amorphous state the substance is isotropic, since there is no long-range order. In the crystalline state the substance is anisotropic. However, in the case of a finely crystalline substance, this anisotropy can be neglected. Therefore, with a sufficient degree of accuracy, we can assume that $\frac{X_a}{X_c} = \frac{Y_a}{Y_c} = \frac{Z_a}{Z_c}$. Taking into account the latter, expression (1.3) takes the final form:

$$\eta = \left(\frac{X_a}{X_c} \right)^3 - 1 . \quad (1.4)$$

Expression (1.4) is the key one in determining the relative change in the density of a substance by the method of electron microscopy "in situ" [19, 20]. In order to determine η, it is necessary to take two electron microscopic photographs of the same section of the film before and after crystallization (Fig. 1.3). After that, it is necessary to measure the distances X_a and X_c between fixed marks, rigidly connected to the sample. If the film is obtained by the method of pulsed laser deposition, then it is convenient to use solidified melt microdroplets as marks (the so-called “splash effect”). The microdroplets are rigidly bound to the film. Therefore, the change in the distance between them as a result of crystallization is due not to the movement of microdroplets relative to the film, but to a change in the density of the film itself.

At Fig. 1.3 and 1.4 such marks are designated as *M* and *M*'. The value of η can be determined by substituting the numerical values of X_a and X_c into (1.4). If there are *n* marks on each of the micrographs, then the number *N* of possible measurements of the distances between the marks before and after crystallization (i.e. X_{ai} and X_{ci}) will be $\frac{n(n-1)}{2}$. In this case, according to (1.4), we obtain $\frac{n(n-1)}{2}$ different values of η, subject to statistical processing. The

reliability of the result increases with growing of the sample size (i.e., with increase of the number N of measured values η). The sample size N can be increased by repeated measurements of the distances between the marks before and after crystallization of the film.

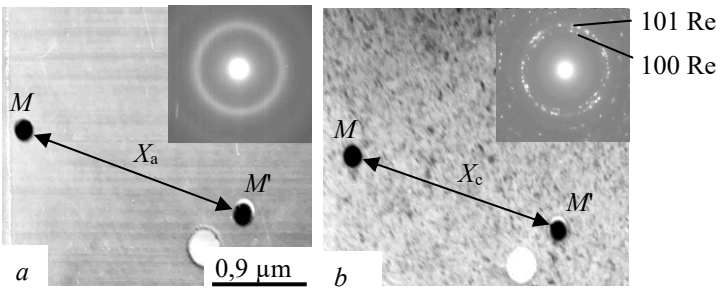

Figure 1.3. Electron microscope image of the Re film at the initial amorphous state (a) and after its crystallization with electron beam (b). In the upper right corner of each image the selected area electron diffraction pattern is shown, indicating the transition of Re from amorphous to a crystalline state with HCP structure [21]e

The values X_a and X_c are determined from micrographs as a result of direct measurements. The values of η are calculated according to relation (1.4) and are indirect measurements. The crystallization of this amorphous film is an irreversible process, and the conditions for conducting indirect measurements are irreproducible. Therefore, the processing of the results should be carried out in the same way as at direct measurements.

The experimental values of the relative change of the density during phase transformation of a number of substances in the thin-film state are given in Table. 1.2.

Table 1.2. The relative change of the density during phase transformations of the substances in thin film state [19]

Substances	Phase transformation	η, %	Error Δη, %
V_2O_3	Amorphous phase - crystal	9,2	1,5
Cr_2O_3	Amorphous phase - crystal	7,2	1,4
Fe_2O_3	Amorphous phase - crystal	6,5	1,3
HfO_2	Amorphous phase - crystal	2,5	1,7
ZrO_2	Amorphous phase - crystal	10,3	2,1
Re	Amorphous phase - crystal	25,9	7,7
Ni	Amorphous phase - crystal	7,5	1,6
Ni	HCP phase - FCC phase	18,5	2,9

1.3. Thermal initiation of the structural changes

1.3.1. Thermal destruction of fluoroplastic films

To study in the electron microscope the effect of thermal exposure on the object, an attachment was used in which part of the object holder was surrounded by a miniature heating oven. The temperature of the object was controlled by the current of the heating element according to the calibration curve. To prevent the formation of carbon at the sample due to the decomposition of oil vapor under the influence of electron beam, a technique was used to protect the object from contamination. Vapours of hydrocarbons located in the area of the object were frozen out with the help of liquid nitrogen.

Fluoroplastic films were obtained by the method of explosive thermal evaporation of powder in vacuum. It is known that as a result of heating of fluoroplast in a vacuum chamber to the evaporation temperature, both monomer molecules and whole fragments of polymer molecules with different molecular weights are formed. When deposited on the surface of a heated substrate, they repolymerize and form a coating. Powder from a copolymer of

tetrafluoroethylene with hexafluoropropylene (fluoroplast-4MB) was loaded into a tantalum boat and evaporated while the boat was rapidly heated by a current pulse. To prevent powder ejections, the boat was covered with a thin lid with holes [22].

Fig. 1.4, a show an electron micrograph of the structure of a fluoroplast film obtained on the face (001) of KCl at 300ºC. The contrast of the electron microscope image was enhanced by defocusing the objective lens of the microscope. Due to the defocusing of the objective lens, developed microfibrillar fibers, lying in the plane of the substrate, are clearly visible. The selected area electron diffraction (SAED) pattern, shown in the upper left corner of Fig. 1.4 a, indicates a partial ordering of spherulite fibrils in the plane of the substrate due to orienting effect during its growth. With an increase of the temperature of the substrate, there is a transition from the fibrillar form of film growth to the islet (Fig. 1.4 b). A further increase in the substrate temperature leads to the reevaporation of the fluoroplast. Above 450ºC only separate islands are observed, apparently already of a different composition.

Fluoroplastic films withstood the impact of intense electron beams without noticeable structural changes, while thermal exposure initiated their destruction. Fig. 1.5 illustrates the evolution of the structure of a fluoroplastic film (4MB) when it was heated in the column of electron microscope. At the initial state (before heating) a network of boundaries is clearly visible, separating the sections of the film, which were formed according to island and fibrillar growth modes (Fig. 1.5 a). The SAED patterns, shown in the upper left corner of each image in fig. 1.5, indicate that prior to heating this film was in an amorphous state.

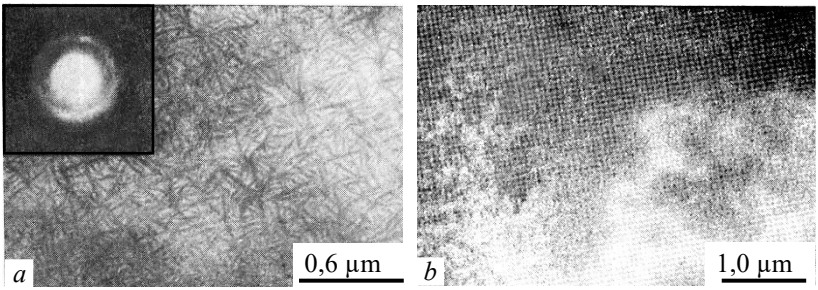

Figure 1.4. Electron microscope images of fluoroplastic films, deposited on KCl by explosive thermal evaporation in vacuum. a). fibrillar form of film growth at 300º C. b). Transition from fibrillar to islet form of growth at 360º [22]º

In the temperature range of 380 - 400ºC, no significant structural changes were observed, with the exception of warping and bending of the film. At temperatures above 400ºC, degradation products formed in the film matrix in the form of dark dots and drop-shaped inclusions (Fig. 1.5 b). The formation of inclusions occurs predominantly along the boundaries of structural formations in the film.

An increase in the size of each dark dot during heating occurs due to the influx of degradation products from the fluoroplastic matrix. A drop-shaped formation is formed, growing due to the absorption of smaller drops by the coalescence mechanism (Fig. 1.5 c). Microdiffraction patterns indicate an increase of the carbon content in the film, which is in the graphitized state. Fig. 1.5 d illustrates the complete destruction of the film at 500ºC.

When volatile degradation products are removed from the fluoroplastic, the degree of crystallinity of the film increases due to an increase in the content of graphitized carbon, as evidenced by the SAED patterns at Fig. 1.5. The destruction of the fluoroplastic is also accompanied by the melting of the film, and the centers of the nucleation of the liquid phase are drop-shaped inhomogeneities and inclusions.

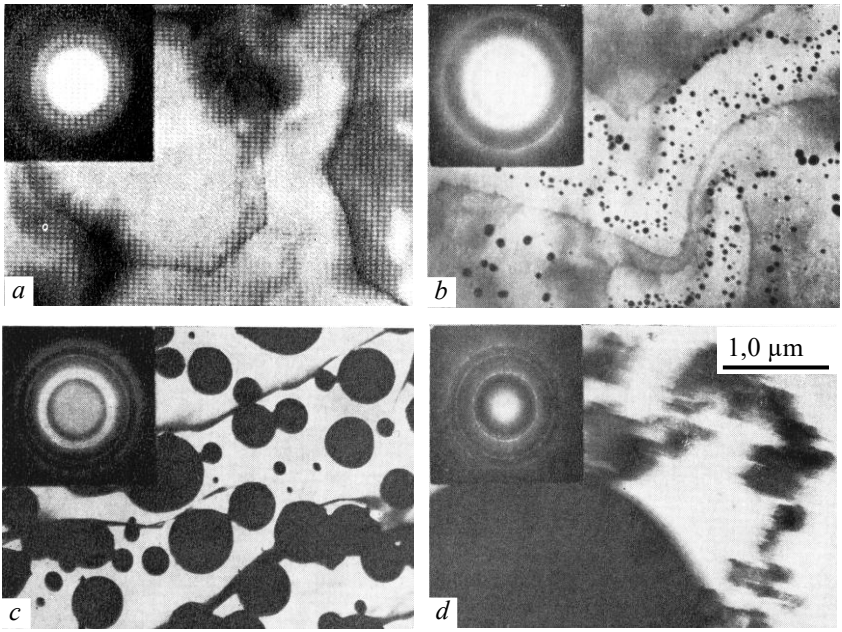

Figure 1.5. Evolution of the destruction of a fluoroplastic film when it is heated in an electron microscope column. a). The initial structure of the film. b). Release of degradation products at ~420ºC. c). Growth and coalescence, release at ~450ºC. d). Complete destruction of the film at ~520ºC [22]

1.3.2. Crystallization and destruction of amorphous films of rhenium

In a solid state, rhenium is a silver-gray metal with hexagonal close-packed crystal lattice. Its melting point comprises 3180°C. Depending on thickness and condensation temperature, either amorphous or crystalline films can be formed in thin-film condition obtained by electron beam evaporation of Re in vacuum [23]. When annealing, the amorphous phase transforms into crystalline one with parameters which are close to

those of massive metal. Data on structure of rhenium are provided in the tables of International Centre for Diffraction Data – JCPDC: a=0.2760 nm, c=0.4458 nm, a/c=1.6152 (file 05-0702). Perfect epitaxial films of Re were obtained on sapphire substrates (α-Al_2O_3) by electron beam evaporation in the range of T_s = 1000 - 1200°C [24].

Rhenium films were obtained on substrates at room temperature by pulsed laser sputtering of a rhenium target in vacuum (10^{-5} Torr) [25]. Fig. 1.6 a shows an electron-diffraction pattern and electron microscopic image of the as deposited film. The diffuse rings at the electron diffraction pattern and the point structure at the high-resolution image indicate the formation of an amorphous structure.

Annealing of amorphous films in vacuum with special adapter for heating in a column of the electron microscope provided their crystallization. Electron-diffraction pattern and images of the film after annealing at 720°C during 1 minute are shown in Fig. 1.6 b. Interpretation of electron-diffraction pattern is given in Table 1.3. According to these data, the rhenium polycrystalline film with face-centered close-packed lattice is formed. The lattice parameters are as follows: a=0.2747 nm, c=0.4459 nm, a/c=1.623. The obtained experimental data are in good agreement with JCPDC (file 05-0702) date.

When increasing the annealing temperature to 750°C, the destructive processes leading to film discontinuity with the following its subsequent disintegration, start. As a result, the spherical (more rare faceted) rhenium micro-particles grow as depicted at Fig. 1.6c. This image shows a so-called film “twisting” that allows interpreting the form of Re micro-particles to be spherical. The growth of Re micro-particles is carried out by diffusive transfer of substance from a film to microspheres. Next, the film becomes thinner and disintegrates. Similar morphological changes were observed earlier when heating ftoroplastic films directly in a column of electron microscope Fig. 1.5 c.

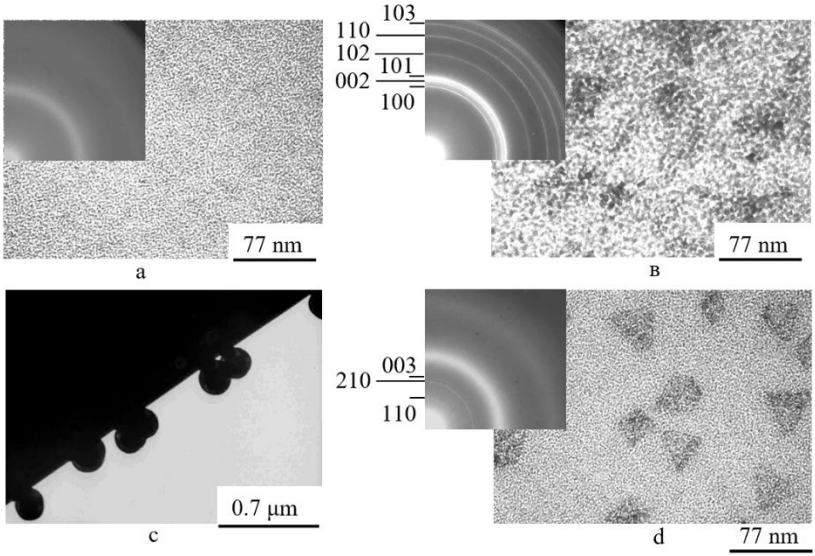

Fig. 1.6. Electron microscopic images of the films obtained by laser sputtering of Re in vacuum. a). Amorphous film after deposition. b). Its crystallization at thermal annealing in a microscope column at 720°C. c). Thermal annealing 810°C. d). Formation of ReO_3 in amorphous matrix of Re as a result of natural aging of films in air within 20 days. Electron-diffraction patterns are given in the left top corner of micro-images [25].

Natural aging at air of rhenium amorphous films on (001) KCl substrates provides their oxidation. On the film surface that not contacting to a substrate, the ReO_3 faceted crystals, grow. Fig. 1.6 d presents an electron-diffraction pattern and electron microscopic image of initial oxidation stage of Re amorphous film after natural aging during 20 days.

Table 1.3. The result of decoding of the electron diffraction pattern at Fig. 1.6 b

Line number	*d* (Å)	*hkl*, phase	*d* (Re), nm (JCPDC 05-0702)
1	0.2382	100 - Re	0.2388
2	0.2217	002 - Re	0.2226
3	0.2089	101 - Re	0.2105
4	0.1622	102 - Re	0.1629
5	0.1372	110 - Re	0.1380
6	0.1259	103 - Re	0.1262
7	0.1190	200 - Re	0.1195
8	0.1169	112 - Re	0.1173
9	0.1151	201 - Re	0.1154

2. POLYMORPHOUS TRANSFORMATION IN Ni AND Ni-Pd FILMS

2.1. Polymorphous transformation in nickel films

Nickel is a polymorphous metal. At temperatures below 380ºC, the low-temperature hexagonal (HCP) α modification of Ni is stable. According to the tables JCPDS Powder Diffraction File Card № 45-1027 (International Centre for Diffraction Data, Swarthmore, PA, 1996) it has the following lattice parameters: a = 2,6515 Å, c = 4,343 Å and c/a = 1,6379. The cubic lattice parameter of the β modification of Ni (FCC lattice) is also given in the tables JCPDS Powder Diffraction File Card № 04-0850: a=3,5238 Å.

At the same time, in the thin-film state, the probability of the implementation of the α-Ni modification increases. This position is interpreted as a phase transition with decreasing film thickness. The transformation is due to a change in the free energy with increasing the relative fraction of the surface [26].

A target, made of high-purity nickel, was sputtered with nanosecond pulses of YAG: Nd^{3+} laser radiation (wavelength 1,06 μm) in the Q-switched mode at a pulse repetition rate ν =25 Hz. The Ni vapor-plasma flow was condensed on orienting substrates made of KCl single crystals split along the (001) cleavage planes. The films were separated in distilled water and transferred to object grids for electron microscopic studies.

The substrate temperature T_S was varied in the range of 290-700 K. The pressure of the residual gases in the evaporation chamber was ~10^{-5} Torr. Phase transformations in films were initiated in two ways. In the first case, we used post condensation annealing of the samples in vacuum without separating the film from the substrate. In the second case, the "in situ" technique was used: the film, separated from the substrate, was heated in a microscope column using a specialized attachment for heating the object. In this case, it was possible to continuously observe all stages of the structural transformation [20].

Structural studies were carried out by electron diffraction and transmission electron microscopy using PEM-100-01 and EM-100L electron microscopes. The orientation of the film relative to the substrate was determined from the angle between the diffraction vector $\boldsymbol{g}$ in the SAED pattern and the known direction in the substrate, which coincided with the image of the film edge (Fig 2.1). The additional rotation, associated with the Lorentz rotation of the image relative to the microdiffraction pattern, was compensated. The known direction in the substrate was the <100> KCl direction. Its coincidence with the image of the film edge was performed automatically when the KCl substrate with the deposited Ni film was cleaved along the {100} cleavage planes [27].

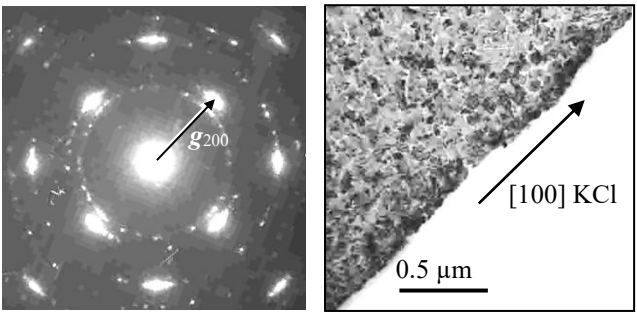

a b

Fig. 2.1. SAED picture (a) and electron microscopic images of Ni film obtained by laser sputtering of Ni in vacuum (б). Rotation, associated with the Lorentz turn of the image relative to the SAED pattern is compensated

The magnetic characteristics of the Ni films immediately after deposition and after annealing at temperatures of 670-700 K were studied using a highly sensitive vibrating magnetometer. The hysteresis loops of the films were measured at room temperature on samples in the form of a square with an area of ~1 cm^2 in fields up to 1000 Oe, applied in the layer plane in two mutually perpendicular directions. The average saturation magnetization I_S was determined by comparing the signals of the reference and test samples with a given area and thickness [27, 28].

2.1.1. Structural and phase states realized during pulsed laser sputtering of Ni

The following structural-phase states of Ni thin-film laser condensates were obtained at various substrate temperatures T_s (Table 2.1) [28].

Table 2.1 – The structure thin-film laser condensates of Ni [28]

T_s, K	290	350	420	520	660	700
Phase	Amor-phous	α-Ni (HCP)	α-Ni (HCP)	α-Ni (HCP)	α-Ni (HCP)	β-Ni (FCC)

1. Amorphous phase. It is formed by condensation of laser erosion plasma of nickel in vacuum at room temperature both on orienting substrates (001)KCl and on non-orienting substrates in the form of crystals (001)KCl covered with a film of amorphous carbon (C/(001)KCl). During annealing this film transforms into a polycrystalline state with the formation of finely dispersed crystals of Ni with an FCC structure.

2. Polycrystalline and textured Ni films with a metastable HCP lattice. They are formed by condensation of Ni in a vacuum in the substrate temperature range of 350 – 660 K. Upon annealing, the film transforms into a stable Ni state with FCC structure.

3. Polycrystalline (on non-orienting substrates) and epitaxial (on orienting substrates) (001) Ni films with FCC lattice. Formed by condensation of Ni in a vacuum in the substrate temperature range of 400–430°C.

Fig. 2.2 a shows electron diffraction pattern and electron microscopic image of Ni film in the initial metastable state (with HCP lattice), deposited in vacuum on (001) KCl at 440 K [29]. The average grain size D_{av} = 5.9 nm. The experimental electron diffraction pattern of the film (upper left part of the figure) is superimposed with the theoretical electron diffraction pattern (lower left part of the figure) for a polycrystal with the HCP structure. The radii of the circles of the theoretical electron diffraction pattern R satisfy the relation:

$$R = G\sqrt{\frac{4}{3}\left(h^2 + hk + k^2\right) + \frac{3}{8}l^2}\,. \qquad (2.1)$$

In (2.1) it is taken into account that for the HCP structure the ratio of the parameters of the elementary cell of the crystal lattice $\gamma = \frac{c}{a} = \sqrt{\frac{8}{3}}$. G is the

scale factor. h, k and l are the Miller indices of the crystal planes. Reflections for which $\frac{4h+2k+3l}{3}$ is odd number are forbidden.

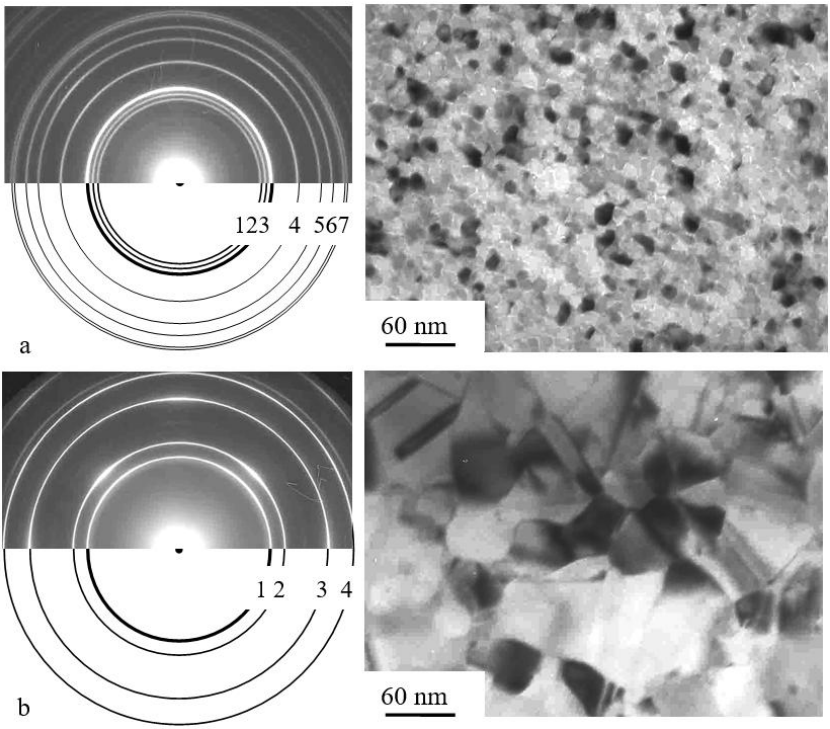

Fig. 2.2. Structure of films deposited by laser sputtering of nickel. a). Electron diffraction pattern and electron microscopic image of the Ni film at the initial metastable state. Condensation of the vapor-plasma flow at a pressure of 5 10^{-3} Pa and T_s = 520 K. b). The same after annealing on the substrate for two hours at 720 K [29]

Therefore, the circles whose diameters satisfy this relationship are not shown in the theoretical electron diffraction pattern. If the experimental electron diffraction pattern corresponds to electron diffraction at the film with HCP structure, then by changing the scale factor G, it is possible to achieve complete coincidence of the rings of the experimental electron diffraction pattern with the circles of the theoretical pattern when they are superimposed. So, the reflections with numbers 1, 2, 3, etc. are assigned indices h, k, l of the HCP lattice.

From the data obtained as a result of decoding the electron diffraction pattern at Fig. 2.2 a it follows, that during laser evaporation of Ni on a KCl substrate at T_s = 520 K, a metastable phase of α-Ni is formed with parameters $a = 0.265 \pm 0.001$ nm, $c = 0.432 \pm 0.001$ nm and $\gamma = 1.63 \pm 0.01$. These values are close to the data of X-ray diffraction analysis of Ni nanoparticles with HCP structure [30].

As a result of the annealing, the crystal lattice of the Ni film is transformed. The electron diffraction pattern, its scheme, and electron microscopic image of the structure are shown at Fig. 2.2 b. After annealing, a weak ordering of the nickel layer appears in the film in an orientation parallel to the (001) KCl substrate. The average size of the nickel grains after annealing increases to 62.7 nm. The radii of the circles of the theoretical electron diffraction pattern from a polycrystal with FCC structure satisfy the relationship:

$$R = G\sqrt{\left(h^2 + k^2 + l^2\right)}, \tag{2.2}$$

where for FCC structures, reflections with the same parity are allowed. Since in Fig. 2.2 b the rings of the experimental electron diffraction pattern coincide with the circles of the theoretical electron diffraction pattern for the FCC structure, reflections 1, 2, 3, etc. are assigned indices h, k, l of the FCC lattice. After annealing, the film acquires an FCC structure with a lattice parameter $a_0 = 0.352 \pm 0.001$ nm.

Fig. 2.3 a shows a diagram, reflecting the dependence of the average grain size of nickel $\langle D \rangle$ on the condensation temperature T_s and subsequent annealing on a (001) KCl substrate [29, 31]. The solid curve 1 is drawn through

the points characterizing the grain size of Ni immediately after film deposition. The arrows connect the data corresponding to the samples before annealing (with the HCP structure) and after annealing (with the FCC structure). According to the graph, in all cases a multiple increase in <*D*> is accompanied by a phase transition of the Ni crystal lattice from the HCP state to the FCC state.

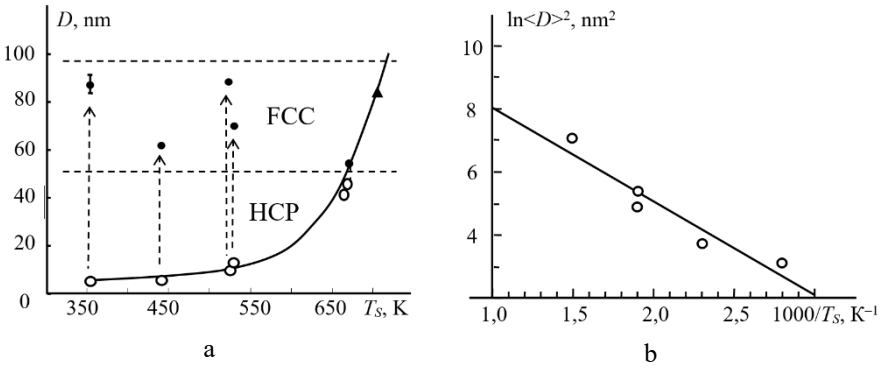

Fig. 2.3. a). The dependence of the average nickel grain size <*D*> on the condensation temperature T_s and subsequent annealing. The curve is drawn through the points, characterizing the Ni grain size immediately after film deposition. Arrows connect the data corresponding to the samples before and after annealing. ○ – HCP nickel phase. ● – FCC nickel phase. ▲ – FCC nickel phase after condensation. b). – Plotting in coordinates $\ln\langle D\rangle^2$ - $1000/T_s$ performed for nickel films with HCP structure [31]

The results of the dependence of the average grain size of nickel <*D*> with HCP structure on the substrate temperature T_s, plotted in coordinates $\ln\langle D\rangle^2$ - $1000/T_s$, are shown at Fig. 2.3 b. It follows from this figure that the experimental points fit satisfactorily onto a straight line, the equation of which has the form:

$$\ln\langle D\rangle^2 = a + b\left(\frac{1000}{T_S}\right), \tag{2.3}$$

where a = 11.06 and b = –2.99.

On the other hand it is known [32] that the dependence of the average grain size <*D*> in condensed films can be described by an exponential function of the form:

$$\langle D\rangle^2 = A\exp\left(-\frac{U}{RT_S}\right), \tag{2.4}$$

where A is the pre-exponential factor, U is the effective value of the activation energy of the processes, controlling grain formation. Comparing equations (2.3) and (2.4) and using the above value of the coefficients a and b we obtain: $A = 6.4\ 10^{-14}$ (m^2) and U = 24.86 kJ/mol (0.26 eV/atom). According to [32] the characteristic values of U for pure metals, deposited in the T_s range, that not exceeding 0.3 of the melting temperature of the metal (the so-called first condensation zone) are 0.2–0.25 eV/atom. It should be concluded that the value of U = 0.26 eV/atom, established in this work for nickel, is in satisfactory agreement with the literature data.

2.1.2. Structural and phase transformations in nickel films

Fig. 2.4 a shows electron diffraction pattern and electron microscopic image of the polycrystalline film, deposited at T_S = 350 K. As a result of the interpretation of the electron diffraction pattern, it was established that a low-temperature (metastable) Ni phase with HCP structure is formed. The average grain size of α-Ni <*D*> = 5.4 nm [28].

An increase of T_S above 400 K initiates the increase of the degree of orientation of the films. Two-position nucleation and growth of α-Ni grains occurs with the following orientation relations between the film and the KCl substrate. At the position 1:

$$(110)[\bar{1}\,1\,\bar{1}]\alpha\text{-Ni}//(110)[001]\text{KCl}; \tag{2.4 a}$$

$$(110)[\bar{2}\,2\,\bar{1}]\alpha\text{-Ni}//(110)[001]\text{KCl}. \tag{2.4 b}$$

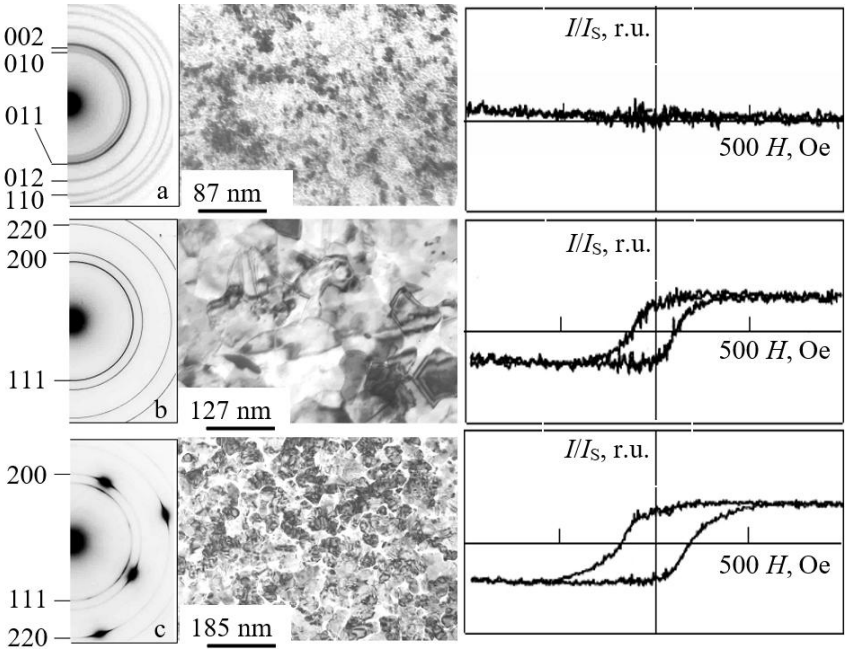

Figure 2.4. Electron diffraction patterns, electron microscope images and magnetization curves of films, deposited from Ni laser erosion plasma. a). α-Ni film with an HCP structure, deposited at T_S = 350 K; b – the same after annealing at 700 K for 120 min. The structure corresponds to the β-Ni phase with the FCC lattice; c – β-Ni epitaxial film with FCC structure, deposited at T_s = 700 K [28]

Relations (2.4 a) and (2.4 b) are valid for crystals belonging to the zone axes [$\bar{1}\,1\,\bar{1}$] and [$\bar{2}\,2\,\bar{1}$], respectively. In the first case, the (001) KCl substrate surface is parallel to the ($\bar{5}$ 59) α-Ni plane; in the second - to the plane (-10 10 9) α-Ni.

In position *2*:

$$(110)[\bar{1}\,1\,\bar{1}]\alpha\text{-Ni}//(\bar{1}\,10)[001]\text{KCl}, \qquad (2.5\ a)$$

$$(110)[\bar{2}\,2\,\bar{1}]\alpha\text{-Ni}//(\bar{1}\,10)[001]\text{KCl}. \qquad 2.5\ b)$$

Ratios (2.5 a) and (2.5 b) are performed for crystals belonging to the zone axes $[\bar{1}\,1\,\bar{1}]$ and $[\bar{2}\,2\,\bar{1}]$ respectively.

At $T_S \geq 700$ K epitaxial films are formed. Fig. 2.4 c shows the electron diffraction pattern and the electron microscope image of the film, deposited at $T_S = 700$ K. The interpretation of the electron diffraction pattern showed that in this case a high-temperature (stable) β-Ni phase with the FCC structure is formed. Average grain size $<D> = 86.4$ nm. The film grows in a parallel orientation with respect to the KCl substrate, observing a simple orientation relation:

$$(001)[110]\beta\text{-Ni} // (001)[110]\text{KCl}, \qquad (2.6)$$

at which the (001) surface of Ni film is parallel to the substrate (001) surface of KCl.

It was established, that post-condensation annealing of films on substrate in vacuum initiates a phase transition, in which the HCP lattice of Ni (Fig. 2.4a) is transformed into an FCC lattice (Fig. 2.4 b). In this case, the average grain size $<D>$ increases from 5.4 to 87.8 nm.

Annealing of the "free standing" Ni films in the microscope column also initiates the HCP → FCC phase transformation. In this case, $<D>$ does not noticeably change. Fig. 2.5 presents the results of "in situ" electron diffraction study of the α-Ni (HCP) → β-Ni (FCC) polymorphous transformation during isothermal annealing of film (750 K, 40 min) in an electron microscope column. The initial film (α-Ni) was deposited at $T_S = 420$ K. Partial ordering is observed with realization of orientation relations (2.4) and (2.5).

The scheme of the electron diffraction pattern and its photograph are shown at Fig. 2.5 a and 2.5 b respectively. The symbol "●" designates reflections belonging to α-Ni crystals with the zone axis $[\bar{1}\,1\,\bar{1}]$ in position 1; ■ – reflections of α-Ni crystals with the zone axis $[\bar{1}\,1\,\bar{1}]$ in position 2, which is rotated in the plane of the figure by 90° relative to position 1; ○ – reflections of α-Ni crystals with the zone axis $[\bar{2}\,2\,\bar{1}]$ in position 1; □ – reflections of α-

Ni crystals with the zone axis [$\bar{2}$ 2 $\bar{1}$] in position 2. As a result of the interpretation of the electron diffraction pattern of the film, obtained after annealing (Fig. 2.5 c), it was shown that the β-Ni phase with the FCC structure is formed.

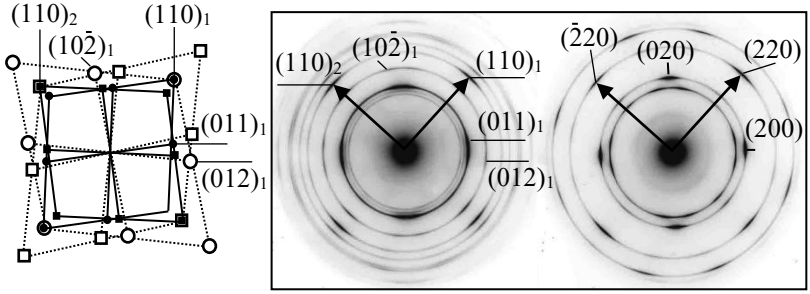

Fig. 2.5 - Electron diffraction study "in situ" of the polymorphous transformation HCP → FCC during isothermal annealing of the Ni film. a, b - scheme and photograph of the electron diffraction pattern of the Ni film before annealing (420 K); ● – reflections of α-Ni crystals with zone axis [$\bar{1}$ 1 $\bar{1}$] in position 1; ■ – reflections of α-Ni crystals with the zone axis [$\bar{1}$ 1 $\bar{1}$] in position 2; ○ – reflections of crystals α-Ni with zone axis [$\bar{2}$ 2 $\bar{1}$] at position 1; □ – reflections of α-Ni crystals with zone axis [$\bar{2}$ 2 $\bar{1}$] in position 2; c - electron diffraction pattern of this film after annealing (40 min. at 750 K)

According to Fig. 2.5 for α-Ni crystals in position 1 with zone axes both [$\bar{1}$ 1 $\bar{1}$] and [$\bar{2}$ 2 $\bar{1}$], the diffraction vector $\boldsymbol{g}$ = 110 is parallel to the diffraction vector $\boldsymbol{g}$ = 220 for β-Ni crystals. This implies the following orientation relationships between the initial α-Ni and final β-Ni phases. For position 1:

$$(110)[\bar{1}\,1\,\bar{1}]\alpha\text{-Ni}//(110)[001]\beta\text{-Ni}; \quad (2.7\ \text{a})$$

$$(110)[\bar{2}\,2\,\bar{1}]\alpha\text{-Ni}//(110)[001]\beta\text{-Ni}. \quad (2.7\ \text{б})$$

Ratios (2.7 a) and (2.7 б) are performed for crystals of position 1, belonging to the zone axes $[\bar{1}\,1\,\bar{1}]$ and $[\bar{2}\,2\,\bar{1}]$ respectively.

For position *2*:

$$(110)[\bar{1}\,1\,\bar{1}]\alpha\text{-Ni}//(\bar{1}\,10)[001]\beta\text{-Ni}; \quad (2.8\ \text{a})$$

$$(110)[\bar{2}\,2\,\bar{1}]\alpha\text{-Ni}//(\bar{1}\,10)[001]\beta\text{-Ni}. \quad (2.8\ \text{б})$$

Ratios (1.8 a) and (5.18, б) are performed for crystals of position *2*, belonging to the zone axes $[\bar{1}\,1\,\bar{1}]$ and $[\bar{2}\,2\,\bar{1}]$ respectively.

Analysis of histograms of distribution of grain size *D* in Ni films before and after annealing showed, that, in free standing films, the polymorphic transformation α-Ni → β-Ni is not accompanied by a significant change in the grain size. In the initial and final states of the film, $\langle D\rangle \approx 12$ nm.

2.1.3. Crystallographic analysis of α → β transformation in nickel

For crystallographic analysis of the α → β transformation in Ni (at heating the sample) it is advisable to use the example of the reverse allotropic transformation β → α [37], which occurs via martensitic pathway in Co (at cooling the sample).

At Fig. 2.6 a the initial two-layer HCP lattice (α-Ni phase) is represented by the sequence (ABAB…) of stacking close-packed layers [31]. The growth of the crystal of the high-temperature β-Ni phase (Fig. 2.6 b) begins from a certain plane of the (001) type of the initial hexagonal crystal, which remains invariant. Let the first two lower layers A_1 and B_1 of the (001) planes of the α-Ni phase correspond to the first two lower layers A_1 and B_1 of the (111) planes of the β-Ni phase. After shifting layers ($A_2B_2A_3B_3$…) of the (001) planes of the α-Ni phase by a vector $\vec{R} = \frac{2}{3}a[\bar{1}\,10]$, the planes A_2 and B_2 of the two-layer packing pass into the (111) planes C_1 and A_2 of the three-layer packing, respectively. Subsequent similar shifts ensure the transition of planes

$A_3 \rightarrow B_2$ and $B_3 \rightarrow C_2$, etc. As a result, the lattice is restructured from a two-layer packing to a three-layer packing.

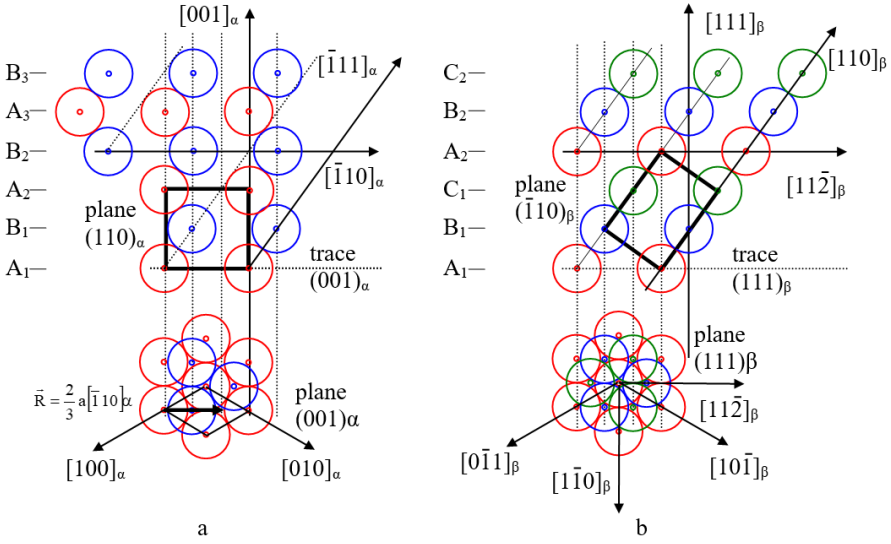

Fig. 2.6. Scheme of phase transformation of low-temperature modification with HCP lattice (α-Ni phase) into high-temperature modification with FCC lattice (β-Ni phase), occurring in laser condensates during annealing. a). HCP crystal lattice in projections on planes (110) and (001). b). FCC crystal lattice in projections on planes ($\bar{1}$10) and (111) [31].

2.1.4. Changes in density and magnetic characteristics during annealing of Ni films

The relative density change η of nickel as a result of the phase transition was determined "in situ" directly in the column of the electron microscope according to [20, 21, 33]. Relation (1.4) was used. It was established that in the case of a phase transition of the Ni film from the amorphous to the crystalline state, the relative density change η = 7.5 ± 1.6% (with a reliability level of

95%). Fig. 2.7 illustrates the crystallization of an amorphous Ni film (condensation at T_s = 20°C), initiated by heating with an electron beam in the microscope column [34].

The phase transition from the structural state with the HCP-Ni lattice to the state with the FCC lattice is also accompanied by an increase of the film density.

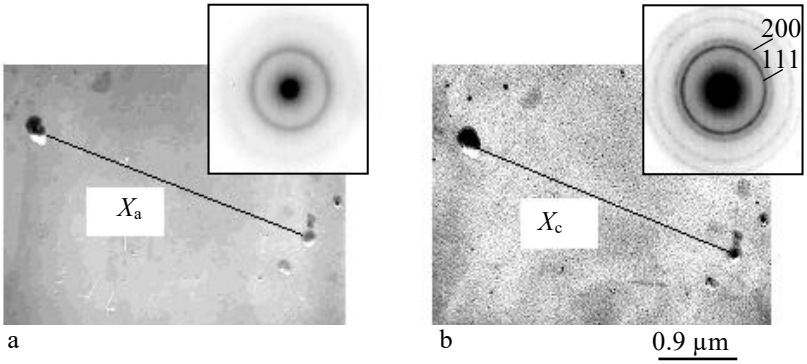

Fig. 2.7. Crystallization of Ni film in a microscope column at the influence of an electron beam. a). Image and SAED pattern of amorphous film at the initial state. b). The same after crystallization of amorphous film. Ni lattice is FCC [34]

Fig. 2.8 illustrates the change in the Ni crystal lattice during annealing of the film in the microscope column using a specialized attachment for heating the sample. The initial state of the film (HCP-Ni) was determined by condensation of the vapor-plasma flow on the substrate at 80°C. Annealing was carried out at a temperature of 480°C for 40 min. Micrographs were taken after complete cooling of the film to room temperature in the microscope column.

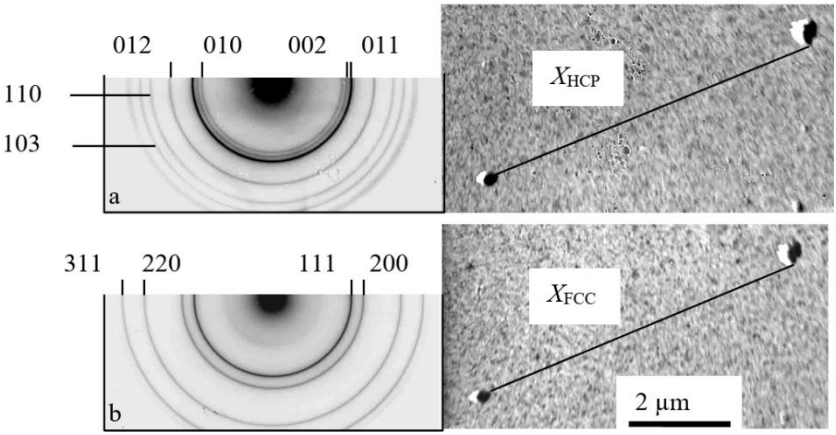

Fig. 2.8. Annealing of Ni film in a microscope column with an attachment for heating of the sample at a temperature of 480°C for 40 min. a). SAED pattern and image of the Ni film at the initial state (with HCP lattice). b). Final state of Ni film (with FCC lattice) [28, 34]

It was established that in the case of the HCP → FCC structural transition, the relative change in the density of nickel is $\gamma = 18.5 \pm 2.9\%$ (with a reliability level of 95%) [28, 34]. The increase in density during this transition is consistent with the data of the JCPDS tables. Thus, according to the data of tables [35] and [36], the density of Ni with the HCP lattice is $\rho_1 = 7.372$ g/cm^3, and with the FCC lattice $\rho_2 = 8.911$ g/cm^3. Following (1.4), for the given data $\gamma = 20.9\%$. This value fits into the confidence interval for γ from 15.6 to 21.4% obtained in this work.

Films of α-Ni with a metastable HCP structure, when magnetized in magnetic fields up to 1000 Oe do not exhibit a magnetic moment, that exceeds the sensitivity threshold of the magnetometer (right side of Fig. 2.4 a). The sensitivity threshold of the magnetometer (for the geometrical parameters of the samples indicated above) corresponds to magnetization less than 1-5 G.

After annealing, which initiates the HCP→ FCC phase transformation, the magnetic state of the film changes dramatically: the magnetic moment increases significantly, and hysteresis was observed during magnetization reversal (right side of Fig. 2.4 b). There was no anisotropy in the layer plane. Coercive force $H_S \approx 110$ Oe, saturation field $H_S \approx 420$ Oe. Similar data for the epitaxial ferromagnetic β-Ni film, which initially after condensation ($T_S = 700$ K) had FCC structure (right side of Fig. 2.4 c) are follows: $H_C \approx 180$ Oe, $H_S \approx 700$ Oe, saturation magnetization $I_S = 320$ G.

The observed variety of structural-phase states of laser condensates of nickel (Table 2.1) are predetermined by the specifics of the method of pulsed laser film deposition. The main physical parameters of this method, which determine the formation of the structure, are: the density of the vapor-plasma flow of the sprayed metal; flux density of gas particles of the atmosphere of the evaporation chamber; the tendency of the metal to adsorb gaseous impurities and to form chemical compounds with them; the presence of ionic component in the deposited stream; substrate orientation and temperature.

In this case the formation of no crystalline solid structures during laser sputtering of a Ni target is predetermined by the following factors. This is the hardening of nonequilibrium states, formed on the substrate immediately after the deposition of each portion of the substance; chemisorption and incorporation into the film of gaseous impurities, activated by high-energy ions of laser erosive plasma. The latter circumstance helps to suppress the migration of adatoms and prevent the coalescence of non-crystalline complexes.

With increasing T_S the capture of gaseous impurities by the growth surface of the film decreases. Accordingly, the migration of adatoms and coalescence of non-crystalline complexes are intensified, that leads to the formation of a crystalline condensate. Discrete nature of the substance deposition on substrate and the small thickness of the layer, deposited at one condensation pulse, initiate the occurrence of the phase size factor. The formation of a film of the metastable α-Ni modification with HCP crystal lattice should be interpreted as a phase transition associated with decreasing of the film thickness.

The transformation is due to a change of free energy with increasing of the relative fraction of the surface [38].

Vacuum annealing of α-Ni films both on the substrate and in the free state at $T_O \approx 700$ - 750 K initiates recrystallization processes. In the case of films on substrate, the result of recrystallization is an increase in the average nickel grain size $<D>$ by an order of magnitude and the transformation of the crystal lattice HCP → FCC. In self-supporting films, the transformation of the crystal lattice occurs without a noticeable change in $<D>$. The lower limit of the indicated temperature interval T_O coincides with the temperature of epitaxial growth of the β-Ni film in the orientation parallel to the (001) KCl substrate, given by relation (2.6). Relation (2.6) is also satisfied in the case of thermal evaporation of Ni on alkali halide crystal substrates.

Two positions of growth of α-Ni films on the (001) KCl substrate, described by relations (2.4) and (2.5), are due to the equivalence of the [110] and [1 $\bar{1}$ 0] directions on the KCl substrate. These relationships are similar to relationships (2.7) and (2.8), which describe the orientation of the α-Ni and β-Ni phases before and after recrystallization of the film. This is also related to the equivalence of the [110] and [1 $\bar{1}$ 0] directions of the FCC phase of β-Ni.

The noted change in the magnetic moment of the films as a result of annealing (Fig. 2.4, a and b) can be explained by a change in the crystal structure of Ni from a metastable HCP (α-Ni phase) to an equilibrium phase with FCC structure (β-Ni phase). There is a well-known model for describing the electronic structure of transition metals, in which Ni with a HCP structure cannot have spontaneous magnetization, while Ni with a FCC structure is ferromagnetic [39]. In this case changes in magnetic properties after film annealing are due to magnetic phase transformation. On the other hand, there are also opposite points of view [40], according to which hexagonal Ni is a ferromagnet and has a magnetic moment of 0.59 μ_B, which is not much less than the magnetic moment of the stable FCC Ni phase (0.60 μ_B). However, in nano dispersed film systems, when the grains are isolated from each other and the volume concentration of the magnetic phase is less than 30%,

superparamagnetism may manifest itself [41]. As a result, a small magnetic moment will be observed in fields up to 1000 Oe.

Films of α-Ni with a HCP structure, deposited on (001) KCl, are characterized by a fine-grained polycrystalline structure (<*D*> = 5.4 nm) and the absence of a magnetic moment. However, the analysis of electron microscope photographs, shown in Figs. 5.8, a, indicates a fairly tight contact of the grains. The transition to the ferromagnetic state as a result of film annealing on the substrate is accompanied by increasing <*D*> to 87.8 nm. This is comparable to the grain size initially (after condensation) of ferromagnetic films, for which <*D*> = 86.4 nm. These circumstances confirm the assumption that the change in the magnetic properties of the films after annealing is due to the magnetic phase transformation [28].

2.2. Phase transformations in films deposited by co-sputtering of Ni and Pd

Rotating disks composed of sectors of high-purity Ni and Pd metals were used as a targets for laser sputtering (Fig. 2.9). The target rotation frequency ω was 55 - 85 s^{-1}. This technique made it possible to alternately deposit laser erosion plasma of nickel and palladium on the substrate [44, 45]. The ratio of the C_M scanning area of the laser beam over the palladium surface S_{Pd} to the total scanning surface area of the disk S_0 ($C_M = S_{Pd}/S_0$) was 0; 0.25; 0.5; 0.75, and 1. This made it possible to obtain both single-element Ni ($C_M = 0$) or Pd ($C_M = 1$) films and Ni-Pd alloys.

As a result of the sputtering of composite targets 0.75Ni – 0.25Pd (C_M=0.25) and 0.5Ni – 0.5Pd (C_M=0.5) on substrates films of nickel-palladium alloy were formed. Their crystal lattice also corresponded to the HCP structure. Fig. 2.10a shows the electron diffraction pattern, its scheme and electron microscopic image of the film, deposited at substrate temperature T_S = 440 K by pulsed laser sputtering of a composite target 0.5Ni – 0.5Pd (C_M = 0.5). The film is polycrystalline with an average grain size $\overline{D}$ = 5.4 nm.

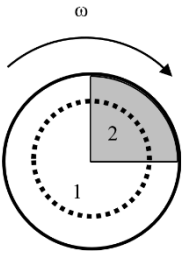

Fig. 2.9. Scheme of the composite target 0.75Ni – 0.25Pd ($C_M = 0.25$) intended for laser sputtering: 1 – Ni sector; 2 – Pd sector [45]

The results of decoding of the electron diffraction patterns at Fig. 2.10 are given at the Table 2.2. According to this table film of the nickel-palladium alloy with a metastable HCP crystal lattice is formed. Its parameters are: a=0.273 ± 0.001 nm, c=0.451 ± 0.001 nm, and γ=1.65 ± 0.01. As a result of the annealing (3 hours at 710 K), the structure of the film is transformed. It acquires FCC crystal lattice (Fig. 2.10b) with the parameter a_0=0.374 ± 0.001 nm. In this case $\overline{D}$ increases to a value of 36.3 nm.

The decoding data of the electron diffraction patterns of films obtained by sputtering targets for which C_M = 0; 0.25; 0.5; 0.75 and 1 (from nickel to palladium) are summarized at Table 2.3. It is evident from the table that when sputtering Ni, 0.75Ni - 0.25Pd and 0.5Ni - 0.5Pd targets on (001) KCl substrates at T_s = 440 K, films with an HCP crystal lattice are formed.

However, when sputtering a 0.25Ni - 0.75Pd target (C_M = 0.75), films are formed in which the HCP and FCC phases are present. For the hexagonal phase a = 0.276 ± 0.001 nm, c = 0.452 ± 0.001 nm, and γ = 1.64 ± 0.01. For the cubic phase, a_0 = 0.380 nm.

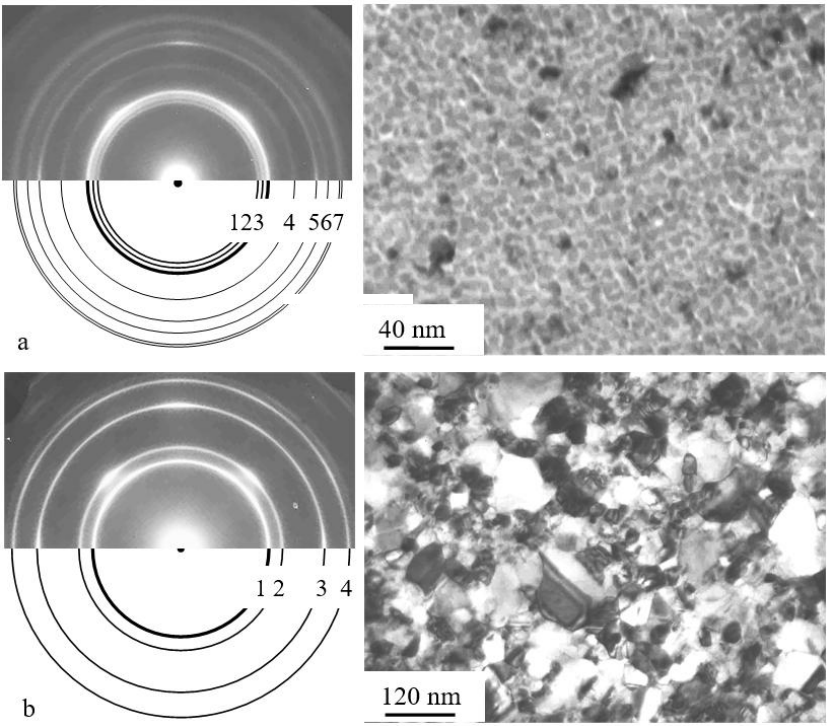

Fig. 2.10. Electron diffraction patterns, their schemes and electron microscopic images of the film, deposited by laser ablation at $T_s = 440$ K. a). Sputtering of a composite target 0.5Ni - 0.5Pd ($C_M = 0.5$). Initial state. b). The same after film annealing [29].

Table 2.2. The decoding data of the electron diffraction patterns at Fig. 2.10

Line number	Before annealing (HCP) a = 0,273 nm, c = 0,451 nm, γ =1,65 $\overline{D}$ = 5,4 nm; σ = 1,0 nm		After annealing (FCC) a_0 = 0.374 nm $\overline{D}$ = 36,3 nm; σ = 14,1 nm	
	d, nm	hkl	d, nm	hkl
1	0,236	010	0.216	(111)
2	0,225	002	0.187	(200)
3	0,207	011	0.132	(220)
4	0,162	012	0.113	(311)
5	0,137	110		
6	0,117	103		
7	0,110	200, 112		

Note: $\overline{D}$ is the average value of film grain diameters; σ is the standard deviation D.

As follows from the table, the parameter γ is close to the ideal value 1.633 for a hexagonal close-packed structure. At the same time, the HCP lattice parameters a and c increase monotonically with increasing palladium content in the film (i.e. with an increase of C_M from 0 to 0.75). The dependence of the parameter a on C_M is shown graphically at Fig. 2.11a. The straight line constructed from the data of Table 2.3 using the least squares method is the regression line of the HCP cell parameter a on C_M. In this case the correlation coefficient, characterizing the tightness of the linear relationship between C_M and a, is close to 1.

According to Table 2.3 in all cases after annealing the film acquires an FCC structure. Assuming that C_M coincides with the molar concentration of Pd in the film, there is satisfactory agreement between the experimental data of our work (column 3) and the literature data (column 4) for Ni-Pd alloys in the bulk state [46]. Figure 2.11b shows the dependence of the lattice constant of

the solid solution of intermediate composition a_0 on C_M. Solid curve 1 is the result of approximating the experimental points by the least squares method using a third-degree polynomial. According to Vegard's law [47], in the simplest case a_0 depends linearly on the molar concentration of one of the components. For comparison Fig. 2.11b shows dotted line 2, constructed according to the relationship:

$$a_0 = a_0(\text{Ni})\cdot(1 - C_M) + a_0(\text{Pd})\cdot C_M. \quad (2.9)$$

Table 2.3. Structural state of films at different ratios of Ni and Pd in the target

Structural state / Composition of the target	Film after condensation	Film after annealing	Massive state [46]
C_M = 0 (Ni)	HCP a = 0.265 nm c = 0.432 nm γ = 1.63	FCC a_0 = 0.352 nm	FCC a_0 = 0.3524 nm
C_M = 0.25 (0.75Ni - 0.25Pd)	HCP a = 0.266 nm c = 0.433 nm γ = 1.63	FCC a_0 = 0,365 nm	FCC a_0 = 0.3639 nm
C_M = 0.50 (0.50Ni - 0.50Pd)	HCP a = 0.273 nm c = 0.451 nm γ = 1.65	FCC a_0 = 0.374 nm	FCC a_0 = 0.3739 nm
C_M = 0,75 (0.25Ni - 0.75Pd)	HCP+FCC a = 0.276 nm c = 0.452 нм γ = 1.64 a_0 = 0.380 nm	FCC a_0 = 0.385 нм	FCC a_0 = 0.822 nm
C_M = 1,0 (Pd)	FCC a_0 = 0.398 nm	FCC a_0 = 0.392 nm	FCC a_0 = 0.3890 nm

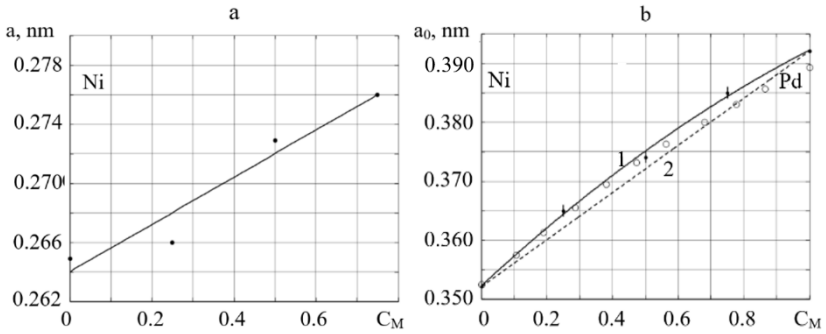

Fig. 2.11. Dependence of the lattice constants of the Ni - Pd solid solution on the composition of the sputtered C_M target. a). Dependence of the HCP cell parameter a on the Pd content in the sputtered target. b. dependence of the FCC lattice constant a_0 of the Ni - Pd solid solution on the composition of the sputtered target (solid curve 1). Dashed line 2 - plotted according to Vegard's law. ● - data from the work for the thin-film state. ○ - data for the Ni - Pd system in the bulk state (according to [47]).

In relation (2.9) a_0(Ni) and a_0(Pd) are the lattice constants of the pure components Ni and Pd, respectively. Comparison of lines 1 and 2 indicates a positive deviation of the dependence of a_0 on C_M from Vegard's law: curve 1 of the measured values of the lattice constants passes above line 2. A positive deviation from Vegard's law is characteristic of alloys with a concave liquidus line in the state diagram, which occurs in the case of the Ni - Pd system [48]. At the same time, the linear dependence of the lattice parameter of the solid solution a (and, consequently, the parameter c) on C_M (the straight line at Fig. 2.11a) suggests that Vegard's law is satisfied in a limited range of Pd concentration, in which the film has an HCP crystal lattice before annealing [49].

2.3. Magnetic state of Ni-Pd films of variable composition

The magnetic characteristics of the films immediately after deposition and after annealing were studied using a highly sensitive vibrating magnetometer. The hysteresis loops of the films were measured at room temperature on square samples with an area of ~ 1 cm^2 in fields up to 1000 Oe applied in the plane of the layer in two mutually perpendicular directions. The average saturation magnetization I_S was determined by comparing the signals of the reference and studied samples with a given area and thickness [49].

Measurement of magnetic characteristics showed that Ni films and Ni–Pd alloy with a metastable HCP structure do not exhibit a magnetic moment exceeding the sensitivity threshold of the magnetometer when magnetized in magnetic fields up to 1000 Oe. The sensitivity threshold of the magnetometer (with the above geometric parameters of the samples) corresponds to a magnetization of less than 1–5 G.

After annealing, which initiates the HCP → FCC phase transformation, the magnetic state of the Ni – Pd films (for which C_M = 0 – 0.5) changes sharply: the magnetic moment increases significantly, and hysteresis is observed during magnetization reversal (Figs. 2.12a-2.12c). Anisotropy in the layer plane is absent. For nickel, the coercive force is $H_C \approx 120$ Oe and the saturation field is $H_S \approx 250$ Oe (Fig. 2.12a).

For 0.75Ni–0.25Pd films, we have $H_C \approx 130$ Oe and $H_S \approx 500$ Oe (Fig. 2.12b). For 0.5Ni–0.5Pd films, we have $H_C \approx 210$ Oe and $H_S \approx 500$ Oe (Fig. 2.123c).

A similar change in the magnetic moment of a nickel film accompanied by a change from an HCP into an FCC structure was detected in [44, 50-52]. Films with a high palladium concentration (C_M = 0.75 or higher) had no magnetic moment both before and after annealing (Fig. 2.12d).

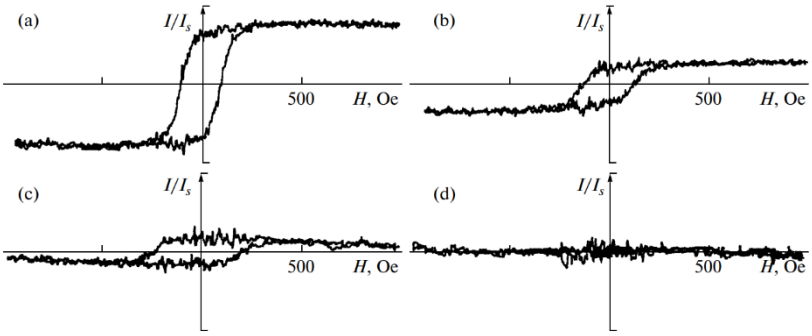

Fig. 2.12. Magnetization curves of the films produced by pulsed laser deposition onto a substrate followed by annealing: (a) sputtering of Ni (C_M=0), (b) 0.75Ni–0.25Pd composite target (C_M = 0.25), (c) 0.5Ni–0.5Pd composite target (C_M = 0.5), and (d) 0.25Ni– 0.75Pd composite target (C_M = 0.75) [49]

The change in the magnetic moment of Ni films upon annealing can be explained as follows [49]. Annealing initiates the transformation of a metastable HCP structure into a stable FCC structure. The electronic structure of transition metals is known to be described in terms of a model [39] in which HCP nickel cannot have spontaneous magnetization and FCC nickel is ferromagnetic. In this case, the annealing induced changes in the magnetic properties of the films are caused by the magnetic phase transformation. On the other hand, there exist alternative view points. The authors of [40] showed that HCP Ni is ferromagnetic and has a magnetic moment (0.59 μB) that is only weakly smaller than the magnetic moment of the stable FCC Ni phase (0.69 μB). However, superparamagnetism can manifest itself in nanofilm systems, where grains are isolated from each other and the volume concentration of the magnetic phase is lower than 30%; as a result, a small magnetic moment exists in

fields up to 1000 Oe. Such a situation was observed in amorphous-crystalline nickel films [50], where FCC β Ni grains were embedded into an amorphous nonferromagnetic matrix.

The HCP α-Ni films deposited at T_S = 440 K are also characterized by a finegrained polycrystalline struc ture ($\overline{D}$ = 5.9 nm) and the absence of a magnetic moment. However, an analysis of electron micro graphs similar to that, shown in Fig. 2.13a, unambiguously indicates tight contact between grains and the absence of layers between them. After annealing, initiating the HCP → FCC phase transition, the grain size increases to $\overline{D}$ = 62.7 nm. As substrate temperature T_S increases, $\overline{D}$ increases similarly. Figure 2.13 illustrates the effect of the condensation and annealing temperatures on the phase composition (HCP, FCC) and average nickel grain size. This curve was plotted with allowance for the data in [50]: it passes through the points that charac terize the Ni grain size in the as-deposited state and corresponds to a monotonic increase in from 5.4 nm at T_S = 350 K to = 86.4 nm at T_S = 700 K. However, in laser ablation, the HCP nickel phase forms in films in the temperature range T_S = 350–670 K and the FCC phase forms above 670 K.

The presence of a magnetic phase transformation in Ni films upon annealing is supported by the structural HCP → FCC phase transition, which is accompanied by an insignificant change in $\overline{D}$. According to Fig. 2.3a, this change occurs near the boundary of condensation of the HCP and FCC phases.

Figure 2.13a shows an electron microscopic image and the electron diffraction pattern of a film, deposited at T_S = 670 K by laser sputtering of a Ni target (C_M = 0). In the as-deposited state, the film is nonferromagnetic (Fig. 2.13b). After annealing, initiating the HCP → FCC phase transformation, the magnetic state of the Ni film changes sharply (Fig. 2.13c): it becomes ferromag netic (coercive force $H_C \approx 110$ Oe, saturation field H_S = 250 Oe). A hysteresis appears during magnetization reversal (Fig. 2.13d). However, annealing does not cause significant changes in both $\overline{D}$ and the D distribution, which is

indicated by the results of statistical process ing of the grain sizes measured in nickel films before and after annealing.

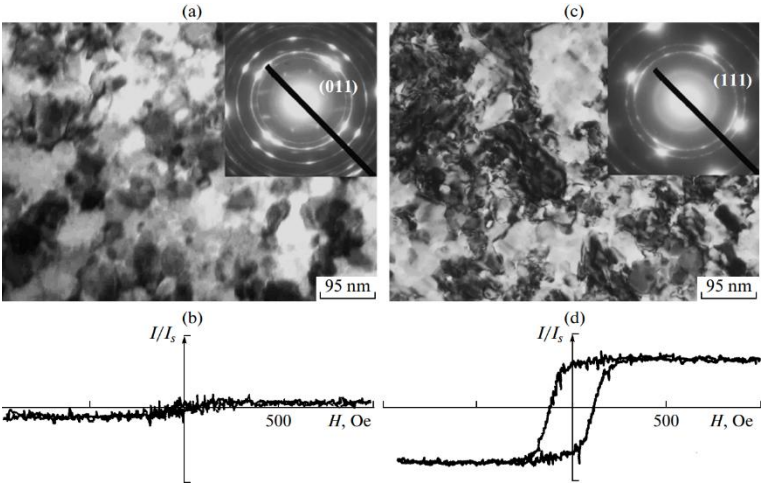

Fig. 2.13. Structure and magnetization curves of a Ni film ($C_M = 0$) deposited at $T_S = 670$ K (a, b) in the as-deposited state and (c, d) after annealing

Figure 2.14 shows histograms that characterize the distributions of grain sizes D in a Ni film in the as-deposited state and after annealing. The ordinate is quantity f corresponding to the density of the relative frequency of the values of D. By definition, we have $f = \frac{n_i}{N\Delta D}$, where n_i is the frequency of the values of D in the i^{th} range, ΔD is the range width, and N is the total number of measurements (which is 111). The dashed line corresponds to the probability density function of normal distribution f_n:

$$f_n = \frac{1}{\sigma\sqrt{2\pi}} \exp\left(\frac{-\left(D-\bar{D}\right)^2}{2\sigma^2}\right), \qquad (2.10)$$

where σ is the standard deviation of D. A comparison of the positions of diagram columns with curve f_n indicates that the size distribution of grains is close to a normal distribution both before and after annealing of the Ni film. As follows from Fig. 2.14, the average grain size before annealing is $\bar{D}$ = 46.6 ± 2.0 nm at a confidence level of 95%. The standard deviation is σ = 10.7 nm and the distribution asymmetry is A_S = 0.24. After annealing, we have $\bar{D}$ = 55.5 ± 2.1 nm, σ = 11.2 nm, and A_S = 0.02. These results can be considered as experimental evidence of the fact that the change in the magnetic properties of the films upon annealing is caused by the magnetic phase transformation.

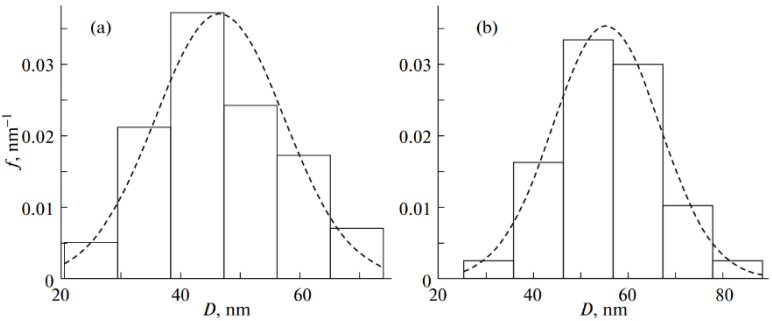

Fig. 2.14. Size D distribution of grains in a Ni film (C_M = 0) deposited at T_S = 670 K (a) in the as-deposited state and (b) after annealing. f is the relative frequency density (dashed line) of the probability density function of normal D distribution.

3. CRYSTALLIZATION OF OXYGEN-CONTAINING AMORPHOUS FILMS

3.1. Amorphized thin-film laser condensates of gold

In [53] a position was formulated, stating that any substance can exist in a non-crystalline solid state (NCS) in one form or another, since this does not contradict any of the physical laws. In addition, many substances and systems with any type of bonding have been obtained in the NCS: metallic, covalent, ionic, hydrogen and van der Waals. Among substances with a metallic type of bonding, obtaining gold in the NCS is particularly difficult due to its inertness to the formation of chemical compounds and the absence of polymorphic forms. According to [54, 55] the number of possible polymorphic forms formed by an element, and consequently the number of variations of bonds and coordination structures possible for a given type of atom, predetermines the probability of the formation of the NCS and the temperature of its crystallization T_{ac}:

$$T_{ac} = \frac{(n_p - 1)T_m}{n_p + 1 + (6 - n_g)}, \tag{3.1}$$

where n_p is the number of polymorphic forms; T_m is the melting temperature; n_g is the group number in the periodic table. In the case of gold, according to (3.1), at $n_p = 1$ $T_{ac} = 0$, i.e. the formation of HTS is impossible.

In most cases, NTS is realized by suppressing the diffusion mobility of adatoms during vapor condensation on a cooled substrate to helium or nitrogen temperatures. Another method of increasing the dispersion of the condensate is the creation of a layer of adsorbed gas impurities on the growth surface. In this case, high dispersion is achieved both by suppressing the surface diffusion of adatoms and by forming impurity clusters along the boundaries of the formed clusters and grains, preventing their unification. The effect of both factors is most noticeable in the case when the gas impurity is insoluble in the

crystal lattice of the substance of the deposited film and, as a rule, leads to the formation of highly dispersed granular or amorphous films [56].

The above considerations allow us to conclude that the pulsed laser method, with the appropriate choice of deposition parameters, can be successfully applied to obtain amorphous condensates of gold without the use of cryogenic cooling of the substrate.

3.1.1. Obtaining and structure of films

An analysis of the characteristics of periodic laser sputtering of a metal target in a gas medium allows us to identify the following moments responsible for the formation of an amorphous film (Fig. 3.1) [57].

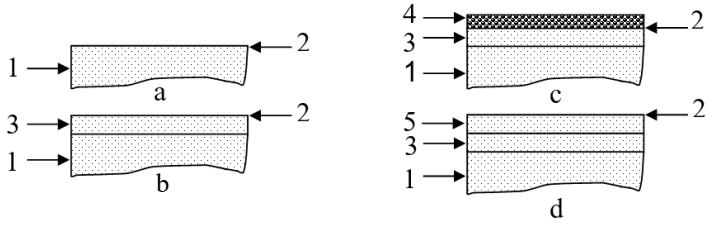

Fig. 3.1. Scheme of the formation of amorphous condensate during laser sputtering of a target in a gas environment (explanation is in the text)

Let condensate 1 and growth surface 2 already exist at an arbitrary time t. During the next condensation pulse, the surface is cleared of adsorbed impurities (stage a) and a layer of substance 3 of thickness d_1 is built up (stage b). During the pause, layer 3 adsorbs gases 4 from the atmosphere of the evaporation chamber, which prevents both the migration of adatoms and the coalescence of islands (stage c). Then, electrons and high-energy ions of the first echelon of laser erosion plasma (LEP) clear the growth surface of adsorbate 4 and a new layer 5 is condensed almost simultaneously (stage d). The effective

movement of the growth surface is $2d_1$. The process is periodically repeated until the layer of the required thickness is built up.

Gold target was sputtered by nanosecond pulses of YAG: Nd 3^+ laser radiation in the Q-modulated mode. The radiation pulse duration τi was ~ 15 ns. The repetition frequency ν could be changed stepwise in the range of 12.5–100 Hz.

The scheme of the evaporation module is shown at Fig. 3.2 [20]. Light beam was introduced into the evaporation chamber and focused by lens 1 on the sputtering target 7. Laser erosion plasma particles at the stage of inertial expansion in the direction opposite to the light beam bombarded the surface of the substrate 2.

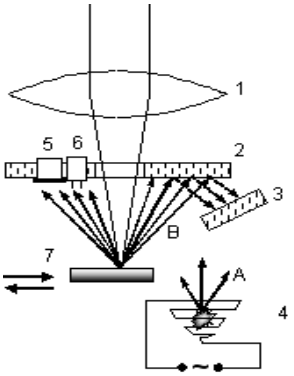

Fig. 3.2. Scheme of the evaporation module for laser film deposition: 1 - focusing lens; 2 - substrate for film deposition from the primary flow; 3 - substrate for film deposition from the secondary flow; 4 - resistive evaporator; 5 - quartz thickness gauge; 6 - dual electric probe; 7 - target

The primary film was condensed on this substrate directly from the vapor-plasma torch. In some experiments, substrate 3 was also installed in the evaporation module. A secondary film formed from a flow of sputtered and

reflected (from the surface of substrate 2) atoms could condense at the inner side of this substrate. The resistive tungsten evaporator 4 could be used for thermal spraying of atoms into the condensation zone of the substrate 2. The rate of thermal evaporation was ~ 0.3 - 1 nm s^{-1}.

The results of electron microscopic studies of laser condensates of gold deposited in an oxygen environment on heated substrates (in the temperature range T_S from room temperature to 600 K) are presented in the form of a semi-quantitative diagram in coordinates $\mathbf{T}_S$ – lg$P$ (Fig. 3.3) [58]. I is the region of existence of the low-temperature NCS (Fig. 3.4a). It has an upper temperature limit equal to the crystallization temperature T_{ac} of the amorphous phase (T_{ac} = 362 K [59]). Region II is polycrystalline films (Fig. 3.4b) and region III is completely or partially oriented films (Fig. 3.4c).

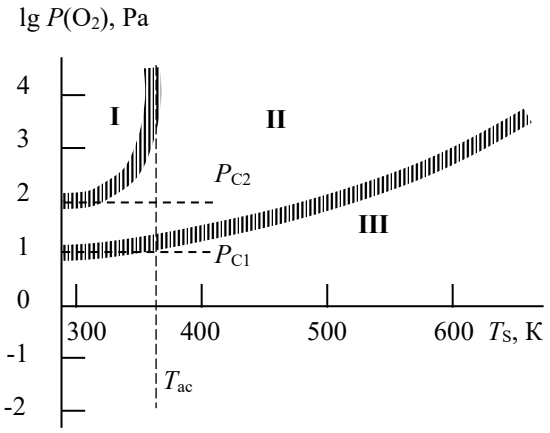

Fig. 3.3. Diagram of structural states of laser condensates of gold deposited in an oxygen environment (explanation is in the text) [58]

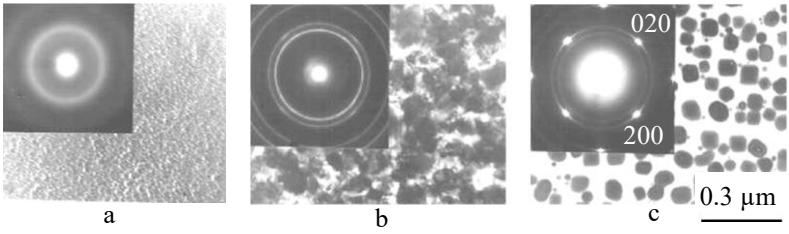

Fig. 3.4. Effect of substrate temperature on the structure of gold laser condensates, deposited in an oxygen atmosphere at $P(O_2)$ = 95 Pa. a). T_S = 293 K; b). T_S = 483 K. c). T_S = 623 K

According to this diagram, to obtain a disordered structure (both amorphous and polycrystalline) at a fixed T_S, the target sputtering should be carried out at high values of $P(O_2)$. This is evidenced by the increasing nature of the curves separating regions I and II, as well as II and III. Since the diffusion mobility of adatoms increases with increasing T_S, high values of $P(O_2)$ are required to suppress it. Similarly, at a fixed value of $P(O_2)$, the degree of orientation of the condensate increases with increasing T_S.

When passing to region I (Fig. 3.3), the position of the first diffraction maximum in the electron diffraction patterns, i.e. the 111 reflection for the crystalline phase and the halo for the amorphous phase, changes abruptly. Photometry of the electron diffraction patterns (Fig. 3.5) showed that in the pressure range where crystalline films are formed, the lattice constant of gold a_0 remains virtually unchanged (the interplanar distance d_{111} = 0.236 nm, which corresponds to the value of the parameter $S = 26.62$ nm^{-1} ($S = 4\pi(\sin\theta)/\lambda$, where λ is the electron wavelength and θ is the scattering angle). For the amorphous state, when $P(O_2) \geq P_{C2}$, the value of S was 23.10 nm^{-1}. The position of the diffusion halos at the electron diffraction patterns does not correspond to the

position of the diffraction maxima of crystalline gold. Therefore, amorphized gold condensates are amorphous, not polycrystalline structures.

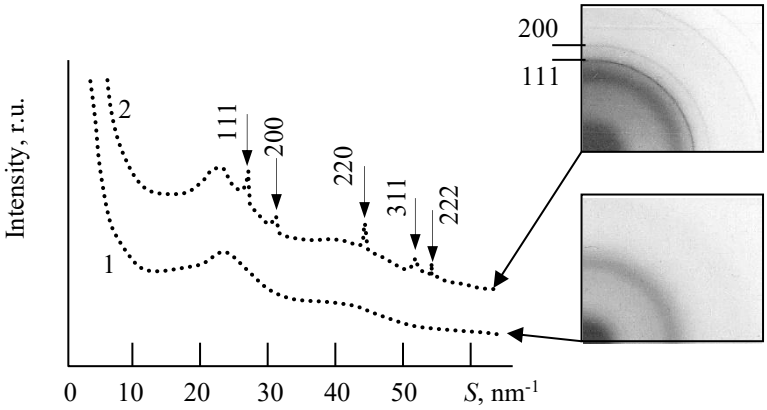

Fig. 3.5. Photometric curves of electron diffraction patterns (contrast is inverted) of gold condensate ($P(O_2)$ = 95 Pa and T_S = 293 K) before (curve 1) and after partial crystallization (curve 2) by local heating of a section of the film with an electron beam

3.1.2. Crystallization of amorphous Au-O films

The concentration of oxygen C(O) in amorphized Au condensates was determined by the Rutherford backscattering (RBS) method of protons. The scattering angle θ was 160°, the beam current ~10 nA. The obtained results of the dependence of C(O) on lg P are shown at fig. 5.6 (curve 1). According to this dependence, the oxygen content in amorphized gold condensates reaches ~ 16 at.% [60]. At the same time, it should be noted that under equilibrium conditions, gold has a high resistance to oxidation and practically excludes the dissolution of oxygen in it both in the liquid and solid states [61].

Capture of oxygen by condensate increases with gas ionization in the evaporation chamber. This is evidenced by a sharp increase of the current on the double electric probe (curve 2 at Fig. 3.6). An increase of the number of charged particles in the precipitated flow initiates capture of the gas by the condensed layer.

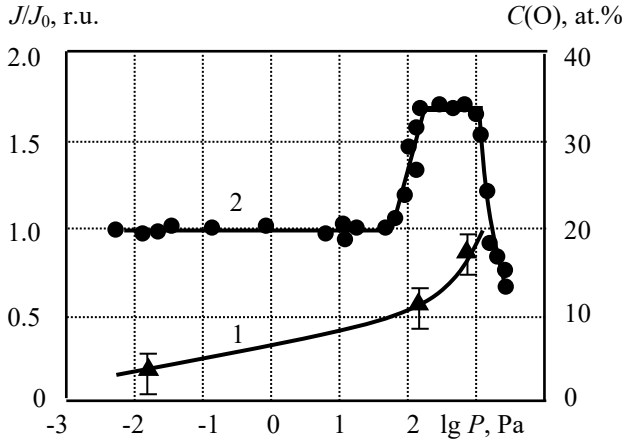

Fig. 3.6. Dependence of the concentration of oxygen in the film (curve 1) and of current on the double electric probe (curve 2) on the pressure of oxygen in the evaporation chamber during laser sputtering of gold [60]

Non-crystalline solid states of Au-O are specific objects, different from liquid and crystalline Au, at least in such parameters as solubility of gas impurities, short-range structure, density and electrical conductivity [60]. This predetermines a very narrow temperature range of the amorphous phase - crystal transition and a high transformation rate, which distinguishes it from the crystallization of finely dispersed media. The time dependence of the electrical resistance $R(t)$ in the vicinity of the amorphous phase - crystal transition point (time t_c) is shown at Fig. 3.7a. A change in the electrical resistance of the

interelectrode gap (filled with the amorphous phase) by three orders of magnitude occurs in a time of $\Delta t \leq 10$ s.

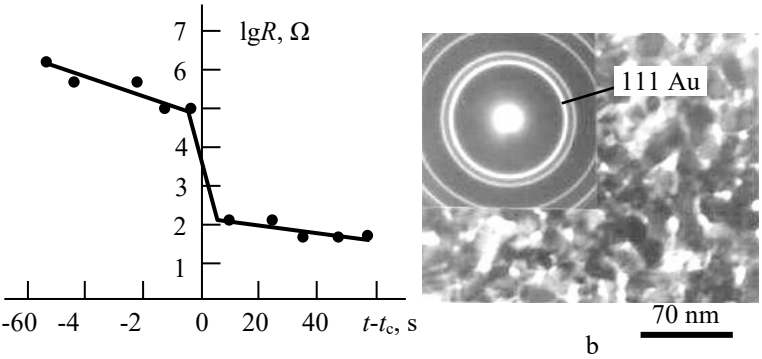

Fig. 3.7. Crystallization of amorphous Au-O film upon thermal heating in vacuum (sputtering of the target at $P(O_2)$ = 110 Pa). a). Dependence of electrical resistance $R(t)$ near the phase transition point. b). Microstructure of crystallized film

The structure of the crystallized region is shown at Fig. 3.7b. Annealing was performed in vacuum on a uniformly heated substrate immediately after film deposition. In the initial state, the amorphous film was continuous. The occurrence of discontinuities after crystallization is associated with a higher density of the crystalline phase. The surface filling coefficient with gold at Fig. 3.7b is 88%. This correlates with the found value of $\Delta\rho/\rho$ ~72% according to [60].

Electron diffraction studies showed that the only product of the crystallization reaction is pure gold with a normal FCC lattice. No new phases or structures were registered. Gaseous impurities that stabilize the amorphous state are released into the vacuum after the transformation or remain in the gold in the form of bubbles located mainly along the grain boundaries.

To determine the crystallization temperature T_{ac}, the dependence of electrical resistance on temperature was plotted in the coordinates $\lg(R_T/R_{293})$ – $1000/T$ (Fig. 3.8). A sharp break in the curve, associated with the restoration of the metallic bond and the FCC structure, occurred at T_{ac}=362K.

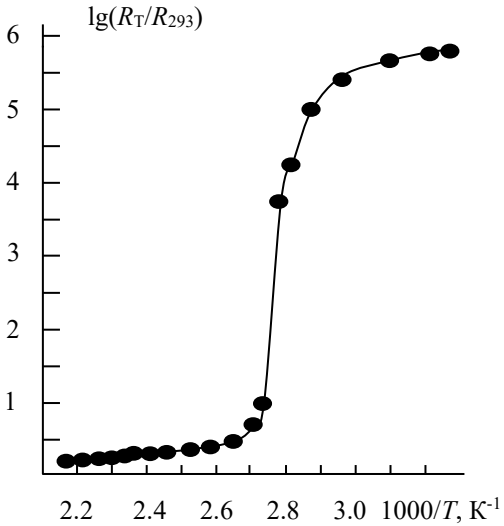

Fig. 3.8. Temperature dependence of electrical resistance of amorphous Au-O film upon thermal annealing in vacuum. Deposition at $P(O_2)$ = 110 Pa)

Knowing the transformation time Δt and the density of grains of the new Au phase on the surface of the substrate (Fig. 3.7), it is possible to estimate the rate of tangential grain growth V_τ. For this, we used Kolmogorov's formula, modified for the case of two-dimensional (flat) crystallization [62], since the film thickness d is many orders of magnitude smaller than the linear dimensions in the plane of the film. The area of the film S crystallized by time t is equal to:

$$S_t = S_0\left\{1 - \exp\left[-\int_0^t J(\zeta)S(R(\zeta,t))d\zeta\right]\right\}, \quad (3.2)$$

where $J(\zeta)$ is the rate of formation of crystallization centers, S_0 is the area of the film, ζ is the current time (integration variable), $S(R)=CR^2$ is the area of the nucleus of radius R, C is the shape constant. For flat nuclei in the form of a circle growing at a rate of V_τ, $R(\zeta,t)= V_\tau(t-\zeta)$ and $S(R(\zeta, t))= \pi V_\tau^2(t-\zeta)^2$. In this case, formula (3.2) takes the form:

$$\eta = 1 - \exp\left[-\int_0^t J(\zeta)\pi V_\tau^2 (t-\zeta)^2 d\zeta\right], \quad (3.3)$$

where the coefficient of surface filling with the crystalline phase is $\eta = S_t/S_0$. At a stationary nucleation rate ($J(\zeta)$ = const) after integrating (3.3) we obtain:

$$\eta = 1 - \exp\left(-\frac{\pi J V_\tau^2 t^3}{3}\right). \quad (3.4)$$

For $\eta \approx 0{,}88$; $J = 4\cdot10^{10}$ sm^{-2s-1} and $t \approx 10$ s, determined from electron micrographs and the $R(t)$ graph, according to (3.4), at the crystallization temperature the linear growth rate of grains in the plane of the substrate $V_\tau \approx 2.2\cdot10^{-3}$ $\mu m\cdot s^{-1}$.

This value of V_τ corresponds in order of magnitude to the so-called "normal" crystallization [63, 64]. The high rate of transformation is achieved not due to V_τ, but due to the high value of the frequency of nucleation of the new phase. The thermal energy released during the transformation process is uniformly distributed over the area of the film and is discharged into the substrate.

3.1.3. Explosive crystallization of amorphous Au-O films

Under certain conditions, another type of transformation can be realized, the so-called "shock" ("explosive") crystallization. It was observed in low-temperature condensates of a number of metals [65], in amorphous antimony films [66], and also in layers of silicon dioxide and silicon oxynitride [63, 64]. In the case of shock crystallization, the velocity of front displacement

V_τ is several orders of magnitude higher than in the case of normal crystallization, and is determined by the value of thermal diffusivity χ of the amorphous phase ($V_\tau \sim \chi/L$, where L is the linear size of the shock crystallization region).

It was established that a similar nature of transformation can also take place during crystallization of amorphized Au condensates, when the film is in a free state, and crystallization is initiated by the local action of an electron beam. In this case, explosive crystallization can be observed directly at a microscope screen by concentrating the electron beam on a selected area of the film. A typical example of explosive crystallization (evaporation of gold at P(Ar)=95 Pa) is shown at Fig. 3.9.

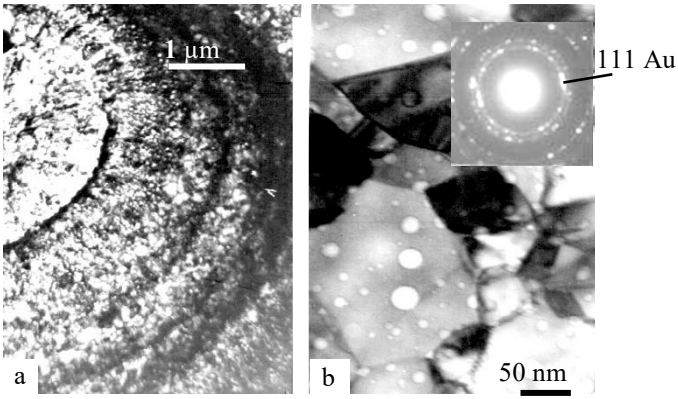

Fig. 3.9. Formation of concentric seams (a) and release of gas bubbles in grains (b) during impact crystallization of amorphized gas-saturated laser condensates of gold. SAED pattern of Au is at the right upper corner

The velocity of the crystallization front motion $V_\tau \approx 20$ μm/s. The explosive crystallization zone is characterized by radial growth of crystals from the center of localization of the electron beam and the presence of concentric seams associated with periodic braking of the front. According to [64],

temporary stops can be caused by the removal of stresses before the crystallization front, since the decrease in the elastic stress field occurs at the speed of sound, and the movement of the crystallization front occurs at a speed controlled by thermal conductivity.

Changes in specific volume and the release of crystallization heat accompanying the transformation cause ruptures and melting of film sections, which complicates a detailed visual study of the process. However, the available micrographs allow us to state the presence of an intermediate liquid phase of gold between the initial amorphous and final crystalline states. The microstructure of such film sections is shown at Fig. 3.9b. The thin-film layer of liquid that arises during the transformation is in a state of strong supercooling. Therefore, it crystallizes almost instantly. Since the gas impurities, that present in amorphous layer are insoluble in either liquid or crystalline phase of gold, they are released in the form of gas-filled bubbles.

The presence of a liquid phase at the moment of transformation was established by electron microscopy methods: the amorphous phase → liquid → crystal (A-L-C) mechanism is realized. The resulting liquid is in a state of strong supercooling and instantly crystallizes. The released heat of transition is used to maintain the explosive crystallization reaction.

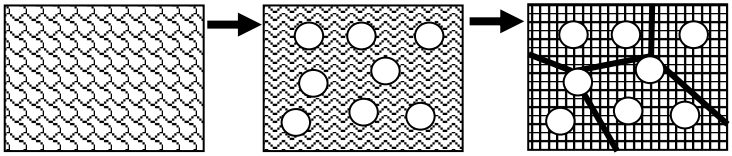

Fig. 3.10. Crystallization scheme of amorphized Au-O condensate by the A-L-C mechanism. 1 – amorphized gas-saturated condensate. 2 – stratification into supercooled liquid and gaseous phases. 3 – crystallization of the liquid phase.

The scheme of the crystallization reaction of amorphized Au-O by the A-L-C mechanism is shown at Fig. 3.10. The onset of the reaction is accompanied by stratification of the medium into gaseous (O_2) and liquid (Au) phases, since gas impurities are insoluble in liquid gold. The supercooled liquid phase crystallizes with the formation of Au grains with a natural FCC lattice (polymorphic crystallization from the liquid phase).

3.2. Amorphized thin-film laser condensates of selenium

Hexagonal modifications of selenium are thermodynamically stable up to the melting temperature [67]. Se crystals consist of helical chains (Se_∞) parallel to the *c* axis. Within the chains, the bond between atoms is covalent, and between chains it is partially metallic and molecular (of the Van der Waals type). The presence of many polymorphic forms of selenium suggests a high probability of formation and thermal stability of its NCS. According to (3.1), the reduced crystallization temperature of amorphous selenium is equal to 0.67 (the number of polymorphic forms with different spatial groups of crystal lattices $n_p = 5$). This agrees well with experimental data (0.62-0.76 [54]).

Amorphous selenium condensates are widely used as photosensitive layers for electrophotography and electroradiography. They can be obtained by thermal spraying in a vacuum or in a controlled gas environment on substrates, whose temperature is no higher than 318 K. At temperatures above 313 K, the process of spontaneous crystallization becomes noticeable, which significantly reduces the area of technical application of Se [68]. At the film-substrate interface single crystal nucleus arise, which are distorted in a regular manner during the growth process and turn into a spherulites (or more precisely, into their flat analogues, a "cylindrites" [69]).

Oxygen improves the parameters of photoconductive layers and also has a stabilizing effect on the amorphous phase. Oxygen doping is carried out by thermal evaporation of Se in an O_2 atmosphere. In this case, the oxygen concentration in film does not exceed 0.12 at.%, that corresponds to oxygen saturation of metallic impurities and the ends of selenium chains [70]. The oxygen content in the amorphous film can be increased in the "intermittent"

selenium deposition mode (single interruption of condensation, maintaining the layer in a gaseous environment, and subsequent resumption of thermal deposition) [71]. Multiple implementations of this mode can be achieved with pulsed laser sputtering of Se according to the scheme, that shown at Fig. 3.1. In this case, the layer of substance deposited in one radiation pulse is exposed to the action of molecules of the gas environment during the pause, as well as to ion bombardment during the condensation of the subsequent layer.

3.2.1. Obtaining of amorphous laser condensates of Se-O

Selenium films were obtained by condensation of laser selenium plasma on substrates in the form of amorphous carbon films, massive glassy carbon plates and (001) KCl at T_s= 293 K. For this purpose, high-purity Se targets were sputtered by laser radiation pulses with a repetition rate v= 12.5 - 100 s^{-1} and a power density of q=(1-3)·10^9 W·cm^{-2}. The $P(O_2)$ value was varied in the range of 10^{-3} -260 Pa using the SNA-2 injection system. At a frequency of v=25 Hz, the average selenium condensation rate in vacuum was ~1.5 nm· s^{-1}.

With increasing of $P(O_2)$, it monotonically decreased due to the scattering of the vapor-plasma flow on oxygen molecules. A selenium layer with a thickness of d_1=0.06 nm and 0.02 nm were deposited in one evaporation pulse at pressures of 10^{-3} and 260 Pa, respectively. The oxygen concentration C(O) in the films was determined by the Rutherford backscattering (RBS) method of protons [72].

The presence of oxygen in selenium films deposited in oxygen atmosphere was detected. The dependence of C(O) on the oxygen pressure in the evaporation chamber $P(O_2)$ is shown at Fig. 3.11a. Concentration C(O) increases monotonically and reaches ~9 at.% at $P(O_2)$≈260 Pa. This graph is constructed for the case of v=25 s^{-1}. With increasing frequency, the time of action of oxygen molecules on the film growth surface decreases. Therefore, C(O) decreases monotonically with increasing v. The dependence of C(O) on v (at $P(O_2)$ = 260 Pa) is shown at Fig. 3.11b.

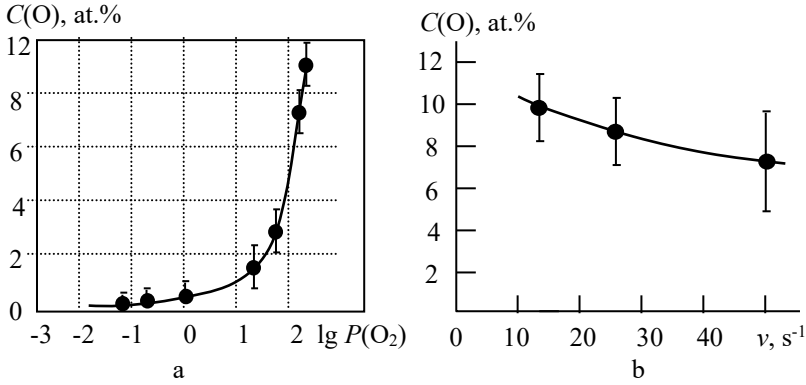

Fig. 3.11. Oxygen concentration C(O) in selenium films deposited by laser evaporation. a). The dependence of C(O) on oxygen pressure $P(O_2)$ at v=25 s^{-1}. b). The dependence of C(O) on v at a fixed pressure $P(O_2)$=260 Pa [72]

In the entire studied range of oxygen pressures the Se films obtained by laser evaporation were amorphous (at room temperature of the substrate). The electron diffraction patterns of the films, deposited in vacuum and at $P(O_2)$ =130 Pa are shown at Fig. 3.12a and 3.12b respectively. Three maxima are observed at the electron diffraction patterns, the S values of which are given in Table 3.1.

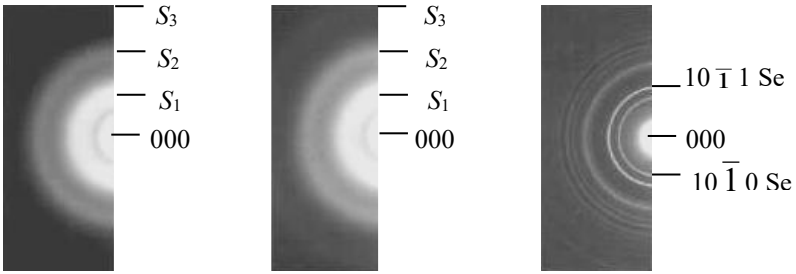

Fig. 3.12. Electron diffraction patterns of films deposited by laser sputtering of Se: a - deposition in vacuum; b - deposition in an O_2 atmosphere at $P(O_2)$ = 130 Pa; c - the same after crystallization of the amorphous phase (hexagonal modification of Se)

Table 3.1 - Position of diffuse halos and reflections in electron diffraction patterns of selenium films*

Specimen	S_1(nm^{-1})	S_2(nm^{-1})	S_3(nm^{-1})
Laser evaporation of Se in vacuum	18.7	34.8	52.9
Laser evaporation of Se in O_2 atmosphere (130 Pa)	18.7	35.1	53.3

*Note: $S = 4\pi(\sin\theta)/\lambda$, where λ is the electron wavelength and θ is the scattering angle

3.2.2. Crystallization of amorphous films of Se-O

Amorphous Se layers deposited both in vacuum and in O_2 atmosphere did not exhibit significant morphological differences. They appeared only at annealing of the films both in air (furnace annealing) and in vacuum (heating with an electron beam in a microscope column). Two types of crystallization

reactions were determined. In Se condensates with a low oxygen content, polymorphic crystallization occurred (according to the classification [73]). The amorphous phase was transformed into a crystalline one due to the formation and growth of spherulites. The ribbon blocks of spherulites were separated by low-angle boundaries and diverged in radial directions. Their crystalline structure corresponded to the hexagonal modification of Se. As a rule, the *c* axis was oriented perpendicular to the plane of the film (Fig. 3.13a).

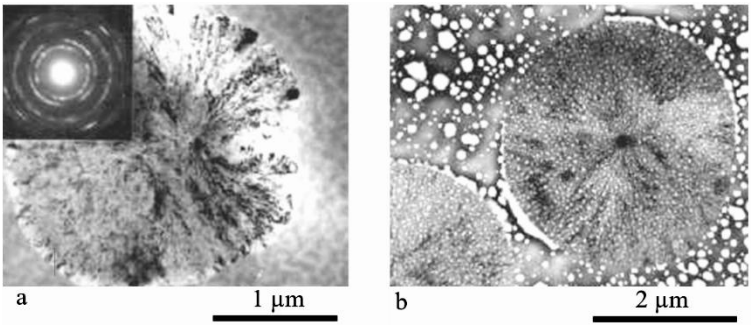

Fig. 3.13. Structural and morphological changes in Se-O films during annealing (361 K): a - laser evaporation of Se at $P(O_2)$=1.3 Pa; b - $P(O_2)$=130 Pa. Annealing time t = 20 min. SAED pattern is in the upper left corner of the micrograph

The transformation in gas-saturated films occurred according to the scheme:

amorphous Se-O→amorphous Se+O_2(gas)→crystalline Se+O_2(gas). (3.5)

At the first stage of transformation, the amorphous phase was separated into two components: Se and excess oxygen, which was released in the amorphous film in the form of bubbles and micropores. At this stage, a metastable

equilibrium of the system was achieved: amorphous Se + gaseous O_2. Later or at a higher annealing temperature, the second stage occurred - polymorphic crystallization of selenium. Growing selenium spherulites had a porous structure due to the capture of gas bubbles from the amorphous matrix. The formation of oxide phases was not detected.

Phase separation is clearly visible at Fig. 3.13b, when selenium was deposited at $P(O_2)$=133 Pa (C(O)~7.2 at.%). The spherulites contain smaller pores than the amorphous matrix. The average diameter D and pore density ρ are, respectively, 22 nm and $5 \cdot 10^{10}$ cm^{-2} (spherulite) and D=130 nm and $\rho = 5 \cdot 10^9$ cm^{-2} (amorphous matrix).

The action of the electron beam initiates diffusion processes in the film at the stage preceding crystallization. Old pores disappear (come to the surface) and new ones form and grow. Figure 3.14 shows a series of microphotographs of the same place on the film during its heating by an electron beam. The reference points, fixing the position of the analyzed field, are four Se microdroplets transferred by the vapor-plasma flow to the substrate ("splash" effect). They are marked with numbers 1-4.

The presented microphotographs illustrate not only the fact of the emergence and growth of pores, but also their disappearance and even the formation of thickenings in place of the disappeared pore (mark 4). The approach of the crystallization front to the pore caused a distortion of its shape: it acquired the shape of a deformed ellipse, the long axis of which is oriented perpendicular to the direction of growth of the ribbon block (Fig. 3.14d).

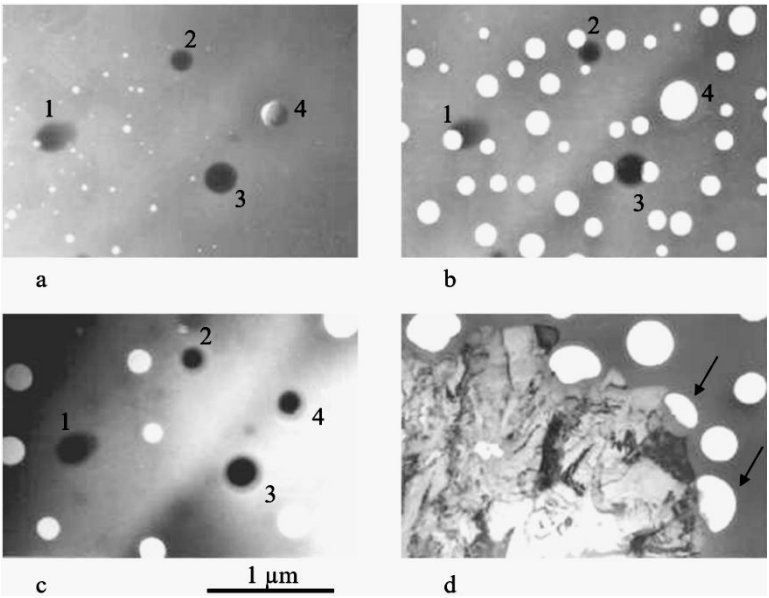

Fig. 3.14. Transformations in amorphous gas-saturated films during annealing with an electron beam: a, b, c - formation of pores in the amorphous matrix. Numbers 1-4 indicate marks fixing the analyzed area. The intensity of heating increases from image a to image c; d - crystallization of the amorphous phase. The arrow indicates the distortion of the pore shape under the influence of the crystallization front [72]

3.2.3. Kinetics of a-c transformation at annealing of Se-O films

The kinetics of transformation from amorphous phase to the crystalline one (a-c transformation) was studied during isothermal annealing of selenium films of a fixed thickness ($d \approx 60$ nm) on substrates of (001) KCl, coated with a thin layer of amorphous carbon. Annealing was carried out in air at temperatures T equal to 361, 378, 388 and 403 K.

Experimental graphs of the dependence of the average spherulite radius R on the annealing duration t of films deposited at different values of $P(O_2)$ are shown at Fig. 3.15a [74]. Each family of straight lines corresponds to a fixed annealing temperature T. The linear nature of the $R(t)$ dependence indicates the constancy of the tangential velocity of the crystallization front motion v_τ, which agrees with [75]. v_τ was determined from the slope of the straight lines to the t axis.

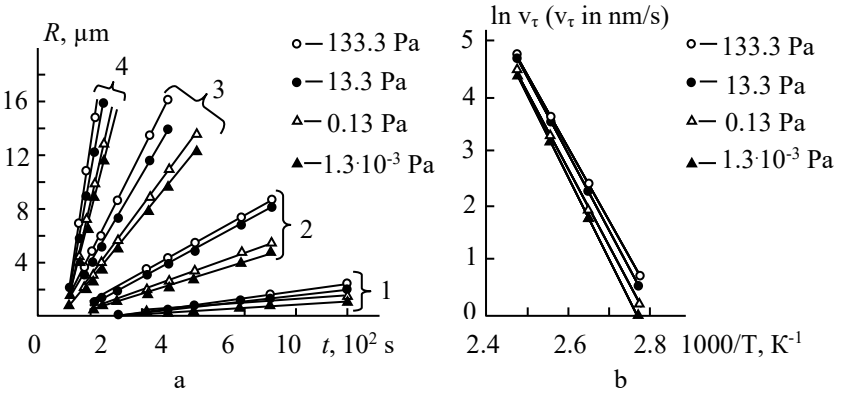

Fig. 3.15. Average radius R (a) and growth rate v_τ (b) of spherulites during isothermal annealing of Se-O films. Family of lines 1 corresponds to annealing at a temperature of 361 K; 2 - at 378 K; 3 - at 388 K; 4 - at 403 K [74]

The temperature dependence of v_τ on T in the coordinates ln v_τ - T^{-1} is shown at Fig. 3.15b. The linear dependence of ln v_τ on T^{-1} suggests that $v_\tau(T)$ is described by the Arrhenius equation [76]:

$$v_\tau = v_o \exp(-U_g/R_gT). \quad (3.6)$$

In expression (3.6) v_o is a constant with the dimension of velocity (μm/s); U_g is the activation energy of growth (kJ/mol); R_g is the gas constant. The values

of U_g and v_o, determined from the graphs at Fig. 3.15b, are given in Table 3.2. They indicate an increase in the tendency to crystallization with increasing of oxygen content in selenium films.

Table 3.2 - Oxygen concentration and crystallization parameters of amorphous Se-O films

$P(O_2)$, Pa	C(O), at.%	v_0, μm/s	U_g, kJ/mol
$1{,}3\cdot10^{-3}$	-	$8.1\cdot10^{14}$	123
0,133	0,2	$3.6\cdot10^{14}$	120
13,3	1,4	$1.8\cdot10^{14}$	117
133	7,2	$1.5\cdot10^{14}$	117

4. ON THE CLASSIFICATION OF CRYSTALLIZATION REACTIONS IN THIN AMORPHOUS FILMS

4.1. Polymorphous, preferential and eutectic crystallization

The stable operation of electronic devices based on amorphous substance in some cases implies the invariance of the amorphous structure (for example, photoelectronic converters). In some cases, the effective operation of the device is associated with the possibility of multiple phase transformations of the type non-crystalline state - crystal - non-crystalline state (for example, optical recording media) in a local area of the object. In all cases, it is necessary to know the features of the transition of amorphous substance into a crystalline substance and the systematization of crystallization reactions according to the selected features.

Amorphous films can crystallize spontaneously or under the influence of physical actions, i.e. move from a metastable no crystalline solid state to a stable crystalline state. In the general case, crystallization occurs according to one of the following schemes [77].

1. Polymorphous crystallization. This is the simplest type of transformation, in which an amorphous substance passes into a crystalline one without changing its composition. It is characteristic of both pure elements and stoichiometric chemical compounds.

2. Preferential crystallization of one of the phases at the first stage of the process and subsequent crystallization of the matrix at the second stage.

3. Eutectic crystallization, in which two crystalline phases are almost simultaneously segregates.

The implementation of the type of crystallization reaction is predetermined by the type of dependence of free energy of various phases on the concentration of chemical elements. To systematize the experimental results, it is advisable to use the classification of crystallization reactions and the hypothetical diagram of the free energy of amorphous and crystalline phases proposed by W. Kester [77] for metallic glasses (in particular, Fe-B). An analogue of such a diagram for gas-saturated laser condensates is shown at Fig. 4.1 [78].

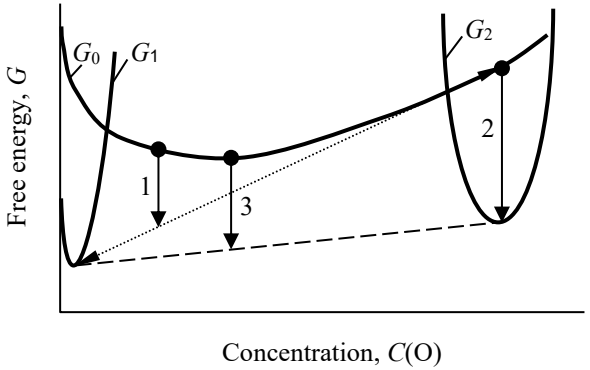

Fig. 4.1. Free energy diagram G for explanation of crystallization reactions of amorphous gas-saturated condensates. Curves G_0, G_1, G_2 - conditional dependences of free energy of the initial amorphous phase, crystalline chromium and crystalline metal on oxygen concentration. 1 - preferential crystallization, 2 - polymorphic, 3 - eutectic crystallization [78]

The driving force of crystallization is the difference in the free energies of the amorphous phase (G_0) and the crystalline phases of the metal (G_1) and its oxide (G_2). For example, in the case of chromium sputtering, the latter corresponds to Cr_2O_3, since this is the only thermodynamically stable oxide [79].

At laser sputtering of chromium in a wide pressure range from 10^{-5} to 10^{-3} Pa, amorphous condensates of non-stoichiometric composition Cr_xO_v are formed, and with increasing of $P(O_2)$ the ratio y/x increases. For this reason, crystallization has a two-stage nature (Fig. 4.2). At the first stage (the so-called predominant crystallization), finely dispersed crystals of chromium are released in the amorphous matrix (at annealing temperature $T_{an} \geq 523$ K), and the matrix itself is enriched with oxygen (arrow 1 at Fig. 4.1).

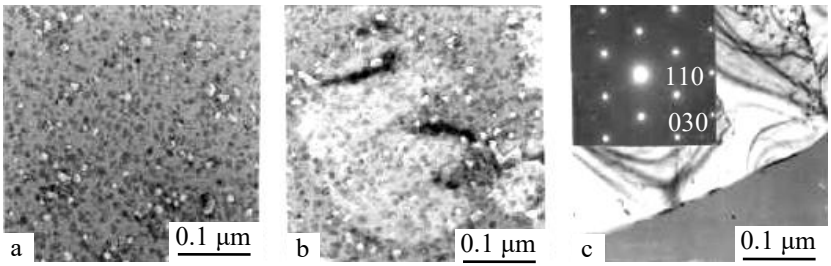

Fig. 4.2. Types of crystallization reactions established for laser chromium condensates: a, b – two-stage (preferential and polymorphic) crystallization of films of non-stoichiometric composition; c – one-stage (polymorphous) crystallization of Cr_2O_3. The size and total volume of chromium crystals depends on the composition of the sample: they decrease monotonically as the composition approaches stoichiometric Cr_2O_3

The primary precipitation of chromium crystals in amorphous films is shown in Fig. 4.2a. With increase of the pressure from $2 \cdot 10^{-5}$ to $8 \cdot 10^{-4}$ Pa, their size decreases from 10 to 3 nm. The reaction of preferential crystallization is completed upon reaching a metastable equilibrium of chromium + amorphous

phase Cr-O. An increase of T_{an} to 593 K (or exposure to an electron beam) initiates the next stage - polymorphic crystallization of the amorphous matrix. Without changing the composition it passes into the crystalline oxide Cr_2O_3 (Fig. 4.2b). A single-stage phase transition by polymorphic crystallization was observed in films deposited by laser sputtering at $P(O_2) \geq 6 \cdot 10^{-2}$ Pa (Fig. 4.2c). In this case, there was no primary precipitation of crystalline chromium. Cr_2O_3 crystals (mainly (001) orientation) were generated in the amorphous matrix, the development of which proceeded according to the spherulitic type.

The structure and composition of precipitates in oxygen-enriched iron films (sputtering at $5 \cdot 10^{-5} < P \leq 8 \cdot 10^{-4}$ Pa) was depended on both the annealing temperature T_{an} and the heating rate V_h [80]. Crystallization of laser condensates of Fe doped with oxygen is shown at Fig. 4.3.

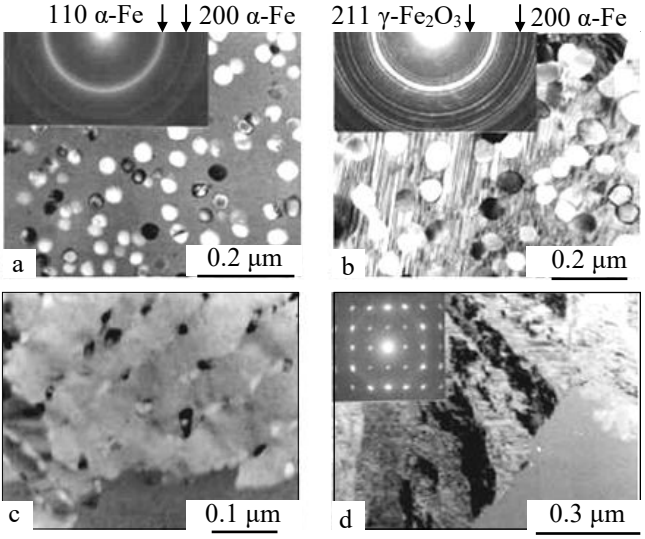

Fig. 4.3. Crystallization of laser condensates of Fe doped with oxygen: a- precipitation of primary crystals of α-Fe at the stage of preferential crystallization; b- polymorphic crystallization of γ-Fe_2O_3; c- eutectic crystallization of α-Fe and γ-Fe_2O_3; d- polymorphic crystallization of γ-Fe_2O_3

At $T_{an} \geq 493$ K and $V_h \approx 0.1$ K/s (annealing on the substrate by resistive heating of the substrate holder), predominant crystallization with the precipitation of primary α-Fe crystals occurred (arrow 1 in Fig. 4.1). Above 593 K, the oxygen-enriched amorphous matrix crystallizes polymorphically with the formation of crystals of the cubic and tetragonal modifications of γ-Fe_2O_3 (respectively, a_0=0.835 nm and a_0=0.833 and c_0=2.499 nm). A pronounced banded contrast (Fig. 4.3b) indicates the ordering of defects in the lattice of γ-Fe_2O_3 during crystallization of the amorphous phase. Domains are formed as a result of phase transitions associated with a change in lattice symmetry. They can be connected to each other by simple translation (for example, antiphase domain boundaries), or by a mirror plane of symmetry (for example, during twinning caused by a polymorphic transition) [81].

Eutectic crystallization (arrow 3 at Fig. 4.1) was observed at high sample heating rates of the order of 10 K/s (pulsed heating of a section of the film by an electron beam in the microscope column). In this case, the formation of α-Fe and γ-Fe_2O_3 crystals occurs almost simultaneously. An image of the eutectic intergrowth of the metallic and oxide phases is shown at Fig. 4.3c.

With increasing of $P(O_2)$, the volume fraction of α-Fe crystals monotonically decreased, and at $P(O_2) \geq 10^{-2}$ Pa only phase of Fe_2O_3 was observed (Fig. 4.3d). Such a single-stage transition from the amorphous to the crystalline state corresponds to the polymorphic type of crystallization.

4.2. Crystallization modes at electron beam impact

The rate of transformation is determined both by the rate of crystal growth and the rate of formation of crystallization centers. Depending on which process prevails, a division is made into growth-driven crystallization and crystal nucleation-driven crystallization [82].

An example of growth-driven crystallization of amorphous film of Ta_2O_5 is shown at Fig. 4.4a. Under the influence of an electron beam, a single crystal grows in the field of electron microscopic observation. Dotted lines 1

and 2 give the position of the crystallization front at times t_1 and $t_2=t_1+\Delta t$. During time t, the increment of diameter D is ΔD.

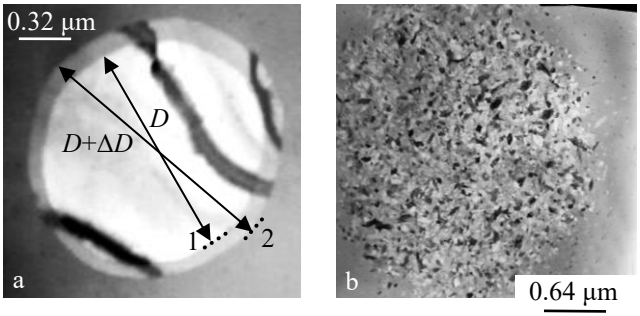

Fig. 4.4. Growth-driven crystallization of Ta_2O_5 (a) and crystal nucleation-driven crystallization of Sb_2Se_3 (b)

An example of nucleation-driven crystallization of amorphous film of Sb_2Se_3 is shown at Fig. 4.4b. Under the influence of an electron beam, a multitude of disoriented small crystals grows in the field of electron microscopic observation.

According to the type of crystal formation, nucleation-driven crystallization can be divided into Site-Saturate Nucleation (SSN) and Constant Nucleation Rate (CNR) [83]. At SSN nucleation happens only at the beginning and growth takes place afterwards (example for ZrO_2 at Fig. 4.5a). At CNR the formation and growth of new crystals occurs throughout the entire period of exposure to the amorphous film (example for Yb_2O_2S at Fig. 4.5b).

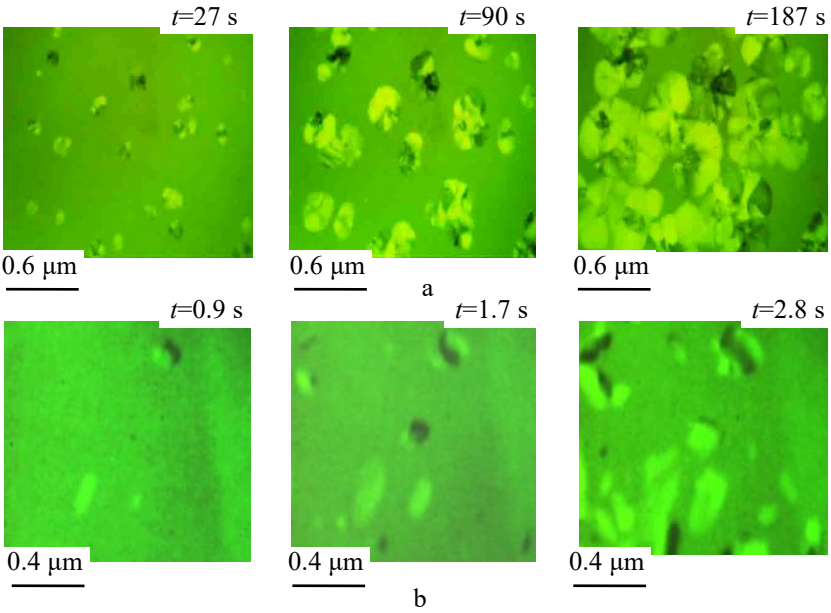

Fig. 4.5. Film footage of Site-Saturate Nucleation in amorphous film of ZrO_2 (a) and Constant Nucleation Rate in amorphous film of Yb_2O_2S (b). In the upper left corner of each frame the time, elapsed since the start of filming is given.

Numerous «in situ» electron microscopic studies have shown that polymorphous crystallization of thin amorphous films is adequately described by a phenomenological scheme, that includes the following types (crystallization modes) of crystal, growth in an amorphous matrix. A schematic representation of the four crystallization modes, realized in amorphous films under the action of an electron beam, is shown at Fig. 4.6 [84].

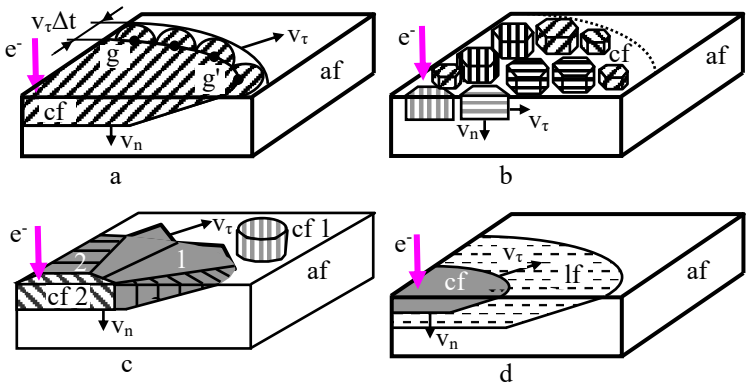

Fig. 4.6. Crystallization modes in amorphous films: a - layer polymorphous crystallization; b - island polymorphous crystallization; c - dendrite polymorphous crystallization; d - fluid-phase crystallization. af - amorphous phase, cf - crystalline phase, lf - liquid phase. Arrow e^- indicates the location of the electron beam impact. 1, 2 - respectively dendritic branches of the first and second orders

1. Layer polymorphous crystallization (LPC). In this case the crystalline phase (the primary single crystal cf at Fig. 4.6 a) is formed in a thin surface layer at the site of action of the electron beam on the film (marked in the figure by the arrow "e^-"). The composition of the crystalline phase (cf) corresponds to the composition of the amorphous phase (af). The interface between amorphous phase and vacuum is the site of nucleation of the crystalline phase, was experimentally identified in [85] during study of the crystallization of amorphous $Ge_2Sb_2Te_5$ films. The velocity v_τ of the crystallization front motion in the tangential direction (parallel to the film surface) significantly exceeds the velocity v_n of the crystallization front motion along the normal to the film surface. The crystalline layer "spreads" over the film surface. The movement of

the crystallization front can be compared with the displacement with the velocity v_τ of the line, corresponding to the contact of the amorphous phase, crystalline phase and vacuum (solid line g-g' at Fig. 4.6a).

As the single crystal grows, the g-g' line (crystallization line) moves in the same way as the front of a light wave moves in accordance with the Huygens-Fresnel principle [86]. Each point of the crystallization line is a source of "flat" secondary crystallization centers. These secondary centers have the same orientation, coinciding with the orientation of the primary crystal (i.e. they are "coherent" with each other). Growing together ("interfering"), over time Δt they provide a displacement of each point of the crystallization line by the value $v_\tau \Delta t$. The new position of the crystallization line corresponds to the envelope of the secondary crystallization centers. In light of the above, the formation of a single-crystal nucleus and its subsequent growth by the LPC mode can be interpreted as a variant of "coherent crystallization" of an amorphous film.

The analogue of the LPC mode for the case of film growth on a substrate from the vapor phase is the layered growth according to Frank and Van der Merwe [87]. In accordance with [88], the energy criterion of the LPC mode can be the ratio:

$$\sigma_a \geq \sigma_c + \sigma_{ac} + \varepsilon_d, \tag{4.1}$$

where σ_a, σ_c, σ_{ac} are the surface energy of the amorphous phase - vacuum interface, the surface energy of the crystalline phase - vacuum interface, and the surface energy of the amorphous - crystalline phase interface respectively; ε_d is the strain energy of the growing crystalline layer. The crystalline phase tends to exclude the free surface of the amorphous film, which has a high σ_a value (the "wetting" condition). The LPC mode is largely inherent in semiconductors (Se, Sb, Sb_2S_3), oxides and metal alloys (Cr_2O_3, V_2O_3, Ta_2O_5, Nb_2O_5, Fe_2O_3 and $Ti_{41}Zr_{41}Ni_{18}$).

An example of the LPC as a result of the local action of an electron beam on amorphous film of Cr_2O_3, obtained by laser sputtering of Cr in an oxygen atmosphere, is shown at Fig. 4.7a. The film thickness $d \sim 21.7$ nm. In

the region of the electron beam action, a single flat Cr_2O_3 crystal is formed in amorphous film and grows with a rate $v_\tau \approx 1.2$ μm·s^{-1}. The same growth rate and a similar mechanism of the LPC occur at annealing in vacuum at a temperature of $T_{an} = 930$ K (Fig. 4.7b). As it grows, the crystal bends in a regular manner due to the action of tensile stresses, and bending extinction contours appear on its image.

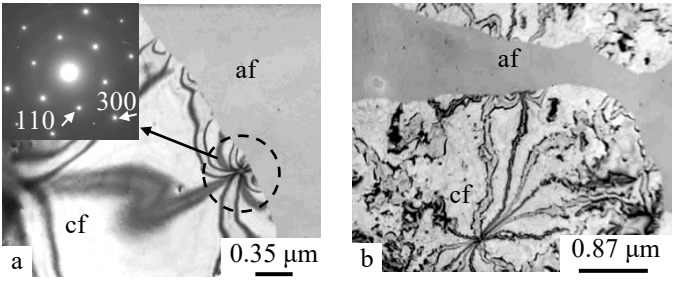

Fig. 4.7. Layer polymorphous crystallization of amorphous films: a - formation of the crystalline phase Cr_2O_3, initiated by local action of an electron beam; b - the same as a result of thermal annealing of the film

In the case when the composition of the amorphous film differs from the stoichiometric composition, the LPC stage is preceded by the precipitation of excess element crystals in the amorphous matrix. The primary precipitation of Sb microcrystals in the amorphous matrix (marked with arrows) and the subsequent layer polymorphous crystallization of Sb_2S_3, initiated by the action of an electron beam, is shown at Fig. 4.8a. It should be noted that the presence of Sb islands in the amorphous layer has virtually no effect on the structure and morphology of the growing Sb_2S_3 crystal.

The presence of an active substance on the surface of an amorphous layer can change the crystallization mechanism. For example, during crystallization of amorphous Sb_2S_3 films, the layer mechanism is clearly manifested

(Fig. 4.8a). The introduction of Au islands onto the surface of amorphous Sb_2S_3 slows down the movement of the crystallization line. The LPC mode is replaced by the IPC mode, which is accompanied by the formation of a finely dispersed polycrystalline structure of Sb_2S_3 (Fig. 4.8b).

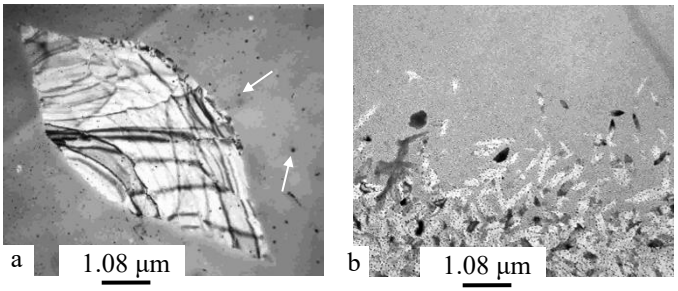

Fig. 4.8. Transition from layer (a) to island (b) polymorphous crystallization in amorphous films of Sb_2S_3. Arrows indicate the primary precipitation of Sb microcrystals in the amorphous matrix of Sb_2S_3

2. Island polymorphic crystallization (IPC). At IPC mode the crystalline phase is formed in the near-surface layer (Fig. 4.6b) and its composition corresponds to the composition of the amorphous phase. However, due to the high rate of formation of disoriented (incoherent) crystallization centers and the fact that $v_\tau \approx v_n$, a finely dispersed polycrystalline layer is formed at the final stage of the process ("incoherent" crystallization of amorphous film). An analogue of the IPC mode in the case of film growth on a substrate from the vapor phase is the island growth according to Volmer and Weber [87, 88]. The energy criterion of the IPC mode can be the ratio:

$$\sigma_a < \sigma_c + \sigma_{ac} + \varepsilon_d. \qquad (4.2)$$

Due to the smallness of σ_a, the crystalline phase does not tend to exclude the free surface of the amorphous film (the "non-wetting" condition).

The IPC mode is characteristic of the crystallization of some amorphous metals, oxides and semiconductors (Ni, Re, Al_2O_3, Yb_2O_2S, ZrO_2 and Sb_2Se_3). The example of IPC mode in amorphous Al_2O_3 film, obtained by laser sputtering of Al in an oxygen atmosphere, is shown at Fig. 4.9a. Electron irradiation initiates in the film formation of a finely dispersed crystals (cf) corresponds to the cubic modification of γ-Al_2O_3 [89]. In the case of uniform heating of the film in a vacuum, a similar structure is formed at T_{an} = 1220 K.

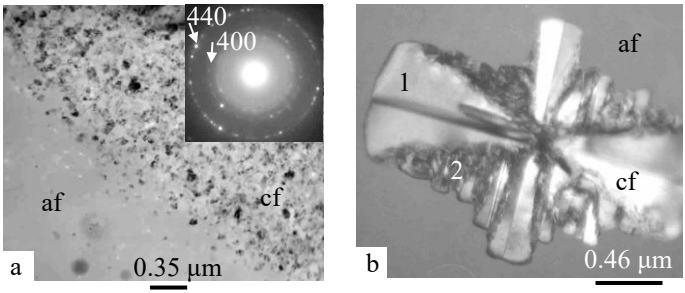

Fig. 4.9. Crystallization of amorphous films under electronic beam heating: island polymorphic crystallization mode in Al_2O_3 (a) and dendrite polymorphous crystallization mode in HfO_2 (b). 1 - first order dendritic branches. 2 - second order dendritic branches.

3. Dendrite polymorphic crystallization (DPC) It can be associated with the Stranski - Krastanov (SK) growth mode (single-crystal layer and subsequent growth of islands on it) [90]. DPC (Fig. 4.6c) is realized when the inequality $\sigma_a \geq \sigma_c + \sigma_{ac} + \varepsilon_d$ is initially satisfied (a single crystal grows in the form of a first-order dendritic branch). After reaching the critical size of the crystal, islands grow on its lateral surface (in this case, the inequality $\sigma_a \leq \sigma_c + \sigma_{ac} + \varepsilon_d$) takes place, which form a polycrystalline interlayer. Dendritic branches of the second and higher order are formed in the process of geometric selection of grains growing from this interlayer (Fig. 4.9b.). The DPC mode is

realized during the crystallization of amorphous films of HfO_2 [12] and Fe-C [92].

Comparison of polymorphous transformations amorphous phase - crystal (during electron-beam crystallization of amorphous film) and vapor - crystal (during vapor deposition on substrate) is given in table. 4.1.

Table 4.1 - Comparison of phase transformations amorphous phase - crystal and vapor - crystal*

Amorphous phase - crystal		Vapor - crystal	
Type of crystallization	Condition	Growth mode	Condition
LPC	$\sigma_a \geq \sigma_c + \sigma_{ac} + \varepsilon_d$	FM	$\gamma_s \geq \gamma_f + \gamma_{sf}$
IPC	$\sigma_a \leq \sigma_c + \sigma_{ac} + \varepsilon_d$	VW	$\gamma_s \leq \gamma_f + \gamma_{sf}$
DPC	Initially $\sigma_a \geq \sigma_c + \sigma_{ac} + \varepsilon_d$, Then $\sigma_a \leq \sigma_c + \sigma_{ac} + \varepsilon_d$	SK	Initially $\gamma_s \geq \gamma_f + \gamma_{sf}$, Then $\gamma_s \leq \gamma_f + \gamma_{sf}$

*LPC - layer polymorphous crystallization; IPC, island polymorphous crystallization; DPC - dendrite polymorphous crystallization; σ_a, σ_c, σ_{ac} are the surface energy of the amorphous phase - vacuum interface, the surface energy of the crystalline phase - vacuum interface, and the surface energy of the amorphous - crystalline phase interface, respectively; ε_d is the strain energy of the growing crystalline layer. FM is the Frank-van der Merwe growth mode, VW is the Volmer - Weber growth mode, SK is the Stranski - Krastanov growth mode; γ_s, γ_f, γ_{sf} are the surface energy of the substrate, film and the interfacial energy between the film and substrate, respectively.

4. Fluid-phase crystallization (FPhC). In this case in amorphous layer, which is in a highly nonequilibrium state, liquid is formed as a result of

physical action (Fig. 4.6d). It almost instantly solidifies. The FPhC type is inherent in gas-saturated Au-O condensates, obtained by laser ablation of gold in a gaseous medium [58, 59]. A detailed description of this type of transformation is given in section 3.1.

4.3. Relative length of crystallization

In the case of a polymorphous transformation, each crystallization mode can be quantitatively characterized by a numerical criterion - the dimensionless relative length of crystallization δ_0 [90]. The relative length of crystallization defined as

$$\delta_0 = \frac{D_0}{a_0} \tag{4.3}$$

in the case of layer polymorphous crystallization, and as

$$\delta_0 = \frac{D_0}{\sqrt[3]{\Omega}} \tag{4.4}$$

in the case of island and dendrite polymorphous crystallization. D_0 is a characteristic unit of length - the conditional size of a crystal by the time t_0, after which the volume of the amorphous phase decreases by a factor of $e = 2.718$ (the so-called characteristic unit of time). In this case, the fraction of crystallized substance $x = 0.632$. In expressions (4.3) and (4.4) a_0 is a cell parameter, and Ω is the volume of a unit cell of a crystal, growing in amorphous matrix.

In the case of LPC a flat crystal grows in the investigated region of the film with an area $\sim D_S^2$ ($D_S \sim 2.9$ μm is the effective diameter of the region, observed in the electron microscope) (Fig. 4.4a). If the growth rate is constant in the film plane, then the crystal will have a shape, close to the shape of a disk with diameter D. Let us define the crystal growth rate in the tangential direction as the derivative of its diameter D with respect to time t: $v_\tau = D'_t$. With this definition, the speed of the crystallization front will be $0{,}5v_\tau$. By the time t_0, its size in the film plane will be $D = D_0 = v_\tau \cdot t_0$ (Fig. 4.10). Increasing of the diameter of the disk (i.e. its growth) can be represented as a sequential attachment

of the elementary cells of the crystal (shaded figures in Fig. 4.10) to the interface between the crystal and the amorphous phase. In this case, according to (6.3), the relative length δ_0 will be the number of cell parameters a_0 that fit at a distance, equal to D_0 [93].

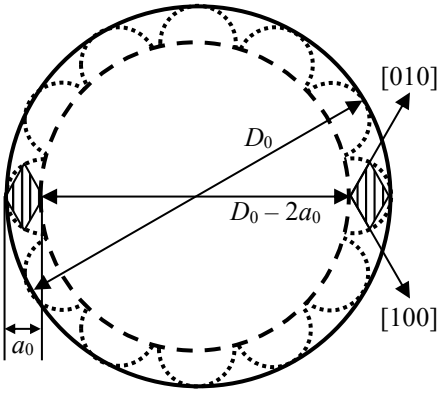

Fig. 4.10 - Scheme of the growth of a hexagonal crystal (in the orientation [001]) according to the mechanism of layer polymorphous crystallization. The shaded rhombuses correspond to the projections of the elementary cells of the crystal onto the plane of the figure [93]

At IPC a lot of small crystals of different orientations grow in the studied region of the film (Fig. 4.1b). The projections of the unit cells of the crystals onto the plane of the film are polygons with different sides and vertex angles. Therefore, to determine δ_0 in this case, a value $\Omega^{-1/3}$ is used. It has the dimension of length and characterizes the elementary cells of crystals in any orientation relative to the film surface. Relation (4.4) is also applied to the case of DPC mode, since the dendritic branches have different orientations relative to the film surface.

4.4. Film preparation and video recording of crystallization "in situ"

Amorphous films were obtained by thermal deposition of material in vacuum, pulsed laser sputtering of a metal in an oxygen atmosphere, anodic oxidation of foils and ion-plasma deposition in argon atmosphere with oxygen on substrates at room temperature. The substrates were KCl crystals at room temperature, cleaved in air along the (001) cleavage planes. After deposition and depressurization of the chamber, the films were separated from substrates in distilled water and transferred to object grids for electron microscopic studies. Structural analysis was carried out by electron diffraction and transmission electron microscopy with electron microscopes EM-100L and FEM-100-01, operating at an accelerating voltage of 100 kV. The film thickness varied in the range from 25 to 50 nm.

Crystallization of a local area of the amorphous film was initiated and maintained all time by an electron beam at a beam current of ~20 μA. The crystallization rate was set by changing the electron current density j through the sample, which was 1.1 - 6.5 $A \cdot mm^{-2}$ depending on the beam focusing. The process of crystallization of the film was recorded from the screen of the electron microscope with a Canon Power Shot G15 camera in the video recording mode at the frame rate of 30 s^{-1} (Fig. 4.11). So, the error in determining of the time $\Delta t = 30^{-1}$ s. Data on the kinetics of the crystallization process was obtained from the analysis of individual frames of the video recorded “in situ” at the fixed electron current density (Fig. 4.12).

Using a specialized computer program, we measured the total area, occupied by the crystals at the electron microscope image of the analyzed space of the film. The analyzed space of the film (a separate film frame) was $\approx 7.19 \cdot 10^{-8}$ cm^2. The fraction of the crystalline phase x we defined as the ratio of the area, occupied by the crystals to the total analyzed area. The minimum reliably measured area of the crystal was 0.0018 μm^2. In this case the error $\Delta x \approx 2.5 \cdot 10^{-4}$.

At the initial stages of crystallization, the emerging crystals did not contact each other. Therefore, it was possible to count visually (on the electron

microscopic photography) the number of crystals N in the analyzed area with an accuracy of 1 crystal per total analyzed area. In this case the error $\Delta N = (7.19 \cdot 10^{-8}\ \text{cm}^2)^{-1} \approx 1.4 \cdot 10^7\ \text{cm}^{-2}$.

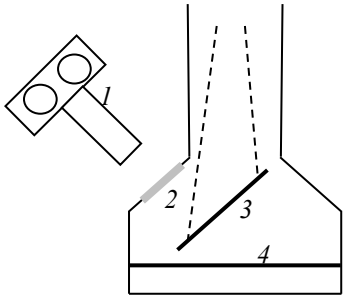

Fig. 4.11. Scheme of the filming method in TEM: 1 - movie camera; 2 - window; 3 - screen; 4 - photographic plate

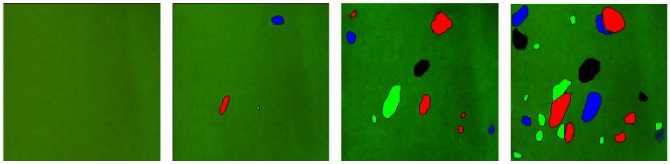

Fig. 4.12. A series of processed video frames to measure the number, size and area of crystals

5. LAYER POLYMORPHOUS CRYSTALLIZATION MODE

5.1. Structure and kinetics of crystal growth in amorphous films of Cr_2O_3 and V_2O_3

Chromium sesquioxide (Cr_2O_3) is the most stable among the numerous oxide phases (CrO, Cr_2O, CrO_2, CrO_3, CrO_5, Cr_2O_5, Cr_2O_3, Cr_3O_4, Cr_8O_{11}, Cr_8O_{21} etc.) [94]. It has a corundum structure (a=4.96 Å, c=13.59 Å, c/a=2.74) compromised of hexagonally closed-packed oxygen atoms and chromium atoms occupying two-thirds of the octahedral sites [95]. In recent years, numerous theoretical and experimental investigations of the structure and properties have been stimulated due to a wide range of possibilities for its technical application in the film state. It is used in the production of refractory, wear-resistant, corrosion-resistant and heat-protective coatings, since it has a high melting temperature (2435°C) and chemical stability [96, 97]. As a semiconductor with an excess of oxygen and a high refractive index, Cr_2O_3 is used as selectively absorbing and shielding films in solar energy converters, and as an electrode material for windows in devices, using the electro chromic effect [98]. Also, Cr_2O_3 films are widely used in magnetic recording heads, bearings and cylinder walls [99, 100].

To obtain films and coatings Cr_2O_3 a wide range of physical and chemical methods is used [94 - 98]. In particular, as-deposited films with a cathode arc ion plating system are primarily amorphous. One of the effective methods for the preparation of amorphous films of the stoichiometric composition is the pulsed laser deposition (PLD) technique [101].

5.1.1. Experimental details

Amorphous films of Cr_2O_3 and V_2O_3 were prepared by the pulsed laser deposition technique. The laser ablation of high-purity chromium and vanadium target was carried out in an oxygen atmosphere at a pressure of ~0.13 Pa with the use of pulsed laser radiation from an LTI-PCh-5 laser operating in the

Q-switched mode. The wavelength and the pulse repetition rate were equal to 1.06 μm and 25 Hz, respectively. The laser target erosion products were deposited on KCl (001) substrates at room temperature. The thickness of the films varied in the range from 25 to 350 nm. Details of the pulsed laser deposition technique were described in [102].

The films were separated from a substrate in distilled water and transferred onto objective grids for electron microscopic investigations. The crystallization of a film was initiated by electron beam irradiation in the column of a transmission electron microscope at a beam current of ~ 20 μA. The crystallization rate was controlled by varying the density j of the electron current through the sample, which was varied in the range from 1.1 to 6.5 $A \cdot mm^{-2}$ depending on the electron beam focusing.

The structural analysis was carried out using the methods of electron diffraction and transmission electron microscopy on EM-100L and PEM-100-01 electron microscopes operating at an accelerating voltage of 100 kV. The process of crystallization of a film was recorded from the screen of an electron microscope with a Canon Power Shot G15 camera in the video recording mode at a frame rate of 30 s^{-1} (Fig. 4.11). Data on the kinetics of the crystallization process were obtained from the analysis of individual frames of the video recorded "in situ" at a fixed tangential crystal growth rate v (specified by the electron current density j), which is determined by the relationship

$$v = \frac{\Delta D}{\Delta t}. \tag{5.1}$$

In expression (4.1) ΔD is the increment in the average value of the crystal diameter D during a time period Δt between the two video frames, corresponding to the moments of the recording t and $t+\Delta t$. The size of crystals was determined from the contrast of their electron microscopy image, because it was different from the contrast of the electron microscopy image of the amorphous matrix.

5.1.2. The basic morphological forms at LPC of Cr_2O_3 and V_2O_3

Pulsed laser evaporation of Cr and V in an oxygen atmosphere leads to formation of amorphous films on substrate at room temperature. Crystallization of this films was initiated with electron beam irradiation.

Amorphous films enriched with chromium crystallize upon heating with the release of Cr crystals and Cr_2O_3 oxide (Fig. 4.2 a and b). Films of stoichiometric composition crystallize with the realization of Cr_2O_3 nanocrystals, which have a hexagonal crystal lattice (Fig. 5.1). V_2O_3 crystals growing in amorphous V-O films of stoichiometric composition have a similar structure and morphology [101].

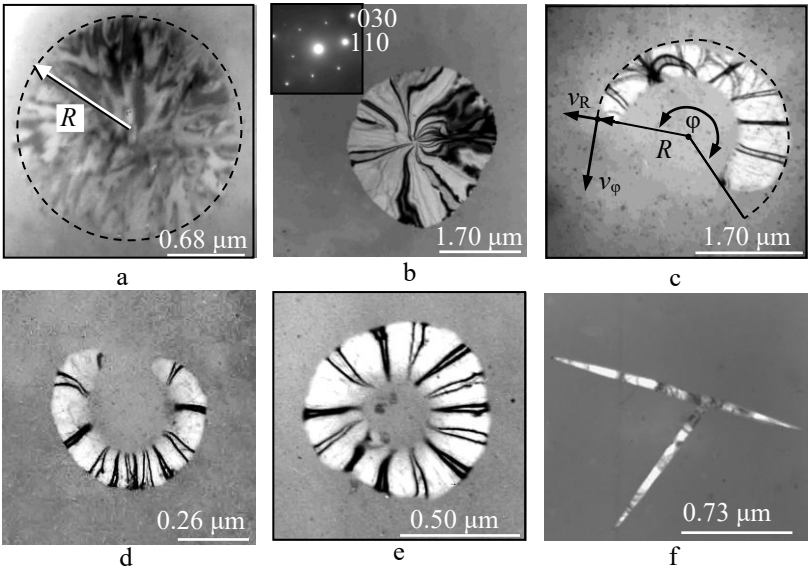

Fig. 5.1. The main morphological forms of crystals growing in amorphous films of vanadium and chromium oxides: a, b - disk-shaped; c, d - sickle -shaped; e - ring-shaped; f - needle-shaped. In the upper left corner at micrograph “b” is a SAED pattern of Cr_2O_3

At the initial stage of transformation crystals of three main morphological types grow in amorphous films [101]. These are disk-shaped crystals, that are always oriented with the basic plane (001) parallel to the film surface (Fig.1a for V_2O_3 and Fig 1b for Cr_2O_3). Sickle-shaped (Fig.1c and 1d for Cr_2O_3), ring-shaped (Fig.1e for Cr_2O_3) and needle-shaped (Fig.1f for Cr_2O_3) crystals are oriented so that the crystallographic planes parallel to the film surface can be different (including the variant when the plane (001) of crystal is oriented parallel to the film surface). A large number of bending extinction contours are observed at electron microscopic images of crystals, which indicates a complex bending of their crystal lattice. Ring-shaped crystals are formed during the growth of sickle-shaped crystals when their ends touch each other (Fig.1d and 1e).

5.1.3. Kinetics of the disk-shaped crystal growth

Disk-shaped crystals grow with a constant speed *v* and unchanged morphology (Fig. 5.2a, 5.2b, 5.2c) [90].

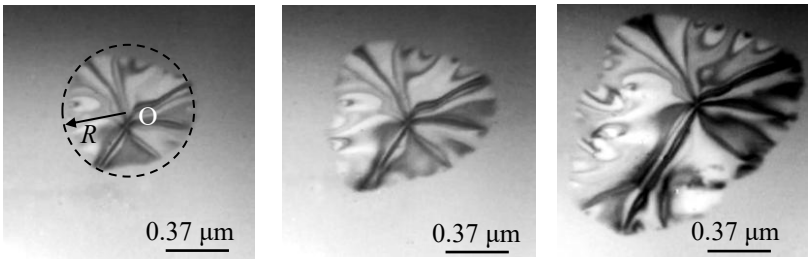

a b c

Fig. 5.2. Kinetic of growth of a disk-shaped crystal in amorphous film of Cr_2O_3. Electron microphotographs correspond to the time moments *t*, which have passed from the beginning of the recording of the crystallization process: (a) t =2.23 *s*; (b) t =2.93 *s*; (c) t =3.83 *s* [90]

Fig. 5.3a shows the dependences of the diameter D of disc-shaped crystals on time t for electron-beam crystallization of amorphous film [102, 103]. The data were obtained from the analysis of three video films of the growth of three separate crystals 1, 2 (for crystals 2 there are film frames at Fig. 5.2), and 3. Based on the frame-by-frame analysis of this videos, for each crystal the dependences $D(t)$ were obtained. Corresponding lines was plotted by the data of D measurements using the least-squares technique. The correlation coefficient, characterizing the closeness of linear relation between D and t, is close to unity. A linear dependences $D(t)$ takes place for each crystal:

$$D_1 = 1.434 \cdot t - 0.025 \text{ μm}, \quad (5.2a)$$

$$D_2 = 0.346 \cdot t - 0.054 \text{ μm}, \quad (5.2b)$$

$$D_3 = 0.179 \cdot t - 0.085 \text{ μm}. \quad (5.2c)$$

Relations (5.2a), (5.2b) and (5.2c) corresponds to crystals 1, 2 and 3 respectively. According to (5.2) the increase of D occurs at a constant rate $v_{1D} = 1.434$ μm·s^{-1}, $v_{2D} = 0.346$ μm·s^{-1} and $v_{3D} = 0.179$ μm·s^{-1} to crystals 1, 2 and 3 respectively.

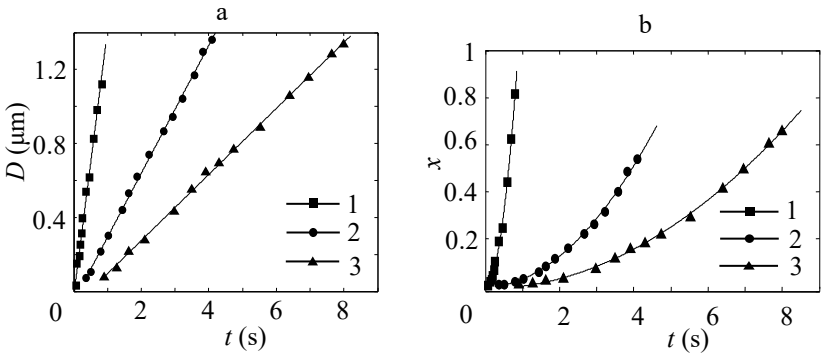

Fig. 5.3 Kinetic curves of growth of the disk-shaped Cr_2O_3 crystals in amorphous film: the dependence of the diameter D of the crystal (a) and of the fraction x of the crystalline phase (b) on the time t. Lines 1, 2 and 3 corresponds to the crystals 1, 2 and 3 respectively

Kinetic curves of crystallization for the given values of v_D are plotted at Fig. 5.3b. They reflect the dependence of the fraction of the crystalline phase x on the time t, which has passed since the moment of the fixation of the onset of crystal formation. Since each crystal grew through the entire thickness of the film, the value of x was determined as the ratio of the area occupied by the crystal to the total area of the object area analyzed in the microscope. The kinetic curves shown at Fig. 5.3b, are parabolas, since in the coordinates x - t^2 the experimental data are placed on straight lines. This indicates a quadratic dependence of x on t:

$$x_1 = 1.276 \cdot t^2 - 0.006, \quad (5.3a)$$

$$x_2 = 0.032 \cdot t^2 - 0.007, \quad (5.3b)$$

$$x_3 = 0.011 \cdot t^2 - 0.016. \quad (5.3c)$$

Relations (5.3a), (5.3b) and (5.3c) correspond to the crystal 1, 2 and 3 respectively. For each value of v_D according to (5.3) a characteristic unit of time t_0, after which the volume of the amorphous phase decreases by a factor of e (wherein x=0.632) and the characteristic unit length $D_0 = v_D \cdot t_0$ (the crystal size at time t_0) was determined. This data are shown in the Table. 5.1.

For a Cr_2O_3 crystal in (001) orientation (Fig. 1b) the projection of the unit cell on the plane of the film is a rhomb with a side $a_0 = 0.496$ nm and apex angle of 120°. In this case, according to (4.4) the relative unit of length δ_0 is the number of cell parameters a_0, stacked at a distance equal to D_0. The values of δ_0 for Cr_2O_3 crystals with different growth rates by the LPC mechanism are given in Table 5.1. The arithmetic mean of these values $\langle\delta_0\rangle = 2644$.

Table 5.1 - Parameters of the layer polymorphous crystallization of amorphous films of Cr_2O_3 at growth of disk-shaped crystals*

Crystal number	1	2	3
v_D, μm·s^{-1}	1.434	0.346	0.179
t_0, s	0.707	4.469	7.675
D_0, μm	1.014	1.546	1.374
δ_0	2044	3117	2770
$<\delta_0>$	2644		

*v_D is the growth rate of Cr_2O_3 crystals in an amorphous film, t_0 is the characteristic unit of time, D_0 is a characteristic unit of length, δ_0 is a relative dimensionless unit of length, $<\delta_0>$ is the average value of the relative dimensionless units of length.

5.1.4. Kinetics of the sickle -shaped crystal growth

Sickle-shaped crystals grow with a variable rate *v* and with a changeable morphology (Fig. 5.4) [90]. To describe the growth of a sickle-shaped crystal, the angle φ and the radius *R* of the sickle arc are introduced (Fig. 5.1c). The crystal growth is accompanied with increasing not only of *R*, but also with increasing of φ. When φ becomes equal 2π, the sickle-shaped crystals form was replaced by a ring-shaped crystals form (Fig. 5.1e) and then by a disco-shaped crystals form after crystallization of the amorphous component inside the ring (Fig. 5.4c).

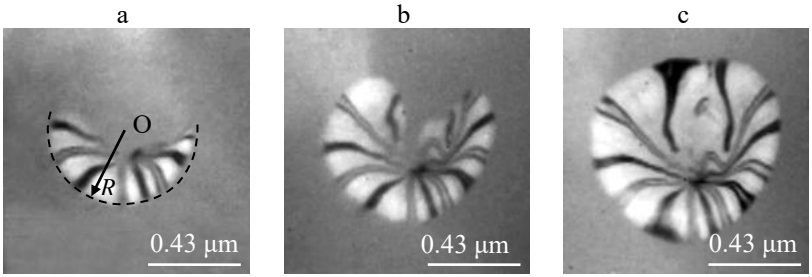

Fig. 5.4. Kinetic of growth of a sickle-shaped crystal in amorphous film of Cr_2O_3. Electron microphotographs correspond to the time moments t, which have passed from the beginning of the recording of the crystallization process: (a) $t = 2.10$ *s*; (b) $t = 2.60$ *s*; (c) $t = 3.07$ *s* [90]

Fig. 5.5a shows the dependence of the arc radius R of the crystallization front at time t. $R(t)$ curves for two sickle-shaped (at the initial stages) crystals I (for crystals I there are film frames at Fig. 5.4) and crystals II, growing independently of each other during electron beam crystallization of the film. According to this, at the initial stages (stages of the sickle and of the ring), there is a parabolic dependence $R \sim t^{0.5}$. At the final stage of growth (stage of the disc), there is a linear dependence $R \sim t$. At this stage the growth of the crystal I occurs with a velocity $v_{IR} = 0.075$ μm·s^{-1}, and of the crystal II with a velocity $v_{IIR} = 0.090$ μm·s^{-1}.

The kinetic curves of the dependence of the fraction of the crystalline phase x on the time t are shown at Fig. 5.5b. In part 1 (the sickle-shaped stage) and in part 3 (disk-shaped stage) $x \sim t^2$, since in the x - t^2 coordinates the experimental data are placed on straight lines. In part 2 (ring-shaped stage) the dependence $x(t)$ is more complex, which is approximates with a polynomial of the sixth power.

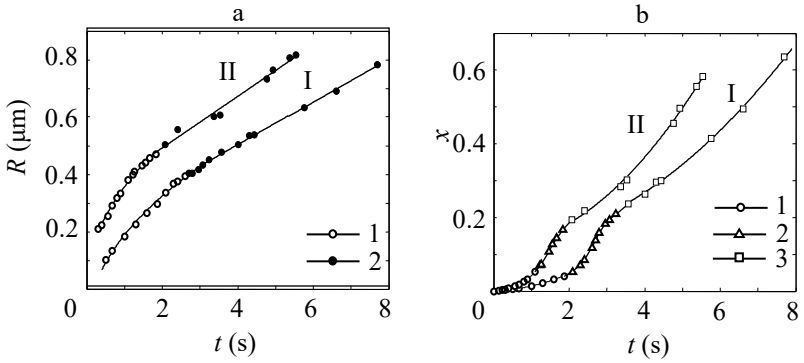

Fig. 5.5. Kinetic curves (I and II) of the crystallization of two sickle-shaped Cr_2O_3 crystals in an amorphous film. (a) The dependence of the arc radius R of the crystallization front at time t. Region 1 - the sickle and ring stages, region 2 - the stage of the disk. (b) The dependence of the fraction x of the crystalline phase on time t. Region 1 - the stage of the sickle, 2 - the stage of the ring, 3 - the stage of the disk.

The growth of a sickle-shaped crystal is characterized both by the normal component of the velocity v_R, and by the tangential component v_φ, which is directed in the plane of the film along the tangent line to the arc of the circle of the outer crystallization front (Fig. 5.1c).

Fig. 5.6a shows the scheme of the growth of the sickle-shaped crystal number II, for which the kinetic curves are shown at Fig. 5.5. This scheme is typical for most sickle-shaped crystals of Cr_2O_3. Arcs and circles of variable radius $R(t)$ with the center of the nucleation of the sickle-shaped crystal at the point "O" determines the position of the external crystallization front at time t. At the "sickle" stage, each arc rests on the angle $2\theta = \varphi < 2\pi$. At this stage (Fig. 5.7a) the velocity component v_φ increases monotonically ($v_\varphi \sim t^{0.5}$), and v_R decreases monotonically ($v_R \sim t^{-0.5}$). The derivative of the angle φ in time $\omega = \varphi'_t$ (the "angular velocity" of the twist of the crystal) is constant ($\omega \approx 2.51\ s^{-1}$).

When the arc is closed (θ = π), the "ring" and "disk" stages occur, for which the concept of the tangential growth rate v_R loses its meaning, and the normal growth rate v_R is constant. In the particular case for crystal number II (Fig. 5.5a), $v_R = 0.09$ μm·s^{-1}.

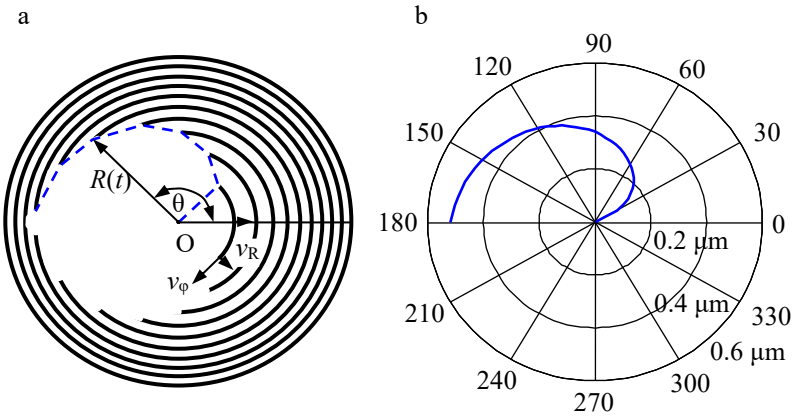

Fig. 5.6. Kinetic curves (I and II) of the crystallization of two sickle-shaped Cr_2O_3 crystals in an amorphous film. (a) The dependence of the arc radius *R* of the crystallization front at time *t*. Region 1 - the sickle and ring stages, region 2 - the stage of the disk. (b) The dependence of the fraction *x* of the crystalline phase on time *t*. Region 1 - the stage of the sickle, 2 - the stage of the ring, 3 - the stage of the disk.

Fig. 5.7b illustrates the difference in the dependence of the rate of change of the fraction of the crystalline phase x'_t (the derivative of *x* by time *t*) versus time in the growth process of disco-shaped (line 1) and sickle-shaped (line 2) of the Cr_2O_3 crystal. Line 1 is constructed from data for the disco-shaped crystal growing with a velocity $v_2 = 0.173$ μm·s^{-1} (Fig. 5.3b). For all

disco-shaped crystals, the rectilinear dependence $x'_t(t)$ takes place, since $x \sim t^2$.

Line 2 is constructed according to the data for the sickle-shaped crystal I (Fig. 5.5b). The linear dependence of $x'_t(t)$ is observed at the initial (growth of the sickle-shaped crystal) and at the final (disk-shaped crystal) sections, since in these regions the fraction of the crystalline phase $x \sim t^2$. At the intermediate section (growth of the ring-shaped crystal), the curve $x'_t(t)$ has a bell-shaped form. At this stage the crystallization of amorphous component of Cr_2O_3 occurs both inside and outside the ring-shaped crystal.

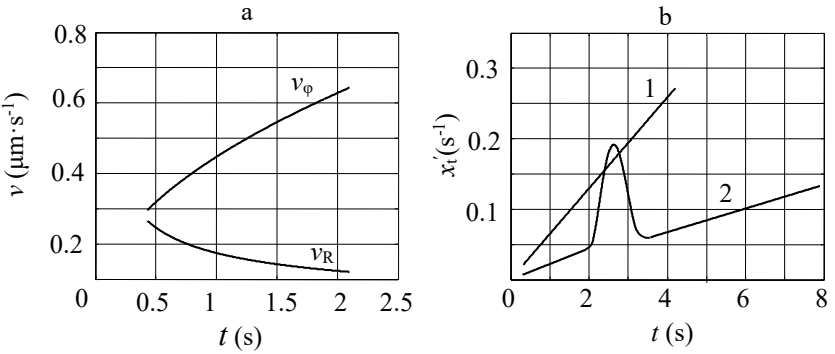

Fig. 5.7. (a) Change in tangential v_φ and normal v_R propagation velocity of the crystallization front during the growth of a crescent-shaped Cr_2O_3 crystal. (b) Dependence of the rate of change of the fraction of the crystalline phase x'_t on time t during the growth of a disk-shaped (line 1) and crescent-shaped (line 2) Cr_2O_3 crystal

The broken dotted line at Fig. 5.6a reflects the position of the end of the radius vector R during the growth of the sickle-shaped crystal. The envelope to it is a spiral, the equation of which is:

$$R = p(\theta - q)^{0.5} + s. \qquad (5.4)$$

The graph of (5.4) in the polar coordinates $R(\theta)$ for the sickle-shaped crystal II is shown at Fig. 5.6b. It is constructed in the range of angles θ from 0.43 to π radians for p = 0.311 μm, q = 0.429 and s = 0.007 μm. It should be noted that for q and s equal to zero, equation (5.4) is the Fermat's spiral equation: $R = p\theta^{05}$ [104].

5.1.5. Kinetics of the needle-shaped crystal growth

Fig. 5.8 shows the sequential frames of the growth video of a needle-shaped crystal of Cr_2O_3 in amorphous film at different time's t, that has passed from the beginning of the recording of the crystallization process. Fig. 5.8a, b corresponds to needle-shaped crystal without lateral growths [103, 105].

The kinetic curves of growth of the needle-shaped crystals without lateral growths are shown at Fig. 5.9. The dependence of the length L and of the width H of the V_2O_3 crystal on time t are shown at fig 8a. Straight lines, constructed from experimental data using the least squares method, reflect the linear dependence of $L(t)$ and $H(t)$:

$$L(t) = v_L t + L_0; \tag{5.5a}$$

$$H(t) = v_H t + H_0. \tag{5.5b}$$

In expressions (5.5a) and (5.5b) v_L and v_H are the rate of increase of the length L and of the width H of the needle-shaped crystal; L_0 and H_0 are the values of L and H at the beginning of the registration of the crystallization process. According to experimental date (Fig. 5.9a) v_L= 0.203 μm·s^{-1}; v_H= 0.009 μm·s^{-1}; L_0= 0.09 μm; H_0= 0.02 μm.

The dependence of the image area S of the V_2O_3 crystal (curve 1) and of the Cr_2O_3 crystal (curve 2) on time t are shown at Fig 5.9b. Lines, constructed from experimental data using the least squares method, reflect the quadratic dependence of $S(t)$:

$$S(t) = G_S t^2 + S_0, \tag{5.6}$$

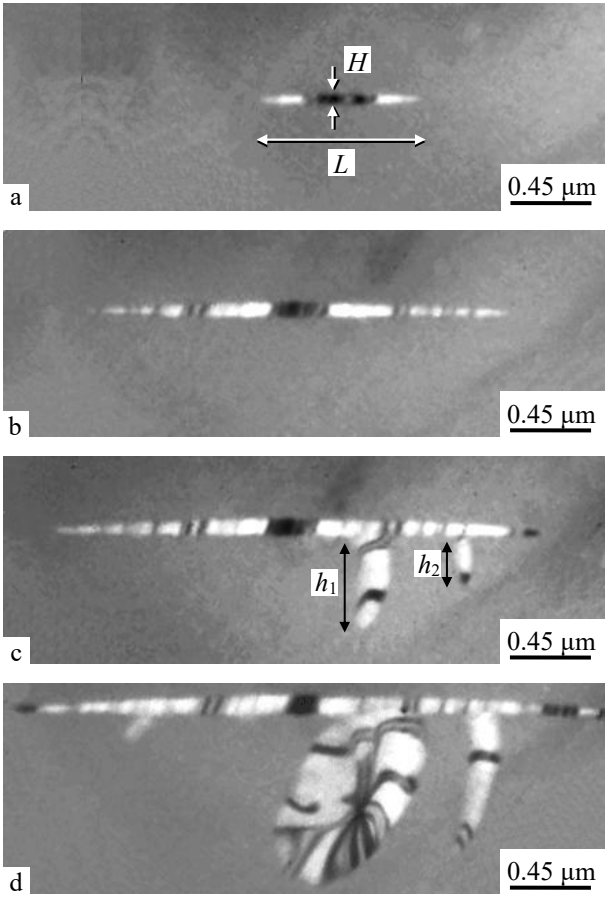

Fig. 5.8. Sequential frames of the growth video of a needle-shaped crystal of Cr_2O_3 in an amorphous film at times t that has passed from the beginning of the recording of the crystallization process: a - t = 0.53 s; b - t = 2.09 s; c - t = 2.52 s; d - t = 3.12 s [105]

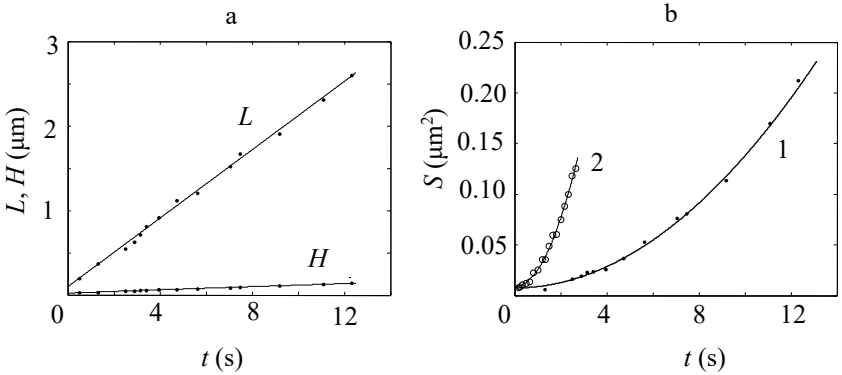

Fig. 5.9. Kinetic curves of growth of the needle-shaped crystals in amorphous films: dependence of the length L and of the width H of the V_2O_3 crystal on time t (a) and dependence of the image area S of the V_2O_3 crystal (curve 1) and of the Cr_2O_3 crystal (curve 2) on time t (b)

where S_0 is value of S at the beginning of the registration of the crystallization process. According to experimental date (Fig. 5.9b) for V_2O_3 crystal (curve 1) $S_0 = 0.007$ μm^2 and for the Cr_2O_3 crystal (curve 2) $S_0 = 0.008$ μm^2. For V_2O_3 crystal coefficient $G_S = 0.001$ μm^2·s^{-2} and for the Cr_2O_3 crystal $G_S = 0.017$ μm^2·s^{-2}.

During growth process on the lateral surface of a needle-shaped crystal is possible the formation of outgrowths with another morphology (for example disc-shaped or sickle-shaped crystals). Kinetic growth curves of a needle-shaped Cr_2O_3 crystal with a changing morphology (Fig. 5.8) are shown at Fig. 5.10. Fig. 5.10a shows the dependence of a crystal length L and length of lateral outgrowths h_1 and h_2 on time t. When outgrowth occurs on the lateral surface of the needle-shape crystal, the rate of increase of L decreases. A straight-line L indicates the dependence of (5.5a) with the coefficient $v_L = 1.746$ μm·s^{-1}, that

is commensurate with the rate of growth of the lateral outgrowth v_{h1} = 1.604 μm·s^{-1} and v_{h2} = 1.453 μm·s^{-1}.

The dependence of the image area S of the Cr_2O_3 crystal on t^2 (corresponding to sequential frames of the growth video Fig 6) is shown at Fig. 5.10b. A straight line (in coordinates S - t^2) indicates the dependence (5.6) with the coefficient G_S = 0.105 μm^2·s^{-2}. When outgrowth occurs on the lateral surface of the needle-shape crystal, the rate of increase in S increases and the linear dependence (5.6) is not satisfied.

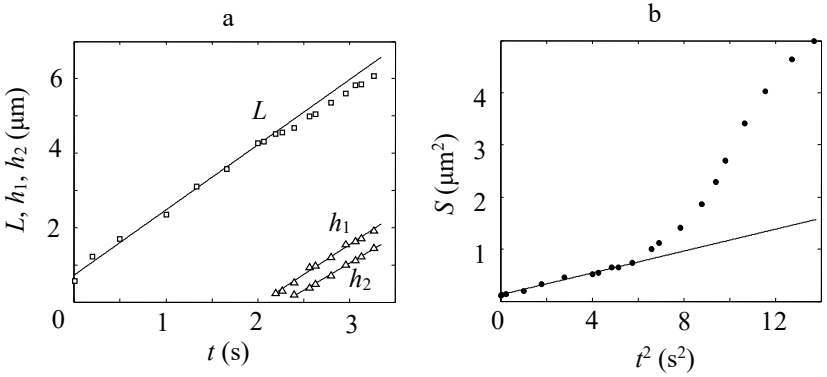

Fig. 5.10. Kinetic growth curves of a needle-shaped crystal with a changing morphology in amorphous Cr_2O_3 film (according to Fig. 5.8). (a) Dependence of a crystal length L and length of lateral outgrowths h_1 and h_2 on time t. (b) Dependence of the image area S of the Cr_2O_3 crystal on t^2

The growth of needle-shaped crystals is possible when the inequality $v_L >> v_H$ takes plase. With increasing of the growth rate v_L, there is a tendency of increasing of the ratio of the length L to the width H of the crystal. Fig. 5.11 shows the dependence of this ratio on the growth rate v_L of the needle-shaped

crystal. Line, constructed from experimental data using the least squares method, reflects that $\frac{L}{H} \sim \sqrt{V_L}$:

$$\frac{L}{H} = \alpha\sqrt{V_L} + \beta\,, \tag{5.7}$$

where $\alpha = 36.193\ \mu m^{-0.5} \cdot s^{0.5}$ and $\beta = 4.980$.

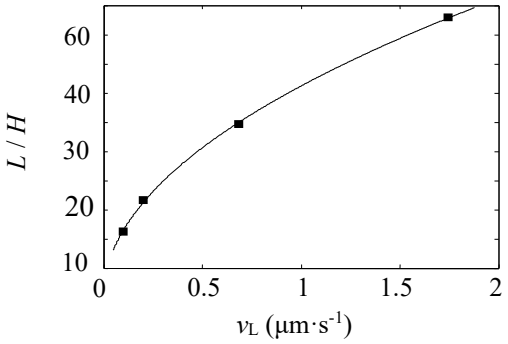

Fig. 5.11. The dependence of the ratio of the length L to the width H on the growth rate v_L of the needle-shaped crystals of Cr_2O_3

5.1.6. Epitaxy at crystallization of amorphous films

Using electron diffraction and in-situ transmission electron microscopy (TEM) it was established, that at electron beam crystallization of Cr_2O_3 and V_2O_3 disk-shaped (Fig. 5.1a,b) and needle-shaped (Fig. 5.1f) crystals are the dominant morphological forms. At the later stages of crystallization of the film, contacting and conjugation along certain crystallographic planes of disk-shaped and needle-shaped crystals takes place. It causes some distortion of their original shape. In the case with Cr_2O_3 and V_2O_3 films, we observed simple

accretion of two crystals of different morphological forms as well as autoepitaxial growth of a disk-shaped crystal on the lateral surface of the needle-shaped one. Fig. 5.12a presents one of numerous variants of contacting between needle-shaped 1 and disk-shaped 2 Cr_2O_3 crystals which are growing independently of each other from different crystallization centers in the amorphous film. During conjugation, a sharp grain boundary was formed, which divided the crystals in the orientation ratio [106, 107]:

$$(\bar{6}65)_1[1\ \bar{1}\ 12]_1 \,//\, (001)_2[\bar{2}10]_2. \qquad (5.8)$$

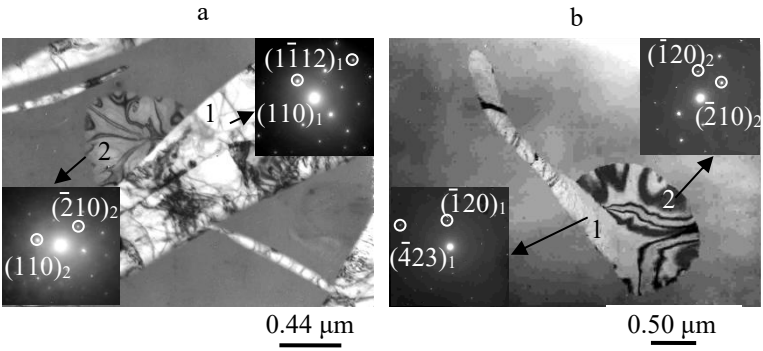

Fig. 5.12. Epitaxial crystal growth in amorphous films. (a) The contact between independently growing disc-shaped crystal 2 and needle-shaped crystal 1 of Cr_2O_3. (b) Autoepitaxy of the disc-shaped crystal 2 on the lateral surface of the needle-shaped crystal 1 of V_2O_3. Corresponding selected area electron diffraction (SAED) patterns are shown in the lower left and upper right corner of each micrograph.

Autoepitaxy is a type of epitaxy when oriented growth of crystalline material takes place on a single crystal substrate of the same material. When autoepitaxy occurs, certain planes and directions of the growing crystal and of the substrate-crystal coincide [108]. Fig. 1b shows the result of autoepitaxial

growth of the disk-shaped V_2O_3 crystal on the side surface of the needle-shaped V_2O_3 crystal [107]. A simple orientation ratio is performed between crystals

$$(\bar{1}20)_1[212]_1 \,//\, (\bar{1}20)_2[001]_2. \qquad (5.9)$$

There is no sharp boundary between them.

Fig. 5.13 shows the sequential frames of the growth of needle-shaped crystal of Cr_2O_3 in amorphous film at different time intervals t, that passed from the moment when the recording of the crystallization process had started.

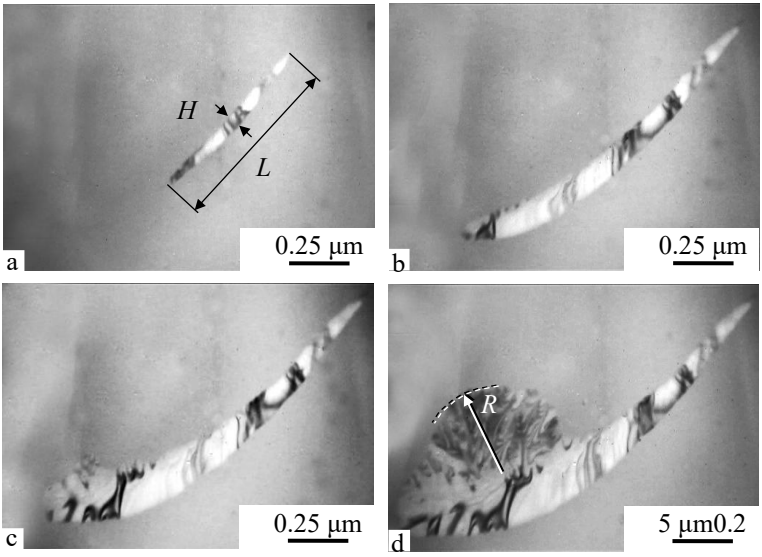

Fig. 5.13. Video recording pictures of crystals, growing in amorphous film of Cr_2O_3. Microphotographs correspond to the time moments t, which passed from the beginning of the recording of the crystallization process: (a) t = 8.0 *s*; (b) t = 16.1 *s*; (c) t = 18.8 *s*; (d) t =21.1 *s*

At the initial stages, a rectilinear needle-shaped crystal (Fig. 5.13a) grows in amorphous film. Before the start of the autoepitaxial growth (Fig. 5.13a) the dependence of the fraction of crystallized material x on time t was quadratic:

$$x(t) = 2.924 \cdot 10^{-4} t^2 + 0.002 \quad (5.10)$$

The linear dependence of the length L and of the thickness H of a needle-shaped crystal on time was observed:

$$L(t) = 0.239\ t + 0.168\ \mu m \quad (5.11a)$$

and

$$H(t) = 0.014\ t + 0.066\ \mu m. \quad (5.11b)$$

Graphically these dependencies (5.10), (5.11a) and (5.11b) are shown at Fig. 514a, 514b and 514c respectively.So, the crystal growth rate in the longitudinal direction $v_L = 0.239\ \mu m \cdot s^{-1}$ and in its transverse direction $v_H = 0.014\ \mu m \cdot s^{-1}$. The linear dependences $L(t)$ and $H(t)$ predetermine the quadratic dependence $x(t) \sim L(t) \cdot H(t)$.

The beginning and further development of autoepitaxial growth of the disk-shaped crystal on the lateral surface of the needle-shaped crystal in orientation ratio (5.9) are illustrated at Fig. 5.13b, 5.13c and 5.13d. After the start of the autoepitaxy, it was observed some curvature of needle-shaped crystal and violation of the quadratic dependence (5.10) in the direction of its noticeable increase (Fig. 5.14a). There was also violation of the linear dependence $L(t)$ (downwards) and $H(t)$ (upwards), as shown at Fig. 5.14b. Violation of the linear dependence (5.11a) and (5.11b) predetermines the violation of the quadratic dependence $x(t)$. The radius R of the arc of a disk-shaped crystal increases linearly with the speed of v_R=0.181 $\mu m \cdot s^{-1}$.

The TEM images of the needle-shaped crystal of Cr_2O_3 show bright, grey, dark regions and dark lines. The variability of the contrast occurred due to the local crystal bends, leading to the change in the diffraction conditions.

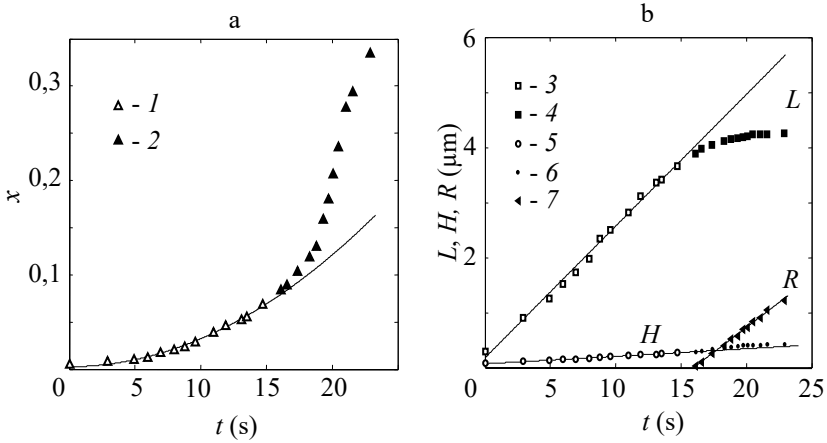

Figure 5.14 - Kinetic growth curves of a needle crystal: a - dependence of the fraction of the crystalline phase x on time t during auto epitaxy of Cr_2O_3; b - dependence of the length L and thickness H of a needle crystal, as well as the radius R of a disk-shape crystal on time t. Data 1, 3, and 5 correspond to the growth of a needle crystal before the beginning of auto-epitaxial growth of a disk-shape crystal. Data 2, 4, and 6 correspond to the growth of a needle crystal after the start of auto epitaxial growth of a disk-shape crystal. Data 7 correspond to auto epitaxial growth of a disk-shape crystal on the side surface of a needle crystal [107]

The crystalline phase of Cr_2O_3 is denser than the amorphous one. The relative change in the density is ~7.2% [91] (Table 1.2). Therefore a crystal, growing in amorphous film, is in the field of tensile stresses, which can change during variation of the size and of the shape of the crystal. This leads to formation on TEM images of extinction bend contours (BC) with different intensities and shapes. The nature of the formation of BC at crystallization of amorphous films was studied in detail in [109].

Crystallization front may be splitting into slices that can move at different speed. Fig. 5.15 shows the motion of slice S_1 with initial velocity $v_1 \approx 0.06$ μm·s^{-1} and slice S_2 with initial velocity $v_2 \approx 0.03$ μm·s^{-1}. After time interval $t \approx 1.89$ s, the layer S_1 merges with the layer S_2 (Fig. 5.15c), after which a single crystallization front S_{12} was formed. According to the classification of crystallization modes, based on structural and morphological features [84], autoepitaxial crystal growth of Cr_2O_3 correspond to layer polymorphic crystallization.

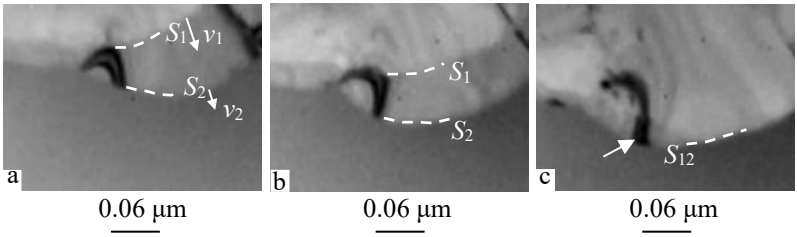

Fig. 5.15. Layer crystallization of Cr_2O_3. Video recording pictures of the moving crystallization front, which is split into slices S_1 and S_2 that move with the speed v_1 and v_2 respectively. Microphotographs correspond to the time moments t, that passed from the start of the recording of the crystallization process: (a) $t = 0$ *s*; (b) $t = 1.0$ *s*; (c) $t = 1.89$ *s*. The arrow marks the bend contour

5.1.7. On the movement of crystallization front in amorphous films

When two crystals growing in an amorphous film meet, a grain boundary is formed (Fig. 5.12a). It is an obstacle for the further propagation of the crystallization front of each crystal in the same direction. One of the crystals is an "aggressor" in relation to the other. An example of aggressor in the form of a needle crystal 3 in relation to a disk-shape crystal 2 in crystallizing amorphous medium 1 is shown at Fig. 5.16 [110].

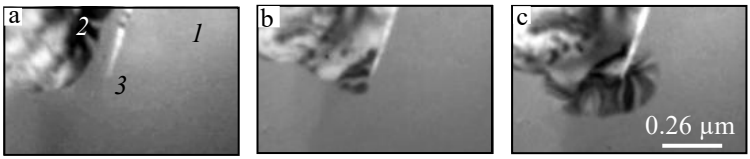

Figure 5.16 - Bypassing the obstacle by the crystallization front. Microphotographs correspond to time points t that have passed since the beginning of filming: (a) $t = 0$ s; (b) $t = 0.42$ s; (c) $t = 1.40$ s; 1 – amorphous phase; 2 – disk-shape Cr2O3 crystal; 3 – needle-shape Cr_2O_3 crystal [110]

The presented film frames demonstrate the enveloping of an obstacle (in the form of a needle crystal) by a crystallization front of a growing disk-shape crystal of Cr_2O_3. The observed phenomenon of the germination of a part of a disk-shape crystal into the region of amorphous film, which is located behind a needle crystal, is in some respects similar to the phenomenon of diffraction (penetration of radiation into the region of a geometric shadow).

Another example of the crystallization front wrapping around obstacles (holes h and h' in an amorphous film) is shown at Fig. 5.17 [111]. It is essential, that before and after the passage of obstacles by the crystallization front, the orientation of the crystallized region and the single crystallinity of the layer are preserved.

The geometric construction of the position of the crystallization front in amorphous medium at different times can be performed similarly to the construction of the front of a light wave according to the Huygens principle. The Huygens principle allows you to find the position of the wave front at time $t+\Delta t$, knowing its position at the previous time t and wave speed v. All points of the wave front at time t are sources of secondary waves, and the position of the front at time $t+\Delta t$ coincides with the surface, that envelops the secondary waves.

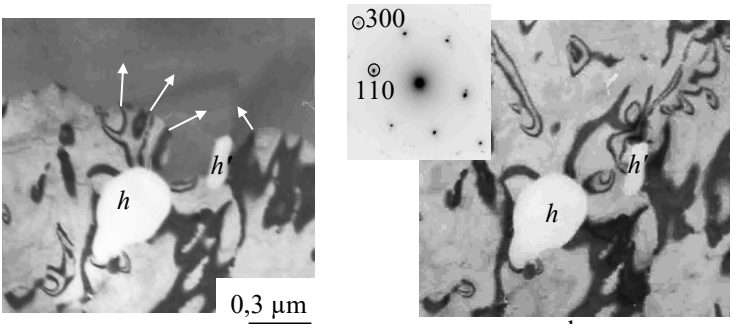

Fig.re 5.17. An example of bypassing of the obstacle by a moving crystallization front: a - the beginning of bypassing (holes h and h' in amorphous film of Cr_2O_3); b - completion of the bypassing. SAED pattern is shown in the upper left corner of the photo (contrast is inverted) [111]

Huygens' principle is a purely geometric way of constructing a wave front. It is not related to the physical nature of the waves, and this makes it possible to use it when considering crystallization processes. The propagation of the crystallization front in amorphous medium is shown at Fig. 5.18. All points of the surface of the interface between the crystal and the amorphous phase at time t are the centers of nucleation of secondary crystals, and the position of the boundary at time $t+\Delta t$ coincides with the surface enveloping secondary crystals [111].

Secondary crystals grow only forward, i.e. in directions, forming acute angles with the outer normal to the crystallization front. They have the same orientation (identical streaking), coinciding with the orientation of the primary crystal (i.e. "coherent" with each other). Growing together (“interfering”) during time Δt they ensure the movement of each point of the crystallization front by the value $v_t\Delta t$. The new position of the crystallization front (dashed line *s-s'* at Fig. 5.18b) corresponds to the envelope of secondary crystals.

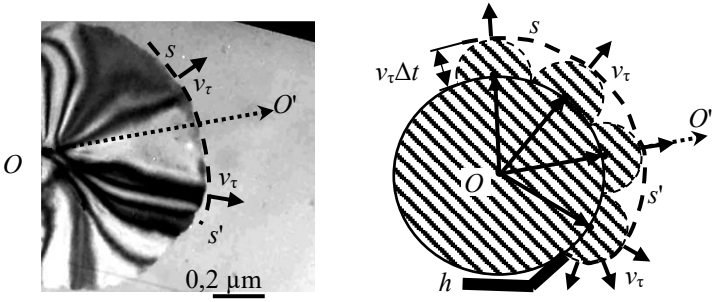

Fig. 5.18. Propagation of crystallization front in amorphous medium: a - layer polymorphous crystallization of amorphous film of Cr_2O_3; b - scheme of the movement and bypassing obstacles (barrier *h*) by the crystallization front, based on the Huygens optical principle [111]

The construction of a surface, that envelops secondary crystals for a certain moment of time, makes it possible to explain the enveloping of an obstacle (barrier *h* at Fig. 5.18b) by the crystallization front (Fig. 5.16 and 5.17), which is similar to the phenomenon of diffraction in optics [111, 112]. Practical implementations of the Huygens principle to the periodic reactions in condensed matter has been proved by Stefan [113, 114]. In our case, the addition of elementary crystalline cells formed from an amorphous medium to a crystal at the crystallization front (s-s' boundary at Fig. 5.18) can be considered as a periodic process [111, 115].

The Huygens principle was supplemented by Fresnel's idea of coherence of secondary waves. In the case of LPC of amorphous film one should imply an ordered formation of secondary nucleation of crystallization centers with equal orientations of elementary cells of the crystal lattices. Intergrowing for the time *t*, they provide transition of crystallization front over a distance of $v_\tau\Delta t$. Each position of the crystallization front corresponds to envelope of

secondary crystallization centers. The disturbance (transformation from amorphous to crystalline phase) is transferred from the point O of primary crystal formed under electronic beam irradiation to an arbitrary point O' in amorphous matrix (Fig. 5.18).

A geometrical construction based on the Huygens principle allowed to explain the diffraction of light, and enveloping of various obstacles during light wave propagation. Such geometrical similarity is adaptable to the LPC mechanism and allows an understanding of the penetration of crystallization line into the geometrical shadow area formed by an obstacle (barrier *h* at Fig. 5.18b). Our experimental investigations have shown the applicability of the Huygens principle to describe LPC of the amorphous films. In the case when secondary crystallization centers are disoriented (non-coherent), the IPC mode is realized. As a result the fine-crystalline polycrystalline film is formed (Fig. 4.4b and 4.6b).

Let us consider the physical factors influencing on the possibility of realization of coherent crystallization of amorphous films. Among the first factors is the presence of covalent bond between atoms of elements. Once the covalent bond is directional and saturated, the particles at the crystallization front are oriented with maximal neighboring bonding. The value of valence angles is also conformed. This provided similar orientation or "coherence" of secondary crystallization centers for realization of LPC mode. It is more inherent for semiconductors (Se, Sb, Sb_2S_3) and oxides (Cr_2O_3, V_2O_3, Fe_2O_3 Ta_2O_5).

In case of amorphous metals, no preferred orientation of particles is revealed at crystallization front due to the metallic bond is not covalent and non-saturated. Secondary crystallization centers turned out to be disoriented and non-coherent. In this case, IPC mode is realized (crystallization of amorphous films of Re and Ni [31].

The second factor influenced on the LPC mechanism realization is high free surface energy σ_a of the amorphous film. The energy criterion of LPC mechanism is the ratio (4.1). The crystalline phase is tent to eliminate the free surface of amorphous film with high value of σ_a ("wetting" condition). The value of σ_a decreases with decreasing the film surface roughness. Therefore,

the film surface should become smoother after crystallization. Distinct relationship between the surface relief changes and crystallization phenomenon is given at [116]. Authors revealed the decrease of surface roughness accompanied with crystallization of fractal branches of Sb clusters deposited onto graphite surface. When the deformation energy accumulated in clusters branches increases critical value, the transition 3D→2D took place.

The third factor, which has an impact on the character of crystallization, is absorption rate of the heat energy by a local area of the amorphous film. The higher the rate, the greater the possibility of realization of IPC mechanism. Changing of crystallization mechanism from LPC to IPC was revealed in the Ta_2O_5 films near hardening microdroplets of this melt (dropped onto the surface due to a so-called "spray" effect). An intensive release of crystallization heat near the droplet initiated realization of IPC mechanism (Fig. 5.19).

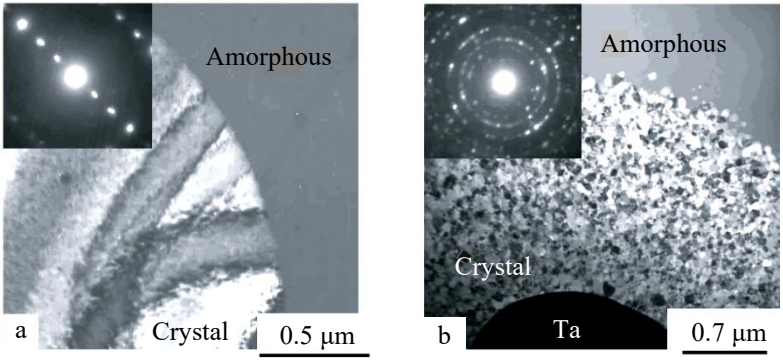

Fig. 5.19. Dependence of the crystallization character of amorphous film of Ta_2O_5 on the type of physical influence applied to the film. a. Layer polymorphous crystallization under the influence of an electron beam. b. Island polymorphous crystallization as a result of heat release near the solidifying microbubble of Ta [111]

5.2. Crystallization of amorphous films of niobium pentoxide

Films of niobium pentoxide (Nb_2O_5) are promising in a wide range of applications in many branches: sensors, solar cells and medicine due to its high resistance to corrosion, good stability and high biocompatibility [117, 118]. Nb_2O_5 is one of the transparent oxide semiconductors with wide band gap (3.6 eV) and high refractive index (2.4). As electrochromic material Nb_2O_5 can change its optical properties when a voltage is applied to it. So, it has great potential for application in different types of optical devices and heterogeneous photocatalysis [119-121].

5.2.1. Obtaining and structure of films

There are many ways to obtain films of niobium pentoxide. Among them, the most common are anodization of metallic niobium in the corresponding electrolytes, thermal oxidation of the metal in an oxygen atmosphere, magnetron sputtering, chemical vapor deposition, and atomic layer deposition [117, 119, 122]. The fabrication method plays an important role in determining the structural, morphological and chemical properties of the films. Niobium oxide has more than 15 polymorphs, which can be obtained by controlling the deposition temperature and by using a specific technique. During the oxide film growth phases of various stoichiometric compositions can form: NbO, NbO_2, Nb_2O_5. [119, 120, 121].

The most thermodynamically stable phase is α-Nb_2O_5. This low-temperature modification can be obtained by heating of amorphous oxide films with electron beam or by annealing in a furnace at temperatures of 350-400°C. This modification is attributed to a hexagonal crystal lattice with parameters a_0 = 0.362 nm and c_0 = 0.394 nm [123, 124].

The samples were free-standing amorphous films of Nb_2O_5 with a thickness h = 30 - 50 nm, obtained by anodic oxidation of niobium foil according to [124, 125]. Crystallization of films was studied using electron diffraction and transmission electron microscopy (TEM) at the accelerating voltage of 100 kV. Phase transition from amorphous to the crystalline state was initiated by

the electron beam impact with a dose rate ~ (4 - 7)·10^4 $e^-/Å^2$·s inside the column of the electron microscope. This made it possible to register the structural transformations in situ.

At the initial state Nb_2O_5 film was amorphous. This is evidenced by the diffuse halos at the selected area electron diffraction (SAED) pattern at Fig. 5.20a. TEM image of this film after its partial crystallization is shown at Fig. 5.20b. It contains extinction bend contours - high contrast stripes, converging at one point and forming a zone-axial pattern. The variability of the contrast occurred due to the local crystal bends, leading to the change in the diffraction conditions. The crystal, growing in amorphous film, is in the field of tensile stresses, which can change during variation of the size and of the shape of the crystal. This leads to the formation of extinction bend contours with different intensities and shapes on TEM images. SAED pattern of the area near the intersection point of the bending contours (Fig. 5.20c) corresponds to the (001) section of the reciprocal lattice of α-Nb_2O_5.

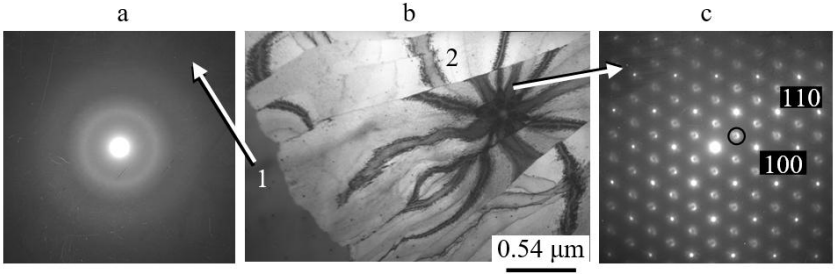

Fig. 5.20. Electron-beam crystallization of the amorphous Nb_2O_5 film: SAED pattern of the initial state (a); TEM image of the film after partial crystallization (b); SAED pattern after crystallization of the film (c). 1 - amorphous phase. 2 - crystal phase

A detailed analysis of such electron diffraction patterns is given in [124-126]. Crystallization of the amorphous film is accompanied by the ordering of oxygen vacancies, leading to the formation of a superstructure lattice, which is also hexagonal. It has parameters $a_s = \sqrt{3}a_0$, $c_s = c_0$ and is rotated with respect to the base lattice by 30º. The ordering of oxygen vacancies leads to the formation of superstructural blocks with a size of $(2\text{-}3)\cdot 10^2$ nm. Each block implements one of three possible orientations of domain boundaries. In films with 30 - 50 nm thick, blocks with different domain orientations overlap along the film thickness. In this case at the electron diffraction patterns in those places, where superstructural reflections should be located, only blurred diffuse spots are visible. One of these spots is circled at Fig. 5.20c.

5.2.2. Crystallization kinetic curves of Nb_2O_5

Fig. 5.21 shows video frames of the growth of three individual crystals (1, 2 and 3) in different areas of the amorphous film of Nb_2O_5. Based on the frame-by-frame analysis of this videos, for each crystal the dependences on time of its diameter $D(t)$ were obtained (Fig. 5.22a). Corresponding lines was plotted by the data of D measurements using the least-squares technique. The correlation coefficient, characterizing the closeness of linear relation between D and t, is close to unity. A nonlinear dependences $D(t)$ takes place:

$$D_1 = 0.40t^{1.55}+0.04\ \mu m, \quad (5.12a)$$

$$D_2 = 0.66t^{1.1}-0.05\ \mu m, \quad (5.12b)$$

$$D_3 = 0.18t^{1.3}-0.04\ \mu m. \quad (5.12c)$$

Relations (5.12a), (5.12b) and (5.12c) correspond to the video frames of crystal 1, 2 and 3 that are shown at Fig. 5.21.

The tangential crystal growth rate v was determined as the derivative of the function $D(t)$:

$$v_1 = 0.62t^{0.55}\ \mu m\cdot s^{-1}, \quad (5.13a)$$

$$v_2 = 0.73t^{0.1}\ \mu m\cdot s^{-1}, \quad (5.13b)$$

$$v_3 = 0.24t^{0.3}\ \mu m\cdot s^{-1}. \quad (5.13c)$$

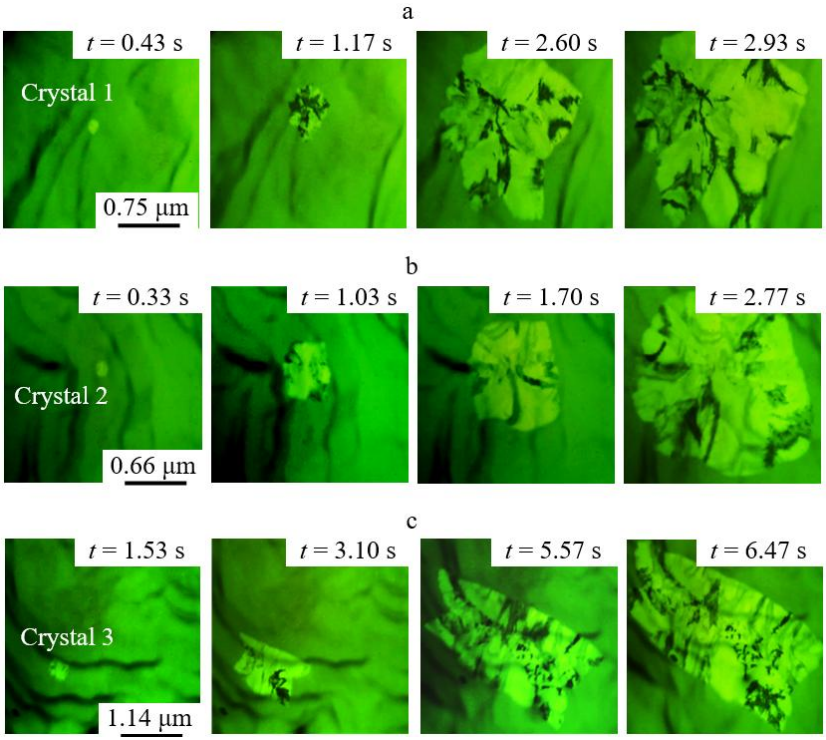

Fig. 5.21. TEM video footage of crystals growth in amorphous films of Nb_2O_5 at electron beam irradiation. a). Crystal growth 1. b). Crystal growth 2. c). Crystal growth 3. Time moments t, that has passed from the beginning of the recording of the crystallization process, is shown in the upper right corner of each frame.

Relations (5.13a), (5.13b) and (5.13c) correspond to the growth rate of crystal 1, 2 and 3 respectively. Graphs of these functions are shown at Fig. 5.22b.

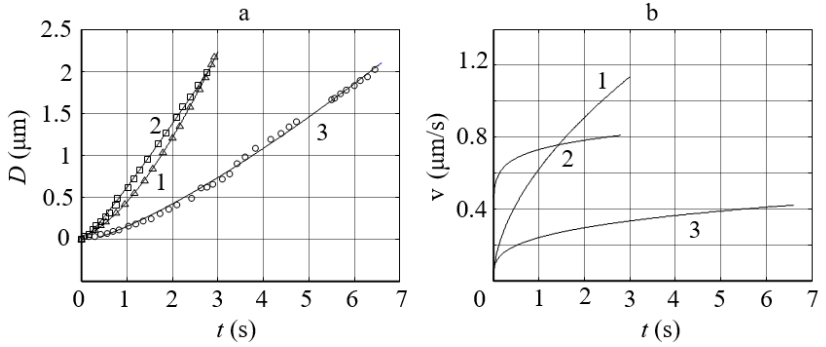

Fig. 5.22. Dependence on time of the diameter D (a) and of the growth rate v (b) of crystals in amorphous film of Nb_2O_5. Lines 1, 2 and 3 are constructed from the video frames data at Fig. 5.21a (for crystal 1), Fig. 5.21b (for crystal 2) and Fig 5.21c (for crystal 3) respectively

Since each crystal grew through the entire thickness of the film, the value of x was determined as the ratio of the area occupied by the crystal to the total area of the object area analyzed in the microscope. The dependence on time of the crystals fraction $x(t)$ of Ta_2O_5 is shown at Fig. 5.23. The following dependencies takes place:

$$x_1 = 0.019t^{3.1}+0.002, \quad (5.14a)$$

$$x_2 = 0.074t^{2.2}-0.007, \quad (5.14b)$$

$$x_3 = 0.004t^{2.6}-0.001. \quad (5.14c)$$

Relations (5.14a), (5.14b) and (5.14c) correspond to the crystal 1, 2 and 3 respectively.

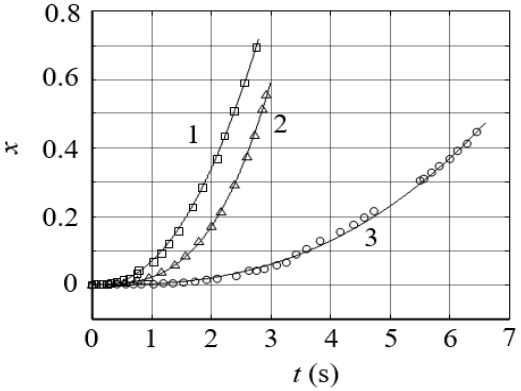

Fig. 5.23. Time dependence of crystalline fraction $x(t)$ in the film. Lines 1, 2 and 3 are constructed from the video frames data at Fig. 2a (for crystal 1), Fig. 2b (for crystal 2) and Fig 3c (for crystal 3) respectively

5.2.3. LPC mode in Nb_2O_5 films

Irradiation of amorphous film of Nb_2O_5 with electron dose rate ~ $(4\text{-}7)\cdot 10^4$ $e^-/Å^2\cdot s$ initiates its crystallization. The transformation has one-stage character. The amorphous medium polymorphically passes into the crystalline one with hexagonal structure of α-Nb_2O_5. According to the video recording data (Fig. 5.21) during crystallization of the film a single crystal grows in the field of observation. The growth rate of each crystal is not constant over time and varies according to the relations (5.13). The observed features of crystal growth allow us to make the qualitative conclusion, that layer polymorphous crystallization of amorphous film of Nb_2O_5 takes place [127].

The quantitative characteristic of crystallization is the value of the relative length δ_0 determined according to (4.3) for the LPC mode. When x=0.632

according to (5.14) the characteristic unit of time t_{01}=3.188 s, t_{02}=2.664 s and t_{03}=7.013 s for crystal 1, 2 and 3 respectively. For this times t_{01}, t_{02} and t_{03} according to (5.12) the characteristic unit of the length $D_{01}\approx$ 2.453 μm, $D_{02}\approx$ 1.889 μm and $D_{03}\approx$ 2.224 μm. For the crystal of Nb_2O_5 with the (001) orientation (Fig. 5.20c) the projection of the unit cell on the plane of the film is a rhomb with the side a_0 = 0.362 nm and apex of 120°. In this case δ_0 is the number of cell parameters a_0, stacked at a distance, equal to D_0. According to (4.3) the relative length $\delta_{01} \approx 6776$, $\delta_{02} \approx 5218$ and $\delta_{03} \approx 6144$ (numeric, typical for LPC crystallization mode [128]). Crystallization parameters of amorphous Nb_2O_5 films are given in Table 5.2.

Table 5.2 - Kinetic characteristics of crystal growth in an amorphous film of Nb_2O_5*

Crystal number	$D(t)$	v_τ	$x(t)$	t_0 (s)	D_0 (μm)	δ_0
1	$\sim t^{1.55}$	$\sim t^{0.55}$	$\sim t^{3.1}$	3.188	2.453	6776
2	$\sim t^{1.1}$	$\sim t^{0.1}$	$\sim t^{2.2}$	2.664	1.889	5218
3	$\sim t^{1.3}$	$\sim t^{0.3}$	$\sim t^{2.6}$	7.013	2.224	6144

Note: $D(t)$ - crystal diameter; v_τ - tangential growth rate; $x(t)$ - crystalline fraction; t_0 - characteristic unit of time; D_0 - characteristic unit of length; δ_0 - relative length.

The values of the dimensionless parameter of the relative length δ_0 corresponds to thousands. This indicates to the implementation of the layer polymorphous crystallization mode of amorphous Nb_2O_5 films. The nonlinear time dependence of the growth rate $v_\tau(t)$ is the reason for the non-quadratic increasing of the $x(t)$ fraction. At the same time most amorphous films, that crystallize according to the LPC mode, are characterized by a constant v_τ and quadratic dependence of the $x(t)$ [103, 128].

The specificity of crystallization in this case may be due to the formation of a domain superstructure in the low-temperature modification of α-Nb_2O_5, which is associated with the deviation of the chemical composition of the oxide from the stoichiometric one [124, 125]. Deviations are local in nature and are a manifestation of polyamorphism [129], that explains the variety of $v_\tau(t)$ at different points of the amorphous film.

5.3. Crystal growth in amorphous films of Ti-Zr-Ni alloy

Practical and scientific interest in Ti-Zr-Ni films and coatings is due to their property to dissolve a large amount of hydrogen (up to two hydrogen atoms for each metallic atom) [130-132]. Moreover, it is known, that these systems present a quasicrystalline phase for the different compositions of Ti, Ni and Zr [132-136]. Quasicrystallinity, suggesting a large number of tetrahedral sites, as well as the affinity of Ti and Zr atoms for hydrogen, makes these compound potentially useful materials for storing hydrogen for fuel cells and batteries [132].

5.3.1. Experimental

Amorphous films with 20 nm thickness were prepared on an Al_2O_3 and KCl single-crystal substrates at 30ºC by the method of direct-current magnetron sputtering of a target with the composition $Ti_{41}Zr_{41}Ni_{18}$ (at. %). Sputtering was carried out in purified argon at the pressure of $2 \cdot 10^{-1}$ Pa. The chemical composition of the grown films corresponded to the composition of the target, that was confirmed by the method of X-ray fluorescence analysis [137]. Description of the preparation procedure of amorphous films is given in [135, 136].

After deposition and depressurization of the chamber substrate of KCl together with the deposited film (the film is on the top of the substrate) were placed in distilled water. The crystal was partially dissolved and the film floated freely on the surface of the water. With the help of tweezers, the film was caught by an object grid (mesh 270 in the form of a disk with a diameter

of 3 mm), which was previously placed in water under the film. Excess water was carefully removed with filter paper at the point of contact between the grid and tweezers.

Crystallisation was initiated with thermal annealing of the film on substrate of Al_2O_3 and by the influence of the electron beam inside the electron microscope. This made it possible to register the structural transformations in situ. Besides using an electron beam focused to a diameter of 2-5 μm at beam current of 20 μA, one can perform the beam density *j* varying from 6.37 A/mm^2 (dose rate ~ $39.8 \cdot 10^4$ e$^-$/Å^2·s) to 1.02 A/mm^2 (dose rate ~ $6.4 \cdot 10^4$ e$^-$/Å^2·s) for different heating conditions. The crystallization rate increased monotonically with increasing of *j* at any desired region of the film.

5.3.2. Structure and crystallization kinetic

Fig. 5.24a shows the electron diffraction pattern from the free-standing film of $Ti_{41}Zr_{41}Ni_{18}$ immediately after its separation from the substrate of KCl. It consists of two diffraction halos. The first halo is intense, while the second one is much weaker in the intensity and very diffuse. These electron diffraction data indicate on the amorphous nature of this film.

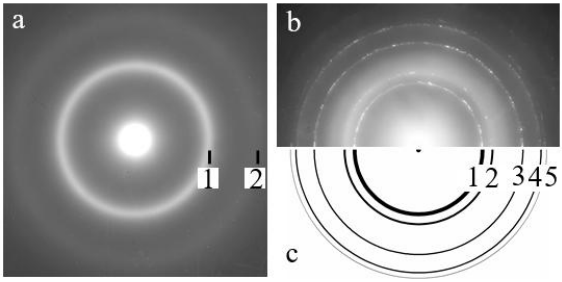

Fig. 5.24. Electron diffraction patterns of $Ti_{41}Zr_{41}Ni_{18}$ film in the initial state (a) and after partial electron beam crystallization (b), as well as its theoretical scheme (c)

Fig. 5.24b shows the electron diffraction pattern of the same $Ti_{41}Zr_{41}Ni_{18}$ film after exposure to an electron beam in microscope column of individual sections of the grid with amorphous film. Electron beam heating of the film did not lead to the complete disappearance of the primary halo, but in addition to them one can see a system of point reflections located in a ring. Second diffraction ring, corresponding to interplanar distance d = 0.251 nm, appear near the diffraction halo number 1, as well as fourth diffraction ring, corresponding to interplanar distance. d = 0.152 nm, appear near the diffraction halo number 2. Analysis shows that all rings correspond to disoriented crystals, which belong to the face centered cubic (FCC) phase.

The experimental electron diffraction pattern (Fig. 5.24b) is superimposed with the theoretical electron diffraction pattern for the polycrystalline film with the FCC structure (Fig. 1c). The radii of the circles of the theoretical electron diffraction pattern ρ satisfy the relation:

$$\rho = G\sqrt{h^2 + k^2 + l^2}\,, \tag{5.15}$$

where G is the scaling factor and h, k, l are the Miller indices of the crystal planes. Reflections for which h, k and l are numbers with different parity are forbidden. The corresponding circles are not shown in the theoretical electron diffraction pattern. Changing the scale factor G, it is possible to achieve complete coincidence of the rings of the experimental electron diffraction pattern with the circles of the theoretical one, when they are superimposed. Therefore, the reflections numbered 1, 2, 3, etc. can be assigned with indices h, k, l of the FCC lattice.

The result of the decoding of the electron diffraction pattern at Fig. 5.24b is summarized in Table 5.3. According to Table 5.3 the FCC $Ti_{41}Zr_{41}Ni_{18}$ phase with the cubic lattice parameter a_0 = 0.502 ± 0.005 nm is formed upon electron beam irradiation of amorphous film.

The electron diffraction data correspond to the X-ray phase analysis data. Figure 5.25 shows diffraction patterns (Cu-Kα radiation, 2Θ scan mode, sample is fixed at the grazing angle of Θ=1.4º) for a $Ti_{41}Zr_{41}Ni_{18}$ coating of 20

nm thick on an Al_2O_3 single-crystal substrate in the initial state and after annealing [6].

Table 5.3 - The results of the decoding of the electron diffraction pattern at Fig. 5.24b

Amorphous state		Crystal state			
Halo number	*d* (nm)	Ring number	*hkl*	*d* (nm)	a_0 (nm)
1	0.25	1	111	0.289	0.502±0.005
		2	200	0.251	
2	0.15	3	220	0.177	
		4	311	0.152	
		5	222	0.145	

At as deposited state the coating is X-ray amorphous. The diffraction pattern shows one wide halo centered near the angle 2Θ=37°. The diffraction maximum near the angle 2Θ=71° is due to diffraction from the sapphire substrate after the passage of the X-ray beam through the coating. As the annealing temperature increases, the halo shifts toward smaller angles. The X-ray amorphous state of the coating is preserved up to a temperature of 650°C.

At a temperature of 700°C, the coating crystallizes. Two diffraction lines appear near the halo 2Θ=32° and 2Θ=36°, as well as two lines near 2Θ=52° and 2Θ=62°. According to estimation from Scherrer formula [138] the coherent scattering region (CSR) size in the direction perpendicular to the film for the most intense lines near the angles 2Θ=31°, 2Θ=52° and 2Θ=62° is ~ 22 nm. This is comparable to a film thickness of 20 nm. That is, the crystalline phase extends over the entire thickness of the film.

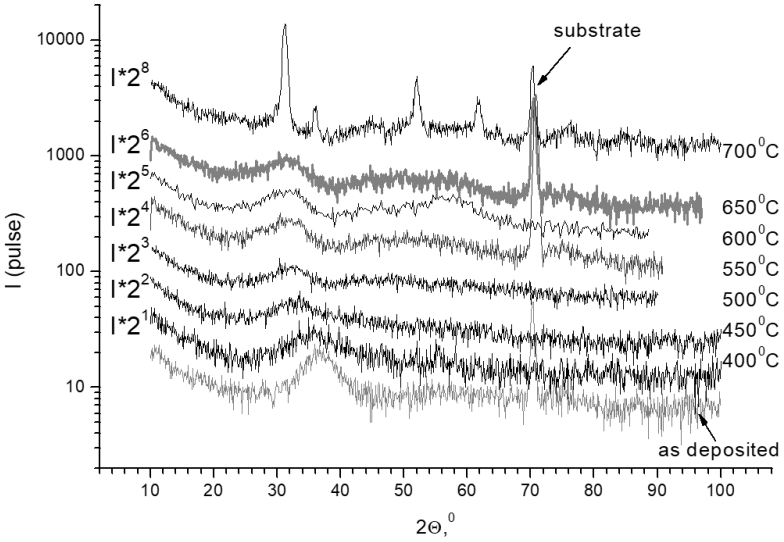

Fig. 5.25. X-ray diffraction patterns (Cu-Kα radiation) for a $Ti_{41}Zr_{41}Ni_{18}$ coating of 20 nm thick on an Al_2O_3 single-crystal substrate in as deposited state and after 1 hour of annealing at each temperature in vacuum (~$7 \cdot 10^{-4}$ Pa) [6]

The result of the decoding of the X-ray diffraction pattern (Fig. 5.25) of coating annealed at the temperature of 700°C is summarized in Table 5.4. According to it follows, that the FCC $Ti_{41}Zr_{41}Ni_{18}$ phase with the cubic lattice parameter $a_0 = 0.497 \pm 0.001$ nm is formed upon annealing of the film. The small discrepancy between the electron diffraction data and X-Ray data can be due to the different magnitudes of the stresses, arising during crystallization of the free-standing film and the film on the Al_2O_3 substrate.

Table 5.4 - The results of the decoding of the X-ray diffraction patterns at Fig. 5.25

Diffraction maximum number	*hkl*	*d* (nm)	a_0 (nm)
1	111	0.287	0.497 ± 0.001
2	200	0.249	
3	220	0.176	
4	311	0.150	

The impact of the electron beam on the local area of amorphous film initiated the formation of the flat disk-shape crystal (Fig. 5.26a, 5.27). In most cases, at the initial stage of growth, its (111) plane was parallel to the film surface. The (111) section of the reciprocal lattice is represented with the selected area electron diffraction (SAED) pattern at Fig. 5.26b. The action of tensile stresses, caused by different densities of the amorphous and crystalline phases, induced bending and subsequent splitting of the crystal into ribbon blocks of different orientations (Fig. 5.26c, 5.26d). This is evidenced by the sharp contrast of the bend contours, which breaks at the grain boundaries.

Fig. 5.27 shows video frames of crystals growth in an amorphous film of $Ti_{41}Zr_{41}Ni_{18}$. Based on the frame-by-frame analysis of this videos, the dependences on time t of the crystal radius $R(t)$ and area $S(t)$ were plotted. The dependence $R(t)$ is shown in at Fig. 5.28a. The straight line was plotted by the data of R measurements using the least-squares technique. The correlation coefficient, characterizing the closeness of linear relation between R and t, is close to unity. A linear dependences $R(t)$ takes place:

$$R = 2.732t + 0.028 \text{ μm}, \quad (5.16a)$$

$$R = 0.953t + 0.001 \text{ μm}. \quad (5.16b)$$

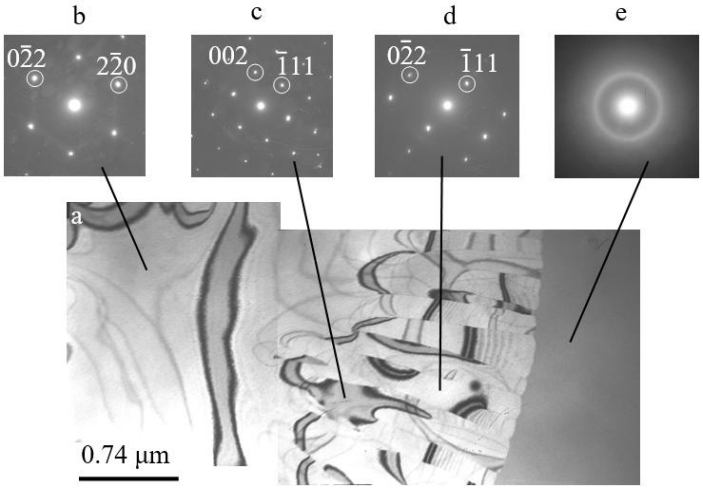

Fig. 5.26. Crystallization of the amorphous $Ti_{41}Zr_{41}Ni_{18}$ film. “a” - electron microscope image of the partially crystallized film. SAED patterns of different grains, that correspond to the cross sections of the reciprocal lattice “b” - (111), “c” - (110) and “d” - (211). e - SAED patterns of amorphous phase.

Relations (5.16a) and (5.15b) correspond to the video frames of crystal 1 and crystal 2, shown at Fig. 5.27a and 5.27b respectively. According to it the tangential growth rate of the crystal 1 $v_{\tau 1} = 2.732$ μm·s^{-1} and of the crystal 2 $v_{\tau 2} = 0.953$ μm·s^{-1} (these data are listed in Table 5.5). The inequality $v_{\tau 1} > v_{\tau 2}$ indicates that the tangential crystal growth rate increases with increasing of the dose rate of the irradiation, which was ~ $39.8 \cdot 10^4$ e$^-$/Å^2·s for the crystal 1 and ~ $6.4 \cdot 10^4$ e$^-$/Å^2·s for the crystal 2. The constancy of the growth rate indicates its independence from the electron dose. However, it determined the final size of the crystal.

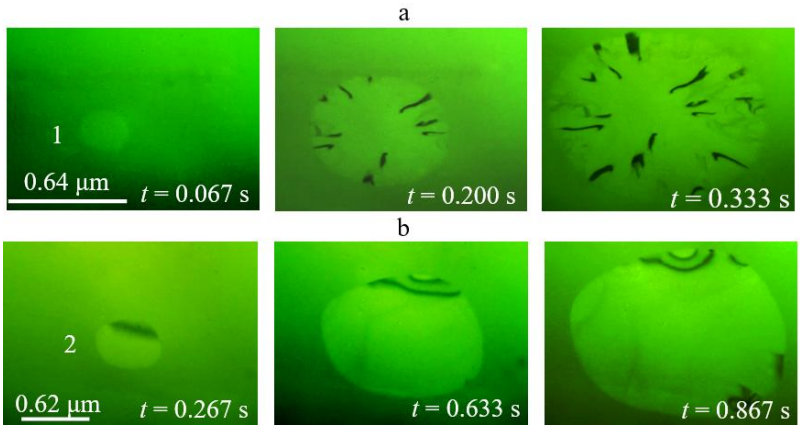

Fig. 5.27. Video frames of the growth of crystal 1 (a) and crystal 2 (b) in the amorphous film of $Ti_{41}Zr_{41}Ni_{18}$. The time t, elapsed since the start of the video recording, is indicated in the lower right corner of each frame

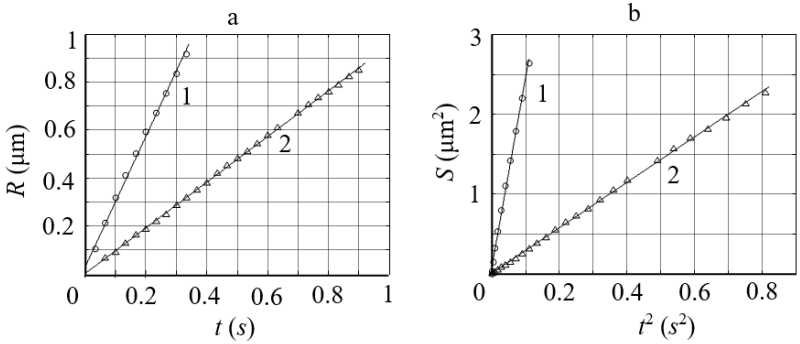

Fig. 5.28. Kinetic curves of growth of the disk-shaped crystals in amorphous film of $Ti_{41}Zr_{41}Ni_{18}$. a - time dependence of the crystal's radius R. b - time dependence of the crystals area S. Lines 1 and 2 are constructed from the video frames data at Fig. 3a (for crystal 1) and Fig 3b (for crystal 2) respectively

According to the relation (5.16a) during the growth time $t = 0.328$ s, the radius of the crystal 1 increased from 0.028 to 0.896 μm. In this case the electron dose was ~ $13.1 \cdot 10^4$ $e^-/Å^2$. According to the relation (5.16b) during the growth time $t = 0.893$ s, the radius of the crystal 2 increased from 0.001 to 0.851 μm. In this case the electron dose was ~ $5.7 \cdot 10^4$ $e^-/Å^2$.

The dependence $S(t)$ is shown at Fig. 5.28b. In the S - t^2 coordinates, the experimental data fit well into straight lines. The quadratic dependence $S(t)$ takes place:

$$S = 23.767t^2 + 0.071 \text{ μm}^2, \tag{5.17a}$$

$$S = 2.845t^2 + 0.004 \text{ μm}^2. \tag{5.17b}$$

Relations (5.17a) and (5.17b) correspond to the video frames of crystal 1 and crystal 2, shown at Fig. 5.27a and 5.27b respectively.

At the end of filming (at time moment $t_f = 0.328$ s) the area, occupied by the crystal 1 $S(t_f) = 2.637$ μm^2. Similarly for crystal 2 $t_f = 0.893$ s and $S(t_f) = 2.272$ μm^2. Since each crystal grew through the entire thickness of the film, the value of x was determined as the ratio $S(t)/S(t_f)$ and time dependence of the crystalline fraction $x(t)$ was plotted (Fig. 5.29). The quadratic dependences $x(t)$ takes place:

$$x = 9.012t^2 + 0.027, \tag{5.18a}$$

$$x = 1.252t^2 + 0.002. \tag{5.18b}$$

Relations (5.18a) and (5.18b) correspond to the video frames of crystal 1 and crystal 2, shown at Fig. 5.27a and 5.27b respectively.

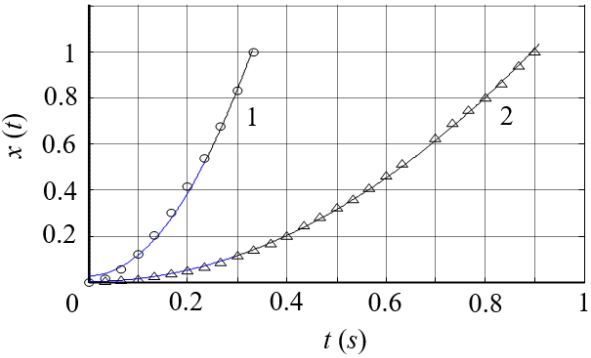

Fig. 5.29. Time dependence of the crystalline fraction $x(t)$ in the film. Lines 1 and 2 are constructed from the video frames data at Fig. 5.27a (for crystal 1) and Fig 5.27b (for crystal 2) respectively

5.3.3. LPC mode in films of Ti-Zr-Ni alloy

X-ray amorphous state of the $Ti_{41}Zr_{41}Ni_{18}$ coating is preserved up to a temperature of 650°C. At a temperature of 700°C, the coating crystallizes. Irradiation of amorphous film of $Ti_{41}Zr_{41}Ni_{18}$ with the electron beam initiates its crystallization. The transformation has one-stage character. The amorphous medium polymorphically passes into the crystalline one with FCC structure. According to the video recording data (Fig. 5.27a and 5.27b) during crystallization of the film a single disc-shaped crystal grows in the field of observation. The crystal grows at the constant rate at the constant intensity of electron beam irradiation of the film. In this case the radius of the crystal $R \sim t$, the area of the crystal $S \sim t^2$ and the crystalline fraction $x \sim t^2$.

The observed features of crystal growth allow us to make the qualitative conclusion, that layer polymorphic crystallization mode takes place [77, 84]. The quantitative feature of LPC is the value of the relative length δ_0 [90],

determined as (4.3). Substituting x_0 = 0.632 into (5.18a) and (5.18b), we obtain the numerical values of t_0. For crystals 1 and 2 (Fig. 5.27a and 5.27b) t_{01} = 0.259 s and t_{02} = 0.709 s respectively. Substituting t_0 into (5.16a) and (5.16b) and multiplying by 2, we obtain the numerical values of D_0. For crystals 1 and 2 D_{01} = 1.471 μm and D_{02} = 1.353 μm respectively. Substituting D_0 into (4.3), we obtain the numerical values of the relative length δ_0. For crystals 1 and 2 $\delta_{01} \approx 2930$ and $\delta_{02} \approx 2700$ respectively. The obtained values of t_0, D_0 and δ_0 are shown in the Table 5.5.

Table 5.5 - Kinetic characteristics of crystal growth in amorphous film of $Ti_{41}Zr_{41}Ni_{18}$

An object	Tangential growth rate v_τ	Characteristic unit of time t_0	Characteristic unit of length D_0	Relative length δ_0
crystal 1	2.732 μm·s^{-1}	0.259 s	1.471 μm	2930
crystal 2	0.953 μm·s^{-1}	0.709 s	1.353 μm	2700

Currently available data, concerning the electron-beam crystallization of amorphous films, are classified by structural and morphological characteristics (qualitatively) and by the numerical value of the relative length δ_0 (quantitatively) [128]. Wherein layer polymorphous crystallization mode, describes the nucleation and growth of a single-crystal layer in the field of the electron-beam impact. For it δ_0 is about several thousand. Time dependence $x(t)$ is quadratic. The structural and morphological characteristics and the numerical value of the relative length δ_0 correspond to the layered polymorphous crystallization mode of the amorphous film of $Ti_{41}Zr_{41}Ni_{18}$.

6. ONE-STAGE AND TWO-STAGE CRYSTALLIZATION OF AMORPHOUS FILMS OF ANTIMONY SULFIDE

The antimony sulfide (Sb_2S_3) is a semiconductor material of V-VI group of periodic table, which has high thermo-electric power and photosensitivity. It is widely used in microwave devices, optoelectronic devices and solar cell absorber [139]. In the crystalline state it has an orthorhombic lattice with periods a = 1.123 nm, b = 1.131 nm and c = 0.3841 nm [140]. Its structure is formed of infinite $(Sb_4S_6)_n$ chains along the [001] direction. A single chain consists of two trigonal SbS_3 and two square SbS_5 pyramids forming a fundamental building block in Sb_2S_3 crystal. Consequently, the chains are linked together and form zigzag sheets perpendicular to a (100) plane [139]. Any deviations from the stoichiometric composition of the Sb_2S_3 strongly affect the physical properties of this material, as demonstrated [141]. With decreasing of S/Sb ratio a near-linear decrease in optical band gaps (E_g) was observed suggesting the dependence of the band gap on film composition. Sb_2S_3 films, deposited in one way or another on a substrate at room temperature (chemical deposition, vacuum evaporation, flash evaporation and other methods), are amorphous. Post condensation annealing of the films (160 - 300^o C) initiates their crystallization. The transition from amorphous to crystalline state (a first-order phase transition) is accompanied with a change in the physical properties of Sb_2S_3. For example, the optical band gaps lie in the region 1.70 - 2.07 and 1.42 - 1.65 eV for amorphous and crystalline films, respectively [141]. Heat treatment of the Sb_2S_3 leads to a violation of stoichiometry due to loss of sulphur content in the film [142]. During crystallization, excess antimony is released in the form of crystals, distributed in an amorphous matrix [143].

6.1. One-stage polymorphous crystallization of Sb_2S_3

Amorphous films of antimony sulfide with layer thicknesses h = 30-40 nm were grown on the cleaved (001) face of KCl single crystals at the room temperature by thermal evaporation at the pressure better, than 10^{-6} Torr [143].

The starting material was a high purity powder of Sb_2S_3. Evaporation was carried out during rapid heating of the tantalum crucible by passing a pulse of electric current. In this case, the amorphous condensate with the excess of antimony was formed on the substrate due to the volatilization of the sulphur.

To preserve the stoichiometric composition of the amorphous phase, a mixture with the addition of sulphur (~ 4 weight percent) was used. The deposited films were separated from the substrate in distilled water and transferred onto subject grids for electron microscopy studies. They were crystallized on the object grids in vacuum under electron beam influence (in a microscope column). In this case the rate of crystallization was controlled by varying the density j of the electron current through the sample, which was varying in the range from 1.1 to 6.5 $A \cdot mm^{-2}$ depending on the electron beam focusing.

Fig. 6.1 illustrates the electron beam crystallization of the amorphous film, obtained by thermal evaporation in vacuum of the mixture of Sb_2S_3 with the addition of S, that compensates the loss of sulphur at evaporation of the charge. Electron microscopic photographs correspond to the periods of time t that passed after the video recording had started: (a) $t = 3.63$ s; (b) $t = 11.87$ s; (c) $t = 19.50$ s. According to this video, an ellipse-shaped crystal of Sb_2S_3 grows in the amorphous matrix during all time of exposure of the film to the electron beam.

The absence of precursive segregation of Sb crystals indicates, that according to the classification scheme [77], the crystallization is polymorphous. A substance converts from the amorphous into the crystalline state without changes in it composition.

The kinetics of polymorphic crystallization of Sb_2S_3 is shown at Fig. 6.2. The dependence on time of the length of the major axis 2OA and minor axis 2OB (Fig. 6.1b) of the ellipse-shaped Sb_2S_3 crystal are shown at Fig. 6.2a. The straight lines were plotted by the experimental data of length measurements using the least-squares technique. The correlation coefficient, characterizing the closeness of linear relation 2OA and 2OB and t, is close to unity. A linear dependence takes place:

$$2OA = 0.087t + 0.059\ \mu m; \quad (6.1a)$$

$$2OB = 0.043t + 0.020\ \mu m, \quad (6.1b)$$

where t is measured in seconds. According to (6.1a) the growth rate v_{2OA} of the major axis 2OA (the tangent of the angle of inclination of the line to the abscissa axis) is equal to 0.087 $\mu m \cdot s^{-1}$. The growth rate v_{2OB} of the minor axis 2OB is half as much and is equal to 0.043 $\mu m \cdot s^{-1}$.

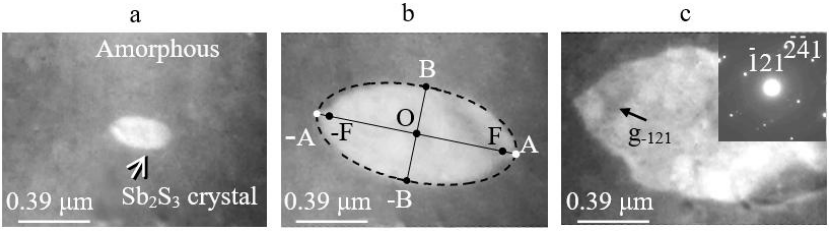

Fig. 6.1. Polymorphous crystallization of amorphous film of Sb_2S_3. Electron microphotographs correspond to the frames at the time moment t, which have passed from the beginning of the recording of the crystallization process: a - t = 3.63 s; b - t = 11.87 s; c - t = 19.50 s. SAED pattern of the crystalline Sb_2S_3 is shown in the upper right corner of the frame 1c. The dotted line marks the ellipse with eccentricity 0.881

The dependence on time of the area S of the ellipse-shaped Sb_2S_3 crystal is shown in Fig. 3b. A quadratic dependence S on t takes place:

$$S = 0.003t^2 + 0.027\ \mu m^2, \quad (6.2)$$

where t is measured in seconds. This dependence correlates well with the $\pi \cdot OA \cdot OB$ product, corresponding to the area of the ellipse (the dotted line at Fig. 6.2b). The numerical characteristic of the ellipse, showing the degree of its deviation from the circle, is the eccentricity ε:

$$\varepsilon = \sqrt{1 - \left(\frac{OB}{OA}\right)^2} \,. \qquad (6.3)$$

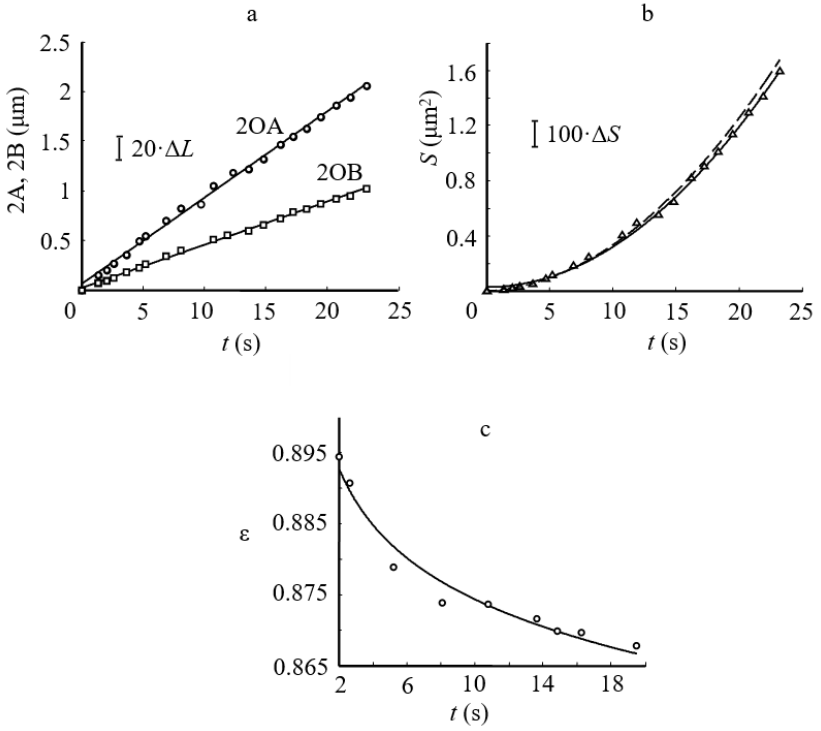

Fig. 6.2 Kinetics of the polymorphous crystallization of amorphous film: (a) time dependence of the length of the major axis 2OA and minor axis 2OB of the ellipse-shaped Sb_2S_3 crystal; (b) time dependence of the area S of the ellipse-shaped Sb_2S_3 crystal. The dotted line corresponds to the $\pi \cdot OA \cdot OB$ product. (c) time dependence of the eccentricity ε of an ellipse-shaped Sb_2S_3 crystal. Errors $\Delta L = 0.012$ μm, $\Delta S = 0.0018$ μm^2

The dependence on time of the ε of an ellipse-shaped Sb_2S_3 crystal is shown at Fig. 3c. There is exponential decrease of the eccentricity of the crystal as it grows:

$$\varepsilon = \exp(-1.282t^{0.01}+1.178), \quad (6.4)$$

where t is measured in seconds. Note that for the circle ε = 0.

6.2. Predominant crystallization of Sb and subsequent polymorphous crystallization of Sb_2S_3

Electron beam crystallization of the amorphous film, obtained by thermal evaporation in vacuum of powder of Sb_2S_3 without additives of S, proceeds differently. In this case, the amorphous condensate is enriched with super stoichiometric antimony due to the predominant evaporation of sulfur. Crystallization of the amorphous film proceeds in two stages. At the first stage, crystals of excess antimony are released. The composition of the amorphous phase approaches to the stoichiometric Sb_2S_3. At the second stage polymorphous crystallization of Sb_2S_3 occurs. Therefore, Sb_2S_3 crystals contain inclusions of Sb.

Fig. 6.3 illustrates the first stage of the electron beam crystallization of amorphous film. Electron microphotographs correspond to the frames at the time moment *t*, which have passed from the beginning of the recording of the crystallization process: a - $t = 0.37$ s; b - $t = 2.36$ s; c - $t = 2.40$ s. The moment of the appearance of Sb_2S_3 crystal is fixed in the upper right corner of the frame 6.3c. The arrow 1Sb marks evolution of a single particle of antimony.

The results of the analysis of the first stage of the crystallization process are present at Fig. 6.4. As the film warms up, the density of antimony micro particles monotonically increases and at saturation $n \approx 7.5 \cdot 10^9$ cm^{-2} (Fig. 6.45a). The experimental points fit satisfactorily on the curve, described by the relation:

$$n = 7.53 \cdot 10^9 (1-\exp(-4.3t)\ sm^{-2}, \quad (6.5)$$

where t is measured in seconds.

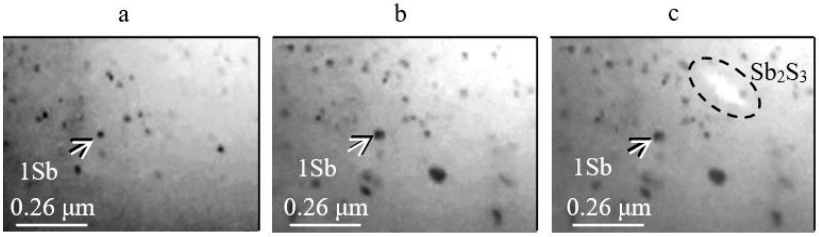

Fig. 6.3. Primary crystallization of Sb in amorphous film. Electron microphotographs correspond to the frames at the time moment t, which have passed from the beginning of the recording of the crystallization process: a - t = 0.37 s; b - t = 2.36 s; c - t = 2.40 s. The moment of the appearance of Sb_2S_3 crystal is fixed in the upper right corner of the frame 6.3c. The arrow 1Sb marks the single particle of antimony

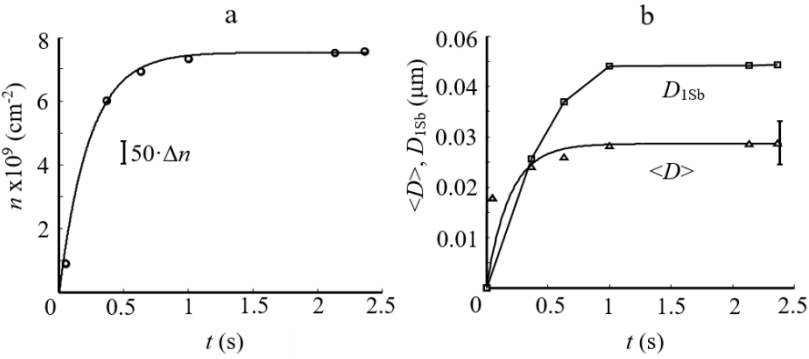

Fig. 6.4. Time dependence of density n (a) and size (b) of the antimony particles in amorphous film. <D> is the average value of the diameter of Sb micro particles. D_{1Sb} is the diameter of micro-particle, marked by the arrow 1Sb at Fig. 6.3. Errors $\Delta n = 1.4 \cdot 10^7$ cm^{-2}.

A similar ratio describes the change over time of the mean diameter of micro-particles of Sb:

$$<D> = 0.029 \cdot (1 - \exp(-5.3t)) \ \mu m. \qquad (6.6)$$

At saturation $<D> \approx 0.029$ μm (Fig. 6.4b). Fig. 6.4b shows the change of the diameter D of one selected micro-particle Sb, marked by the arrow 1Sb at Fig. 6.3. There is qualitative coincidence of the dependence of $<D>(t)$ and $D(t)$.

The successive frames of the film, reflecting the secondary crystallization of Sb_2S_3, are shown at Fig. 6.5. Electron microphotographs correspond to the frames at the time moment t, which have passed from the beginning of the recording of the crystallization process: a - $t = 0$ s; b - $t = 0.60$ s; c - $t = 3.17$ s. Crystal of Sb_2S_3, the nucleation moment of which is shown at Fig. 6.3c, grows in the amorphous matrix with inclusions of Sb micro crystals. Ellipse shape is maintained throughout the growth of the crystal.

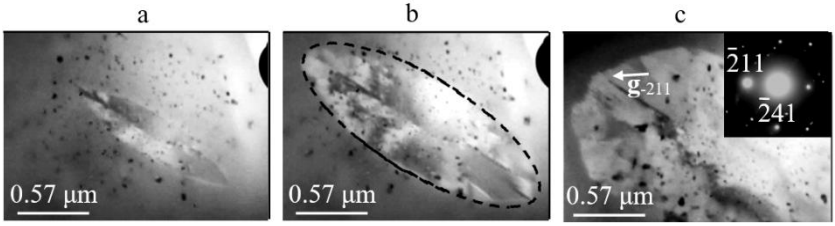

Fig. 6.5. Secondary crystallization of Sb_2S_3 in amorphous film. Electron microphotographs correspond to the frames at the time moment t, which have passed from the beginning of the recording of the crystallization process: a - $t = 0$ s; b - $t = 0.60$ s; c - $t = 3.17$ s. SAED pattern of the crystalline Sb_2S_3 is shown in the upper right corner of the frame 3c.

The kinetics of secondary crystallization of Sb_2S_3 is shown at Fig. 6.6.

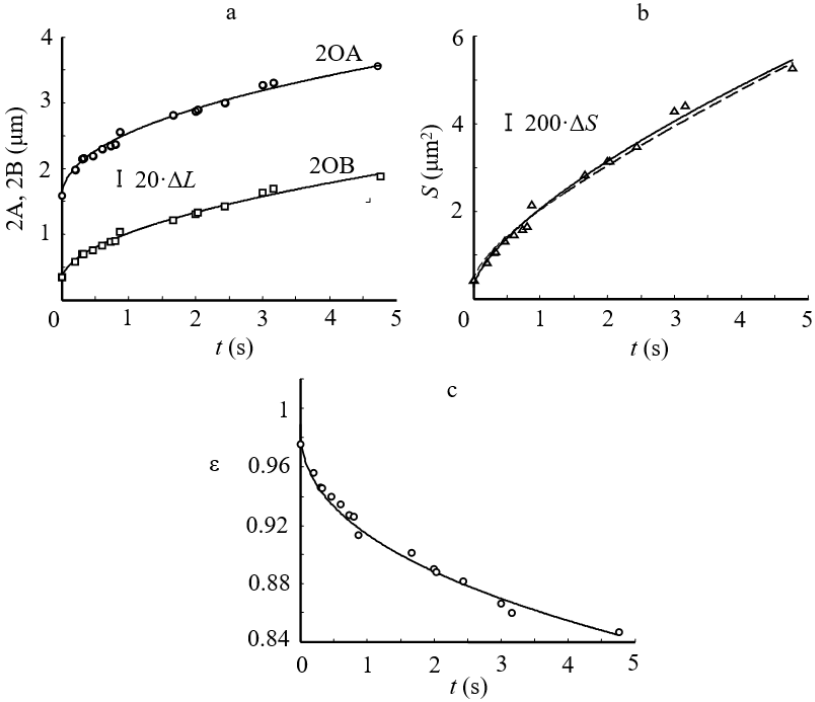

Fig. 6.6 Kinetics of the secondary crystallization of Sb_2S_3 in amorphous film: (a) time dependence of the length of the major axis 2OA and minor axis 2OB of the ellipse-shaped Sb_2S_3 crystal; (b) time dependence of the area S of the ellipse-shaped Sb_2S_3 crystal. The dotted line corresponds to the $\pi \cdot OA \cdot OB$ product. (c) time dependence of the eccentricity ε of the ellipse-shaped Sb_2S_3 crystal. Errors $\Delta L = 0.012$ μm, $\Delta S = 0.0018$ μm^2

The dependence on time of the length of the major axis 2OA and minor axis 2OB of the ellipse-shaped Sb_2S_3 crystal are shown in Fig. 6.6a. In this case nonlinear dependence takes place:

$$2OA = 1.014t^{0.45}+1.523\ \mu m; \quad (6.7a)$$

$$2OB = 0.721t^{0.52}+0.295\ \mu m. \quad (6.7b)$$

According to (6.7a,b) the growth rate v_{2OA} of the major axis 2OA and v_{2OB} of the minor axis 2OB is not constant, but decreases with time. The dependence on time of the area S of the ellipse-shaped Sb_2S_3 crystal is shown at Fig. 6.6b. In this case non quadratic dependence takes place:

$$S = 1.796t^{0.68}+ 0.258\ \mu m^2. \quad (6.8)$$

This dependence correlates well with $\pi \cdot OA \cdot OB$ product, corresponding to the area of the ellipse (the dotted line at Fig. 6.6b). The dependence on time of the eccentricity ε of the ellipse-shaped Sb_2S_3 crystal is shown in Fig. 6.6c. There is exponential decrease in the eccentricity of the crystal as it grows:

$$\varepsilon = \exp(-0.078t^{0.44}-0.0106). \quad (6.9)$$

6.3. Classification of the type of the transformation in amorphous Sb_2S_3

Both in the case of primary and secondary polymorphous crystallization of amorphous film a single ellipse-shaped Sb_2S_3 crystal grows in the field of observation (on the microscope screen). This is the main qualitative feature of the layer polymorphous crystallization [84, 90]. A quantitative feature of LPC is the value of relative length δ_0, determined by (4.3). To use this relation, we must determine quantities analogous to D_0 and a_0, taking into account the shapes and orientations of Sb_2S_3 crystals at the final stage of their growth. In turn, this requires knowledge of the dependence of the fraction of the

crystalline phase x on time t. The small thickness of the object of study makes it possible to determine x as the ratio of the crystal area S to the area of the field of the study S_0.

As S_0, we can use the area of the crystal at the final stage of the electron microscopy motion picture. Then in the case of primary polymorphous crystallization of Sb_2S_3 (Fig. 6.1) $S_0 = 1.55$ μm^2, and in the case of secondary polymorphous crystallization of Sb_2S_3 (Fig. 6.5) $S_0 = 5.27$ μm^2. The dependence x(t) for the case of primary polymorphous crystallization of Sb_2S_3 we can get by dividing the data $S(t)$ (Fig. 6.2b) by the $S_0 = 1.55$ μm^2. The result in coordinates of x - t^2 is presented at Fig. 6.7a. Its analytical dependence has the form:

$$x = 0.002t^2+0.017. \qquad (6.10)$$

According to (6.10), the value $x = 0.632$ corresponds to the characteristic time $t = t_0 = 17.536$ s. Substituting this value to (6.1a) for 2OA we get 2OA ≈ $D_0 = 1.526$ μm. The SAED pattern of the Sb_2S_3 crystal (Fig. 6.1c) sets the position of the diffraction vector $\mathbf{g}_{\bar{1}21}$. In this direction, the increasing of the major axis 2OA of the ellipse-shaped Sb_2S_3 crystal takes place. This is done by attaching of ($\bar{1}$ 21) planes with the interplanar distance $d_{\bar{1}21} = 0.3057$ nm. Then, according to (4.3), using $d_{\bar{1}21}$ instead of a_0, we get the relative length δ_0 ≈ 5000.

Similarly, the dependence $x(t)$ for the case of secondary polymorphous crystallization of Sb_2S_3 we can get by dividing the data $S(t)$ (Fig. 6.6b) by the $S_0 = 5.27$ μm^2. The result in coordinates of x - $t^{0.68}$ is presented at Fig. 6.7b. Its analytical dependence has the form:

$$x = 0.341t^{0.68}+0.049. \qquad (6.11)$$

In both cases (of primary and secondary polymorphous crystallization), the experimental data satisfactorily fits into straight lines, plotted respectively in the coordinates of x - t^2 and x - $t^{0.68}$ (Fig. 6.7).

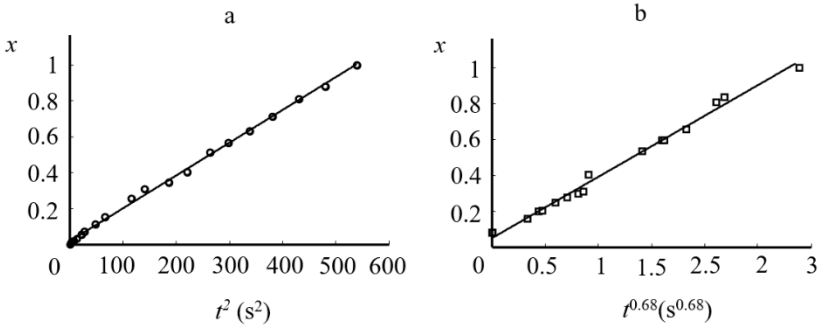

Fig. 6.7 Time dependence of the fraction crystallized for polymorphous (a) and for secondary (b) crystallization of Sb_2S_3 in amorphous film

According to (6.11) the value $x = 0.632$ corresponds to the characteristic time $t = t_0 = 2.2$ s. Substituting this value to (6.7a) we get $2OA \approx D_0 = 2.969$ μm. The SAED pattern of the Sb_2S_3 crystal (Fig. 6.5c) sets the position of the diffraction vector $\mathbf{g}_{\bar{2}11}$. In direction, close to $\mathbf{g}_{\bar{2}11}$, the increasing of the major axis 2OA of the ellipse-shaped Sb_2S_3 crystal takes place. This is done by attaching of ($\bar{2}$ 11) planes with the interplanar distance $d_{\bar{2}11} = 0.3053$ nm. Then, according to (4.3), using $d_{\bar{2}11}$ instead of a_0, we get the relative length $\delta_0 \approx 9700$.

Conclusions. Amorphous films of Sb_2S_3 with stoichiometric composition were formed on substrates at room temperature in the process of thermal evaporation of powder of Sb_2S_3 with S additives. Amorphous films of Sb_2S_3 with the excess of Sb were formed on substrates at room temperature in the process of thermal evaporation of powder of pure antimony sulfide. Electron beam irradiation of amorphous film of Sb_2S_3 with stoichiometric composition causes phase transformation that occurs according to the scheme of layer polymorphous crystallization. A single flat ellipse-shaped crystal of Sb_2S_3 nucleates and grows in the film region under investigation. The dependence on time

of the length of major and minor ellipse axis of this crystal has a linear character. As the ellipse-shaped crystal grows, its eccentricity decreases exponentially with time. This corresponds to decreasing in its elongation along the major axis. The dependence on time of the area of *S* of ellipse-shaped crystal and of the fraction crystallized *x* at layer polymorphous crystallization of Sb_2S_3 has a quadratic character. Wherein the relative length $\delta_0 \approx 5000$.

Electron beam irradiation of amorphous non-stoichiometric films with excess of antimony initiates the predominant crystallization of Sb during the first stage of the process, and subsequent matrix Sb_2S_3 crystallization during the second stage. As the film warms up, the density *n* and average value of the diameter $\langle D \rangle$ of antimony particles monotonically increases and at saturation $n \approx 7.5 \cdot 10^9$ cm^{-2} and $\langle D \rangle \approx 0.029$ μm. Then in the amorphous matrix with inclusions of micro-crystals of Sb a single flat ellipse-shaped crystal of Sb_2S_3 is growing. At the same time Sb particles are not nucleation centres of Sb_2S_3 crystals. Growth of Sb_2S_3 crystal practically does not change the spatial distribution of Sb particles. In rare cases, a displacement of particles in the direction of motion of the crystallization front was observed.

The dependence on time of the length of major and minor ellipse axis of this crystal has a nonlinear character. So, the growth rate of the major axis and of the minor axis is not constant, but decreases with time. As the ellipse-shaped crystal grows, its eccentricity decreases exponentially with time. This corresponds to decreasing in its elongation along the major axis. The dependence on time of the area of *S* of ellipse-shaped crystal and of the fraction crystallized *x* at secondary polymorphous crystallization of Sb_2S_3 described by a power function with the exponent of 0.68. Wherein the relative length $\delta_0 \approx 9700$.

7. POLYMODAL POLYMORPHOUS CRYSTALLIZATION OF TANTALUM PENTOXIDE

Tantalum pentoxide (Ta_2O_5) is the material with relatively high dielectric constant, good thermal and chemical stability. In addition, it has acceptable insulating properties. Therefore, thin films of Ta_2O_5 are promising for the use as dielectric in metal-oxide-semiconductor (MOS) devices, optical devices and as thin-film electroluminescent devices [144-147]. Nanoparticles of Ta_2O_5 are considered as perspective material for heterogeneous catalysis and for splitting of water into H_2 and O_2 [148]. Ta_2O_5 can be fabricated with the usage of anodic or thermal oxidation of Ta, atomic layer deposition (ALD), sputtering, sol-gel methods and various processes, based on chemical vapor deposition (CVD) [147].

In most of the cases, the films of Ta_2O_5, deposited on substrates at temperatures below 650°C, are amorphous [147, 149]. They require post deposition annealing to eliminate gas impurities (C and H), incorporated during the deposition step [147]. Post deposition treatments at high temperature initiates crystallization of the films that is accompanied by the change of density and dielectric constant [147, 149, 150]. Depending on the thickness and concentration of gas impurities in the amorphous film, after its annealing the growth of crystals with orthorhombic (β-Ta_2O_5) and hexagonal (δ-Ta_2O_5) structures were observed [147, 149].

Transmission electron microscopy (TEM) and electron diffraction studies “in situ” of electron-beam crystallization of amorphous Ta_2O_5 films revealed the long-period domain superstructure [125, 151]. It was demonstrated, that the main hexagonal lattice of Ta_2O_5 becomes rhombic after the formation of the shear superstructure in it as the result of the ordering of the oxygen vacancies. Detailed studies using in situ TEM heating experiments on the microstructure and crystallization kinetics of Ta_2O_5 thin films, prepared by ALD method, were clearly elucidated in [152]. It was demonstrated, that the crystallization behavior, accompanied by the growth of crystals of orthorhombic L-

Ta_2O_5 phase, can be approximated by the Johnson-Mail-Avrami-Kolmogorov (JMAK) equation.

7.1. Obtaining and structure of films

The films were obtained by pulsed laser sputtering of rotary Ta target in oxygen atmosphere and by subsequent deposition of laser erosion plasma on the substrate of (001) KCl at room temperature. The target was sputtered by pulses of radiation of AIG: Nd^{3+} laser (LTIPCH-5), operating in the Q-switched mode. The laser wavelength and the pulse repetition rate were 1.06 μm and 25 Hz respectively. The oxygen in the evaporation chamber (~ 0.13 Pa) was embedded by the usage of the specialized system for gas introduction SNA-2 of JSC "SELMI" (Sumy, Ukraine). The thickness of the films was determined by the number of laser pulses and was 10-15 nm (transparent for the electron beam).

As deposited films were separated from the substrate in distilled water and transferred onto the subject grids for electron microscopy studies. They were crystallized on the object grids in vacuum under the electron beam influence (in the microscope column). The rate of crystallization was set by the density *j* of the electron current through the sample, which was varying in the range from 1.1 to 6.5 $A \cdot mm^{-2}$ depending on the electron beam focusing. The structural analysis was carried out by the methods of electron diffraction and transmission electron microscopy. Experimental electron-diffraction data was compared with the JCPDS Powder Diffraction File (International Centre for Diffraction Data, Swarthmore, PA, 1996) [153].

Fig. 7.1 illustrates electron beam crystallization of the amorphous film, obtained by laser beam sputtering of Ta target in oxygen atmosphere. According to SAED pattern, presented at Fig. 7.1a, the film is amorphous at the initial state. The action of the electron beam initiates in it the growth of disoriented crystal grains, as evidenced by the SAED pattern and electron microscope image, shown at Fig. 1b and Fig. 1c respectively. The result of decoding of the SAED pattern, presented at Fig. 1b, is summarized in Table 7.1.

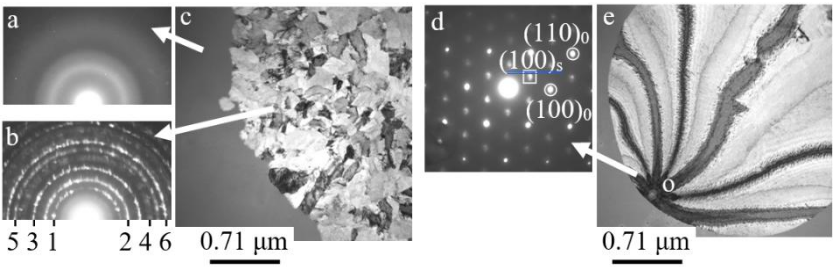

Fig. 7.1. Electron-beam crystallization of the amorphous Ta_2O_5 film. (a) SAED pattern of the amorphous part of the film. (b) SAED pattern of the polycrystalline part of the film. (c) Electron microscopic image of the partially crystallized film. SAED pattern (d) and electron microscopic image (e) of the disc-shape crystal of Ta_2O_5.

Table 7.1 - The results of the decoding of the SAED pattern at Fig. 1b

Diffraction ring number	This work *d* (nm)	hkl, phase	δ-(Ta, O) JCPDS 19-1299 [153] *d* (nm)	δ-Ta_2O_5 JCPDS 18-1304 [153] *d* (nm)
1	0.387	001- Ta_2O_5	0.3880	0.3870
2	0.311	100 - Ta_2O_5	0.3140	0.3130
3	0.242	101 - Ta_2O_5	0.2440	0.2436
4	0.198	002 - Ta_2O_5	0.1940	0.1936
5	0.180	110 - Ta_2O_5	0.1811	0.1809
6	0.164	102 - Ta_2O_5	0.1650	

The interplanar distances *d*, calculated from the measured ring diameters, were compared with the literature data [153]. The observed diffraction peaks can be ascribed as the hexagonal phase of δ-Ta_2O_5 with unit cell

parameters a_0=0.3624 nm and c_0=0.3880 nm (JCPDS 19-1299). The absence of reflections, associated with tantalum, indicates on the one-stage (polymorphous [77]) character of the transformation amorphous phase - crystal.

Fig. 7.1d and 7.1e illustrate one-stage polymorphous crystallization of the same amorphous film, accompanied with the growth of a disk-shape single crystal of Ta_2O_5. Electron microscopic image of this crystal contains extinction bend contours - high contrast stripes, converging at point “o”. The variability of the contrast occurred due to the local crystal bends, leading to the change in the diffraction conditions. The crystal, growing in amorphous film, is in the field of tensile stresses, which can change during variation of the size and of the shape of the crystal. This leads to the formation of extinction bend contours (BC) with different intensities and shapes at TEM images. The nature of the formation of BC at crystallization of amorphous films was studied in detail in [154].

SAED pattern of the area near the point “o” corresponds to the (001) section of the reciprocal lattice of Ta_2O_5. A detailed analysis of such electron diffraction patterns is given in [125, 151]. Crystallization of the amorphous film is accompanied by the ordering of oxygen vacancies. In this case, a superstructure lattice is formed, which is also hexagonal. It has parameters $a_s = \sqrt{3}a_0$ and $c_s = c_0$ that rotated with respect to the base lattice by 30º. In the SAED pattern (Fig 7.1d) the reflections of the main and superstructure lattice are marked with indices “0” and “s” respectively.

7.2. Electron beam crystallization modes

7.2.1. Layer polymorphous crystallization mode of Ta_2O_5

Fig. 7.2 explains the growth kinetics of a single Ta_2O_5 crystal in amorphous film [155]. The photomicrographs correspond to the periods of time t that passed after the video recording had started: (a) t = 2.07 s; (b) t = 6.57 s; (c) t = 9.63 s. The dependence on time of the crystal diameter $D(t)$ is shown at Fig. 7.2d. The straight line was plotted by the data of D measurements using the least-squares technique. The correlation coefficient, characterizing the

closeness of linear relation between D and t, is close to unity. A linear dependence takes place:

$$D = 0.120t + 0.037 \text{ μm}. \quad (7.1)$$

According to (7.1) the tangential crystal growth rate $v_\tau = 0.120$ μm·s^{-1}.

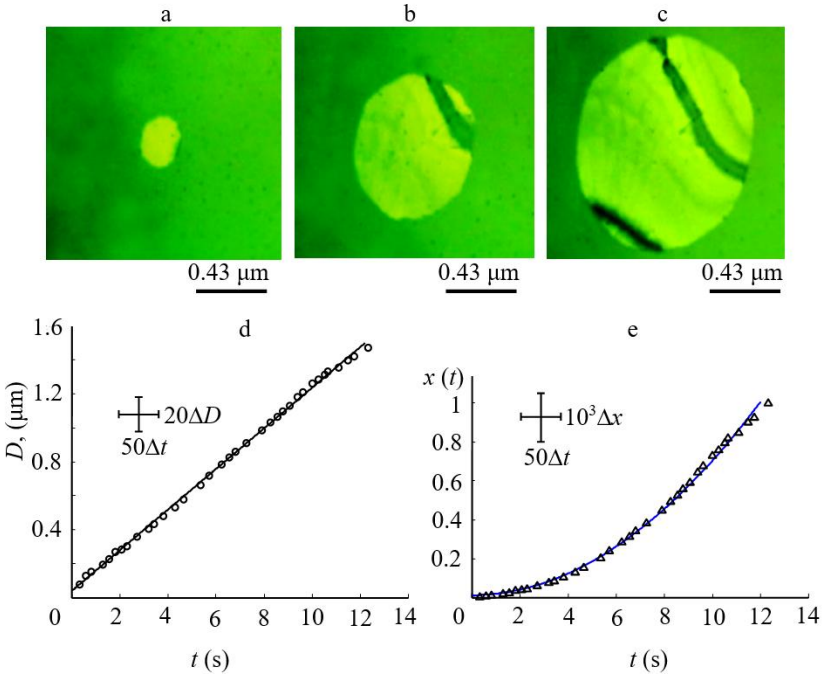

Fig. 7.2. LPC of amorphous film of Ta_2O_5. The micrographs correspond to the periods of time t, that passed after the video recording had started: (a) $t = 2.07$ s; (b) $t = 6.57$ s; (c) $t = 9.63$ s. (d) The dependence on time of the crystal diameter D. (e) The dependence on time of the crystals fraction x of Ta_2O_5. Errors $\Delta t = 0.033$ s; $\Delta D = 0.01$ μm; $\Delta x = 2.5 \cdot 10^{-4}$ [155]

Fig. 2e shows the dependence on time of the crystallization fraction $x(t)$. A quadratic dependence takes place:

$$x = 0.007t^2 + 0.011. \quad (7.2)$$

When the fraction of the crystalline phase $x = 0.632$, according to (7.2) the characteristic unit of time $t_0 = 9.419$ s. For t_0=9.484 s the characteristic unit of length $D_0 = v_\tau \cdot t_0 \cdot \approx 1.13$ μm. For the crystal of Ta_2O_5 with the [001] zone axis (Fig. 1d) the projection of the unit cell on the plane of the film is a rhomb with the side $a_0 = 0.3624$ nm and apex of 120°. In this case δ_0 is the number of cell parameters a_0, stacked at a distance, equal to D_0. According to (4.3) the relative length $\delta_0 \approx 3100$ (numeric, typical for LPC mode [90, 128]).

7.2.2. Interjacent character of crystallization of Ta_2O_5

Fig. 7.3 explains the growth kinetics of several crystals of Ta_2O_5 in the amorphous film. The beginning of the video recording of the process corresponds to the simultaneous appearance of two crystals numbered 1 and 2. Then crystal 3 appears. At the final stage of video recording, crystal 4 appears. The photomicrographs correspond to the periods of time t that passed after the video recording had started: (a) $t = 1.03$ s; (b) $t = 2.40$ s; (c) $t = 3.60$ s. Fig. 3d illustrates the dependence on time of the diameters D_1, D_2, D_3, and D_4 of the crystals 1, 2, 3 and 4 respectively. Linear dependence on time $D_i(t)$ takes place for each crystal:

$$D_1 = 0.337t + 0.063 \text{ μm}; \quad (7.3a)$$
$$D_2 = 0.238t - 0.012 \text{ μm}; \quad (7.3b)$$
$$D_3 = 0.242t - 0.154 \text{ μm}; \quad (7.3c)$$
$$D_4 = 0.168t - 0.291 \text{ μm}, \quad (7.3d)$$

where t is measured in seconds. According to (7.3a) - (7.3d) the tangential growth rate of the crystals $v_{\tau 1} = 0.337 \text{μm} \cdot \text{s}^{-1}$; $v_{\tau 2} = 0.238 \text{μm} \cdot \text{s}^{-1}$; $v_{\tau 3} = 0.242$ $\text{μm} \cdot \text{s}^{-1}$; $v_{\tau 4} = 0.168$ $\text{μm} \cdot \text{s}^{-1}$. In this case, the arithmetic mean speed $\langle v_\tau \rangle = 0.246$ $\text{μm} \cdot \text{s}^{-1}$.

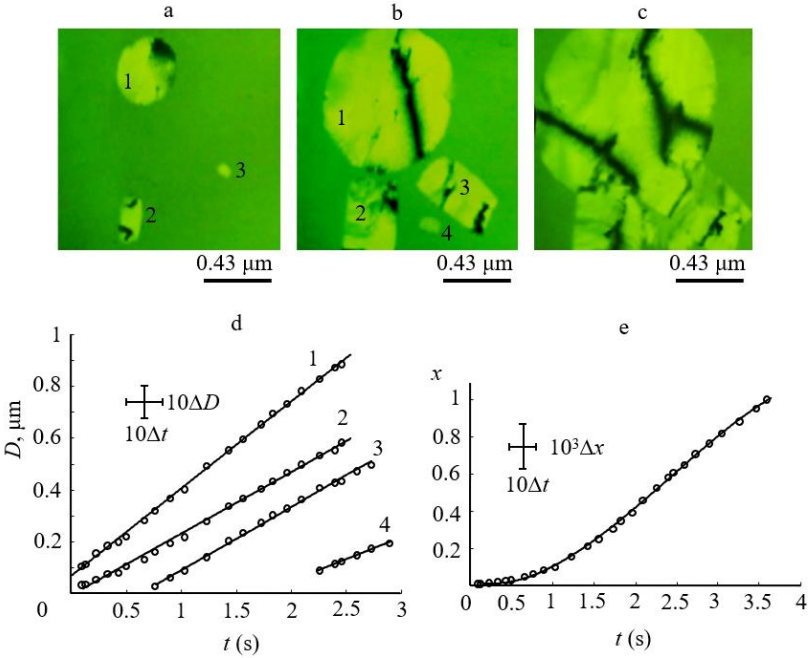

Fig. 7.3. Crystal's growth in amorphous film of Ta_2O_5. The micrographs correspond to the periods of time t, that passed after the video recording had started: (a) t = 1.03 s; (b) t = 2.40 s; (c) t = 3.60 s. (d) The dependence on time of the diameters D_1, D_2, D_3, and D_4 of the crystals 1, 2, 3 and 4 respectively. (e) The dependence on time of the crystals fraction x. Errors Δt = 0.033 s; ΔD = 0.01 μm; $\Delta x = 2.5 \cdot 10^{-4}$

Fig. 7.3e illustrates the dependence on time of the crystals fraction $x(t)$ of Ta_2O_5. The line corresponds to the equation:

$$x = -0.029t^3 + 0.208t^2 - 0.106t + 0.024 \text{ μm}. \quad (7.4)$$

When the fraction of the crystalline phase $x = 0.632$, according to (7.4) characteristic unit of time $t_0 = 2.560$ s. For average tangential crystal growth rate $\langle v_\tau \rangle = 0.246$ μm·s^{-1} the characteristic unit of the length $D_0 = \langle v_\tau \rangle \cdot t_0 \approx 0.630$ μm. For Ta_2O_5 the volume of unit cell $\Omega = 4.413 \cdot 10^{-11}$ μm^3 ([153], card 19-1299). In this case, according to (4.4), the relative length $\delta_0 \approx 1783$ (numeric, interjacent between LPC and IPC modes [90]).

7.2.3. Island polymorphous crystallization mode of Ta_2O_5

Fig. 7.4 illustrates kinetics of the formation of the polycrystalline film of Ta_2O_5. The photomicrographs correspond to the periods of time t that passed after the video recording had started: (a) $t = 0{,}27$ s; (b) $t = 0{,}70$ s; (c) $t = 2{,}23$ s. The dependence on time of the crystallization centers density $N(t)$ is shown at Fig. 7.4d. This dependence is described by the curve with saturation:

$$N = 16.8 \cdot 10^8 (1-\exp(-1.6t)) \text{ cm}^{-2}, \tag{7.5}$$

which is achieved at $N_s \approx 1.67 \cdot 10^9$ cm^{-2}.

The dependence on time of the average crystal diameter $\langle D \rangle$ is shown at Fig. 7.4e. The linear dependence takes place:

$$\langle D \rangle = 0.086t + 0.065 \text{ μm}, \tag{7.6}$$

where t is measured in seconds. According to (7.6) the average tangential crystal growth rate $\langle v_\tau \rangle = 0.086$ μm·s^{-1}.

Fig. 7.5a shows the dependence on time of the crystallization fraction x. Experimental data, presented in the coordinates $\ln[-\ln(1-x)]$ - $\ln t$, forms a straight line (Fig. 7.5b). The correlation coefficient, characterizing the tightness of the linear relationship between $\ln[-\ln(1-x)]$ and $\ln t$ is close to unity. This fact indicates the applicability to the process of phase transformation of the Johnson-Mail-Avrami-Kolmogorov formula (JMAK) [62, 156, 157]:

$$x = 1-\exp(-kt^n), \tag{7.7}$$

where n is the Avrami coefficient (reaction order) and k is the effective rate constant, describing both nucleation and growth. [157, 158].

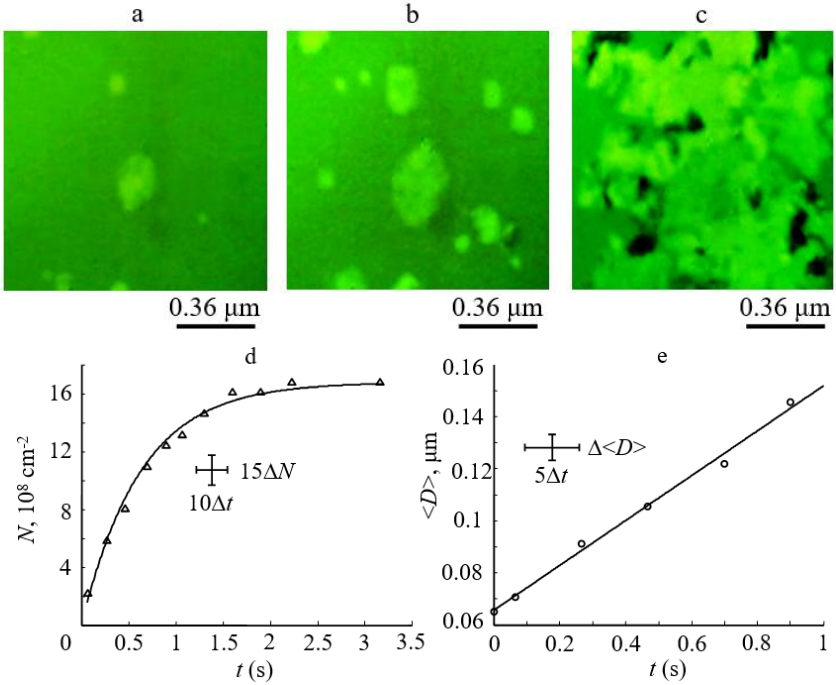

Fig. 7.4. IPC of amorphous film of Ta_2O_5. The micrographs correspond to the periods of time t, that passed after the video recording had started: (a) t = 0.27 s; (b) t = 0.70 s; (c) t = 2.23 s. (d) The dependence on time of the crystallization centers density N. (e) The dependence on time of the average crystal diameter $\langle D \rangle$. Errors Δt = 0.033 s; $\Delta N = 1.4 \cdot 10^7$ cm^{-2}; $\Delta \langle D \rangle$ = 0.01 μm.

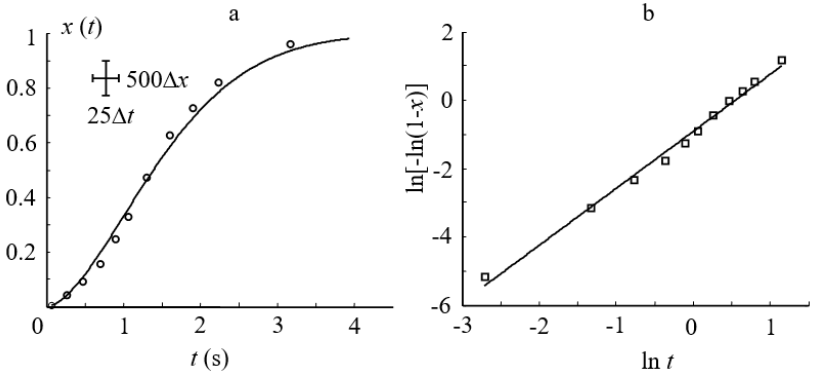

Fig. 7.5. (a) The dependence on time of the crystals' fraction x of Ta_2O_5. (b) The dependence of the ln[-ln(1-x)] on ln$t$. Errors Δt = 0.033 s; Δx = $2.5 \cdot 10^{-4}$.

To determine them, the expression (7.7) was reformulated as follows:

$$\ln[-\ln(1-x)] = n\ln t + \ln k. \quad (7.8)$$

According to (7.8) and Fig. 7.5b the tangent of the angle of inclination of the line to the abscissa axis n = 1.7. The point of the intersection with the ordinate axis $\ln k$ = -0.9 and k = 0.4 $s^{-1.7}$. Taking into account numerical values of n and k (7.7), the curve at Fig. 7.5a will fit the equation:

$$x = 1-\exp(-0.4t^{1.7}), \quad (7.9)$$

where t is measured in seconds.

When the fraction of the crystalline phase x = 0.632, according to (7.9) the characteristic unit of time t_0 = 1.713 s. According to (7.6) for average tangential crystal growth rate $\langle v_\tau \rangle$ = 0.086 μm·s^{-1} the characteristic unit of the length $D_0 = \langle v_\tau \rangle \cdot t_0 \approx$ 0.147 μm. For Ta_2O_5 the volume of unit cell

$\Omega=4.413\cdot10^{-11}$ μm^3 ([153], card 19-1299). In this case, according to (4.4), the relative length $\delta_0 \approx 416$ (numeric, typical for IPC mode [90]).

7.3. Polymodality of crystallization as a manifestation of polyamorphism in Ta_2O_5 films

Amorphous films are formed on substrates at the room temperature in the process of pulsed laser sputtering of rotary Ta target in oxygen atmosphere. Electron beam irradiation causes their crystallization with the formation of Ta_2O_5 crystals with hexagonal lattice. Electron microscopic investigation, including "in situ" and video recording methods, revealed the following crystallization modes in different regions of the same amorphous film of Ta_2O_5 (Table 7.2).

Table 7.2 - Crystallization modes in amorphous film of Ta_2O_5*

Parameter	Layer polymorphous crystallization	Interjacent character of crystallization	Island polymorphous crystallization
t_0, s	9.419	2.560	1.713
D_0, μm	1.13	0.63	0.147
δ_0	3100	1783	416

*t_0 is the characteristic time unit, D_0 is the characteristic length unit, and δ_0 is the relative length.

1. Layer polymorphous crystallization. In the studied area of the amorphous film, a single crystal nucleates and grows. In this case time dependence of the crystal diameter $D \sim t$, time dependence of the fraction of the crystalline phase $x \sim t^2$ and the relative length $\delta_0 \approx 3100$. In the case of (001) Ta_2O_5 the relative length is the number of cell parameters a_0, stacked at the distance, equal to the characteristic unit of length D_0

2. Interjacent character of crystallization is characterized by the nucleation and growth of several (3-4) disoriented crystals. Each crystal grows at the constant rate until it touches with the neighboring crystal. The dependence $x(t)$ can be successfully approximated by the polynomial of the third power. The relative length $\delta_0 \approx 1783$.

3. Island polymorphous crystallization mode. At the influence of the electron beam irradiation in amorphous film, a great number of disoriented crystals nucleate and grow. The dependence on time of the crystallization centers density is described by the curve with saturation, which is achieved at $N_s \approx 1.67 \cdot 10^9$ cm^{-2}. Time dependence of the average crystal diameter $\langle D \rangle \sim t$. The relative length $\delta_0 \approx 416$. The dependence of the fraction of the crystalline phase x on time t has the exponential character, described by the JMAK formula with the reaction order $n = 1.7$ and the effective rate constant $k = 0.4$ s$^{-1.7}$. According to [158] when $n = 1.5$-1.8 the crystallization processes corresponds to the grain growth with the nucleation and with the decreasing of the nucleation rate. This is the situation, which is realized in our case of crystallization of amorphous film of Ta_2O_5 (Fig. 7.4 a, b, c, d). The crystallization process ends with the formation of the polycrystalline film.

The results of electron microscopic studies are summarized in Table 7.2. According to it the phase transformation amorphous - crystal Ta_2O_5 is polymorphous. However, different regions of the same amorphous film can exhibit different modes of crystallization. The reason for this can be explained by the phenomenon of polyamorphism [129, 160]: the existence of two or more forms with different short-range order of arrangement of atoms in the first coordination sphere. Regions of amorphous film with different short-range order will crystallize in different ways. Polyamorphism may be a consequence of the presence of local structural inhomogeneities in the amorphous state of the substance, which is realized due to the specifics of the pulsed laser deposition method.

The following features of the method of deposition take place. The amorphous film grows on the substrate during the deposition of laser erosion plasma. Therefore, the deposition is of the echeloned nature: electrons are

followed by high-energy ions, then come the ions with the lower energy, and at the end of the condensation pulse, neutral atoms are deposited. Ions, the energy and angular distribution of which is rather inhomogeneous, create in the substrate of (001) KCl defects such as color centers.

All of them are centers for the deposition of matter (traps for atoms), but they have different capture efficiency. For example, orienting F-color centers (anionic vacancies that captured electrons) are more efficient traps than their aggregation products [159]. The inhomogeneity of their distribution over the condensation surface provides local inhomogeneities in the distribution of oxygen vacancies in the amorphous film. The latter is the reason for the realization of different crystallization modes in the same film. Previously, LPC and IPC crystallization modes were observed in amorphous V_2O_3 films, deposited by laser sputtering of vanadium in oxygen atmosphere [7]. Also the formation of structures of different types (dendrites, cells) within a single film due to the presence of structural inhomogeneities in the material was observed during the electron beam induced crystallization of iron–carbon films [2].

8. ISLAND POLYMORPHOUS CRYSTALLIZATION MODE

8.1. Crystallization of amorphous films of zirconia

Zirconia (zirconium dioxide ZrO_2) has a wide range of technical applications, since it has high strength, heat insulating and dielectric properties and high thermal and chemical resistance to aggressive media. ZrO_2 has various polymorphous modifications: the monoclinic modification exists below 1170°C [161]. The data on its structure are given in the International Centre for Diffraction Data tables (JCPDC tables) [153]: $a = 0.53129$ nm, $b = 0.52125$ nm, $c = 0.51471$ nm, and $\beta = 99.218°$ (file 37-1484). Above 1170°C, this modification transforms to the tetragonal one with parameters $a = 0.512$ nm and $c = 0.525$ nm (file 17-0923 of JCPDC tables). At $T \geq 2370$°C, the polymorphous transformation of the tetragonal phase to the cubic one, for which $a = 0.509$

nm, space group Fm3m (file 27-0997 of JCPDC tables), occurs.

Exactly the tetragonal and cubic ZrO_2 phases find wide technical applications. However, they are unstable at room temperature. The tetragonal phase is formed from the cubic one during the transformation of the cubic oxygen sublattice and unit cell extension along the oxygen atomic displacement. The monoclinic phase is formed from the tetragonal one by shear deformation of the entire unit cell and changes in lengths of its sides [162]. High-temperature phases are stabilized by doping zirconium dioxide with Y_2O_3 impurity. However, ZrO_2–Y_2O_3 solid solution formation results in an increase in the ionic conductivity due to the formations of a large number of oxygen vacancies [162]. This is accompanied by a strong degradation of dielectric characteristics of a material at temperatures above 1000°C.

Interest in zirconium dioxide in the thin-film and nanocrystalline state is caused by its possible application as a barrier layer between a high-temperature superconductor film and a Si substrate, as coatings used in biomedicine and prosthetics, and as components of solid-state oxide fuel cells [163]. In the nanocrystalline state, high-temperature zirconium dioxide phases can exist even without adding a stabilizing component. Zirconium dioxide nanoparticles with tetragonal and cubic structures are synthesized in lowpressure arc discharge plasma and during laser ablation of a bulk ZrO_2 target [161].

It was shown that pulsed laser radiation causes sputtering of the zirconium dioxide surface. Being deposited on the Si substrate, laser erosion products form a high-temperature cubic ZrO_2 phase [163]. During pulsed laser deposition (PLD) of materials, cluster formation and growth on the substrate occur under nonequilibrium conditions further predetermining the possibility of forming metastable structure states. Alongside the PLD method, ion-plasma sputtering (IPS) is widely applied to obtain amorphous and nanocrystalline films and coatings. For this reason, the objective of this work is to obtain amorphous ZrO_2 films by PLD and IPS, to study their structure, and compare the kinetics of their electron beam induced crystallization.

8.1.1. Obtaining and structure of samples

Amorphous zirconia films were obtained by both ion-plasma sputtering and laser ablation of Zr targets [10, 164]. Target ablation products were deposited onto (001) KCl substrates at room temperature. The thickness of films was 30 - 40 nm. Ion-plasma sputtering was performed on an URM-3 setup [165] with a magnetron equipped with a system of passive protection against microarcs to decrease the amount of Zr microdrops in a deposited film. The sputtering of a film was performed at a discharge current of 7.7 A and a magnetron power supply voltage of 650 V. The ablation of a Zr target was performed in an argon-oxygen mixture at a pressure of 0.083 Pa. The partial Ar pressure was 0.078 Pa, and the oxygen flow rate was 24 cm^3/min.

The laser ablation of a Zr target was performed in an oxygen atmosphere at a pressure of ~0.13 Pa. Pulsed radiation from an LTI-PCh-5 laser operated at a Q - switch regime was used. The wavelength and the pulse repetition frequency were 1.06 μm and 25 Hz, respectively. The films deposited onto (001) KCl were separated from a substrate in distilled water and transferred onto objective grids for microscopic studies. The crystallization of a film was initiated by the effect of an electron beam in the column of a microscope at a beam current of ~20 μA. The crystallization rate was adjusted by changing the density j of electron current through a sample within 1.1– 6.5 A/mm^2 depending on the focusing of a beam.

Structural analysis was performed by electron diffraction and transmission electron microscopy. The film crystallization process was recorded from the screen of an electron microscope on a Canon Power Shot G15 camera in the video record mode at a frame rate of 30 s^{-1}.

Both PLD and IPS of Zr in an oxygen atmosphere lead to the formation of amorphous ZrO_2 films on substrates at room temperature. Fig. 8.1a shows the electron diffraction pattern from the free-standing film of ZrO_2 immediately after its separation from the substrate of KCl. It consists of two diffraction halos. The first halo is intense, while the second one is much weaker in the

intensity and very diffuse. These electron diffraction data indicate on the amorphous nature of this film.

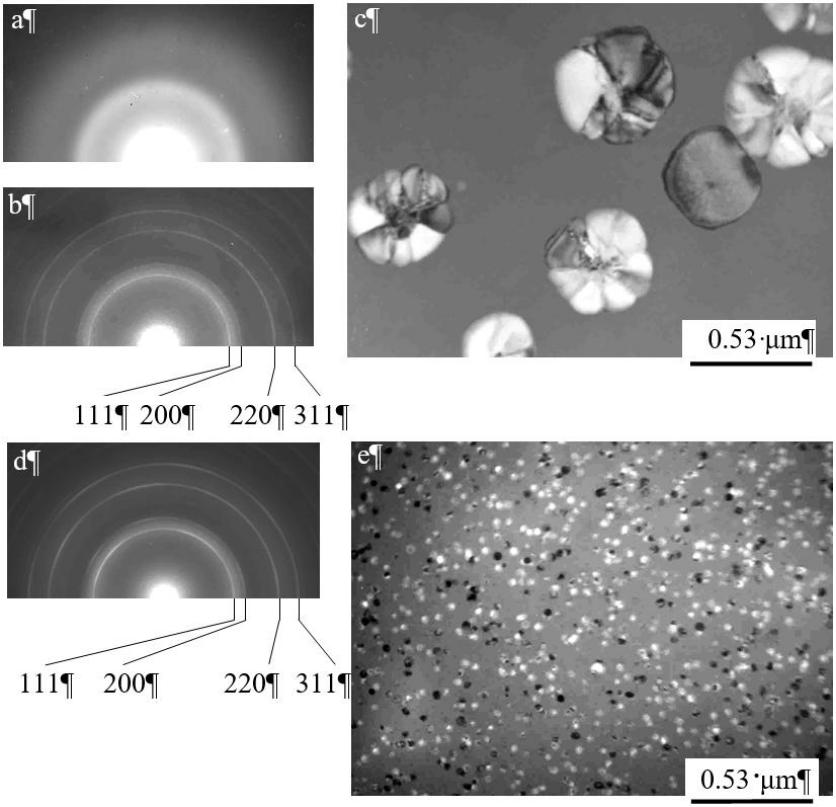

Fig. 8.1. Growth of crystals of cubic ZrO_2 modification in amorphous films under electron beam irradiation: (a, b, d) electron diffraction patterns and (c, e) electron microscopic photos of the amorphous-crystalline films deposited by (a, b,c) laser and (d, e) ion-plasma sputtering [10]

According to the data of this table the crystallization of an amorphous layer obtained by laser evaporation leads to the formation of a cubic FCC ZrO_2 phase with a lattice constant a_0 = 0.5094 nm. The crystallization of an amorphous layer obtained by ion-plasma evaporation also gives a cubic FCC ZrO_2 phase with a close lattice constant a_0 = 0.5098 nm. These data are in good agreement with the data of JCPDS tables [153] (card no. 27-0997).

Table 8.1 - Data of the electron diffraction analysis of the ZrO_2 films deposited by laser and ion-plasma sputtering after partial crystallization

Line no.	*hkl*	Laser sputtering		Ion-plasma-sputtering		Data of JCPDS tables (card no. 27-0997)	
		d, nm	a_0, nm	*d*, nm	a_0, nm	*d*, nm	a_0, nm
1	(111)	0.2931	0.5094	0.2937	0.5098	0.2930	0.509
2	(200)	0.2553		0.2558		0.2550	
3	(220)	0.1802		0.1809		0.1801	
4	(311)	0.1536		0.1529		0.1534	

The comparison of the electron microscopic photos shown at Figs. 1c and 1e argues that the number of microcrystals per unit film surface area is much higher when the IPS method is used. At the same time, the average diameter of microcrystals *D* in the films obtained by PLS is much larger than the diameter of microcrystals in the films deposited by IPS.

8.1.2. Density changes during film crystallization

The electron microscopy image of the ZrO_2 film partially crystallized by the electron beam is shown at Fig. 8.2. ZrO_2 microcrystals indicated by numbers 1 and 2 have FCC lattice. For microcrystals 1 and 2 the film plane is perpendicular to the [211] ZrO_2 (Fig. 8.2a) and [110] ZrO_2 zone axis (Fig. 8.2c), respectively.

The presence of crossed contrast bending extinction contours in the images of microcrystals suggests that their bend is dome-shaped. The bend is caused by the circumstance that the crystal growth occurs in the presence of tensile stresses caused by an increase in the film material density during crystallization. The relative change in the density γ due to the phase transition of a film material from the amorphous state with the density ρ_a to the crystalline state with the density ρ_c was determined according to (1.2) and (1.4).

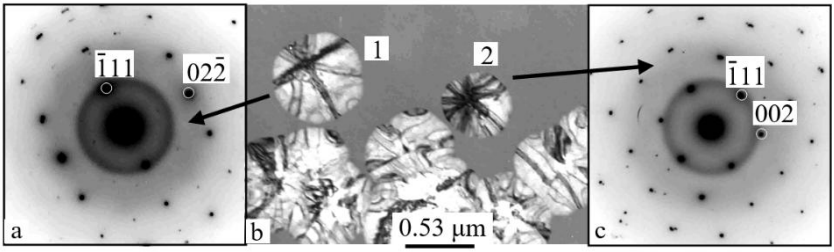

Fig. 8.2. Electron-beam crystallization of amorphous ZrO_2 deposited at T_S= 290 K. (a) SAED pattern of the ZrO_2 microcrystal with the [211] zone axis, (b) the electron microscopy image of the partially crystallized film, and (c) the SAED pattern of the ZrO_2 microcrystal with the [110] zone axis. The contrast in SAED patterns is inverted [164]

Fig. 8.3 shows two micrographs of the same section of the Zr_2O_2 film in the initial amorphous state (Fig. 8.3a) and after its complete crystallization by an electron beam (Fig. 8.3b). The film contains microdroplets of Zr, brought from the target to the substrate by the vapor-plasma flow. This is a manifestation of the so-called "splash effect", characteristic of the laser deposition method. They are rigidly connected to the film. The length of the line connecting the Zr microdroplets in amorphous (X_a at Fig 8.3a) and crystalline (X_c at

Fig 8.3b). The relation $X_a > X_c$ suggests that the density ρ_a of amorphous ZrO_2 is lower than the density ρ_c of crystalline ZrO_2.

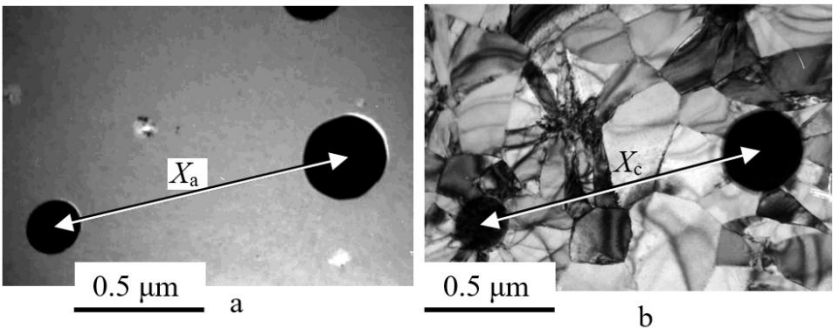

Fig. 8.3. Electron microscopy image of the ZrO_2 film area (a) before and (b) after crystallization. X_a and X_c are the distances between hardened zirconium microdrops before and after film crystallization, respectively

The results of statistical treatment of measured relative density changes γ during amorphous ZrO_2 crystallization are shown in the form of frequency histograms at Fig. 8.4. The γ distribution is characterized by the corrected root-mean-square deviation of 3.15%, the negative asymmetry of -0.0634, and the positive excess of 0.90 [164]. For comparison Fig. 8.4 also shows the γ curve corresponding to the Gaussian distribution. At the reliability level of 0.5, the relative density changes during zirconium dioxide film crystallization is γ=10.3±2.1% (Table 1.2).

Hence, the growing microcrystal from the time of its nucleation and during growth is continuously subjected to tensile stresses from the side of the amorphous matrix, which can be a cause of high-temperature cubic ZrO_2 phase stabilization. This is consistent with the data of [163] where the cubic phase

stabilization was explained by the development of thermoelastic forces on the surface of ZrO_2 particles due to their rapid crystallization.

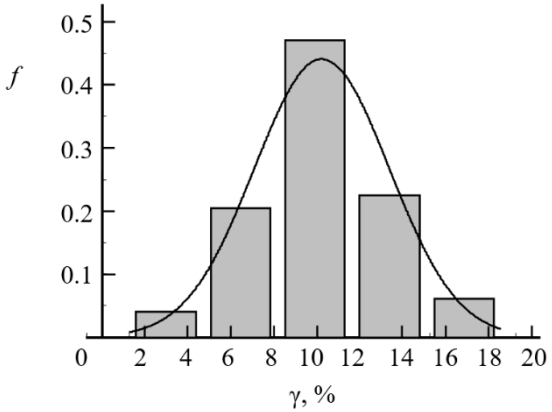

Fig. 8.4. Histogram of relative frequencies *f* of the appearance of measured relative ZrO_2 density changes during crystallization and the γ curve corresponding to the Gaussian distribution

8.1.3. Crystallization kinetics of laser condensates of ZrO_2

Fig. 8.5 shows TEM video footage of crystals growth in amorphous films of laser condensates of ZrO_2. Time moments *t* that has passed from the beginning of the recording of the crystallization process is shown in the upper right corner of each frame. A one-stage transformation is realized: amorphous phase - crystal ZrO_2 of a cubic modification [166].

Fig. 8.6a shows the dependence on time of the average diameter <*D*> of crystals, growing in amorphous film of ZrO_2. This line corresponds to the equation:

$$<D> = 0.110t - 0.010 \text{ μm}. \quad (8.1)$$

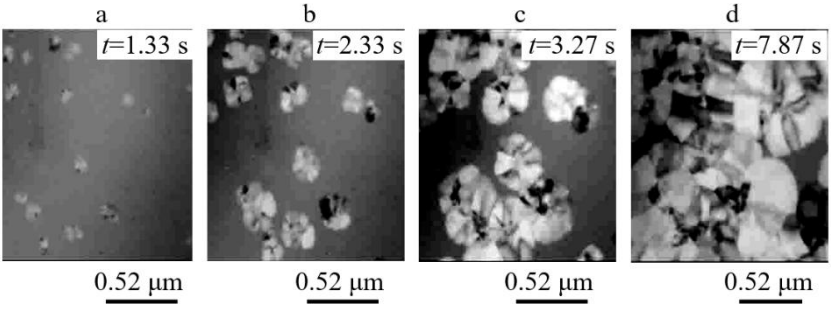

Fig. 8.5. TEM video footage of crystals growth in amorphous films of zirconia. Time moments t, that has passed from the beginning of the recording of the crystallization process, are shown in the upper right corner of each frame [166]

According to (8.1) the increase of $\langle D \rangle$ occurs at a constant rate $v_{\langle D \rangle}=0.110\ \mu m \cdot s^{-1}$.

Time dependence of the crystallized volume fraction $x(t)$ of zirconia is shown at Fig. 8.6b. This experimental data, presented in the coordinates $\ln[-\ln(1-x)] - \ln t$, form a straight line (Fig. 8.6c). This fact indicates the applicability to the process of a-c phase transformation of the JMAK formulas (7.7).

Drawing $\ln[-\ln(1-x)]$ against $\ln(t)$ should be straight line:

$$\ln[-\ln(1-x)] = n\ln t + \ln k. \qquad (8.2)$$

In this case n is the tangent of the angle of inclination of the line to the abscissa and the point of the intersection with the ordinate is $\ln k$. According to (8.2) and Fig. 8.6, c $n = 2.03$, $\ln k = -2.976$ and $k = 0.051$.

Taking into account numerical values of n and k, the curve at Fig. 8.6, b will fit the equation:

$$x = 1-\exp(-0.051t^{2.03}). \qquad (8.3)$$

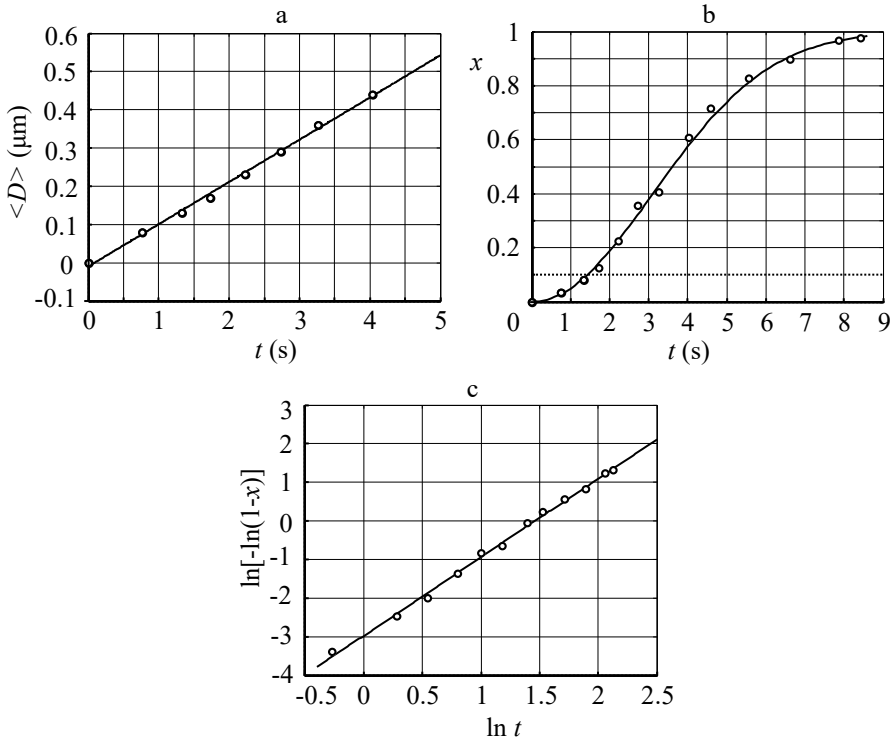

Fig. 8.6. The dependence on time of the average diameter <*D*> (a), crystallized volume fraction $x(t)$ in coordinates x - t (b) and in in coordinates $\ln[-\ln(1-x)]$ - $\ln t$ (b)

When the fraction of the crystalline phase $x = 0.632$, according to (8.3) and Fig. 8.6, b the characteristic unit of time $t_0 = 4.331$ s. In agreement with (8.2) and Fig. 8.6, a the characteristic unit of the length $D_0 \approx 0.486$ μm. For ZrO_2 the volume of unit cell $\Omega = 1.3187 \cdot 10^{-10}$ μm^3 JCPDS tables [153] (card no. 27-0997). In this case, according to (4.4), the relative length $\delta_0 \approx 950$

(several hundred is a numeric, typical for IPC mode [90]). The kinetic parameters of crystallization are given in Table 8.2.

8.1.4. Crystallization kinetics of ion-plasma condensates of ZrO_2

Fig. 8.7 shows TEM video footage of crystals growth in amorphous films of ion-plasma condensates of ZrO_2. Time moments t that has passed from the beginning of the recording of the crystallization process is shown in the upper right corner of each frame. A one-stage transformation is realized: amorphous phase - crystal ZrO_2 of a cubic modification [167].

Fig. 8.8a show the dependence on time of the average diameter $<D>$ of crystals, growing in amorphous film of ZrO_2. This line corresponds to the equation:

$$<D> = 0.012t+0.007 \text{ μm}. \quad (8.4)$$

According to (8.4) the increase of $<D>$ occurs at a constant rate $v_{<D>}=0.012$ μm·s^{-1}.

Time dependence of the crystallized volume fraction $x(t)$ of zirconia is shown at Fig. 8.8b. This experimental data, presented in the coordinates $\ln[-\ln(1-x)] - \ln t$, form a straight line (Fig. 8.8c). This fact indicates the applicability to the process of a-c phase transformation of the JMAK formulas (7.7).

Drawing $\ln[-\ln(1-x)]$ against $\ln(t)$ should be straight line (8.2). In our case it is:

$$\ln[-\ln(1-x)] = 3.63\ln t -4.190. \quad (8.5)$$

According to (8.5) and Fig. 8.8c Avrami exponent $n = 3.63$ and rate constant $k = 0.015$. Taking into account numerical values of n and k, the curve at Fig. 8.8b will fit the equation:

$$x = 1-\exp(-0.015t^{3.63}). \quad (8.6)$$

When the fraction of the crystalline phase $x = 0.632$, according to (8.6) and Fig. 8.8b the characteristic unit of time $t_0 = 3.180$ s. In agreement with (8.4) and Fig. 8.8a the characteristic unit of the length $D_0 \approx 0.045$ μm. For ZrO_2 the volume of unit cell $\Omega = 1.3187 \cdot 10^{-10}$ μm^3 JCPDS tables [153] (card no. 27-0997). In this case, according to (4.4), the relative length $\delta_0 \approx 88$ (several hundred is a numeric, typical for IPC mode [90]). These data are presented in Table 8.2.

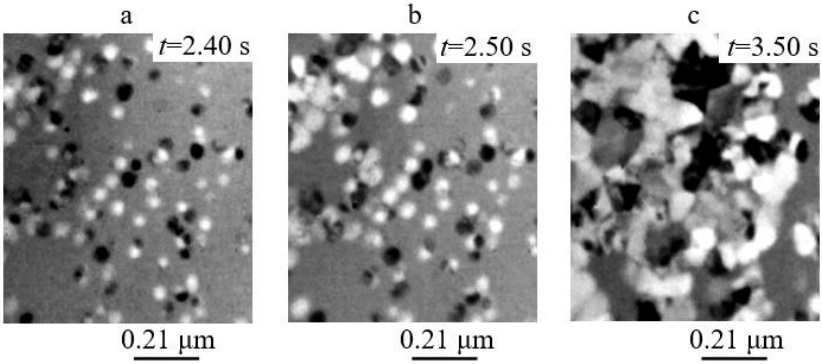

Fig. 8.7. TEM video footage of crystals growth in amorphous films of zirconia. Time moments *t*, that has passed from the beginning of the recording of the crystallization process, are shown in the upper right corner of each frame [167]

8.1.5. Comparison of crystallization parameters of laser and ion-plasma amorphous condensates of ZrO_2

The kinetic parameters of crystal growth in amorphous ZrO_2 films for laser and ion-plasma condensates are given in Table 8.2.

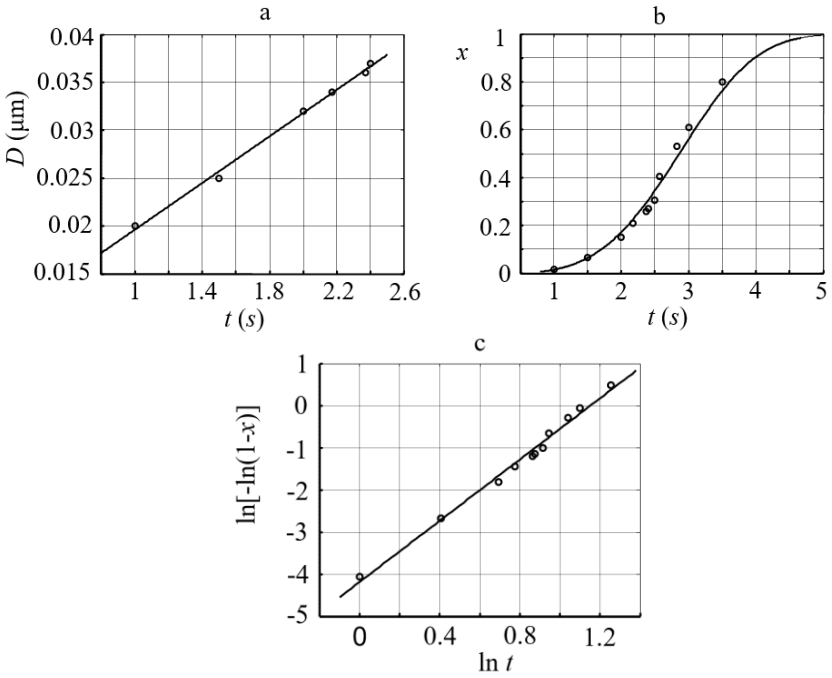

Fig. 8.8. The dependence on time of the average diameter <*D*> (a), crystallized volume fraction $x(t)$ in coordinates x - t (b) and in in coordinates $\ln[-\ln(1-x)]$ - $\ln t$ (b)

Table 8.2 - Parameters of the electron beam induced crystallization of amorphous ZrO_2 films*

Parameter	Laser evaporation	Ion-plasma evaporation
v, μm/s	0.110	0.012
β, cm^{-2}	7.5×10^8	1.3×10^{10}
n	2.03	3.63
k	0.051	0.015
t_0, s	4.331	3.180
D_0, μm	0.486	0.045
δ_0	950	88

*v is the tangential growth rate of ZrO_2 crystals in an amorphous film, β is the density of crystallization nuclei, n and k are the kinetic parameters of crystallization, t_0 is the characteristic time unit, and D_0 is the characteristic length unit, δ_0.is the relative length.

According to the video recording data (Fig. 8.5 and 8.7) during crystallization of the film multiple crystals grows in the field of observation. Nucleation happens only at the beginning and growth takes place afterwards. The density of crystallization nuclei $\beta \sim 7.5 \cdot 10^8$ cm^{-2} for laser condensates and $\beta \sim 1.3 \cdot 10^{10}$ cm^{-2} for ion-plasma condensates. Each crystal grows at the constant rate at the constant intensity of electron beam irradiation of the film. This nucleation mechanism would be identified as a Site-Saturate Nucleation (SSN) [168]. In this case $<D> \sim t$ and $x(t)=1-\exp(-kt^n)$.

For laser condensates of ZrO_2 the Avrami exponent n = 2.03 (two-dimensional growth). For ion-plasma condensates of ZrO_2 the Avrami exponent n = 3.63, which may indicate the formation of crystals throughout the entire volume of the amorphous film (three-dimensional growth).

These structural and morphological characteristics in conjunction with numerical data on relative length δ_0 qualitatively and quantitatively indicate the implementation of the IPC mode in ZrO_2.

8.2. Amorphous films of antimony selenide

Antimony selenide (Sb_2Se_3) belongs to the narrow-gap semiconductors of the V_2VI_3 group and has a structure similar to Sb_2S_3 [169]. The compound has an orthorhombic lattice with parameters a = 1.163 nm, b = 1.178 nm, c = 0.3985 nm [170]. It is a promising photoelectric absorbing material due to its high electro-optical properties [171-174] and can be used for the creation of thin-film solar cells [172, 173]. It was reported that at annealing of Sb_2Se_3 a-c phase transition occurs at 423 K [170].

8.2.1. Preparation and structure of films

Amorphous films of antimony sulfide with layer thicknesses $h \approx 30$ nm were grown on the cleaved (001) face of KCl single crystals at room temperature by thermal evaporation at the pressure better, than 10^{-6} Torr. The starting material was a high purity ingot of Sb_2Se_3. Evaporation was carried out during rapid heating of the tantalum crucible by passing a pulse of electric current.

Films were separated from the substrate in distilled water and transferred onto subject grids for electron microscopy studies. Homogeneous areas of amorphous film with a uniform electron-microscopic thickness contrast were studied. The correspondence of their composition to the stoichiometric one was controlled by the nature of its crystallization and the results of decoding of the selected area electron diffraction (SAED) patterns of the crystallized sections of the film.

Features of the a-c phase transformation were studied by electron diffraction and transmission electron microscopy (TEM) at the accelerating voltage of 100 kV. Crystallisation was initiated by the electron beam impact inside the column of the electron microscope. This made it possible to register the structural transformations “in situ”. The radiation dose rate was estimated from the beam current and the diameter of the electron beam focused at the sample. At a current of 20 μA and a diameter of 5 μm the radiation dose rate was ~ $6 \cdot 10^4$ $e^-/Å^2 \cdot s$.

At the initial state the film of Sb_2Se_3, deposited on the substrate at room temperature, was amorphous. This is evidenced by three diffuse halos at the electron diffraction pattern at Fig. 8.9a. The second halo is intense, while the first and third are much weaker in the intensity and very diffuse. The positions of the maxima of the first, second and third diffuse halo correspond to interplanar distances of 0.5, 0.3 and 0.2 nm of the object under study respectively.

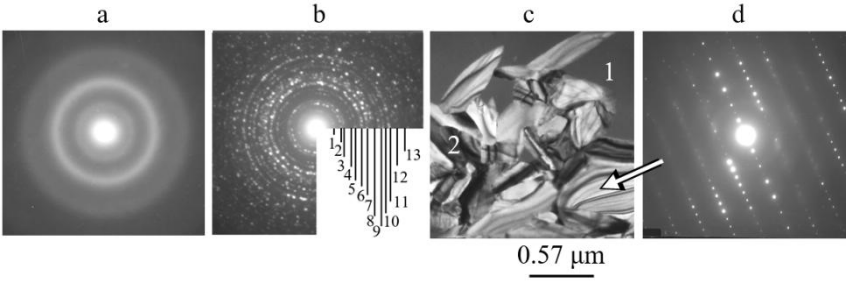

Fig. 8.9. Crystallization of the amorphous Sb_2Se_3 film: a - electron diffraction pattern at the initial state; b - the same after partial crystallization by the electron beam; c - TEM image of the partially crystallized film (1-amorphous phase, 2-crystalline phase); d - SAED pattern from one of the grains of Sb_2Se_3

Fig. 8.9b show the electron diffraction pattern of the same film after its partial electron beam crystallization. The film is two-phase: amorphous and polycrystalline components. TEM image of the partially crystallized film (1-amorphous phase, 2-crystalline phase) and SAED pattern from one of the grains of Sb_2Se_3 are presented at Fig. 8.9c and 8.9d respectively.

The results of the decoding of the electron diffraction pattern presented at Fig. 8.9b are summarized at Table 8.3. Correspondence between experimental and literature data [169, 170] was observed. The absence of

reflections, associated with Sb and Se indicates on the one-stage of the polymorphous a-c transformation in Sb_2Se_3.

Table 8.3 - Results of the decoding of the electron diffraction pattern at Fig. 8.9b

Diffraction ring number	*d* (nm)	*hkl*	Data [169] *d* (nm)	Data [170] *d* (nm)
1	0.826	110	0.828473	0.8280
2	0.585	020	0.589384	0.5890
3	0.521	120	0.526006	0.5250
4	0.416	220	0.414212	0.414
5	0.369	310	0.368730	0.3682
6	0.316	211	0.316357	0.3162
7	0.282	221	0.286798	0.2868
8	0.252	321	-	0.2513
9	0.228	510	-	0.2282
10	0.213	520	0.216460	0.2164
11	0.198	002	0.198935	0.1989
12	0.195	600	0.193782	0.1938
13	0.171	360	-	0.1752

8.2.2. Crystal growth and kinetics of a-c transformations

Fig. 8.10 show video frames of crystals growth in an amorphous film of Sb_2Se_3. Based on the frame-by-frame analysis of this videos, the dependences on time *t* of the number density of crystals *N* was obtained.

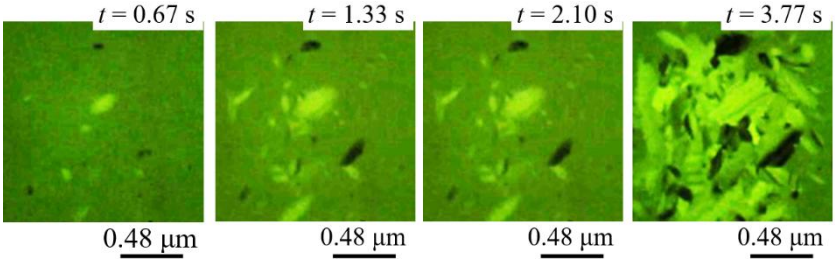

Fig. 8.10. Video frames of crystal growth in amorphous films of Sb_2Se_3 at electron beam irradiation. Time moments t, that has passed from the beginning of the recording of the crystallization process, are shown in the upper right corner of each frame

At a fixed electron dose rate N increases linearly with time. The dependence $N(t)$ is shown at Fig. 8.11a. Straight line correspond to the equation:

$$N = 7.41 \cdot 10^8 t + 1.63 \cdot 10^7 \text{ cm}^{-2}, \quad (8.7)$$

where t is measured in seconds. According to (8.7) the nucleation rate $\alpha = 7.41 \cdot 10^8 \text{ cm}^{-2}\text{s}^{-1}$.

The dependences on time of the average crystal diameter $\langle D \rangle$ and of maximum crystal diameter D_{max} are shown at Fig. 8.11b by the lines 1 and 2 respectively. Straight lines correspond to the equations:

$$\langle D \rangle = 0.052t + 0.037 \text{ μm}, \quad (8.8a)$$

$$D_{max} = 0.173t + 0.056 \text{ μm}. \quad (8.8b)$$

According to (8.8a) the average tangential crystal growth rate $\langle v_\tau \rangle = 0.052 \text{ μm} \cdot \text{s}^{-1}$ and maximum tangential crystal growth rate according to

(8.8b) $v_{\tau max} = 0.173$ μm·s^{-1}. Thus, the average crystal growth rate $\langle v_\tau \rangle$ is more than three times less than the $v_{\tau max}$. Data relating to α, $\langle v_\tau \rangle$ and $v_{\tau max}$ are given in Table 8.4.

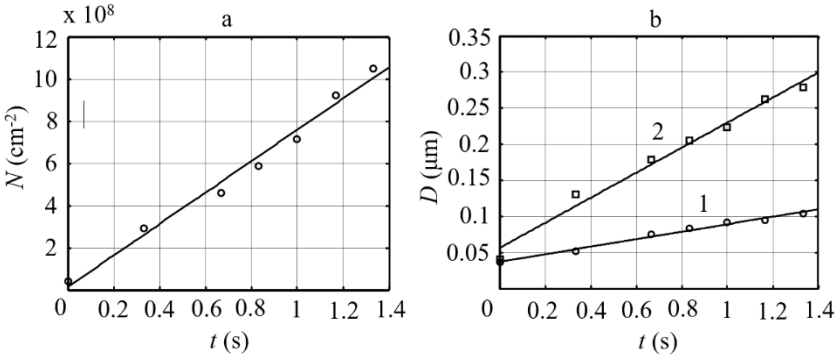

Fig. 8.11. The dependence on time of the number density of crystals N (a) and of their diameters D (b) in amorphous Sb_2Se_3 film. 1 - average diameter $\langle D \rangle$. 2 - maximum diameter D_{max}

The distributions of crystal sizes D in amorphous Sb_2Se_3 film at times t= 0.67 s (Fig. 8.10a) and t = 1.33 s (Fig.10b) after beginning of the recording of a-c process are shown at Fig. 8.12a and 8.12b respectively. The histogram data indicate an increase over time in both asymmetry and kurtosis in the distribution of crystal diameters. At t = 0.67 s the asymmetry coefficient is 2.08, kurtosis is 6.50 and $\langle D \rangle$=0.085 μm. Similar data for the distribution at t=1.33 s are: asymmetry coefficient is 2.19, kurtosis is 8.60 and $\langle D \rangle$ = 0.091 μm.

Time dependence of the crystallized volume fraction $x(t)$ is shown at Fig. 8.13a. This experimental data, presented in the coordinates ln[-ln(1-x)] - ln$t$, form a straight line (Fig. 8.13b):

$$\ln [-\ln (1-x)] = 2.16 \ln t - 2.44 \qquad (8.9)$$

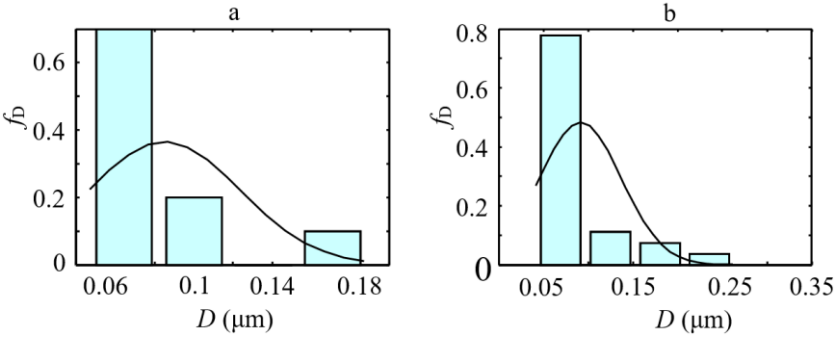

Fig. 8.12. Histograms of the relative frequencies f_D of the crystals diameters D in amorphous film of Sb_2Se_3 at times t = 0.67 s (a) and t = 1.33 s (b) after beginning of the recording of a-c process and the curve, corresponding to the Gaussian distribution

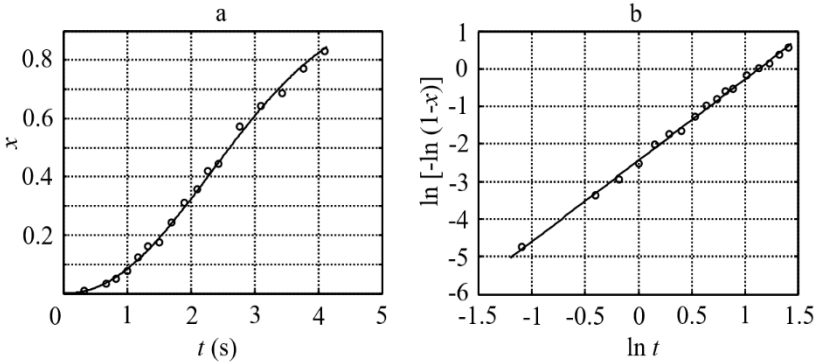

Fig. 8.13. The dependence on time of the crystallized volume fraction $x(t)$ in amorphous Sb_2Se_3 film in coordinates x - t (a) and in coordinates ln[-ln(1-x)] – ln t (b)

This fact indicates the applicability to the process of a-c phase transformation of the JMAK formulas (7.7). According to (8.9) and Fig. 8.13b n = 2.16, $\ln k$ = -2.44 and k = 0.087 s^{-2}. The case α = const and $\langle v_\tau \rangle$ = const corresponds to the α-version of Kolmogorov's model [156]. This is the case of the continuous nucleation, when the system keeps adding nuclei with the same rate over the entire transformation period [174]. Data relating to n and k are given in Table 8.4.

Table 8.4 - crystallization parameters of amorphous films of Sb_2Se_3*

$\langle v_\tau \rangle$ (μm/s)	0.052
$v_{\tau max}$ (μm/s)	0.173
t_0 (s)	3.10
D_0 (μm)	0.20
n	2.16
k (s^{-2})	0.087
α ($cm^{-2} \cdot s^{-1}$)	$7.41 \cdot 10^8$
δ_0	245

* $\langle v_\tau \rangle$ is the average tangential growth rate of the crystals, $v_{\tau max}$ is the maximum tangential crystal growth rate, t_0 is the characteristic time unit, D_0 is the characteristic length unit, n is the Avrami exponent, k is the rate constant, α is the nucleation rate, δ_0 is the relative length.

Taking into account numerical values of n and k, the curve at Fig. 8.13a will fit the equation[175]:

$$x = 1\text{-}\exp(-0.087t^{2.16}). \qquad (8.10)$$

If during a-c transformation the fraction of the amorphous phase decreases by a factor of e = 2.72, then the fraction of the crystalline phase x = 0.632. When for a film the fraction of the crystalline phase x = 0.632, according to (8.10) characteristic unit of time t_0 = 3.10 s. For this value according

to (8a) the characteristic unit of the length $D_0 \approx 0.20$ μm. For Sb_2Se_3 the volume of unit cell $\Omega = 546.09 \cdot 10^{-12}$ μm^3 [170]. In this case, according to (4.4) the relative length $\delta_0 \approx 245$ (Table 8.4).

Polycrystalline film forms at the constant crystal growth rate and constant nucleation rate corresponding to the α - version of the Kolmogorov model (continuous nucleation process). The Avrami exponent $n = 2.16$ (the nearest integer is 2) and the relative length $\delta_0 \approx 245$.

This value of n and δ_0 for Sb_2Se_3 films with a thickness $h = 30$ nm correlates well with the data of work [176] for Sb_2Se_3 films with $h = 25$ nm ($n = 2.20$, $\delta_0 \approx 183$) and $h = 40$ nm (n = 2.14, $\delta_0 \approx 489$). They are typical for the crystallization process in which the grain growth occurs with nucleation. These structural and morphological characteristics in conjunction with numerical data on relative length δ_0 qualitatively and quantitatively indicate the implementation of the IPC mode in Sb_2Se_3.

8.3. Kinetics of electron beam crystallization of amorphous films of Yb_2O_2S

8.3.1. Material, methods and structure

Films with layer thicknesses $h = 20$-50 nm were grown on a cleaved (001) face of KCl single crystals by the electron beam evaporation method [177]. Condensation of matter was carried out in an oil-free vacuum system on the substrates at room temperature. Starting material of high purity YbS was used. The background pressure during evaporation in the vacuum chamber was between 10^{-6}-10^{-7} Pa. The film thickness was controlled in situ by calibrated quartz resonator. Quartz was calibrated according to X-ray reflectometry for a series of single-layer films. The error in determining of the film thickness $\Delta h = 0.5$ nm. The rate of film growth was in the range 0.5 - 1.0 nm·s^{-1}.

The deposited films were separated from the substrate in distilled water and transferred onto subject grids for electron microscopy studies. They were crystallized on the object grids in vacuum both under thermal ("furnace" annealing on a copper plate) and electron beam (in a microscope column) influence. In the latter case the rate of crystallization was controlled by varying the

density j of the electron current through the sample, which was varying in the range from 1.1 to 6.5 $A \cdot mm^{-2}$ depending on the electron beam focusing.

The structural analysis was carried out by the methods of electron diffraction and transmission electron microscopy on EM-100L and PEM-100-01 electron microscopes operating at the accelerating voltage of 100 kV. The process of crystallization of the film was recorded from the screen of the electron microscope with a Canon Power Shot G15 camera in the video recording mode at the frame rate of 30 s^{-1}

Fig. 8.14 illustrates the electron beam crystallization of the amorphous film, obtained by electron beam evaporation in vacuum of YbS target. According to the SAED pattern at Fig. 8.14a, the film is amorphous at the initial state. This is evidenced by three diffuse halos at the electron diffraction pattern. The first halo is intense, while the second and third are much weaker in the intensity and very diffuse. The action of the electron beam initiates in it the growth of crystals, as evidenced by the SAED pattern and electron microscope image, shown at Fig. 8.14b and 8.14c respectively. The result of decoding of the SAED pattern, presented in Fig. 8.1b, is summarized in Table 8.5.

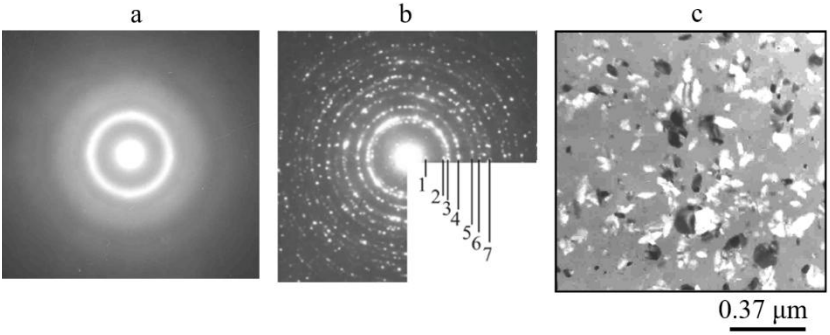

Fig. 8.14. Electron-beam crystallization of the amorphous Yb_2O_2S film: SAED pattern of the initial state (a) and after partial crystallization of the same place of the film (b); electron microscopic image of the film after partial crystallization (c)

Table 8.5 - Results of the decoding of the electron diffraction pattern at Fig. 8.14b

Diffraction ring number	*d* (nm)	hkl, phase	Data [178] *d* (nm)
1	0.643	001- Yb_2O_2S	0.650
2	0.323	002 - Yb_2O_2S	0.324
3	0.289	101 - Yb_2O_2S	0.2887
4	0.228	102 - Yb_2O_2S	0.2287
5	0.186	110 - Yb_2O_2S	0.1861
6	0.164	200 - Yb_2O_2S	0.1613
7	0.146	105 - Yb_2O_2S	0.1450

The interplanar distances *d*, calculated from the measured ring diameters, were compared with the data from literature. Correspondence between the experimental and the literature data was observed only for Yb_2O_2S (ytterbium oxide sulfide) hexagonal modification with unit cell parameters $a = 0.3722$ nm and $c = 0.6496$ nm [178]. The formation of Yb_2O_2S is due to the oxidation of the YbS film when it was separated from the substrate in distilled water.

8.3.2. Kinetics of Yb_2O_2S crystals growth in amorphous film

Fig. 8.15 show video frames of crystals growth in amorphous film of Yb_2O_2S [179]. Based on the frame-by-frame analysis of this videos, the dependences on time *t* of the number density of crystals *N* was obtained. At a fixed electron dose rate *N* increases linearly with time. The dependence $N(t)$ is shown at Fig. 8.16a. Straight line correspond to the equation:

$$N = 3.93 \cdot 10^8 t + 9.54 \cdot 10^7 \text{ cm}^{-2}, \quad (8.11)$$

where *t* is measured in seconds. According to (8.11) the nucleation rate $\alpha = 3.93 \cdot 10^8$ $\text{cm}^{-2}\text{s}^{-1}$.

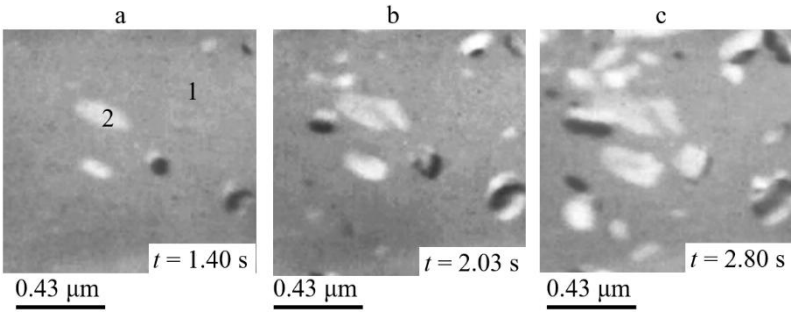

Fig. 8.15. Video frames of crystal growth in amorphous films of Yb_2O_2S at electron beam irradiation. Time moments t, that has passed from the beginning of the recording of the crystallization process, are shown in the lower right corner of each frame [179]

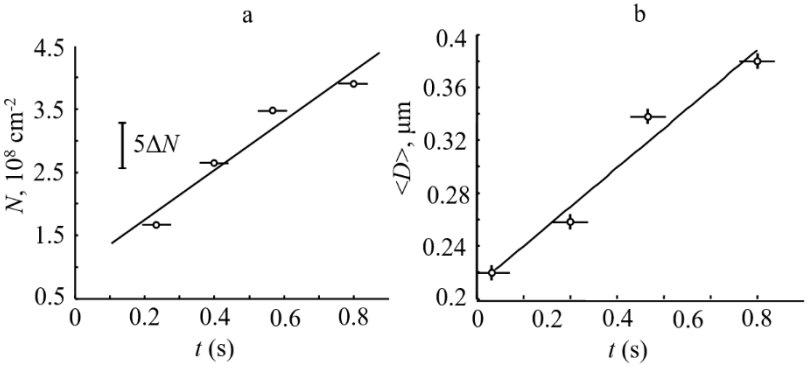

Fig. 8.16. The dependence on time of the number density of crystals N (a) and of their average diameters $\langle D \rangle$ (b) in amorphous Yb_2O_2S film

The dependence on time of the average crystal diameter $<D>$ is shown at Fig. 8.16b. A linear dependence takes place:

$$<D> = 0.297t+0.150 \text{ μm}, \tag{8.12}$$

where t is measured in seconds. According to (8.12) the average tangential crystal growth rate $<v_\tau> = 0.297$ μm·s^{-1}.

Time dependence of the crystallized volume fraction $x(t)$ is shown at Fig. 8.17a. This experimental data, presented in the coordinates ln[-ln(1-x)] - ln$t$, form a straight line (Fig. 8.17b):

$$\ln[-\ln(1-x)] = 1.8\ln t - 0.7. \tag{8.13}$$

This fact indicates the applicability to the process of a-c phase transformation of the JMAK formulas (7.7).

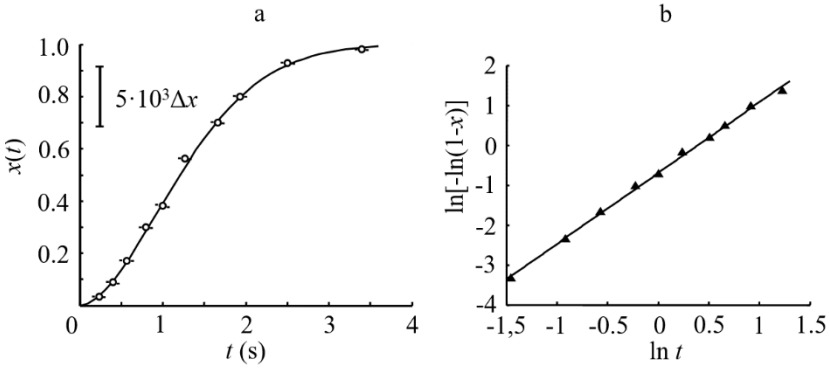

Fig. 8.17. The dependence on time of the crystallized volume fraction $x(t)$ in amorphous Yb_2O_2S film in coordinates x - t (a) and in coordinates ln[-ln(1-x)] – ln t (b)

According to (8.13) and Fig. 8.17b n =1.8, ln$k$ = -0.7 and k = 0.5 s^{-k}. The case α = const and $<v_\tau>$ = const corresponds to the α-version of Kolmogorov's model [156]. This is the case of the continuous nucleation, when the system keeps adding nuclei with the same rate over the entire transformation period [174]. Data relating to n and k are given in Table 8.6.

Table 8.6. Ccrystallization parameters of amorphous films of Yb_2O_2S*

$<v_\tau>$ (μm/s)	0.297
t_0 (s)	1.47
D_0 (μm)	0.44
n	1.8
k	0.5
α ($cm^{-2}\cdot s^{-1}$)	$3.93\cdot10^8$
δ_0	1000

*$<v_\tau>$ is the average tangential growth rate of the crystals, $v_{\tau max}$ is the maximum tangential crystal growth rate, t_0 is the characteristic time unit, D_0 is the characteristic length unit, n is the Avrami exponent, k is the rate constant, α is the nucleation rate, δ_0 is the relative length.

Taking into account numerical values of n and k, the curve at Fig. 8.17a will fit the equation:

$$x = 1\text{-}\exp(-0.5t^{1.8}), \qquad (8.14)$$

where t is measured in seconds.

When the fraction of the crystalline phase x = 0.632, according to (8.14) characteristic unit of time t_0 = 1.47 s. And the characteristic unit of the length $D_0 = <v_\tau>t_0 \approx 0.44$ μm. For Yb_2O_2S the volume of unit cell $\Omega=7.793\cdot10^{-11}$ μm^3 [178]. In this case, according to (4.4), the relative length is

$\delta_0 \approx 1000$. This value of n and δ_0 for Yb_2O_2S films are typical for the crystallization process in which the grain growth occurs with nucleation. These structural and morphological characteristics in conjunction with numerical data on relative length δ_0 qualitatively and quantitatively indicate the implementation of the IPC mode in films of Yb_2O_2S.

8.3.3. Crystallization of Yb_2O_2S films at thermal annealing

Fig. 8.18 illustrates the effect of film thickness h on the fraction of the crystalline phase x at crystallization of amorphous Yb_2O_2S upon thermal annealing in vacuum (180 min at 575ºC). At this temperature, films of thickness with $h \approx 20$ nm remain amorphous. Crystallization occurs at $h \geq 25$ nm. The fraction of the crystalline phase in the film increases with the growth of film thickness and on the level of higher than 50 nm is equal to 1 (Fig. 8.18c).

Graphically the dependence of the fraction of the crystalline phase x on the film thickness h is presented in Fig. 8.18d. The straight line was plotted by the data of x measurements using the least-squares technique. A linear dependence takes place:

$$x = 0.032h - 0.637, \tag{8.15}$$

where x is measured in nm.

The stabilization of the amorphous state at the small layer thicknesses was previously observed during electron-beam crystallization of amorphous Cr_2O_3 and V_2O_3 films [101]. The results, obtained for Yb_2O_2S, are additional confirmation of the fact, that the stability of the amorphous state decreases with increasing of the film thickness [143, 180, 181]. In [182] was found for $Ge_2Sb_2Te_5$ (GST), N-doped GST, $Ge_{15}Sb_{85}$, Sb_2Te, and Ag- and In-doped Sb_2Te that the crystallization temperature increases as the film thickness is reduced below 10 nm.

The slowdown of crystallization at decreasing of the film thickness can be connected with increasing of the surface energy during crystallization. In addition, crystallization is associated with overcoming of the activation barrier

that separates the amorphous and crystal states. The height of the barrier increases with decreasing of the film thickness.

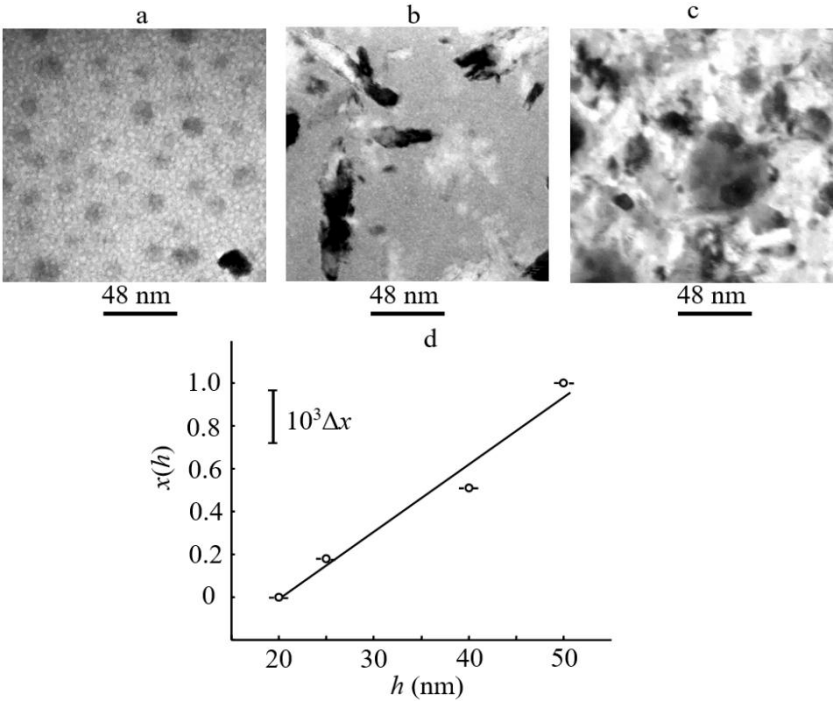

Fig. 8.18. The effect of thickness h on the crystallization of amorphous films of Yb_2O_2S upon thermal annealing in vacuum (180 min at 575ºC): h = 25 nm (a); h = 40 nm (b); d = 50 nm (c). The dependence of the fraction of the crystalline phase x on the film thickness h (d).

9. DENDRITE POLYMORPHOUS CRYSTALLIZATION MODE OF HfO_2

Films and coatings of hafnium dioxide (HfO_2) are widely used in engineering owing to their high values of its dielectric constant, refractive index, neutron absorption cross section, and thermal stability (melting point ~2800°C) [183]. Amorphous gate insulators are usually desirable since they can effectively reduce the problems arising from the crystal orientation, grain boundary, and the lattice mismatch at the interfaces [184].

The monoclinic modification of HfO_2 is stable up to 2196 K. Its structural data presented in the tables of the International Centre for Diffraction Data (JCPDC) are as follows: a=0.51157 nm, b=0.51819 nm, c=0.52851 nm, and $\beta = 99.259°$ [185]. At above 1923 K, this modification transforms into the tetragonal modification with parameters a=0.514 nm and c=0.525 nm [186]. The orthorhombic modification of HfO_2 has the following parameters: a=0.5008 nm, b=0.5062 nm, and c=0.5223 nm [187].

9.1. Sample preparation and structural changes in films during annealing

9.1.1. Experimental

We grew films by pulsed laser sputtering of hafnium in an oxygen atmosphere. A vapor-plasma flow was deposited onto both orienting single crystal KCl (001) substrates and neutral KCl substrates covered with a thin layer of amorphous carbon. We used the pulsed nanosecond radiation of a Q-switched laser operating at a wavelength of 1.06 μm. The radiation was introduced into an evaporation chamber and focused onto a rotating target made of high purity Hf plates. The laser pulse repetition frequency was 25 Hz. The film thickness was varied in the range 28-30 nm, and the substrate temperature was varied in the range T_s = 290 - 700 K. An Hf target was sputtered in an oxygen flow at a pressure $P(O_2) \sim 0.13$ Pa. The structures of the films were studied by

electron diffraction and transmission electron microscopy (TEM) using EM-100L and PEM-100-01 electron microscopes operating at an accelerating voltage of 100 kV. Phase transformations in the films were initiated by the following methods:

(1) thermal heating of a film on a supporting grid in an air atmosphere in a muffle furnace,

(2) vacuum annealing in the column of an electron microscope using the special-purpose heating attachment of the EM-100L microscope,

(3) radiation action of a high-intensity electron beam in vacuum (microscope column) on a local region of the film.

9.1.2. Structure and phase state of condensed films

Depending on substrate temperature T_s, the deposition of a Hf vapor plasma flux in an oxygen atmosphere was found to result in the formation of the following structure-phase states. Amorphous films form in the range T_s = 290-360 K. An increase in the condensation temperature initiates the formation of a crystalline HfO_2 phase in a film. The nuclei of a crystalline HfO_2 phase of size $D \approx 10$ nm were revealed by TEM in an amorphous matrix at $T_s = 370$ K. The precipitate size and the volume fraction of the crystalline phase increase monotonically with *Ts*.

Figures 9.1a and 9.1b show the electron diffraction pattern and electron microscopic image, respectively, of a two-phase film deposited at $T_s = 410$ K [188]. The average crystallite size in an amorphous matrix is $\langle D \rangle \approx 60$ nm. The results of identification of the electron diffraction pattern at Fig. 9.1a are given in the table 9.1. As follows from these data, the crystalline phase in the film is represented by the tetragonal and monoclinic modifications of HfO_2. The type and arrangement of the reflections in the electron diffraction pattern indicate that the crystals of the monoclinic modification of HfO_2 have no preferred orientation with respect to the KCl (001) substrate. However, crystals of the tetragonal modification of HfO_2 grow in an orientation parallel to the substrate, and the orientation relationship (9.1) holds true:

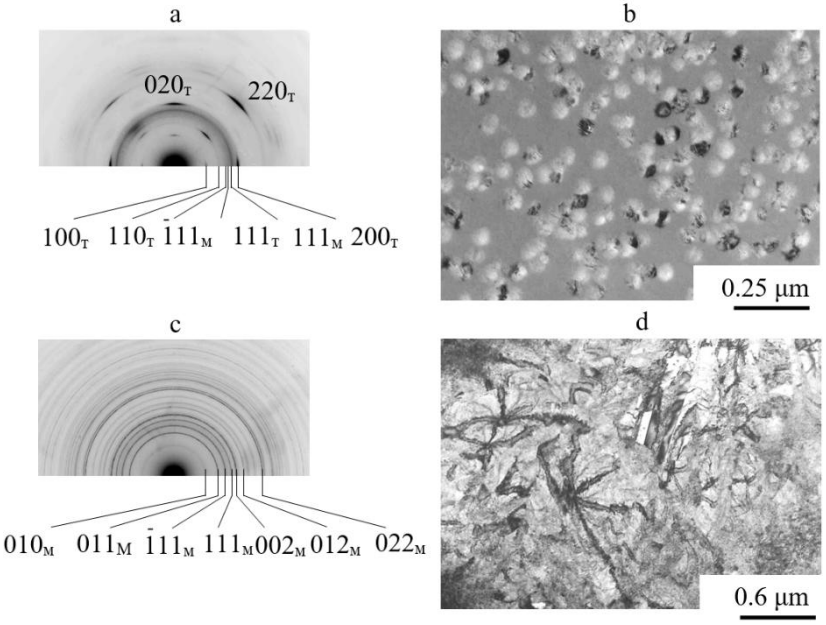

Fig. 9.1. Structures of the films deposited by pulsed laser sputtering of a Hf target in an oxygen atmosphere: (a, b) electron diffraction pattern and electron microscopic image of the HfO_2 film deposited at T_s = 410 K; (c, d) electron diffraction pattern and electron microscopic image of the HfO_2 film deposited at T_s = 290 K after air annealing at 770 K for 20 min. The contrast in the electron diffraction patterns is inverted [188]

$$[100](001)\ HfO_2\ //\ [100](001)\ KCl. \qquad (9.1)$$

The zone axis of the crystals corresponds to the [001] HfO_2 direction.

Table 9.1. Results of electron diffraction analysis of the films deposited by pulsed laser sputtering of an Hf target in an oxygen atmosphere*

№	Deposition at T_s = 410 K				Deposition at T_s = 290 K and air annealing at 770 K		
	d, nm	*hkl*	*d*, nm T-phase [186]	*d*, nm M-phase [185]	*d*, nm	*hkl*	*d*, nm M-phase [185]
1	0.5145	$(100)_T$	0.5140		0.5190	$(010)_M$	0.5182
2	0.3627	$(110)_T$	0.3635		0.3693	$(011)_M$	0.3676
3	0.3177	$(\bar{1}11)_M$		0.3147	0.3178	$(\bar{1}11)_M$	0.3147
4	0.3010	$(111)_T$	0.2988		0.2840	$(111)_M$	0.2823
5	0.2853	$(111)_M$		0.2823	0.2606	$(002)_M$	0.2608
6	0.2552	$(200)_T$	0.2555		0.2333	$(012)_M$	0.2330
7	0.2301	$(120)_M$		0.2305	0.2182	$(102)_M$	0.2179
8	0.1808	$(220)_T$	0.1811		0.2020	$(112)_M$	0.2008
9	0.1623	$(310)_T$	01623		0.1847	$(022)_M$	0.1838
10	01552	$(311)_T$	0.1546		0.1813	$(220)_M$	0.1808
11					0.1682	$(202)_M$	0.1683
					0.1649	$(013)_M$	0.1648

*T stands for the tetragonal HfO_2 phase and M for the monoclinic HfO_2 phase.

The absence of a preferred orientation in the crystals of the monoclinic modification of HfO_2 and its presence in the crystals of the tetragonal modification of HfO_2 point to different distributions of these phases across the film thickness. Most crystals of the tetragonal modification of HfO_2 form near the KCl (001) substrate and undergo its orientation effect. The crystals of the monoclinic modification of HfO_2 form at the later stages of film formation near the free film surface. They do not undergo the orienting effect of the substrate, since they are screened by the amorphous HfO_2 layer. The orienting effect of the KCl (001) substrate also manifests itself in initiating the formation of a crystalline phase in the film.

The passivation of the KCl (001) surface by an amorphous carbon layer prevents the formation of a crystalline phase in the film. The amorphous HfO_2 film forms on the surface of amorphous carbon at the same temperature (T_s =

410 K). At $T_s \geq 640$ K, a crystalline HfO_2 film forms and the tetragonal phase of HfO_2 retains orientation relationship (9.1).

9.1.3. Phase transformations at annealing of the films

The conditions of annealing of the amorphous laser condensates determine the structure and phase composition of the HfO_2 films. Figures 9.1c and 9.1d show the electron diffraction pattern and electron microscopic image respectively of the HfO_2 film deposited at T_s = 290 K after air annealing (in a muffle furnace) at 770 K for 20 min.

The results of identification of the electron diffraction pattern are given in the Table 9.1. After annealing, the crystalline phase in the film consists of the monoclinic modification of HfO_2. The type and arrangement of the reflections in this electron diffraction pattern (Fig. 9.1c) indicate that the crystals of the monoclinic modification of HfO_2 form a polycrystalline film without a preferred orientation. A similar result was obtained upon thermal annealing of the amorphous film in vacuum in the column of an electron microscope.

Another picture was observed during the radiation action of an electron beam on a local region in the amorphous film: the crystallization of the amorphous layer was accompanied by the formation of both the monoclinic and orthorhombic modifications of HfO_2. We revealed two versions of crystallization. In both cases, the monoclinic modification of HfO_2 was found to dominate at the final stage of transformation [189].

The one-stage transformation proceeds without a change in the type of the crystal lattice of a growing nucleus. An HfO_2 crystal with a monoclinic structure form in the region irradiated by an electron beam, and a dendrite forms from this crystal in time. All dendrite branches retain a monoclinic structure. Fig. 9.2 shows the electron diffraction pattern (a) and electron microscopic image (b) of a nucleus and the related dendrite with primary and secondary branches. As follows from the electron diffraction pattern, it has the monoclinic lattice, and the zone axis of the crystal is $[10\,\bar{1}]$ HfO_2.

Fig. 9.2c shows an electron microscope image of dendrite HfO_2, formed by non-crystallographic branches of various orders. The first order branches are localized within the AOB and COD sectors. Breaks in the bend extinction contours at the boundary of the branches indicate the presence of a misorientation between the branches, i.e. the branches are non-crystallographic. Branches of the second and higher orders are localized inside the BOC and AOD sectors with an angle γ at the apex at point O.

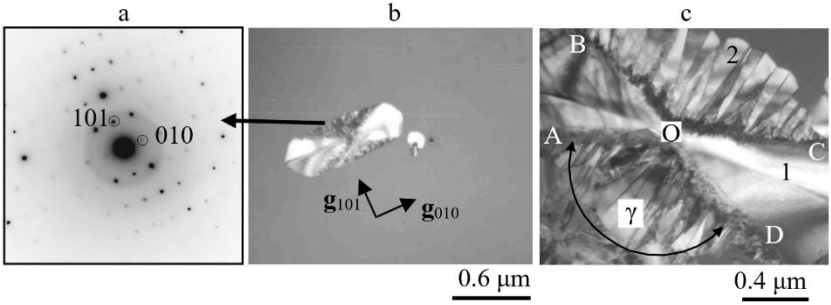

Fig. 9.2. One-stage electron beam crystallization of amorphous HfO_2 deposited at T_s = 290 K: SAED pattern of a crystalline HfO_2 nucleus of the monoclinic modification (a); electron microscopic images of the nucleus and dendrite with primary (1) and secondary (2) branches (b, c) [189]. The contrast at the SAED pattern is inverted

The two-stage transformation is accompanied by a change in the type of the crystal lattice of a growing nucleus. Fig. 9.3 shows the electron diffraction pattern and electron microscopic image of two sequential stages of film crystallization.

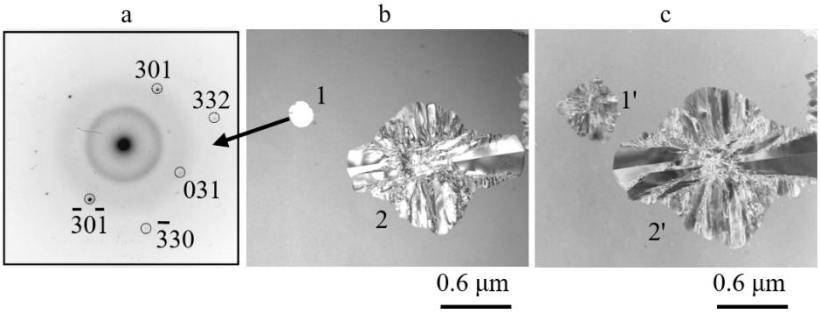

Fig. 9.3. Two-stage electron-beam crystallization of amorphous HfO_2 deposited at T_s = 290 K: SAED pattern of a crystalline HfO_2 nucleus of the orthorhombic modification (a); electron microscopic images of two sequential stages of crystallization (b, c). The contrast at the SAED pattern is inverted

Under the action of an electron beam, disc-shaped crystals of the orthorhombic modification, which are similar to crystal 1 at Fig. 9.3b, nucleate and grow in the film. The electron diffraction pattern of crystal 1 is shown at Fig. 3a. For clarity, weak reflections of the orthorhombic modification of HfO_2 are encircled. These reflections belong to the zone the axis of which is oriented along the [11 $\bar{3}$] direction in the orthorhombic modification. When the crystal size is larger than the critical size (0.1-0.4 μm), et decomposes into blocks (crystal 1' at Fig. 9.3c), from which dendrite branches form. The crystal lattice of the dendrite branches corresponds to the monoclinic modification of HfO_2 (Figs. 3b, 3c; dendrites 2 and 2', respectively) [189].

At the final stage of crystallization, the monoclinic modification, which is represented by HfO_2 dendrites, is predominant. These dendrites form from HfO_2 nuclei of the monoclinic and orthorhombic modifications. In the latter case, a size-phase effect manifests itself: when reaching the critical size (0.1-0.4 μm), an HfO_2 crystal of the orthorhombic modification undergoes a

structural transformation, which is likely to be the martensitic transformation (Fig. 9.4a).

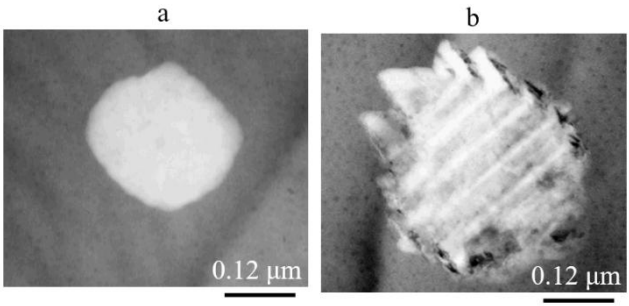

Fig. 9.4. Crystalline HfO_2 nucleus of the orthorhombic modification in an amorphous matrix (a) and plates of the low temperature monoclinic modification in an orthorhombic HfO_2 matrix (b)

The low temperature monoclinic modification of HfO_2 forms as plates or domens in an orthorhombic HfO_2 matrix (Fig. 9.4b) in orientation relation [190]:

$$(30\bar{3})_{or}\,[\bar{1}\,1\,\bar{1}]_{or} \,//\, (\bar{2}\bar{2}\bar{3})_{m}\,[1\,\bar{1}\,0]_{m}. \qquad (9.2)$$

The phase size effect detected in PLD films agrees qualitatively with the data [191] in where a small crystal size was shown to be a factor preventing the transformation of the cubic HfO_2 phase into the monoclinic phase.

9.2. Kinetics of two-stage transformation

The formation of dendrite from a disk-shape HfO_2 crystal of the orthorhombic modification is illustrated by the film frames, shown at Fig. 9.5 [192]. Electron microphotographs at Fig. 9.5a, and 9.5b correspond to a disco-shape crystal. The moment of the beginning of the structural-morphological transformation, when the disk has reached a critical size (D^*~ 0.25 μm) and the contrast of its image has changed dramatically, is depicted at Fig. 9.5c. The successive stages of dendrite formation are shown at fig. 9.5d - 9.5f.

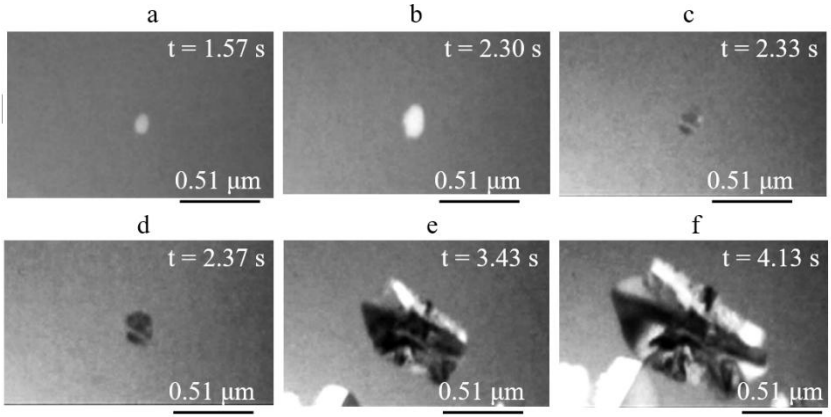

Fig. 9.5. Formation of a dendrite during two-stage crystallization of amorphous HfO_2 film. Time moments t, that has passed from the beginning of the recording of the crystallization process, are shown in the upper right corner of each frame [192]

When moving from a disk-shape crystal to a dendrite, the kinetic characteristics of crystallization also change. Fig. 9.6 shows the kinetic crystallization curves, corresponding to the frames at Fig. 9.5. The dependence of the area of the crystalline phase S at the electron microscopic image on time t is shown at Fig. 9.6a. This crystallization curve in S - t coordinates have the form of parabola (a straight line in the S - t^2 coordinates) with a break at the point t corresponding to the moment, when $D = D^*$:

$$S = \alpha t^2 + \beta; \qquad (9.3a)$$

$$S = \alpha' t^2 + \beta'. \qquad (9.3б)$$

Expression (9.3a) for $D < D^*$ and (9.3b) for $D > D^*$. Wherein $\alpha = 0.01$ $\mu m^2 s^{-2}$, $\alpha' = 0.09$ $\mu m^2 s^{-2}$, $\beta = -6.15 \cdot 10^{-4}$ μm^2 and $\beta' = -0.48$ μm^2.

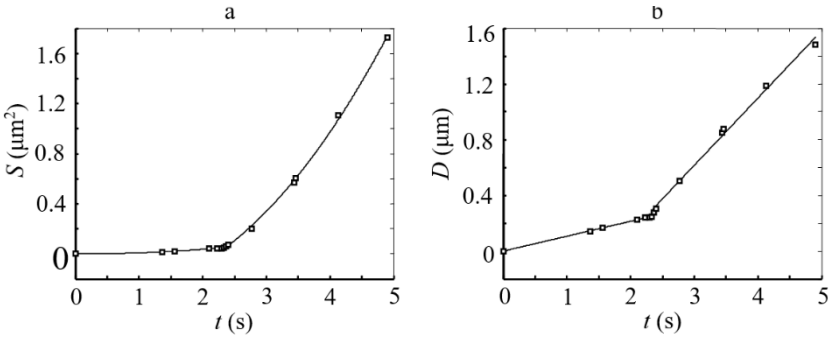

Fig. 9.6. Kinetic curves of two-stage crystallization of amorphous film of HfO_2. The dependence of the area of the crystalline region S on time t (a). The dependence of the diameter of the crystalline region D on time t (b)

The dependence of the diameter D of the crystalline region ($D = (4S/\pi)^{0.5}$) on time t are shown at Fig. 9.6b. While $D < D^*$, the disk-shaped crystals growth with a constant speed v. It was determined by the slope of the straight line to the abscissa axis. After transformation it appreciably increases (more than four times). So, before splitting the growth rate of a crystal v = 0.11 μm·s^{-1}, then after splitting its growth rate v' = 0.48 μm·s^{-1}.

The result of a statistical treatment of measured D^* for a number of crystallization experiments are shown in the form of frequency f histogram at Fig. 9.7. According to this histogram, the average value of the critical diameter $\langle D^* \rangle$ = 0.18 μm.

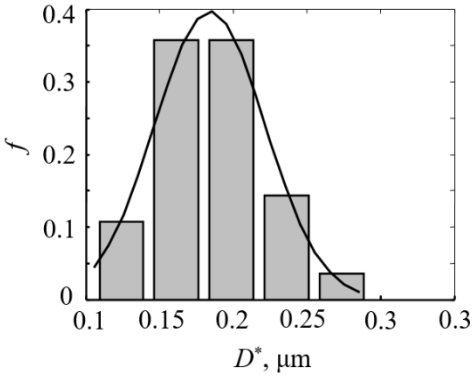

Fig. 9.7. Histogram of the relative frequencies f of the critical diameters D^* of HfO_2 crystals and the curve, corresponding to the Gaussian distribution.

9.3. Kinetics of one-stage transformation

A one-stage phase transformation amorphous phase - dendrite HfO_2 of a monoclinic modification represents several sequential frames of the growth video at Fig. 9.8. The kinetic curves of the dendrite growth are

shown at Fig. 9.9. They correspond to the frames at Fig. 9.8. In the case of one-stage phase transformation the graphs do not contain kinks.

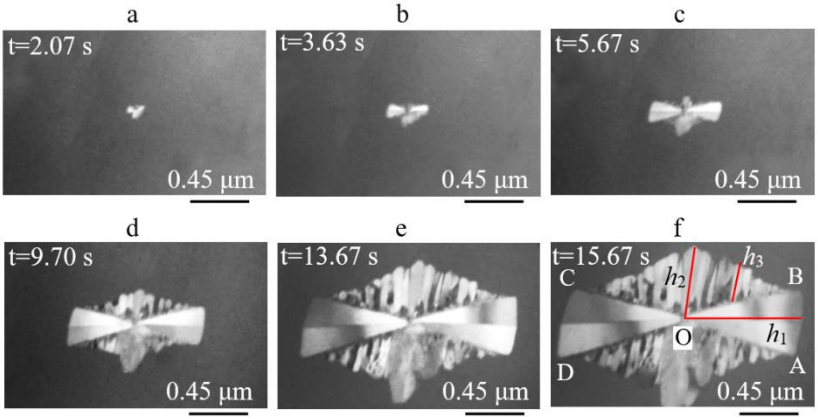

Fig. 9.8. Dendrite formation at one-stage crystallization of amorphous film of HfO_2. Time moments t, that has passed from the beginning of the recording of the crystallization process, are shown in the upper left corner of each frame [192]

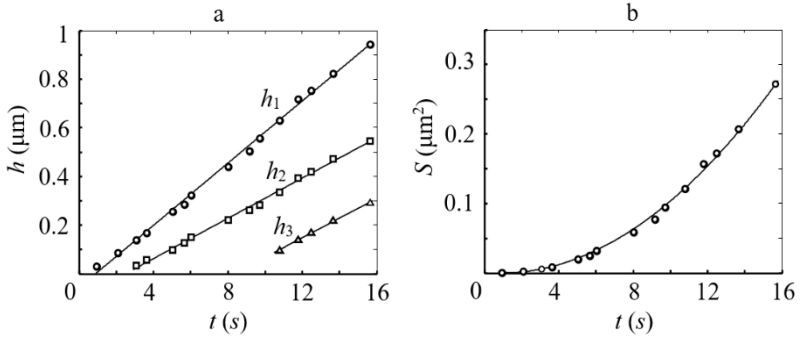

Fig. 9.9. Kinetic curves of one-stage crystallization of amorphous HfO_2 film: a - time dependence of the length of dendritic branches h_1, h_2 and h_3; b - time dependence of the area S of the AOB sector (Fig. 9.8f)

Fig. 9.9a shows the dependence of the length h_1 of the first order dendrite branch and of the length h_2 and h_3 of the second order dendrite branches (Fig. 9.8f) on time t. The increase of h_1, h_2 and h_3 occurs at a constant rate $v_1 = 0.064$ μm·s^{-1}, $v_2 = 0.041$ μm·s^{-1}, $v_3 = 0.040$ μm·s^{-1} respectively. The ratio $v_1 > v_2 > v_3$ shows, that the dendrite branches of the first order grow faster than all. The later the branch appeared, the more slowly it grows. Fig. 9.9b shows the quadratic dependence of the area S of the sector AOB (Fig. 9.95f) on time t.

The dependence on time of the HfO_2 crystals fraction is shown at Fig. 9.10. A quadratic relation takes place:

$$x = 0.0026t^2 - 0.001. \quad (9.4)$$

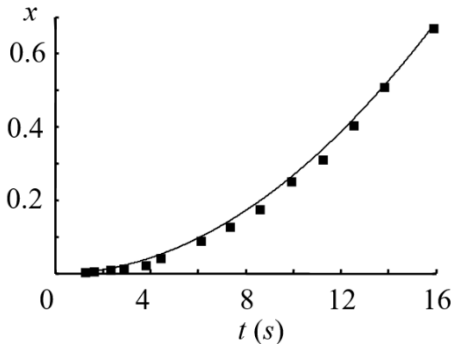

Fig. 9.10. The dependence on time of the crystallized volume fraction $x(t)$ in amorphous HfO_2 film

When x = 0.632, according to (9.3) characteristic unit of time t_0=15.6 s. Whereas the growth rate of the dendrite $v_\tau = 2v_1$, = 0.128 μm·s^{-1}, we get the value $D_0 = 2v_1t_0 \approx 1.99$ μm. Lattice parameters of HfO_2 crystals of monoclinic

modification are as follows: a_0 = 0.51157 nm; b_0 = 0.51819 nm; c_0 = 0.52851 nm; β = 99.259°, and Ω = $1.3828 \cdot 10^{-10}$ μm^3 [185]. According to (4.4) the relative length δ_0 = 3848 (~4000). Relation (4.4) is also applied to the case of DPC mode, since the dendritic branches have different orientations relative to the film surface.

Note that the structural and morphological characteristics of dendritic and layer polymorphic crystallization differ greatly. However, the value of δ_0 in several thousand is fulfilled for both DPC mode and for LPC mode.

9.4. Geometric selection and density changes at DPC mode

9.4.1. Geometric selection

Term "dendrite" can be referred to polycrystalline aggregates, composed of an ensemble of tiny crystals nucleated on one another [193]. During crystallization of amorphous HfO_2 film on the lateral surface of dendrite branches of the first order, crystallographically misoriented branches of the second order ("tiny crystals") arise, on the lateral surface of which the branches of the third order can be generated (Fig. 9.8 and 9.11a). Thus, the lateral surface of the branch of the first order is the surface of the initial crystallization (the "basal surface" [194]) of the branches of the second order, and so on.

A typical dendrite of the monoclinic modification of HfO_2 is shown in Fig. 9.11a. The pairs of the first order dendrite branches forms the sectors AOB and DOC. In the upper left corner of the microphotograph there is the SAED pattern from the crystalline section inside the AOB sector (preferably from branch 1). Most reflexes occupy the positions of the grid nodes, corresponding to the section (-3 1 -4) of the reciprocal lattice of HfO_2 of the monoclinic modification. The rest of the reflections are due to diffraction on the 1' branch, which is disoriented with respect to branch 1. On the right border of the AOB sector along the line OB ("baseline"), which is a trace of the basal flat surface (plane (-1 1 1), crystallographically misoriented branches of the second order are formed.

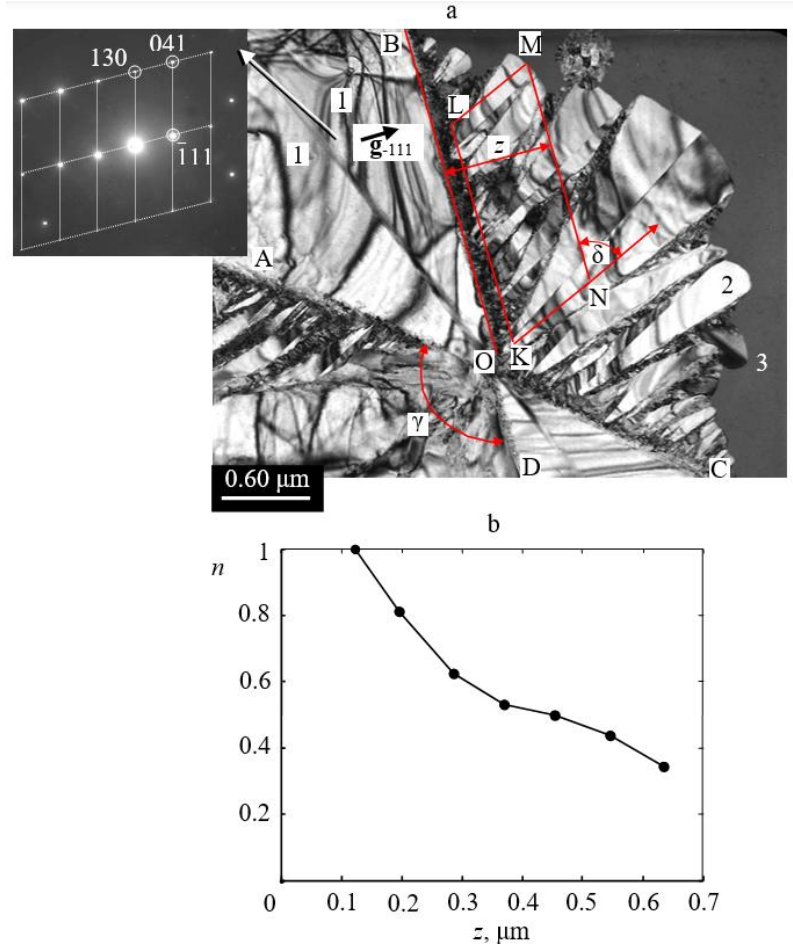

Figure 9.11 - Geometric selection during formation of the dendrite in amorphous HfO_2 film: a - electron microscope image of dendrite with the non-crystallographic axes of the first (1), second (2) and third (3) order. The upper left corner of the micrograph is the SAED pattern from the dendritic branch (1) inside the AOB sector. b - the dependence of the fraction of "surviving" crystals *n* on the distance *z* to the baseline OB at microscope image of dendrite

Branches are formed from a number of randomly oriented crystals in the process of geometric selection [194]. The direction of its highest growth rate in this case form an angle $\delta \approx 58°$ with a baseline line OB.

The graph of the dependence of the fraction of surviving crystals n on the distance z from the baseline OB is shown in Fig. 9.11b. The measurements are carried out inside the parallelepiped KLMN (Fig 9.11a). The left boundary KL is separated from the baseline OB by a distance $x_0 = 0.12$ μm, which ensures a sufficient accuracy of the counting of the number of crystals. The position of the right boundary MN excludes the entry of an amorphous phase into the analyzed region. According to the graph above, the percentage of "surviving" crystals decreases from 100% near the baseline OB to 34% near the boundary MN with the amorphous phase.

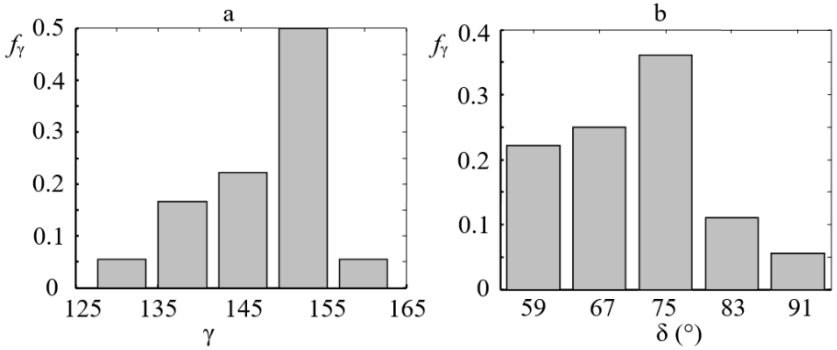

Figure 9.12 - Results of statistical processing of the angular characteristics of dendritic crystals, growing in amorphous HfO_2 films: a - histogram of the relative frequencies f_γ of the values of the angles γ of the growth sectors of dendritic branches of the second order; b – histogram of relative frequencies f_δ of the values of angles δ between the directions of the most rapid growth of dendritic branches and the baseline

During one-stage crystallization of HfO_2, the shape of the dendrites is similar to that, shown at Fig. 9.8 up to contact with other dendrites, growing in amorphous film. The branches of the second and third order are concentrated inside the sectors BOC or AOD with angle γ, the apex of which is at the point O. For the dendrite at Fig. 9.11a this angle $\gamma \approx 130°$.

The results of statistical processing of the revealed values of the angles γ and δ during dendrite crystallization of HfO_2 are shown at Figs. 9.12a and 9.12b respectively. According to the above bar graphs, the average values of the angles $\langle\gamma\rangle = 147°$ and $\langle\delta\rangle = 71°$.

According to [194] the process of geometric selection in a growing aggregate of crystals assumes, that the vector of the highest growth rate is directed along the normal to the basal surface (i.e. $\delta = 90°$). In the case of growth of dendrites of HfO_2 this angle $\delta < 90°$ The reason for the difference is that the base surface is not stationary, but is formed by a moving crystallization front. This leads to a deviation of the highest growth rate of dendrite branches of the second order towards the growth direction of the first-order branch, which forms the basal surface.

9.4.2. Density changes

The relative change of the density during crystallization of amorphous HfO_2 was determined according to (1.2) and (1.4). Figure 9.13 shows the electron microscopy image of the HfO_2 film area before (a) and after (b) its complete crystallization. X_a and X_c are the distances between hardened Hf micro drops before and after film crystallization, respectively.

The results of statistical treatment of measured relative density changes γ during amorphous HfO_2 crystallization are shown in the form of frequency histograms at Fig. 9.13c. The γ distribution is characterized by the corrected root-mean-square deviation of 2.41%, the positive asymmetry of 0.45, and the positive excess of 3.14. For comparison Fig. 9.13c also shows the γ curve corresponding to the Gaussian distribution. At the reliability level of 0.5, the relative density changes during hafnium dioxide film crystallization $\gamma=2.51\pm1.66\%$ [190].

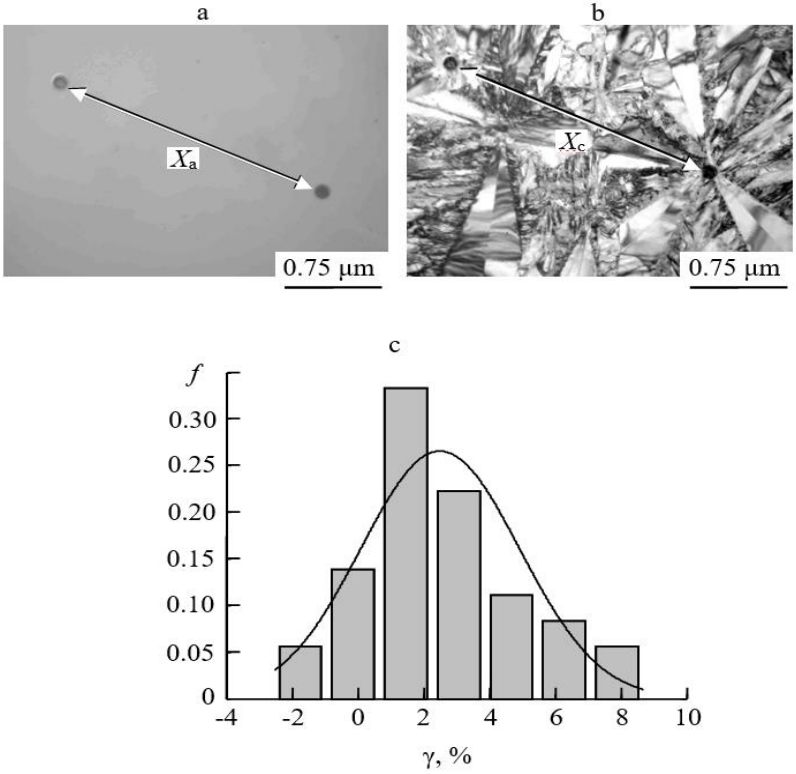

Figure 9.13. Electron microscopy image of the HfO_2 film area before (a) and after (b) crystallization. X_a and X_c are the distances between hardened hafnium micro drops before and after film crystallization, respectively. Histogram (c) of relative frequencies f of the appearance of measured values of relative density changes γ during crystallization of the film and the curve, corresponding to the Gaussian distribution.

The increasing of density of the film matter during crystallization of amorphous ZrO_2 is much higher than in the case of amorphous HfO_2 (Tab. 1.2). According [195] with increasing temperature from room temperature (amorphous HfO_2) to 750°C (crystalline HfO_2) the density of matter rises from 8.96 $g \cdot cm^{-3}$ to 9.40 $g \cdot cm^{-3}$. For this case, according to (1.2), $\gamma = 4.91\%$, which is slightly higher than the upper limit of the confidence interval 4.17%. For monoclinic phase of HfO_2 the density of matter $\rho_c = 9.68$ $g \cdot cm^{-3}$ [196]. For amorphous phase of HfO_2 the density of matter $\rho_a = 9.39$ $g \cdot cm^{-3}$ [197]. In this case according to (1.2) $\gamma = 3.09\%$. This value of γ falls within the confidence interval from 0.85% to 4.17%, established in this work.

REFERENCES

1. L.W. Hobbs, Radiation effects in analysis of inorganic specimens by TEM, in: J. J. Hren, J. I. Goldstein, D. C. Joy (Eds.), Introduction to Analytical Electron Microscopy, Plenum, New York, 1979, pp. 437 - 490. https://link.springer.com/chapter/10.1007/978-1-4757-5581-7_17

2. S.M. Zharkov, L.I. Kveglis, Phys. Solid State, 46, 969-974 (2004) https://link.springer.com/article/10.1134/1.1744977

3. H König, Naturwissenschaften 34, 108 (1947). https://doi.org/10.1007/BF00602631

4. M.W. Thompson. Defects and Radiation Damage in Metals, London: Cambridge U.P., 1969 https://catalogue.nla.gov.au/Record/2506345

5. Bagmut A.G., Bagmut I.A. Kinetics of electron beam crystallization of amorphous films of Yb_2O_2S // Journal of Non-Crystalline Solids, Volume 547, 1 November 2020, 120286. https://doi.org/10.1016/j.jnoncrysol.2020.120286

6. Bagmut A., Bagmut I., Devizenko A., In situ TEM study of crystals growth in amorphous Ti-Zr-Ni films at electron beam irradiation // Eur. Phys. J. Appl. Phys.- 2023 V. 98, № 34, P. 1-8. https://doi.org/10.1051/epjap/2023220293

7. Bagmut A.G. Electron Microscopic Investigation of the Kinetics of the Layer and Island Crystallization of Amorphous V_2O_3 Films Deposited by Pulsed Laser Evaporation // Physics of the Solid State.- 2017.- V. 59, № 6, P. 1225 – 1232. https://doi.org/10.1134/S1063783417060038

8. Bagmut A.G. Morphology and kinetics of crystals growth in amorphous films of Cr_2O_3, deposited by laser ablation // Journal of Crystal Growth.- 2018.- V. 492, № 6, P. 92 – 97. https://doi.org/10.1016/j.jcrysgro.2018.03.038

9. A. Bagmut, I. Bagmut, In situ crystallization of amorphous Sb_2Se_3 films at electron beam irradiation // Molecular Crystals and Liquid Crystals. 2024.- V. 768, № 5, P. 63-71. https://doi.org/10.1080/15421406.2024.2309774

10. Bagmut A.G., Beresnev V.M. Kinetics of the Electron Beam Induced Crystallization of Amorphous ZrO_2 Films Obtained via Ion-Plasma and

Laser Sputtering // Physics of the Solid State.- 2017.- V. 59, № 1, P. 151-155. https://link.springer.com/article/10.1134/S1063783417010024

11. A. Bagmut, Radiation-enhanced crystallization of amorphous Nb_2O_5 films according to TEM with in situ video recording // Molecular Crystals and Liquid Crystals.- 2024.- V.768, № 14.- P. 693-700. https://doi.org/10.1080/15421406.2024.2358729

12. Bagmut A.G. Dendrite Growth in Amorphous films of HfO_2 Under Electron-Beam Irradiation "*In Situ*" // Journal of Advanced Microscopy Research.- 2018.- V.13, № 4. – P. 451 - 457. https://doi.org/10.1166/jamr.2018.1413

13. Bagmut A.G., Bagmut I.A. Kinetics of crystals growth under electron-beam crystallization of amorphous films of hafnium dioxide // Functional Materials.- 2018.- V.25, № 3.- P. 525–533. https://doi.org/10.15407/fm25.03.525.

14. Bagmut A.G. Layer, interjacent and island polymorphous crystallization of amorphous Ta_2O_5 films // Functional Materials.- 2022.- V.29, № 1.- P. 52–61. doi:https://doi.org/10.15407/fm29.01.52

15. A.G. Bagmut, V.A. Zhuchkov, D.V. Melnichenko, Functional Materials 14, 351 (2007) Corel Ventura - FM143-14.CHP (functmaterials.org.ua)

16. V.Yu. Kolosov, K.L. Shvamm, A.G. Bagmut, S.N. Grigorov, Journal of Surface Investigation: X-ray, Synchrotron and Neutron Techniques 10, 100 (2004) [In Russian].

17. Long Ba and Yong Qin, J. Appl. Phys. 80, 6170 (1996). https://doi.org/10.1063/1.363691

18. B.J. Kooi, W.M.G. Groot, J.Th.M. De Hosson, J. Appl. Phys. 95, 924 (2004) https://doi.org/10.1063/1.1636259.

19. Bagmut O. G., Bagmut I. O. Iintroduction to Transmission Electron Microscopy «*In Situ*» [Електронний ресурс]: навч. посібник / O. G. Bagmut, I. A. Bagmut; Нац. техн. ун-т "Харків. політехн. ін-т". – Електрон. текст. дані. – Харків, 2024. – 171 с. – URI: https://repository.kpi.kharkov.ua/handle/KhPI-Press/75917

20. Багмут А. Г. Электронная микроскопия пленок, осажденных лазерным испарением: монография / А. Г. Багмут; Нац. техн. ун-т "Харьков. политехн. ин-т". – Харьков: Підручник НТУ "ХПІ", 2014. - 304 с. - URI: https://repository.kpi.kharkov.ua/handle/KhPI-Press/10107

21. Bagmut A.G. Electron Microscopic Investigations of the Layer, Island, and Dendrite Polymorphic Crystallizations of Amorphous Films // Journal of Surface Investigation. X-ray, Synchrotron and Neutron Techniques.- 2013.- V. 7, No 5.- P. 884 – 891(https://doi.org/10.1134/S1027451013050054)

22. Bagmut A.G., Nikitskiy V.P., Pusan V.F., Svechkin V.P., Sokol A.A., Tartakovskaya I.X. // High-molecular compounds. 1982. V. (A) XXIV. №4. P. 773-777 (in Russian).

23. Protsenko I.Yu., Severin V.M., Skorobagat'ko A.F. // Kristall und Tecnik. 1976. T. 11, № 9. C. 941.

24. Burik I.P., Odnodvorets L.V. // Journal of nano- and electronic physics. 2009. V. 1. № 3. P. 24.

25. Bagmut A.G., Bagmut I.A., Murav'ev T.K., Slabokrug D.V. Crystallization and natural aging of thin films produced by pulsed laser evaporation of rhenium // Functional Materials.- 2013.- V.20, № 2.- P. 180–185. http://dx.doi.org/10.15407/fm20.02.180

26. Бублик А.И. Фазовый переход при изменении толщины в тонких металлических пленках / А.И. Бублик, Б.Я. Пинес // ДАН СССР. – 1952 – № 2. – Т. 87. – С. 215–218.

27. Багмут А.Г., Косевич В.М., Шипкова И.Г., Жучков В.А., Олейник Е.Е. Ориентационные соотношения и ферромагнетизм при трансформации кристаллической решетки лазерных конденсатов Ni // Физическая инженерия поверхности.-2009.- Т. 7, № 1-2.- С. 5 - 13.

28. Bagmut A.G., Shipkova I.G., Zhuchkov V.A. Structure and magnetic state of films, deposited by laser sputtering of nickel // Functional Materials.- 2009.- V.16, № 4.- P. 405 – 411

29. Bagmut A.G., Shipkova I.G., Zhuchkov V.A. Structure and Magnetic State of the Films Deposited by Laser Ablation of Composite Nickel and

Palladium Targets // Technical Physics.- 2011.- V. 56, No 4.- P. 531–539 https://link.springer.com/article/10.1134/S1063784211040050

30. Tian W., Sun H.P., Pan X.Q. et. all. Hexagonal close-packed Ni nanostructures grown on the (001) surface of MgO, Applied Physics Letters 86, 13915 (2005).

31. Bagmut A.G., Shipkova I.G., Zhuchkov V.A. Structure, phase states and change of magnetic properties at recrystallization of thin-film Ni laser condensates // Functional Materials.- 2009.- V.16, № 2.- P. 161 – 169.

32. Мовчан Б.А. Жаростойкие покрытия, осаждаемые в вакууме /Б.А. Мовчан, И.С. Малашенко. – К.: Наукова думка, 1983.

33. А.С. 1689794 СССР, МКИ G 01 N9 / 00. Способ определения относительного изменения плотности / А.Г. Багмут, Г.П. Николайчук (СССР). – № 4713629/25; Заявлено 04.07.89; Опубл. 07.11.91, Бюл. № 41. – 3 с.

34. Багмут А.Г., Жучков В.А., Шипкова И.Г., Олейник Е.Е. Объемные изменения и фазовые трансформации в тонкопленочных лазерных конденсатах никеля при отжиге // Поверхность. Рентгеновские, синхротронные и нейтронные исследования.-2009.-№ 10.- С. 54 - 58.

35. International Centre for Diffraction Data-JCPDC. 1996. Card № 45–1027.

36. International Centre for Diffraction Data-JCPDC. 1996. Card № 04–0850.

37. Уманский Я.С. Физика металлов / Я.С. Уманский, Ю.А. Скаков. – М.: Атомиздат, 1978. – 352 с.

38. Бублик А.И., Пинес Б.Я. Фазовый переход при изменении толщины в тонких металлических пленках // ДАН СССР. 1952. Т.87, №2, С. 215-218.

39. J.B. Goodenough, “Band Structure of Transition Met als and Their Alloys,” in Ferromagnetism of Metals and Alloys (Phys. Rev. 120, 67 (1960); Inostrannaya Literatura, Moscow, 1963).

40. X. He, L.T. Kong, B.X. Liu, J. Appl. Phys., 97, 106107 (2005).

41. A. Frydman, T.L. Kirk, R.C. Dynes, Solid State Communications, 114, 481 (2000).

42. Багмут А.Г. Формирование пленок при импульсном лазерном распылении составных мишеней Ni-Pd / А.Г. Багмут, И.Г. Шипкова, В.А. Жучков // Письма в ЖТФ. – 2010. – Т.36, № 8. – С. 52–59.

43. Багмут А.Г. Наноструктурные состояния в пленках, осажденных лазерной абляцией составных мишеней Ni-Pd и Ni-Au / А.Г. Багмут, И.А. Багмут, И.Г. Шипкова, В.А. Жучков // Вестник Самарского государственного // Металлофиз. новейшие технол. – 2011. – Т.33, №2. – С. 211–222.

44. Bagmut A.G., Shipkova I.G., Zhuchkov V.A. Film Formation during Pulsed Laser Ablation of Nickel–Palladium Composite Targets // Technical Physics Letters.- 2010.- V. 36, No 4.- P. 371–374 Film formation during pulsed laser ablation of nickel-palladium composite targets | SpringerLink.

45. Багмут А.Г., Шипкова И.Г., Жучков В.А. Структура и фазовые превращения в пленках, осажденных совместным лазерным распылением Ni и Pd // Вісник Харківського Національного Університету імені В.Н. Каразіна. Серія “Фізика”.- 2010.- № 914.- Вып. 13.-С. 54 – 59.

46. Барабаш О.М. Структура и свойства металлов и сплавов / О.М. Барабаш, Ю.Н. Коваль: Справочник. - К.: Наук. Думка, 1986. – 598 с.

47. Vegard L. Die Konstitution der Mischkristalle und die Raumfüllung der Atome / L. Vegard // Zeitschrift für Physik. – 1921. – V. 5, № 1. – P. 17–26.

48. G.B. Bokiy, Crystal Chemistry (MGU, Moscow, 1960) [in Russian].

49. Bagmut A.G., Shipkova I.G., Zhuchkov V.A. Structure and Magnetic State of the Films Deposited by Laser Ablation of Composite Nickel and Palladium Targets // Technical Physics.- 2011.- V. 56, No 4.- P. 531–539 https://link.springer.com/article/10.1134/S1063784211040050

50. Bagmut A.G., Shipkova I.G., Zhuchkov V.A. Structure, phase states and change of magnetic properties at recrystallization of thin-film Ni laser condensates // Functional Materials.- 2009.- V.16, № 2.- P. 161 – 169. http://functmaterials.org.ua/contents/16-2/

51. Багмут А.Г., Шипкова И.Г., Жучков В.А. Структурные превращения и изменение магнитных свойств при отжиге тонкопленочных лазерных конденсатов Ni // Металлофиз. новейшие технол.- 2009.- Т.31, №6.- С. 827–836.

52. Bagmut A.G., Shipkova I.G., Zhuchkov V.A. Structure and magnetic state of films, deposited by laser sputtering of nickel // Functional Materials.- 2009.- V.16, № 4.- P. 405 – 411. http://functmaterials.org.ua/contents/16-4/

53. Бондарь В.В. Некоторые аспекты некристаллического твердого состояния // Итоги науки и техники. Сер. химия твердого тела. Т.2.-М.: ВИНИТИ, 1984.- С. 4-14.

54. Wang R., Merz M.D. Polimorphic bonding and thermal stability of elemental non crystalline solids / /Phys. stat. solidi (a).-1977.-V.39, №2.-P. 697-703.

55. Комник Ю.Ф. Получение и структура низкотемпературных аморфных конденсатов металлов // ФНТ.-1982.-Т.8, №1.-С. 3-33.

56. Barna P.B. Umpurity effect in the structural development of vacuum deposited thin films // Proc. 9 Int.Vac.Congr.-Madrid.-1983.-P. 382-396.

57. Багмут А.Г., Косевич В.М., Сарана В.Д., Николайчук Г.П., Зубарев Е.И. Бурлакова М.В. Аморфизированные лазерные конденсаты золота: получение, структура и свойства // Вопросы атомной науки и техники. Сер. вакуум, чистые материалы, сверхпроводники.- 1999.- № 1(9).- С. 63– 68.

58. Bagmut A.G. Formation condition and crystallization features of amorphized laser condensates of gold // Fanctional Materials.- 1999.- V.6, №4.- P. 666 – 673.

59. Багмут А.Г. Особенности структурообразования при лазерном распылении золота в газовой среде // Изв.АН СССР.Сер.физическая.- 1993.-Т.57, №2.-С. 112-116.

60. Багмут А.Г., Косевич В.М., Сарана В.Д., Николайчук Г.П., Зубарев Е.И. Бурлакова М.В. Аморфизированные лазерные конденсаты золота: получение, структура и свойства // Вопросы атомной науки и

техники. Сер. вакуум, чистые материалы, сверхпроводники.- 1999.- № 1(9).- С. 63– 68.

61. Фромм Е., Гебхард Е. Газы и углерод в металлах. М.: Металлургия, 1980.-711 с.

62. Беленький В.З. Геометрико-вероятностные модели кристаллизации.-М.: Наука, 1980.-84 с.

63. Александров Л.Н., Эдельман Ф.Л. О некоторых особенностях кристаллизации диэлектрических пленок на кремнии//Изв. АН СССР. Сер. физическая.-1977.-Т.41, №11.-С. 2310-2314.

64. Александров Л.Н., Эдельман Ф.Л. Ударная кристаллизация в аморфных пленках // Синтез и рост совершеных кристаллов и пленок полупроводников.-Новосибирск: Наука, 1981.-С. 38-43.

65. Шкловский И.А., Кузьменко В.М. Взрывная кристаллизация аморфных веществ // УФН.-1989.-Т.157, №2.-С. 311-338.

66. Палатник Л.С., Косевич В.М. Исследование диффузионного и бездиффузионного превращений в аморфных пленках сурьмы//ДАН СССР.-1958.-Т.121, №1.-С.97-100.

67. Фельц А. Аморфные и стеклообразные неорганические твердые тела.-М.: Мир, 1986.-556 с.

68. Смирнов В.Д., Школьников Е.В., Ормонт Б.Ф. Кинетика кристаллизации стеклообразного селена, легированного элементами IV-А группы // Физ. и хим. стекла.-1977.-Т.3, №5.-С.480 - 486.

69. Kim K.S., Turnbull D. Crystallization of amorphous selenium films. Morphology and Kinetiks // J. Appl.Phys.-1973.-V.44, №12.-P.5237-5244.

70. Шулаев В.М., Коган В.С., Кулинич В.М. и др. Легирование электрофотографических селеновых слоев кислородом. // ВАНТ.Сер.: ЯФИ.-1991.-Вып.1(19).-С. 75-77.

71. Болотов И.Е., Клепцова Г.Н., Серков Л.А., Швалев В.О. Особенности кристаллизации аморфных вакуумных конденсатов селена // Изв. АН СССР. Сер. Неорг. матер.-1981.-Т.17, №9.-С.1533-1536.

72. Багмут А.Г., Сарана В.Д., Машкаров Ю.Г. Получение и структурный анализ кислородосодержащих пленок селена, осажденных из

лазерной эрозионной плазмы // ВАНТ. Сер.: ЯФИ. -1994.-Вып. 1(27).- С. 63-68.

73. Гюнтеродт Г., Бек Г. Металлические стекла. Ионная структура, электронный перенос и кристаллизация.-М.: Мир, 1983.-330 с.

74. Bagmut A.G. Morphology and crystallization kinetics of Se–O films deposited by laser sputtering // Functional Materials.-1996.- V.7, № 6.- P. 42–46.

75. Kim K.S., Turnbull D. Crystallization of amorphous selenium films. Morphology and Kinetiks // J. Appl.Phys.-1973.-V.44, №12.-P.5237-5244.

76. Stiller W. Arrhenius equation and non-equilibrium kinetics: 100 years Arrhenius equation. BSB B.G. Teubner, 1989, 160 p.

77. U. Köster, U. Herold, in: Glassy Metals I. Ionic Structure, Electronic Transport, and Crystallization, edited by H.-J. Güntherodt and H. Beck. (Springer, Berlin Heidelberg, New York, 1981) https://www.springer.com/gp/book/9783662308981.

78. Bagmut A.G., Kosevich V.M., Nikolaychuk G.P., Kirichenko V.G., Sarana V.D. Oxygen influence on structurization in transitional metal films, deposited from laser erosion plasma // Functional Materials.- 1999.- V.6, №5.- P. 951–957.

79. Лазарев В.Б., Соболев В.В., Шаплыгин И.С. Химические и физические свойства простых оксидов металлов.-М.: Наука, 1983.-239 с.

80. Багмут А.Г., Косевич В.М., Николайчук Г.П. Структура и фазовые превращения в аморфных пленках, осажденных лазерным испарением переходных металлов // ВАНТ.Сер. Ядерно-физ.исслед.-1990.-№4(12).-С. 59-64.

81. Венк Г.Р. Электронная микроскопия в минералогии.-М.:Мир, 1979.- 541 с.

82. Guo-Fu Zhou. Materials aspects in phase change optical recording // Materials Science and Engineering: A.- 2001.- V.304-306, P. 73-80. https://doi.org/10.1016/S0921-5093(00)01448-9

83. Moghadam, P. Voorhees. Thin film phase transformation kinetics: from theory to experiment // *Scripta Materialia*, 2016, V. 124, p. 164-168. https://doi.org/10.1016/j.scriptamat.2016.07.010

84. Bagmut A.G. Classification of the Amorphous Film Crystallization Types with Respect to Structure and Morphology Features // Technical Physics Letters.- 2012.- V. 38, No 5.- P. 488–491 http://link.springer.com/article/10.1134/S1063785012050197)

85. Kooi B.J. In situ transmission electron microscopy study of the crystallization of $Ge_2Sb_2Te_5$ / B.J. Kooi , W.M.G. Groot, J.T.M. Hosson // Journal of Applied Physics. – 2004. – V. 95. – № 3. – P. 924–932. https://doi.org/10.1063/1.1636259

86. Матвеев А.Н. Оптика / А.Н. Матвеев. – М. : Высшая школа, 1985. 351 с.

87. Палатник Л.С. Ориентированная кристаллизация / Л.С. Палатник, И.И. Папиров. – М. : Металлургия, 1964. - 408 с.

88. Иевлев В.М. Тонкие пленки неорганических материалов: механизм роста и структура / В.М. Иевлев. – Воронеж: издательство Воронежского государственного университета, 2008. – 496 с.

89. Bagmut A.G. Structural and morphological features of crystallization reactions of amorphous films according to the electron microscopy data // Functional Materials.- 2012.- V.19, № 3.- P. 370 – 377. Corel Ventura - FM193-10.CHP (functmaterials.org.ua)

90. Bagmut A.G. Layer, island and dendrite crystallizations of amorphous films as analogs of Frank–van der Merwe, Volmer–Weber and Stranski–Krastanov growth modes // Functional Materials.- 2019.- V.26, № 1.- P. 6–15. https://doi.org/10.15407/fm26.01.6.
http://functmaterials.org.ua/contents/26-1/fm261-6.pdf

91. Bagmut A.G. “In Situ” Electron Microscopy Measurements of the Relative Density changes Upon Phase Transformations in Thin Solid Films // J. Adv. Microsc. Res.- 2013.- V.8, № 4. –P. 305 - 308. https://doi.org/10.1166/jamr.2013.1175

92. Zharkov, S.M., Kveglis, L.I. Electron-beam-initiated crystallization of iron-carbon films. *Phys. Solid State* 46, 969–974 (2004). https://doi.org/10.1134/1.1744977

93. Bagmut A.G., Bagmut I.A., Structural and kinetic aspects of electron-beam crystallization of amorphous films of antimony sulfide // Molecular Crystals and Liquid Crystals.- 2021.- V. 720, № 1, P. 26–37. https://doi.org/10.1080/15421406.2021.1905279

94. Y. Gao, H. Leiste, M. Stueber, S.Ulrich, The process of growing Cr_2O_3 thin films on α-Al_2O_3 substrates at low temperature by r.f. magnetron sputtering, J. Cryst. Growth 457 (2017) 158–163, https://doi.org/10.1016/j.jcrysgro.2016.08.009

95. J. Wang, A. Gupta, T.M. Klein, Plasma enhanced chemical vapor deposition of Cr_2O_3 thin films using chromium hexacarbonyl ($Cr(CO)_6$) precursor, Thin Solid Films 516 (2008) 7366-7372, https://doi.org/10.1016/j.tsf.2008.02.027

96. H. Mändar, T. Uustare, J. Aarik, A. Tarre, A. Rosental, Characterizationof asymmetric rhombohedral twinin epitaxial α-Cr_2O_3 thin films by X-ray and electron diffraction, Thin Solid Films 515 (2007) 4570–4579, http://dx.doi.org/ 10.1016/j.tsf.2006.11.037

97. S.J. Dong, B. Song, B. Hansz, H.L. Liao, C. Coddet, Microstructure and properties of Cr_2O_3 coating deposited by plasma spraying and dry-ice blasting, Surf. Coat. Technol. 225 (2013) 58-65, https://doi.org/10.1016/j.surfcoat.2013.03.016

98. C. Cheng, H. Gomi, H. Sakata, Electrical and Optical Properties of Cr_2O_3 Films Prepared by Chemical Vapour Deposition, Phys. Stat. Sol. (a) 155 (1996) 417-425, https://doi.org/10.1002/pssa.2211550215

99. E. Sourty, J.L. Sullivan, M.D. Bijker, Numerical modelling of subsurface stress in magnetic data tape heads due to the dynamic contact with a tape, Tribol. Int. 35 (2002) 171-184, https://doi.org/10.1016/S0301-679X(01)00113-X

100. H. Cetinel, E. Celikb, M.I. Kusoglu, Tribological behavior of Cr_2O_3 coatings as bearing materials, J. Mater. Process. Technol. 196 (2008), 259-265, https://doi.org/10.1016/j.jmatprotec.2007.05.048

101. A.G. Bagmut, S.N. Grigorov, V.A. Zhuchkov, V.Yu. Kolosov, V.M. Kosevich, D.V. Melnichenko, Morphology and conjunction of nanocrystals growing in Cr-O and V-O amorphous films during annealing, Russian Phys. Journal 50 (2007), 1071–1078, (https://link.springer.com/article/10.1007/s11182-007-0157-6)

102. Bagmut A.G. Morphology and kinetics of crystals growth in amorphous films of Cr_2O_3, deposited by laser ablation // Journal of Crystal Growth.- 2018.- V. 492, № 6, P. 92 – 97. https://doi.org/10.1016/j.jcrysgro.2018.03.038

103. Bagmut A.G., Bagmut I.A., Layer polymorphous crystallizations of amorphous films: structural and kinetic aspects // Molecular Crystals and Liquid Crystals.- 2023.- V. 750, № 1, P. 1-12. https://www.tandfonline.com/doi/full/10.1080/15421406.2022.2073031

104. E.H. Lockwood, A Book of Curves, Cambridge University Press, Cambridge, 1967. https://www.amazon.com/exec/obidos/ASIN/0521055857/ref=nosim/ericstreasuretro

105. Bagmut A.G. Growth of Needle-Shaped Crystals in Amorphous Films of Cr_2O_3 and V_2O_3 Under Electron-Beam Irradiation // J. Adv. Microsc. Res.- 2018.- V.13, № 3. –P. 376 - 380. https://doi.org/10.1166/jamr.2018.1405

106. Bagmut A.G., Zhuchkov V.A., Melnichenko D.V. Autoepitaxy and the main orientational relations at crystallization out of amorphous state in Cr-O and V-O films // Functional Materials.- 2007.- V.14, № 3.- P. 351 - 355. http://functmaterials.org.ua/contents/14-3/fm143-14.pdf

107. Bagmut A.G., Bagmut I.A., Kinetics of autoepitaxial crystal growth in amorphous films of Cr_2O_3 // Journal of Crystal Growth.- 2019.- V. 517, P. 68 – 71. https://doi.org/10.1016/j.jcrysgro.2019.04.016 https://www.sciencedirect.com/science/article/pii/S0022024819302301?via%3Dihub

108. A. Chernov. Modern Crystallography III. Crystal Growth; Springer: Berlin, (1984). https://www.springer.com/la/book/9783642818370.

109. V.Yu. Kolosov, A.R. Thölén, Transmission electron microscopy studies of the specific structure of crystals formed by phase transition in iron oxide amorphous films, Acta Materialia 48 (2000), 1829-1840. https://doi.org/10.1016/S1359-6454(99)00471-1

110. Bagmut A.G. 'In-Situ' Electron Microscopy Video Registration of Thin Amorphous Films Crystallization // Metallofiz. Noveishie Tekhnol.- 2020.- V. 42, № 8, P. 1065 – 1068. https://doi.org/10.15407/mfint.42.08.1065

111. Bagmut A.G., Taran A.V. Coherent Crystallization of Amorphous Films According to *In Situ* Transmission Electron Microscopy Data // J. Adv. Microsc. Res.- 2013.- V.8, № 1. –P. 57-60. DOI: https://doi.org/10.1166/jamr.2013.1137

112. Bagmut A.G. Electron Microscopic Investigations of the Layer, Island, and Dendrite Polymorphic Crystallizations of Amorphous Films // Journal of Surface Investigation. X-ray, Synchrotron and Neutron Techniques.- 2013.- V. 7, No 5.- P. 884–891(https://doi.org/10.1134/S1027451013050054)

113. F. M. Shemyakin and P. F. Mihalev, Physical-Chemical Periodic Processes, AS USSR, Moscow (1938).

114. S. Le Duc, Théorie Physico-Chimique de la Vie et Générations Spontanées (Paris A: Poinat: 1910) (in French).

115. Bagmut A.G., Shipkova I.G., Zhuchkov V.A. Structure and magnetic state of films, deposited by laser sputtering of nickel // Functional Materials.- 2009.- V.16, № 4.- P. 405 - 411. http://functmaterials.org.ua/contents/16-4/

116. F. Carlier, S. Benrezzak, Ph. Cahuzac, N. Kebaili, A. Masson, A. K. Srivastava, C. Colliex, and C. Bréchignac. Dynamics of polymorphic nanostructures: from growth to collapse // Nano Lett.- 2006.- V.6(9), P. 1875-9. DOI: 10.1021/nl060781n

117. S. Dub, V. Starikov. Elasticity module and hardness niobium and tantalum anode oxide films. Functional Materials. 2007.- V. 14, № 3.- P. 347-350. Corel Ventura - FM143-06.CHP (functmaterials.org.ua)

118. E. Pieretti, M. Pillis. Electrochemical Behavior of Nb_2O_5 Films Produced by Magnetron Sputtering. *Int. J. Electrochem. Sci.*, 13(2018)8108-8115 (PDF 221 K). doi: 10.20964/2018.08.78

119. J. Hwang, N. Kim, S. Shin, H. Lee, J. Ryu, T. Eom, B. Park, C. Kim, T. Chung. Synthesis of novel volatile niobium precursors containing carboxamide for Nb_2O_5 thin films. Polyhedron 200 (2021) 11513. https://doi.org/10.1016/j.poly.2021.115134

120. C. Ücker, F. Riemke, N. Neto, A. Santiago, T. Siebeneichler, N. Carreno, M. Moreira, C. Raubach, S. Cava. Influence of Nb_2O_5 crystal structure on photocatalytic efficiency. Chemical Physics Letters 764 (2021) 138271. https://doi.org/10.1016/j.cplett.2020.138271

121. R. Romero, E. Dalchiele, F. Martín, D. Leinen, J. Ramos-Barrado. Electrochromic behaviour of Nb_2O_5 thin films with different morphologies obtained by spray pyrolysis. Solar Energy Materials and Solar Cells. V. 93, № 2 (2009), P. 222-229. https://doi.org/10.1016/j.solmat.2008.10.012

122. C. Nico, L. Rino, M. Matos, R. Monteiro, F. Costa, T. Monteiro, M. Graca. NbO/Nb_2O_5 core–shells by thermal oxidation. J. Eur. Ceram. Soc. 33 (2013) 3077-3083. https://doi.org/10.1016/j.jeurceramsoc.2013.06.020

123. N. Terao. Structures des Oxydes de Niobium. *Jpn. J. Appl. Phys. 1963.* 2 156. https://doi.org/10.1143/JJAP.2.156

124. V. Kosevich, A. Sokol, T. Dzina. Defective structure of niobium and tantalum nonstoichiometric oxides. Surface. Physics, chemistry, mechanics. 1984. 3. 107-113 [in Russian].

125. V. Kosevich, A. Sokol, Yu. Dyakonenko. Features of electron diffraction patterns of Nb_2O_5 crystals with a long-period shear superstructure. Crystallography. 1983. 28, № 3, 483-487 [in Russian].

126. 9. J. Spyridelis, P. Delavignette, S. Amelinckx. On the Superstructures of Ta_2O_5 and Nb_2O_5. Phys. stat. sol. 19, 683-704 (1967). https://doi.org/10.1002/pssb.19670190220

127. A. Bagmut, Radiation-enhanced crystallization of amorphous Nb_2O_5 films according to TEM with in situ video recording // Molecular

Crystals and Liquid Crystals.- 2024.- V.768, № 14.- P. 693-700. https://doi.org/10.1080/15421406.2024.2358729

128. Bagmut A.G. Relative length as a classification parameter of the crystallization mode of amorphous films // Problems of Atomic Science and Technology.- 2022.- V. 137(1) - P. 64–68. https://doi.org/10.46813/2022-137-064

129. L.S. Palatnik, A.A. Nechitailo, A.A. Kozma, Polyamorphism and substructure of short-range order in amorphous boron films, Dokl. Akad. Nauk SSSR 261 (1981) 1134–1137. http://www.mathnet.ru/links/43bf05d9ca4a07388e704574f004525a/dan44940.pdf

130. K.F. Kelton, W.J. Kim, R.M. Stroud, A stable Ti-based quasicrystal. Appl. Phys. Lett. 70, 3230 (1997) https://doi.org/10.1063/1.119133

131. A.M. Viano, E.H. Majzoub, R.M. Stroud, M.J. Kramer, S.T. Misture, P.C. Gibbons, K.F. Kelton, Hydrogen absorption and storage in quasicrystalline and related Ti-Zr-Ni alloys. Phil. Mag. A78, 132 (1998) DOI:10.1080/014186198253714

132. V. Brien, A. Dauscher, P. Weisbecker, F. Machizaud, Growth of a textured quasicrystalline phase in Ti-Ni-Zr films prepared by pulsed laser deposition. Appl. Phys. A76, 187 (2003) https://doi.org/10.1007/s003390201405

133. V Brien, A. Dauscher, P. Weisbecker, J. Ghanbaja, F. Machizau, Transversal growth microstructures of quasicrystalline Ti–Zr–Ni films. J. Cryst. Growth 256, 407 (2003) https://doi.org/10.1016/S0022-0248(03)01350-2

134. V. Azhazha, S. Dub, G. Khadzhay, B. Merisov, S. Malykhiny, A. Pugachov, Structure and peculiarities of nanodeformation in Ti–Zr–Ni quasicrystals. Phil. Mag. 84, 983 (2004) http://dx.doi.org/10.1080/14786430310001641975

135. S.V. Malykhin, V.V. Kondratenko, I.A. Kopylets, S.V. Surovitskiy, I.G. Shipkova, I.F. Mikhailov, E.N. Zubarev, Yu.S. Bogdanov, Features of the Initial Stage of the Formation of Ti-Zr-Ni Quasicrystalline Thin

Films. J. Nano- Electron. Phys. 11, 04011 (2020) https://doi.org/10.21272/jnep.12(4).04011

136. S.V. Malykhin, V.V. Kondratenko, I.A. Kopylets, S.V. Surovitskiy, A.A. Baturin, I.F. Mikhailov, M.V. Reshetnyak, S.S. Borisova, Yu.S. Bogdanov, Structure and Phase Formation Features of Ti-Zr-Ni Quasi-crystalline Films under Heating. J. Nano- Electron. Phys., 11, 03009 (2019) https://doi.org/10.21272/jnep.11(3).03009

137. 10. I.F. Mikhailov, A.A. Baturin, A.I. Mikhailov, S.S. Borisova, Contrast enhancement of X-ray fluorescence spectra using the secondary two-layer radiator. Functional Materials 18, 150 (2011) http://functmaterials.org.ua/contents/18-2/fm182-02.pdf

138. A.L. Patterson, The Scherrer Formula for X-Ray Particle Size Determination. Phys. Rev. 56 (1939) https://doi.org/10.1103/PhysRev.56.978

139. Rokas Kondrotas, Chao Chen, Jiang Tang, Sb_2S_3 Solar Cells. Joule, 2, p. 857-878 (2018) https://doi.org/10.1016/j.joule.2018.04.003

140. JCPDS Powder Diffraction File Card No. 42-1393 (International Centre for Diffraction Data, Swarthmore, PA, 1996).

141. S. Mahanty, J. Merino, M. Lerona, Preparation and optical studies on flash evaporated Sb_2S_3 thin films. J. Vac. Sci. Technol. *A* 15, p. 3060-3064 (1997) https://doi.org/10.1116/1.580847

142. P. Arun, A. Vedeshwar, Phase modification by instantaneous heat treatment of Sb_2S_3 films and their potential for photothermal optical recording. J. Appl. Phys., 79, p. 4029-4036 (1996). https://doi.org/10.1063/1.361832

143. A. Bagmut., S. Grigorov, V. Kosevich, E. Lyubchenko, G. Nikolaychuk, D. Samoylenko. Growth of crystals with bent crystalline lattice in amorphous semiconductor films // Functional Materials.- 2008.- V.15, № 3.- p 332-337. http://functmaterials.org.ua/contents/15-3/fm153-06.pdf.

144. Y. Yang, H.-H. Nahm, O. Sugino, and T. Ohno, Electronic structures of oxygen-deficient Ta_2O_5, AIP Advances 3, (2013) 042101-042108. https://doi.org/10.1063/1.4800899

145. E. Atanassova and A. Paskaleva, Challenges of Ta_2O_5 as high-*k* dielectric for nanoscale DRAMs, Microelectron. Reliab. 47, (2007) 913-923. https://doi.org/10.1016/j.microrel.2006.06.006

146. C. Chaneliere, J. L. Autran, R. A. B. Devine, B. Balland, Tantalum pentoxide (Ta_2O_5) thin films for advanced dielectric applications, Mater. Sci. Eng. R. Rep., 22 (1998) 269-322. https://doi.org/10.1016/S0927-796X(97)00023-5

147. C. Chaneliere, S. Four, J. L. Autran, R. A. B. Devine, and N. P. Sandler, Properties of amorphous and crystalline Ta_2O_5 thin films deposited on Si from a Ta(OC2H5)5 precursor, J. Appl. Phys., 83 (1998) 4823-4829. http://dx.doi.org/10.1063/1.367277

148. A. Krishnaprasanth, and M. Seetha, Solvent free synthesis of Ta_2O_5 nanoparticles and their photocatalytic properties, AIP Advances, 8 (2018) 055017-1 - 055017-7. https://doi.org/10.1063/1.5019423

149. T. Dimitrova, U, K. Arshak, E. Atanassova, Crystallization effects in oxygen annealed Ta_2O_5 thin films on Si, Thin Solid Films, 381 (2001) 31 - 34. https://doi.org/10.1016/S0040-6090(00)01569-8

150 S. Shibata, Dielectric constants of Ta_20_5 thin films deposited by r.f. sputtering, Thin Solid Films, 277 (1996) 1-4. https://doi.org/10.1016/0040-6090(95)08234-4

151. Spyridelis, P. Delavignette, S. Amelinckx, On the Superstructures of Ta_2O_5 and Nb_2O_5, Phys. stat. sol., 19 (1967) 683-704. https://doi.org/10.1002/pssb.19670190220

152. K.-H. Min, R. Sinclair, I.-S. Park, S.-T. Kim and U.-I. Chung, Crystallization behaviour of ALD-Ta_2O_5 thin films: the application of in-situ TEM, Phil. Mag., 85 (2005) 2049-2063. https://doi.org/10.1080/14786430500036546

153. JCPDS Powder Diffraction File (International Centre for Diffraction Data, Swarthmore, PA, 1996).

154. V.Yu. Kolosov, A.R. Thölén, Transmission electron microscopy studies of the specific structure of crystals formed by phase transition in iron

oxide amorphous films, Acta Mater. 48 (2000) 1829-1840. https://doi.org/10.1016/S1359-6454(99)00471-1.

155. Bagmut A.G. Layer, interjacent and island polymorphous crystallization of amorphous Ta_2O_5 films // Functional Materials.- 2022.- V.29, № 1.- P. 52–61. doi:https://doi.org/10.15407/fm29.01.52 http://functmaterials.org.ua/contents/29-1/fm291-52.pdf

156. A.N. Kolmogorov, On the statistical theory of crystallization of metals, Izv. Acad. Sci. USSR, Ser. Math. 1 (1937) 355-359 [in Russian]. https://www.scirp.org/(S(i43dyn45teexjx455qlt3d2q))/reference/ReferencesPapers.aspx?ReferenceID=880675.

157. G. Ruitenberg, A.K. Petford-Long, R.C. Doole, Determination of the isothermal nucleation and growth parameters for the crystallization of thin $Ge_2Sb_2Te_5$ films, J. Appl. Phys. 2 (2002) 3116-3123. https://doi.org/10.1063/1.1503166

158. N. Ohshima, Crystallization of germanium–antimony–tellurium amorphous thin film sandwiched between various dielectric protective films, J. Appl. Phys. 79 (1996) 8357-8363. https://doi.org/10.1063/1.362548.

159. A.I. Zubkov, M.B. Guseva, V.G. Babaev, Point defects, light stimulation and oriented growth of thin gold films on AHC, Izv. Acad. Sci. USSR, Ser. Phys. 44 (1980) 1276-1284.

160. Bagmut A. Crystal growth in amorphous films of tantalum pentoxide // Molecular Crystals and Liquid Crystals.- 2023.- V. 765, № 1, P. 105-113. https://doi.org/10.1080/15421406.2023.2215032

161. A. V. Ushakov, I. V. Karpov, and A. A. Lepeshev. Influence of the oxygen concentration on the formation of crystalline phases of ZrO_2 nanoparticles during the low-pressure arc-discharge plasma synthesis // Phys. Solid State.- 2015.- V. 57, № 11, P. 2320-2322. https://link.springer.com/article/10.1134/S1063783415110359

162. V. G. Zavodinsky and A. N. Chibisov. Stability of cubic zirconia and of stoichiometric zirconia nanoparticles // Phys. Solid State.- 2006.- V. 48, № 2, P. 363-368. https://link.springer.com/article/10.1134/S1063783406020296

163. M. A. Pugachevskii, V. G. Zavodinskii, and A. P. Kuz'menko. Dispersion of zirconium dioxide by pulsed laser radiation // Tech. Phys.- 2011.- V. 56, № 2, 254-258. https://link.springer.com/article/10.1134/S1063784211020241

164. Bagmut A.G., Bagmut I.A., Reznik. N.A. Formation of ZrO_2 cubic phase microcrystals during crystallization of amorphous films deposited by laser ablation of Zr in an oxygen atmosphere // Physics of the Solid State.- 2016.- V. 58, № 6, P. 1262-1265. http://link.springer.com/article/10.1134/S1063783416060056

165. V. M. Beresnev, S. A. Klimenko, I. N. Toryanik, A. D. Pogrebnjak, O. V. Sobol, P. V. Turbin, and S. S. Grankin. Superhard coatings of the (Zr-Ti-Si)N and (Ti-Hf-Si)N systems produced by vacuum-arc deposition from a separated flow // J. Superhard Mater.- 2014.- V. 36, P. 29-34. https://link.springer.com/article/10.3103/S1063457614010055

166. Bagmut A.G. Radiation enhanced crystallization of amorphous laser condensates of hafnia and zirconia // Problems of Atomic Science and Technology.- 2025.- V. 2(156) - P. 43–48. https://doi.org/10.46813/2025-156-043

167. Bagmut A.G., Bagmut I.A., Modes and kinetics of crystals growth in amorphous films of oxides // Molecular Crystals and Liquid Crystals.- 2018.- V. 673, № 1, P. 120 – 124. https://www.tandfonline.com/doi/abs/10.1080/15421406.2019.1578501.

168. M. Moghadam, P. Voorhees. Thin film phase transformation kinetics: from theory to experiment // Scripta Materialia. 2016, v. 124, p. 164-168. https://doi.org/10.1016/j.scriptamat.2016.07.010

169. E.A. El-Sayad, A.M. Moustafa, S.Y. Marzouk. Effect of heat treatment on the structural and optical properties of amorphous Sb_2Se_3 and Sb_2Se_2S thin films // Physica B. 2009, v. 404, p. 1119-1127. https://doi.org/10.1016/j.physb.2008.11.086

170. JCPDS Powder Diffraction File Card No. 15-0861 (International Centre for Diffraction Data, Swarthmore, PA, 1996).

171. P. Sun, Z. Wu, C. Ai et. al. Thermal Evaporation of Sb_2Se_3 as

Novel Counter Electrode for Dye-Sensitized Solar Cells // ChemistrySelect. 2016, v. 1, p. 1824-1831. https://doi.org/10.1002/slct.201600289

172. Chao Chen, Weiqi Li, Ying Zhou et. al. Optical properties of amorphous and polycrystalline Sb_2Se_3 thin films prepared by thermal evaporation // *Appl. Phys. Lett.* 2015, v. 107, p. 043905. https://doi.org/10.1063/1.4927741

173. Chao Chen, Xinxing Liu, Kanghua Li et. al. High-efficient Sb_2Se_3 solar cell using $Zn_xCd_{1-x}S$ n-type layer // Appl. Phys. Lett., 2021, v. 118, p. 172103. https://doi.org/10.1063/5.0030430

173. M.-Z. Xue, Z.-W. Fu. Pulsed laser deposited Sb_2Se_3 anode for lithium-ion batteries // J. Alloys Compounds. 2008, v. 458, p. 351-356. https://doi.org/10.1016/j.jallcom.2007.03.109

174. M. Castro, F. Domınguez-Adame, A. Sanchez, T. Rodrıguez. Model for crystallization kinetics: Deviations from Kolmogorov-Johnson-Meh-Avrami kinetics // Appl. Phys. Lett. 1999, v. 75, p. 2205-2207. https://doi.org/10.1063/1.124965

175. A. Bagmut. Crystallization of amorphous Sb_2Se_3 films according to TEM with in situ video recording // Funct. Mater.- 2024.- V.31, № 1.- P. 18-25. https://doi.org/10.15407/fm31.01.18

176. A. Bagmut, I. Bagmut, In situ crystallization of amorphous Sb_2Se_3 films at electron beam irradiation // Molecular Crystals and Liquid Crystals. 2024.- V. 768, № 5, P. 63-71. https://doi.org/10.1080/15421406.2024.2309774

177. V.V. Tetyorkin, A.Yu. Sipatov F.F. Sizov, A.I. Fedorenko, A. Fedorov, (001)-oriented lead selenide films grown on silicon substrates // Infrared Phys. & Technol. 1966.- V. 37, P. 379-384. https://doi.org/10.1016/1350-4495(95)00065-8.

178 JCPDS, Powder Diffraction File Card No. 26-0614, (International Centre for Diffraction Data, Swarthmore, PA), 1996.

179. Bagmut A.G., Bagmut I.A. Kinetics of electron beam crystallization of amorphous films of Yb_2O_2S // Journal of Non-Crystalline Solids, Volume 547, 1 November 2020, 120286. https://doi.org/10.1016/j.jnoncrysol.2020.120286.

180. V.P. Zakharov, V.S. Gersasimenko, Structure Features of

Semiconductors in Amorphous State, Naukova Dumka, Kiev, 1976 in Russian https://urss.ru/cgi-bin/ db.pl?lang=Ru&blang=ru&page=Book&id=70586

181. L.S. Palatnik, V.M. Kosevich, M.Ya. Fuks, Formation Mechanism and Substrucnure of Condensed Films, Nauka, Moscow, 1972 (in Russian). http://books.zntu.edu.ua/book_info.pl?id=205938

182. S. Raoux, J.L. Jordan-Sweet, A.J. Kellock, Crystallization properties of ultrathin phase change films, J. Appl. Phys. 103 (2008) 114310-1 - 114310-7. https://doi.org/10.1063/1.2938076.

183. N. Pi, M. Zhang, J. Jiang, A. Belosludtsev, J. Vlček, J. Houška, E. Meletis. Microstructure of hard and optically transparent HfO_2 films prepared by high-power impulse magnetron sputtering with a pulsed oxygen flow control // Thin Solid Films. 2016, v 619, p. 239-249. https://doi.org/10.1016/j.tsf.2016.10.059

184. F. Li, B. Bayer, S. Hofmann, S. Speakman, C. Ducati, W. Milne, A. Flewitt. High-density remote plasma sputtering of high-dielectric-constant amorphous hafnium oxide films // Phys. Status Solidi B. 2013, v. 250, p. 957-967. https://doi.org/10.1002/pssb.201248553

185. JCPDS, Powder Diffraction File Card No. 43-1017, (International Centre for Diffraction Data, Swarthmore, PA), 1996.

186. JCPDS, Powder Diffraction File Card No. 08-0342, (International Centre for Diffraction Data, Swarthmore, PA), 1996.

187. JCPDS, Powder Diffraction File Card No. 21-0904, (International Centre for Diffraction Data, Swarthmore, PA), 1996.

188. A.Bagmut, I. Bagmut, V. Zhuchkov, M. Shevchenko. Laser Deposited Thin Hafnium Dioxide Condensates: Electron Microscopic study // Technical Physics Letters.- 2012.- V. 38, №1.- P. 22-24 http://link.springer.com/article/10.1134/S1063785012010038

189. A. Bagmut, I. Bagmut, V. Zhuchkov, M. Shevchenko. Phase Transformations in Films Deposited by Laser Ablation of Hf in an Oxygen Atmosphere // Technical Physics.- 2012.- V. 57, № 6.- P. 856-860 http://link.springer.com/article/10.1134/S1063784212060035

190. A.Bagmut, I. Bagmut. Kinetics of crystals growth under electron-beam crystallization of amorphous films of hafnium dioxide // Functional Materials.- 2018.- V.25, № 3.- P. 525–533. https://doi.org/10.15407/fm25.03.525.

191. J. Aarik, A. Aidla, H. Mändar, T. Uustare, K. Kukli, M. Schuisky. Phase transformations in hafnium dioxide thin films grown by atomic layer deposition at high temperatures // Appl. Surf. Sci. 2001, v. 173, p. 15-21. https://doi.org/10.1016/S0169-4332(00)00859-X

192. A.Bagmut. Dendrite Growth in Amorphous films of HfO_2 Under Electron-Beam Irradiation "*In Situ*" // Journal of Advanced Microscopy Research.- 2018.- V. 13, № 4.- P. 451-457. https://doi.org/10.1166/jamr.2018.1413

193. A. Shtukenberg, Yu. Punin, E. Gunn, B. Kahr. Spherulites // Chem. Rev.- 2012.- V. 112, P. 1805-1838. https://doi.org/10.1021/cr200297f

194. G. Laemmlein. The process of geometric selection in a growing crystal aggregate // Dokl. Akad. Nauk SSSR.- 1945.- V. 48, P. 177.

195. M. Modreanu, J. Sancho-Parramon, D. O'Connell, J. Justice, O. Durand, B. Servet. Solid phase crystallisation of HfO_2 thin films // Materials Science and Engineering B.- 2005.- V. 118, P. 127-132. https://doi.org/10.1016/j.mseb.2004.12.068

196. S. Ushakov, A. Navrotsky, Y. Yang, S. Stemmer, K. Kukli, M. Ritala, M. Leskelä, P. Fejes, A. Demkov, C. Wang, B.-Y. Nguyen, D. Triyoso, P. Tobin. Crystallization in hafnia- and zirconia-based systems // Physica status solidi (b).- 2004.- V. 241, P. 2268-2278. https://doi.org/10.1002/pssb.200404935

197. D. Ceresoli and D. Vanderbilt. Structural and dielectric properties of amorphous ZrO_2 and HfO_2 // Physical review B.- 2006.- V. 74, P. 125108. https://doi.org/10.1103/PhysRevB.74.125108

CONTENT

Наукове видання

БАГМУТ Олександр Григорович

ТРАНСМІСІЙНА ЕЛЕКТРОННА МІКРОСКОПІЯ СТРУКТУРНИХ ТА ФАЗОВИХ ПЕРЕТВОРЕНЬ У ПЛІВКАХ ПРИ ВПЛИВІ "IN SITU"

Англійською мовою

Відповідальна за випуск проф. Любченко О. А.

В авторській редакції

Видавничий центр НТУ «ХПІ». 61002 Харків, вул. Кирпичова, 2
Свідоцтво про державну реєстрацію ДК № 5478 від 21.08.2017 р.

Електронне видання